FABRICATION OF SILICON-CARBON NANOCOMPOSITES VIA ELECTROSPINNING AND ELECTROSPRAYING PROCESSES FOR THE NEXT GENERATION OF HIGH-RATE LITHIUM-ION BATTERY ANODES

A Dissertation

Presented to the Faculty of the Graduate School

of Cornell University

in Partial Fulfillment of the Requirements for the Degree of

Doctor of Philosophy

by

Ghazal Shoorideh

May 2019

FABRICATION OF SILICON-CARBON NANOCOMPOSITES VIA ELECTROSPINNING AND ELECTROSPRAYING PROCESSES FOR THE NEXT GENERATION OF HIGH-RATE LITHIUM-ION BATTERY ANODES

Ghazal Shoorideh, Ph.D.

Cornell University, 2019.

In the recent years, batteries, especially lithium-ion batteries have garnered a lot of attention for the large-scale energy storage solutions and consumer electronics application. Other applications like transportation also have become a fast-growing market for deployment of different type of batteries. Lithium-ion batteries were introduced to the market in the 90s as a safer alternative to the lithium metal batteries and ever since have dominate multiple markets with even more growth projected. In spite of their ubiquity, the state-of-the-art lithium ion batteries have been using the same carbon anode since their conception. A significant improvement in the capacity of these batteries is only realizable by a change in the chemistry of the electrodes.

For this reason, a lot of research has been dedicated to identifying the most viable candidates for electrode material. Silicon is a promising choice, due to the large theoretical capacity, abundance and non-toxicity. However, the large volume expansion of silicon that occurs during the lithiation process, fatigues the material and results in pulverization and loss of electric contact of the active material. In addition, the 300% volume change makes passivation of the surface difficult, therefore lithium ions get consumed over each cycle. These two mechanisms cause fast capacity fading of the electrode with cycling. Reducing the size of the active material to nano scale is a powerful remedy for pulverization. At the same time introducing material like

carbon that can make a stable passivation layer, and provide electric conductivity that silicon lacks, improves the electrochemical performance of silicon-based anodes.

The work that is presented at this dissertation is aiming to develop robust, environmentally friendly and economical methods for electrode fabrication for the next generation of the lithium ion batteries. Electrospinning was studied as a facile technique for electrode fabrication. A novel process was developed to directly deposit nanofibers of PVA-silicon-carbon nanotubes on the surface of the current collector, which resulted in bypassing multiple steps in the conventional electrode fabrication process. The non-woven fiber mat provided ample space for silicon expansion and ease of access for the electrolyte to the active sites, which resulted in great electrochemical performance of the mat especially at higher currents. The directly deposited method allowed for an in-situ comparison between the different conductive agents added in the nanocomposite. It was found that graphene nanoribbons are superior to their precursor carbon nanotubes, due to their edge groups and flexibility even at a lithiated state. In addition, the dimensions of the nanoribbons were significant in their efficacy as conductive pathways, with larger ribbons surpassing small nanoribbons since they can electronically connect individual nanofibers together.

An effective use of the void spaces in between the can greatly enhance the electrochemical performance of the nanofiber mat. For this reason, aluminum oxide precursor was spin casted onto the fibers and the solution was cured to get a composite of the metal oxide coating and the fiber mat. The resulting electrode exhibited three-fold enhancement in longevity and significant improvement in high-rate performance compared to the uncoated fibers as well as improving the volumetric energy density. In order to reduce the void spaces, electrospraying was employed to directly spray a porous film of silicon and graphene sheets on the surface of the current collector.

To ensure a uniform dispersion of the binder and nanoinclusions a controlled airflow was applied to the sheath layer of the nozzle. The electrochemical performance of these electrodes could further be improved by addition of carbon nanoribbons that can connect the silicon particles that are not directly in contact with graphene sheets. The use of bimodal conductive agent resulted in excellent performance at high currents.

The current work investigated modified electrospinning and electrospraying as facile and economic electrode fabrication techniques for the next generation of lithium ion batteries. Methods developed here are versatile and can be applied to a wide array of chemistries and particle geometry and allows for precise control of the nanoinclusions, which is crucial for an enhancement of electrochemical performance.

BIOGRAPHICAL SKETCH

Ghazal Shoorideh was born in 1987 in Tehran, Iran as the first child of Nazila Morisi and Ali Shoorideh. She completed her elementary and high school education in Tehran in one of the most reputable schools in Tehran. All through her life Ghazal was extremely interested in math and sciences, and under guidance of her parents and teachers, she took part in a number of extracurricular activities throughout her academic career such as science olympiads and projects with schools of different countries. She graduated with honors from high school at 2005 and upon ranking in the top 5% nationwide in the national universities entrance exam, she started her education in polymer engineering at Amirkabir University of Technology, Tehran.

Soon her parents decided that migrating to the United States will be beneficial for the future of Ghazal and her younger sister, so in the summer of 2007 they moved to Los Angeles, CA. Ghazal started her undergraduate education again and graduated from University of Southern California with a bachelor's in chemical engineering. During her undergrad education she became interested in research and started working under the supervision of Dr. Sahimi. To continue with the newly ignited passion for research Ghazal started her master's degree chemical engineering department of Cornell University in 2012, where she started working with professor Joo on metal and metal oxide nanofibers for fuel cell applications. She won the best Master of Engineering Project award for that work and was determined to continue her education. In Fall of 2014 Ghazal started her PhD program at Cornell University with professor Joo as her adviser. The present dissertation is the result of her research on developing fabrication methods for the next generation of lithium ion battery anodes.

To my wonderful sister Taraneh Shoorideh for being my constant source of inspiration.

To the best father in the world Ali Shoorideh for being my confidence in life.

To my extraordinary mother Nazila Morisi for her unconditional love and patience.

ACKNOWLEDGEMENTS

I am so grateful to have so many people who made my life in Ithaca more enjoyable and made my Ph.D. journey possible. First off, I want to thank my thesis adviser professor Yong L. Joo, for giving me a chance and believing in me when I first joined Cornell as a masters student; for encouraging and supporting me in each step of the way and for pushing me to become a better scientist. His knowledge, hard work and his unique approach to solving various problems has continuously served as a source of inspiration for my Ph.D. work.

I also want to thank my committee members professor Archer and Suntivich for constructive feedback and questions that had significant impact in enhancement of my Ph.D work and shaping my views as a scientist. Professor Archer never hesitated to provide me with his time and graciously allowed me to use his lab's facilities. His cheerful comments in our brief encounters in the hallways delighted some of my days in Olin Hall. Special gratitude for professor Abruna not only for teaching the most useful subject to me and doing it with passion and energy, but for always making time for me and providing invaluable feedback.

I gratefully acknowledge my funding from, Axium Nano, LLC, EMD Functional Materials and Hyundai Motors for making this work possible. I am grateful for Sang Mok Park and the practical knowledge that he offered while working together. Additionally, I want to thank Cornell Center for Materials Research (CCMR) for funding and shared facilities that were instrumental in my Ph.D. work. CCMR staff, Phil Carubia, professor Umbach, Don Werder, and Anthony Condo trained me and helped me with instrument issues. Especial thanks to John Grazul for training me and being extremely patient with me and for interesting conversations, and for his entertaining emails.

I am so grateful for my Olin Hall family that made my journey possible. Professor Center who has been a great mentor and advocate for me. Professor Daniel for being a wonderful DGS and my go to person for a variety of issues. Carol Casler, Johanna Tuttle, Stephanie Palcich and Glen Swan for helping throughout my year at Olin Hall. I want to thank all the current and former members of the Joo group for making work so enjoyable day in and day out. I want to especially acknowledge Yevgen Zhmayev, Andrew Shah, Brian Williams and Joe Carlin for their help and support in my research. My excellent undergraduate helpers: Byunghee Ko and Adam Berry for their outstanding work ethic and commitment to research. Snehashis Choudhury was a great source of knowledge with lab and electrochemical related matters and a delight to work with.

I have had the pleasure of meeting so many amazing people during my time in Ithaca and each of them hold a piece of my heart and has made my journey more pleasant and meaningful. I am especially thankful for Dr. Kat Chemelewski for being a great mentor and advocate for me. She has had an immense impact in both my personal and professional life. I am extremely grateful for Marie-Rose and Sharon, for being the best roommates that I could have and for creating and flourishing a friendship that I will forever cherish. For Jenny and her joyful spirit, her listening to me complain and for boosting my mood through the tough times. For my wonderful yoga instructor Melissa, whose classes helped me achieve peace, strength and balance in my life. For my good friends Gizem, Henry, Blaire, Mat, Al, Rick and Lakshmi who has always been there for me and encouraged me to get out of comfort zone. For all my friends at law school, business school and hotel school, who knowing them has made me a better person. For Dan who became the sweetest reason for me to stay in Ithaca, when all I wanted was to leave, and for being my role model for hard work and dedication to achieving goals.

I am forever thankful for people who hold a special place in my heart. For Jessica, her patience and graciousness in dealing with me and everyone around her and for inspiring me to be the best version of myself. For Hugh and his sarcasm, his great stories, for being my travel buddy and my support when I needed it the most. For Zhenia, my amazing friend, for literally picking me up when I was down, for sharing so many memories, conversations and emotions with me. His strategic approach, discipline and work ethic combined with his kindest heart were the reasons why I always looked up to him. Kenville was one of my first friends at Cornell, and still after 6 year our friendship only becomes stronger and stronger every day. He has had such a positive influence on my life and always been there for me. He helped me through multiple critical crossroads, and I am forever for having such a kind-hearted, open minded and sincere friend in my life. The last, but not least in my best friend Borja. We have had such a great time together in Ithaca and abroad and together we met a lot of new people and made great friends. He is by far the most interesting person I know in my life. His sarcasm and dark sense of humor are just disguises for the most caring and kindest heart underneath. I am so happy and thankful to have made such a wonderful friend for life.

I also want to thank my friends from back home Tina, Mobina, Saba, Amsi, Parastoo and my dear cousin Amin who truly is like a brother to me. They have motivated me with their love and loyalty, and their support was the source of my strength throughout my life. I am so lucky and grateful to have an amazing family. They have always been my biggest fans, my support, source of inspiration and strength. Especially my parents Ali Shoorideh and Nazila Morisi to whom I have to contribute anything I achieved in life. My dad's unconditional love, encouragement, support for all my decision and selfless giving reassured me every step of the way. My mom's kindness, patience, intelligence and strength have always motivated me to strive for more. My beautiful,

brilliant, joyful and exuberant sister, Taraneh, is continuously my biggest proponent. She is the person I turn to with all my problems, and her creativity and capabilities have been instrumental to my success and her love is my most prized possession.

TABLE OF CONTENTS

LIST OF FIGURES

Chapter Two

Chapter Three

Chapter Four

Chapter Fiver

LIST OF TABLES

CHAPTER ONE

INTRODUCTION

1.1. Introduction

Energy is one of the primary concerns of the modern humans. With proliferation of technology in every aspect of lives, industrialization and modernization of manufacturing processes, the need for cheap and reliable energy is almost as important to human existence as water is. At the present time, 80% of the total US energy consumption is sourced from fossil fuels which equates to about 78.16 quadrillion Btu per year[1]. Such a heavy dependency on the non-renewable resources is not sustainable due to the limited quantity of these resources and the greenhouse gases produced, which harm the environment. There are a plethora of research and literature predicting the doomed future of the human beings on this planet if continued on the same path. Interested readers can also find resources on the harmful effect of burning fossil fuels on the U.S. Environmental Protection Agency (EPA) website and documents. We are at a critical time where there is still time to reverse the heavy impact of human activities on the environment with the hope of reduction in global warming and preservation of wildlife on our beautiful blue planet. In the recent climate, where some politicians shamelessly deny the destructive effects of human activities on the environment for more financial profit, there is even more need for education and change in the lifestyle of the conscious members of the society in order to save our only habitat. Fortunately, in the past decade there has been a push towards renewable energy sources by the government, environmental activist and conscious consumers as a way to fight global warming.

Most renewable energy sources such as solar and wind are intermittent by nature. They need some sort of energy storage to accompany them to become a reliable source to provide energy to the grid even when no production is taking place (at night, or when wind is not blowing)[2]. A cheap and dependable energy storage solution is highly desirable and crucial for market penetration of renewables. Batteries are one of the most viable solutions for large-scale energy storage. In addition, as mentioned before with the advancement of technology and the prevalence of mobile lifestyle, batteries have become a vital part of everyday lives. However, the state-of-the-art batteries used in the electronic devices are not satisfactory for the average consumer. Therefore, there is a demand for enhancement of battery performances from large-scale energy production and consumer electronics sectors. In addition, other applications such as transportation and defense are rapidly becoming more and more dependent on batteries as well. In response to this growing demand, a lot of investment has been made on research and development of more efficient batteries.

Batteries can have a variety of different chemistries and the choice is highly dependent on the application. In the recent years, lithium ion batteries have dominated the large scale, transportation and consumer electronic sectors, due to their high energy density, relatively lower costs, safety and low rate of self-discharge and high cyclability. For example, according to U.S. Energy Information Administration (eia), more than 80% of the large-scale battery storage capacity installed at 2016 is lithium ion with the rest being made up of nickel-based, sodium-based, lead acid and flow batteries[3]. Improvement in the energy and power density of Li-ion batteries has been an ongoing effort, but slow and marginal. The commercial Li-ion batteries usually use a layered oxide cathode, such as $LiCoO_2$, and graphite as anode[4]. Most of the improvement in the energy and power density of the commercialized Li-ion batteries is due to optimization of their

form factor and geometry, enhancement of the separators[5]–[7] and electrolyte[8] being used in the batteries which can drastically decrease cell impedance, doping and coating[9]–[12] of the electrode materials and better manufacturing processes. However, with the same chemistry or small variation of the same chemistry the current lithium ion batteries are almost at the limit of their practical capacities.

In order to have batteries with higher capacity, a change in the chemistry of the cathode and anode or at least one of the two is necessary. In the recent years, a lot of effort and attention has been given to change of the chemistry of the anode since it has been the same carbon material since the early commercialization of the Li-ion batteries in the 90s by Sony. There exists a plethora of literature on different viable chemistries for the negative electrode of the Lithium ion cells. The most notable of the intercalation negative electrode materials are graphite and $Li_4Ti_5O_{12}$ (LTO), where lithium ions intercalate into the structure of these material upon charging and deintercalate during the discharge of the battery cell[13]. LTO undergoes a highly reversible, zero-strain intercalation process with, with a long voltage plateau (at about 1.5V vs. Li) for the majority of the charge and discharge process[14]. In addition, LTO anodes can be cycled very fast and since the reduction voltage is so high there are no side reactions and reduction of the liquid electrolyte resulting in prolonged cycle life for this material[13], [15]. However, this LTO is inferior to graphite both in terms of specific capacity, which is only about 160 mAh/g, and voltage, that limits the attainable voltage of the full cell, if paired with the already commercialized cathodes.

The next group of anode materials explored are conversion material, where nanoparticles of transition metal oxides, phosphides and fluorides such as CuO and Fe_2O_3 undergo a reduction reaction with lithium ions to produce Li_2O and nano-metals[13], [16]. With this type of materials higher capacities up to 1000 mAh/g were demonstrated, but the conversion reaction usually

happens outside the voltage threshold for most liquid electrolytes which makes passivating the layer very difficult. In addition, these materials have limited performance at higher temperatures and high hysteresis of charge and discharge due to the structural changes that the complete conversion brings about are troublesome inside of a full cell[17].

The next prominent family of negative electrode materials are the ones that undergo an alloying reaction such as Sn and Si. Silicon and tin can be lithiated up to 4.4 Li ions for each Si/Sn atom resulting in high specific capacities of 4200 mAh/g and 900 mAh/g respectively[13]. In this work, we are focusing on Silicon as the material of choice due to its high capacity at room temperature, its abundance in the nature, and the knowledge and infrastructure that has been built over the past couple of decades on silicon processing by the semi-conductor industry. In addition, silicon proposes no health and environmental hazard and is moderately priced in comparison with the other materials and can be sourced from inexpensive origins. Unfortunately, alloying materials exhibit volume expansions of about 300% percent due to hosting high number of lithium ions inside of their structure[18]. This large volume changes during lithiation and delithiation, causes huge stresses on the material and makes achieving a passivation layer difficult, consuming electrolyte at each cycle. At the same time, the high mechanical stress results in fracturing and pulverization of the active material, which leads to isolation of the active material and capacity fading with cycling[19]. Additionally, silicon has a limited conductivity by nature that results in limited ability for high rate applications and in the need for a conductive agent in the electrode.

Multiple approaches to mitigate the problems with silicon has been explored in the literature. Namely, nanostructuring[20]–[22] and making composites[23]–[25] with more stable materials like carbon. Mixing silicon with carbon not only can helps in making a stable passivation films, but it also helps with the conductivity of the electrode material. It has been shown that

making the particles nano-sized helps in alleviation of the mechanical strain and keeping the integrity of the active mass[18], [26]. It should be kept in mind that any effort to improve silicon cyclability has to be done in an economical manner if commercialization and real-world application is desired. In the present effort, a combination of multiple approaches is examined to improve the cycle life, capacity and rate capability of silicon-based materials as negative electrode for lithium ion batteries.

In this dissertation we focused only on the negative electrode and more specifically on silicon for the next generation of anodes for lithium ion batteries. To achieve the aforementioned goals of high capacity, high rate capability and device longevity, nano-structuring and compositing of silicon with carbonous material was done via scalable methods such as electrospinning and electrospraying. These two methods are easily scalable and can make a variety of nano-morphologies in a facile manner. Both use a high voltage source to induce large deformations on a charged polymeric jet or droplet via strong electric field[27], [28]. In this case, the polymer solution includes the active material (silicon) and conductive agent (carbon), and acts as the binder to keep the nanoparticles at the surface of the current collector for electrical integrity of the electrode. The polymeric solution is pumped through a nozzle. The extensional forces applied to the material in the electric field rapidly decrease the dimensions to sub-micron and smaller, meanwhile solvent is quickly evaporating and kinetically locking the nano-particles in place. Sub-micron and nano-fibers or nano-films are gathered on a grounded collector.

Scalability with these processes is effortlessly achieved through increasing the number of spinnerets and depending on the type of polymer used and the rheology of the solution a variety of morphologies such as nanofibers, beaded fibers, and nano-films with different porosity can be attained[28], [29]. In this thesis work, we hypothesized that the morphology of the electrode and

the geometry of the particles used can have a large impact on the electrochemical performance of the resulting material. Therefore, in this work the main focus is on physical manipulation of the electrode material through processing rather than chemically altering the nanoparticles. The primary goal is to develop electrode fabrication processes that can decrease the cost and time of manufacturing while still maintaining a good electrochemical performance of the electrodes and doing all that in an environmentally friendly manner for high-rate applications. For this reason, water was the only solvent utilized for the fabrication of the electrode materials. At the same time, with the application of electrospinning and electrospraying multiple of the conventional electrode fabrication steps can be eliminated and fibers/films can be directly deposited on the surface of the current collector which can result in lower fabrication cost and time. Emphasis was placed on testing at higher rates for all electrodes, and rigorous electrochemical techniques were used to understand the factors contributing to the enhancement of the rate-capability of the cells

1.2. Scope of the Investigation

1.2.1. Electrospinning:

The first process investigated as an effective route to manufacturing negative electrode materials for lithium ion batteries in a facile and environmentally benign manner is electrospinning. In this process, the polymer has to be spinning, since not all polymers have the ability to form continuous fibers. Electrospinning has been studied extensively for fiber and nano-fiber fabrication pertinent to filtration, biological scaffolding for cell cultures and also electrode fabrication[29]–[35], due to the versatility and ease of setup. Electrospinning has been used as an electrode fabrication method by several groups before, however this thesis work gave careful deliberation to significant modification of the process which was necessary to achieve the goals of high-rate electrochemical performance and cutting back on manufacturing steps. Additionally, the

process parameters had to be adjusted in order to effectively disperse the nanoparticle inclusions throughout the nanofiber composite[36]. In the present work, polyvinyl alcohol (PVA) was chosen as the spinning agent. Silicon nanoparticles (SiNPs) and one-dimensional carbon materials such as carbon nanotubes (CNTs) or graphene nanoribbons (GNRs) were mixed into the PVA solution as the active and conductive materials respectively. PVA was chosen both based on the spinnability in a wide range of solution and nanoparticle concentrations and its ability to dissolve in water to eliminate use of toxic organic solvents.

Water-based solutions of the PVA, SiNPs and conductive agent were prepared and pumped through a nozzle. With the application of high electric field to the nozzle, nanofibers of 100-200 nm in diameter and multiple microns long are formed, which are fully packed with nano-particles. The resulting non-woven nanofibers have large void spaces in between them to accommodate the large volume changes that the silicon nanoparticles exhibit upon lithiation/delithiation process. In this manner, high rate-capability of the electrodes are also improved since the electrolyte has an ease of access to the active sites. In chapter two of this thesis work the detailed investigation of the morphology and electrochemical performance PVA/SiNP/CNT nanofibers are presented. These fibers show a reversible expansion/contraction due to the cycling and the PVA backbone keeps the particles in place that grant this nanocomposite a great cyclability and also rate capability.

In the electrospinning technique the conductive agent is only mixed into the polymeric solution and is directly deposited on the current collector during the spinning. Therefore, utilization of this technique gave us a unique opportunity for an in-situ examination of different geometry of conductive carbon and their effect on the electrochemical performance of the nanofibers. In chapter three of this dissertation, rigorous investigation was done on the effect of utilization of

carbon nanotubes vs. graphene nanoribbons made from the same CNT source. Our results indicate that GNRs are superior to their precursor CNTs both in terms of specific capacity and capacity retention. At the same time, the unique morphology of the nanoribbons with the edge groups makes them a better conductor for Li-ion hopping, therefore, the nanofibers with GNRs also have much better rate capability. The work done on this system indicated that the dimensions of the carbon inclusion can have a drastic effect on how the overall non-woven fiber mat performs. Having conductive pathways that can connect the individual fibers can significantly improve fiber mat's electrochemical performance especially when a higher current is applied.

In chapter four of this work, we engineered the void spaces between the fibers with a ceramic solution that is formed rapidly through a moderate increase in the temperature for a short period of time. An Al containing precursor solution was spin casted on the electrodes and through a short thermal annealing this material was converted to aluminum oxide. In our investigation we found that this ceramic addition can greatly improve cyclability of the nanofibers through protection of the fibers from further reaction with the liquid electrolyte. At the same time, inclusion of Al_yO_x in the electrode increases the ionic conductivity of the fiber mat, which enhances high rate performance of the nanofibers.

1.2.2. Electrospraying:

In the effort to fine tune electrode fabrication processes which are economically viable and are more relevant to large scale manufacturing, utilization of electrospraying was investigated it the present thesis. This technique is more versatile than electrospinning since it is not limited to spinning polymers only. At the same time, the resulted morphology which is a porous film can eliminate the concern with volumetric energy density of non-woven nanofibers. In order to improve morphology and be able to control topology and dispersion of the nanoparticles in the

nanocomposite film, in this dissertation work air-controlled electrospraying was employed in lieu of conventional electrospraying. In this method a circumferentially uniform air flow is applied to the sheath layer of the nozzle during the spraying process to ensure better control of the nanoparticle dispersion.

Chapter five of this dissertation, is a rigorous investigation of the morphology and electrochemical performance of electrosprayed films that include graphene sheets along with silicon nanoparticles. Change in the morphology of the electrode from nanofibers to porous films opens the door to inclusion of particles that cannot be accommodated in the limited confinement of a nanofiber such as larger graphene sheets. With this novel methodology a uniform film with a homogenous dispersion of silicon nanoparticles and graphene sheets with controllable porosity can achieved. Electrospraying can also be modified to accommodate for a single-step fabrication of the electrode material, which is more time effective than the conventional fabrication techniques used today. Silicon nanoparticles are encapsulated within pockets of graphene that provide structural stability and conductivity for extraction of electrons. On the basis of the results of previous chapters, enhancing the ionic and electronic conductivity of the porous films with addition of graphene nanoribbons was also studied. The effect of addition of bi-modal conductive agents and their respective concentrations, on the morphology and electrochemical performance of the films were examined.

1.3 Summary

In this chapter some relevant background, motivation for the present dissertation, the scope of the investigated problems and formulation of our approach is provided. The robust, scalable and environmentally friendly methodologies presented in this work can be a basis for larger single-step manufacturing efforts. With the precise control of nano-inclusion and morphology of the

electrodes afforded by the techniques in this thesis, more innovative designs can be realized, which have the potential to greatly enhance the capacity and life cycle of the lithium ion batteries

REFERENCES

[1] "U.S. Energy Facts - Energy Explained, Your Guide To Understanding Energy - Energy Information Administration." [Online]. Available: https://www.eia.gov/energyexplained/?page=us_energy_home. [Accessed: 21-Jan-2019].

[2] P. Denholm, E. Ela, B. Kirby, and M. Milligan, "The Role of Energy Storage with Renewable Electricity Generation," *Tech. Rep.*, p. 61, 2010.

[3] "EIA - U.S. Battery Storage Market Trends." [Online]. Available: https://www.eia.gov/analysis/studies/electricity/batterystorage/. [Accessed: 20-Jan-2019].

[4] B. Scrosati, K. M. Abraham, W. A. van Schalkwijk, and J. Hassoun, *Lithium batteries: advanced technologies and applications*. 2013.

[5] X. Huang, "Separator technologies for lithium-ion batteries," *J. Solid State Electrochem.*, vol. 15, no. 4, pp. 649–662, Apr. 2011.

[6] P. G. Balakrishnan, R. Ramesh, and T. Prem Kumar, "Safety mechanisms in lithium-ion batteries," *J. Power Sources*, vol. 155, no. 2, pp. 401–414, Apr. 2006.

[7] H. Lee, M. Yanilmaz, O. Toprakci, K. Fu, and X. Zhang, "A review of recent developments in membrane separators for rechargeable lithium-ion batteries," *Energy Environ. Sci.*, vol. 7, no. 12, pp. 3857–3886, 2014.

[8] K. Xu, "Nonaqueous Liquid Electrolytes for Lithium-Based Rechargeable Batteries," *Chem. Rev.*, vol. 104, no. 10, pp. 4303–4418, Oct. 2004.

[9] Z. Chen Qin, Yan, Amine, Khalil, Sun, Y. K., "Role of surface coating on cathode materials for lithium-ion batteries," *J. Mater. Chem.*, vol. 20, no. 36, pp. 7606–7612, 2010.

[10] Z. Chen and J. R. Dahn, "Studies of LiCoO2 Coated with Metal Oxides," *Electrochem. Solid-State Lett.*, vol. 6, no. 11, pp. A221–A224, Nov. 2003.

[11] Z. Chen and J. R. Dahn, “Effect of a ZrO2 Coating on the Structure and Electrochemistry of Li x CoO2 When Cycled to 4.5 V,” *Electrochem. Solid-State Lett.*, vol. 5, no. 10, pp. A213–A216, Oct. 2002.

[12] J. Cho Kim, Young-Woon, Kim, Byoungsoo, Lee, Joon-Gon, Park, Byungwoo, “A Breakthrough in the Safety of Lithium Secondary Batteries by Coating the Cathode Material with $AlPO_4$ Nanoparticles,” *ANGE Angew. Chem.*, vol. 115, no. 14, pp. 1656–1659, 2003.

[13] V. Etacheri, R. Marom, R. Elazari, G. Salitra, and D. Aurbach, “Challenges in the development of advanced Li-ion batteries: a review,” *Energy Environ. Sci.*, vol. 4, no. 9, p. 3243, 2011.

[14] N. Schweikert, H. Hahn, and S. Indris, “Cycling behaviour of Li/Li 4 Ti 5 O 12 cells studied by electrochemical impedance spectroscopy,” *Phys. Chem. Chem. Phys.*, vol. 13, no. 13, pp. 6234–6240, 2011.

[15] B. Guo *et al.*, “Electrospun Li4Ti5O12/C composites for lithium-ion batteries with high rate performance,” *Solid State Ion.*, vol. 204–205, pp. 61–65, Dec. 2011.

[16] M.-S. Balogun *et al.*, “A review of the development of full cell lithium-ion batteries: The impact of nanostructured anode materials,” *Nano Res.*, pp. 1–29, Jul. 2016.

[17] S.-H. Yu, S. H. Lee, D. J. Lee, Y.-E. Sung, and T. Hyeon, “Conversion Reaction-Based Oxide Nanomaterials for Lithium Ion Battery Anodes,” *Small*, vol. 12, no. 16, pp. 2146–2172, 2016.

[18] M. T. McDowell, S. W. Lee, W. D. Nix, and Y. Cui, “25th Anniversary Article: Understanding the Lithiation of Silicon and Other Alloying Anodes for Lithium-Ion Batteries,” *Adv. Mater.*, vol. 25, no. 36, pp. 4966–4985, Sep. 2013.

[19] M. Ko, S. Chae, and J. Cho, “Challenges in Accommodating Volume Change of Si Anodes for Li-Ion Batteries,” *ChemElectroChem*, vol. 2, no. 11, pp. 1645–1651, Nov. 2015.

[20] C. K. Chan *et al.*, “High-performance lithium battery anodes using silicon nanowires,” *Nat. Nanotechnol.*, vol. 3, no. 1, pp. 31–35, Jan. 2008.

[21] A. S. Aricò, P. Bruce, B. Scrosati, J.-M. Tarascon, and W. van Schalkwijk, “Nanostructured materials for advanced energy conversion and storage devices,” *Nat. Mater.*, vol. 4, no. 5, pp. 366–377, May 2005.

[22] M. M. Yao Y Ryu I, Wu H, Liu N, Hu L, Nix WD, Cui Y., “Interconnected silicon hollow nanospheres for lithium-ion battery anodes with long cycle life.,” *Nano Lett.*, vol. 11, no. 7, pp. 2949–54, 2011.

[23] N. Badi, A. R. Erra, F. C. R. Hernandez, A. O. Okonkwo, M. Hobosyan, and K. S. Martirosyan, “Low-cost carbon-silicon nanocomposite anodes for lithium ion batteries,” *Nanoscale Res. Lett.*, vol. 9, no. 1, pp. 1–8, Dec. 2014.

[24] S. Chen, P. Bao, X. Huang, B. Sun, and G. Wang, “Hierarchical 3D mesoporous silicon@graphene nanoarchitectures for lithium ion batteries with superior performance,” *Nano Res.*, vol. 7, no. 1, pp. 85–94, Nov. 2013.

[25] A. Gohier *et al.*, “High-Rate Capability Silicon Decorated Vertically Aligned Carbon Nanotubes for Li-Ion Batteries,” *Adv. Mater.*, vol. 24, no. 19, pp. 2592–2597, 2012.

[26] W.-R. Liu *et al.*, “Effect of electrode structure on performance of Si anode in Li-ion batteries: Si particle size and conductive additive,” *J. Power Sources*, vol. 140, no. 1, pp. 139–144, Jan. 2005.

[27] N. Bhardwaj and S. C. Kundu, “Electrospinning: A fascinating fiber fabrication technique,” *Biotechnol. Adv.*, vol. 28, no. 3, pp. 325–347, May 2010.

[28] A. M. Gañán-Calvo, “THE SURFACE CHARGE IN ELECTROSPRAYING: ITS NATURE AND ITS UNIVERSAL SCALING LAWS,” *J. Aerosol Sci.*, vol. 30, no. 7, pp. 863–872, Aug. 1999.

[29] Z.-M. Huang, Y.-Z. Zhang, M. Kotaki, and S. Ramakrishna, “A review on polymer nanofibers by electrospinning and their applications in nanocomposites,” *Compos. Sci. Technol.*, vol. 63, no. 15, pp. 2223–2253, Nov. 2003.

[30] J. Doshi and D. H. Reneker, “Electrospinning process and applications of electrospun fibers,” *J. Electrost.*, vol. 35, no. 2–3, pp. 151–160, Aug. 1995.

[31] J.-B. Ko *et al.*, “Fabrication of SiO2-ZrO2 composite fiber mats via electrospinning,” *J. Porous Mater.*, vol. 13, no. 3–4, pp. 325–330, Aug. 2006.

[32] S. W. Lee, Y. U. Kim, S.-S. Choi, T. Y. Park, Y. L. Joo, and S. G. Lee, “Preparation of SiO2/TiO2 composite fibers by sol–gel reaction and electrospinning,” *Mater. Lett.*, vol. 61, no. 3, pp. 889–893, Feb. 2007.

[33] D. Li and Y. Xia, “Electrospinning of Nanofibers: Reinventing the Wheel?,” *Adv. Mater.*, vol. 16, no. 14, pp. 1151–1170, Jul. 2004.

[34] N. S. Hansen, D. Cho, and Y. L. Joo, “Metal Nanofibers with Highly Tunable Electrical and Magnetic Properties via Highly Loaded Water-Based Electrospinning,” *Small*, vol. 8, no. 10, pp. 1510–1514, May 2012.

[35] X. Liu, H. Xu, Y. Huang, and X. Hu, “Direct planting of ultrafine MoO2+δ nanoparticles in carbon nanofibers by electrospinning: self-supported mats as binder-free and long-life anodes for lithium-ion batteries,” *Phys Chem Chem Phys*, 2016.

[36] Y. Zhmayev *et al.*, “Controlling the Placement of Spherical Nanoparticles in Electrically Driven Polymer Jets and its Application to Li-Ion Battery Anodes,” *Small*, p. n/a-n/a, Aug. 2016.

CHAPTER TWO

FACILE, WATER-BASED, DIRECT-DEPOSITE FABRICATION OF HYBRID SILICON ASSEMBLIES FOR SCALABLE AND HIGH-PERFORMANCE LITHIUM ION BATTERY ANODES

2.1. Introduction

Consumer electronics and hybrid vehicle industries constantly impose high volumetric and gravimetric energy density standards for the next generation of Li-ion batteries [1-5]. For this reason, silicon has come into the spotlight as the anode candidate with the highest theoretical gravimetric capacity of 4200 $mAhg^{-1}$, which is an order of magnitude larger than the state of the art commercial anodes [6-10]. However, silicon suffers from more than 300% volume expansion upon lithiation; Figure 2.1a shows a silicon nanoparticle (Si NP) that swells according to $xLi + ySi \rightarrow Li_xSi_y$. Extraction of lithium ions brings on a decrease in volume of the nanoparticle, and upon cycling, the exorbitant volume changes eventually result in fracture and pulverization of material and loss of electric contact with the current collector [11-13]. Irreversible reactions with the electrolyte form a solid electrolyte interface (SEI) layer on the surface of particles, and the colossal volume changes lead to constant fragmentation and formation of SEI giving rise to unstable performance [14,15]. In addition, silicon has a low electrical conductivity that hinders its effectiveness at fast rate applications [16,17]. To date, in order to overcome these phenomena silicon have been hybridized with polymers and nano-scale carbons. Conductive polymers have been explored in the literature [18-21], as a remedy for the low electrical conductivity and structural integrity of anode systems. Bao group introduced a self-healing polymer as binder, which would correct formed cracks due to cycling [22]. Carbon nanotubes (CNTs) and

nanostructured graphene has incurred a lot of attention due to their high conductivity and theoretical capacity. Gohier *et al.* fabricated anodes based on vertical nanotubes decorated with silicon nanoparticles [1]. Wang *et al.* utilized multilayer silicon nanoparticles sandwiched between reduced graphene oxide sheets [2], and assemblies of silicon nanospheres on graphene foams to create a hierarchical mesoporous structure with great rate capability performance [3]. Unfortunately, most of nano-fabrication methods require high vacuum processes or ultra-high temperature treatments, making them not feasible for high throughput production.

In the current study, water-based electrospinning was employed as a facile method for scalable fabrication of silicon nanocomposite with polyvinyl alcohol (PVA) and multi-wall carbon nanotubes. Figure 2.1b shows schematic of the conventional slurry process on top and directly-deposited electrodes on the bottom. For conventional procedure active material is first made. This can include a variety of methodologies explored in literature and mentioned before. A slurry is obtained upon grinding and mixing of active material with conductive carbon, binder and usually an organic solvent via ball milling or other mixing techniques. The acquired paste is then coated on current collector by doctor blading or slot and reverse roll coating to get a uniform film. After drying, the electrodes can be ready for assembly. Conversely this study explores a novel technique, where electrode surface is directly covered by nanofibers resulting from electrospinning as can be seen in the lower part of Figure 2.1b. This combines the preparation of active material and coating of the current collector in one step. One dimensional nanomaterials offer high surface area for electrochemical reactions, thus have been subject of intensive investigation for application in energy storage.[26,27] Electrospinning have been utilized in the literature as a scalable method of active material preparation [4–6], with various chemistries and active material. However, when these materials were to be electrochemically tested, the created morphology was destroyed by

grinding with conductive carbon and binder in a conventional manner. In the present approach water is used in place of toxic organic solvents such as N-Methyl-2-pyrrolidone (traditionally employed in electrode preparation), and steps mentioned above are by-passed. Scaling up the production is easily achieved by controlling electrospinning parameters such as spinning time, number of nozzles, feeding rate and solution volume [31-33]. This procedure is compatible with a roll to roll production, and has the versatility to be used with different particle geometries and material chemistries. Using this process, a 18cm x 20 cm piece of copper foil was uniformly coated, by only 5 ml of solution. This area is equivalent to about hundred and fifty 2032 coin-type electrode disks. Whereas using the doctor-blade to achieve a homogeneous coating for the same area is known to be a challenge due to particle agglomeration [34-36]. Using water-based electrospinning to directly deposit (DD) PVA/Si/CNT nanofibers onto the current collector provides advantages to alleviate the aforementioned decay mechanism. First, PVA matrix gives Si NPs structural integrity, while protecting them from direct contact with the electrolyte. Figure 2.1c is a schematic showing of the system and safekeeping of nanoparticles by the PVA fiber around them. Second, ample space between nanofibers offers room for expansion of particles. Third, the transport of lithium ions can be aided by penetration of electrolyte to the nearest proximity of active material through the micro and nano sized pores of the fiber mat. From there, Li ions only have a short length to diffuse to get to the active material which will result in faster response times and improvement in Si NP utilization. Electrodes fabricated by this approach will be referred to as DD from this point on.

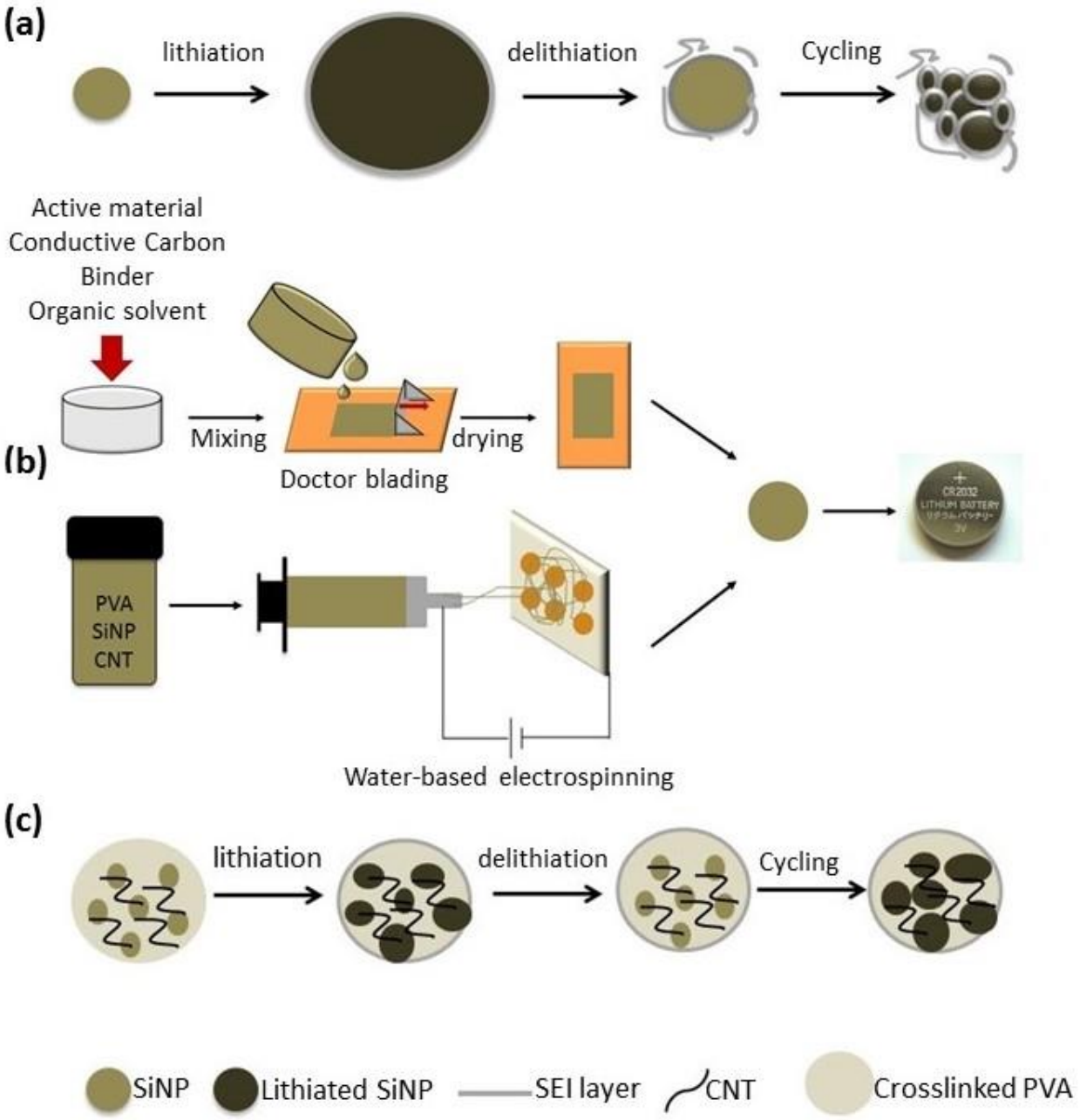

Figure 2. 1. a) Schematic illustrating fracturing of Si particle and SEI layer due to cycling; (b) overall preparation procedure for conventional slurry method at the top and directly–deposited PVA/Si/CNTs nanocomposite via water-based electrospinning at the bottom, for 2032 coin-type Li-ion batteries; (c) schematic of PVA/Si/CNT to represent how PVA helps in suppression of SEI creation on the particles, and overall capacity decay during battery cycling

2.2. Experimental section

Preparation of DD silicon nanofibers via water-based electrospinning: 0.5g of PVA (Polyscience Inc., Mw~78,000) was dissolved in 5g of deionized water at 50˚C and then short and thin carbon nanotubes (Sigma Aldrich) were added to the solution. Finally, 0.5g of silicon nanoparticles *ca.* 100 nm (MTI Co.) was blended in with everything else. A probe sonicator (Qsonicator Co.) was used to ensure proper dispersion of nanoparticles. The solution was then pumped from a syringe at a rate of 10 $\mu L min^{-1}$ towards a copper collector placed 12 cm away from tip of the needle. In presence of 10 KV applied to the system, PVA/Si/CNTs composite nanofibers were directly collected on copper foil. As-spun fibers were then heat treated at a ramp of 1°C min^{-1} to 200°C in an air furnace. This resulted in 0.4-0.6 $mg cm^{-2}$ of nanofibers on copper current collector to be used for electrochemical tests. Higher areal mass loading of the fibers on the current collector can simply be achieved by longer spinning time or additional nozzles.

Material characterization of the directly deposited nanofibers. Composite nanofibers were characterized using a scanning electron microscopy (SEM, LEO 1550), energy dispersive spectroscopy (Bruker) and transition electron microscope (TEM, FEI F20 TENCAI) to assess morphology changes before and after heat treatment. Thermogravimertric analysis (TGA, TA instruments Q500) was conducted on the nanofiber mats to measure silicon content. To observe the changes in the bond structure of the polymer before and after heat treatment Fourier transform infrared (FT-IR, Bruker Co.) were carried out on the samples.

Battery fabrication and electrochemical measurements of directly deposited Si nanofibers. To ensure the adhesion of the nanofiber mat on the copper current collector, a 10% solution of poly(acrylic acid) (Sigma Mw=3,000,000) was spin coated on the surface of the electrodes. 2032 type coin cells were fabricated using the directly deposited fibers as working electrode, Li metal

disk as counter electrode and a polyethylene separator to test the performance of half cells. A homemade electrolyte, with 1M $LiPF_6$ (Sigma) as salt and dimethyl carbonate (Sigma) and fluoroethylene carbonate (Sigma) (50:50 wt%) as solvents, was used inside of both half and full cells. Full cell batteries were assembled by stacking DD anode, a polyethylene separator and $LiCoO_2$ (MTI Co.) cathode. Electrochemical properties of cells were characterized by electrochemical impedance spectroscopy (PARSAT 4000, Princeton applied research) and cyclic voltammetry (BST8-STAT, MTI Co.) and galvanostatic charge and discharge cycles (MTI). A voltage window of 0.01-1.5V vs Li/Li+ was applied to the half cells. Weight ratio of anode to cathode in the prepared cells were 1 to 67 for full cells, therefore, they were subjected to a capacity cut-off of 1,200 $mAhg^{-1}_{anode}$ that was obtained from half-cell measurements.

2.3. Results

Material characterization. Morphology of the DD PVA/Si/CNT anode materials before and after heat treatment at 200˚C are shown in Figure 2.2. As apparent from SEM images of 2a, electrospinning creates a non-woven mat of nanofibers; highly porous on micron and sub-micron scale. As-spun nanofibers have 1-D morphology where Si and CNTs are encapsulated by PVA with an average fiber diameter of 200 nm. After heat treatment, fibers still maintain their 1-D structure, but average diameter shrunk to 130 nm as a result of PVA cross-linking and mass reduction. Figure 2.2b and 2c show top and cross-sectional views of the nanofibers on copper current collector respectively after heat treatment under air. Extensional deformations during electrospinning disperse nanoparticles inside of the polymer matrix, and rapid solidification of the fibers [29, 30] ensures that particles do not agglomerate. TEM Figure of 2.3a and 2.3b illustrates the packing of nanoparticles inside PVA fibers. The polymer also alleviates volume expansion and

prevents pulverization during cycling. Nanoparticles create a percolated network, free of large clusters, but tightly connected to be able to accommodate electronic and ionic transfers.

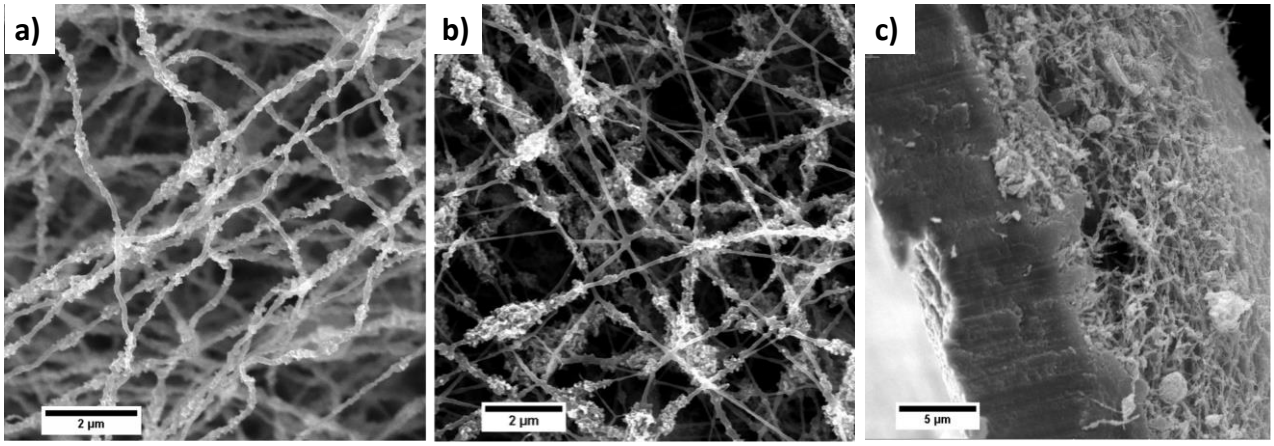

Figure 2. 2. (a) SEM image of as–spun DD PVA/Si/CNT nanofibers on copper substrate before heat treatment; SEM images (c) top view (d) cross-section of DD PVA/Si/CNT after heat treatment under air.

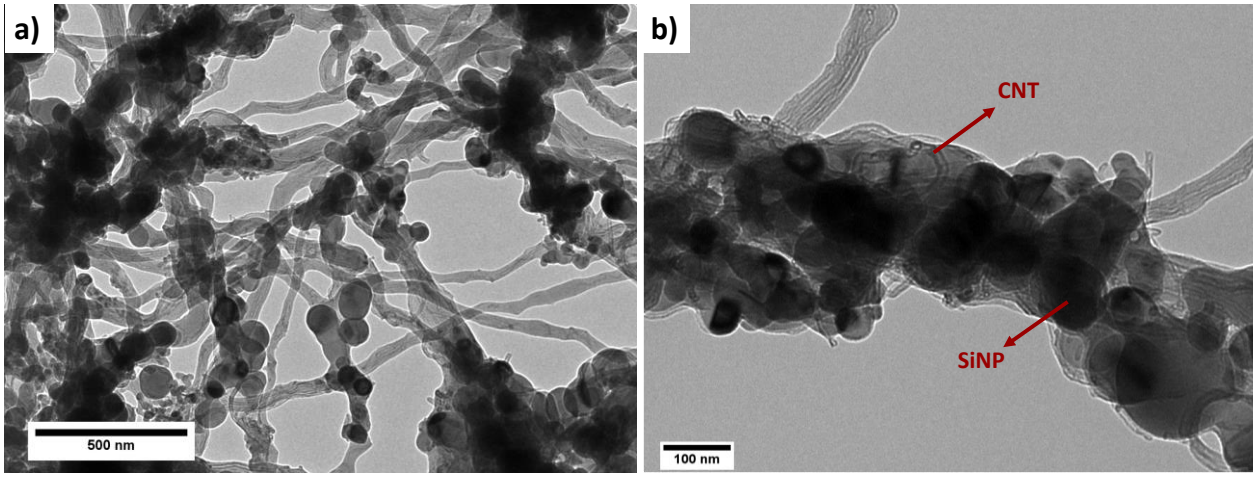

Figure 2. 3. TEM images of as-spun nanofibers at a) low magnification b) high magnification

EDS elemental mapping of the as-spun nanofibers in Figure 2.4 exhibit that the nanoparticles are homogenously dispersed throughout the system without any agglomeration. Line scan of the non-woven fiber mat reveals that the signal reaches the detector from multiple layers of the fiber mat. It can be observed from Figure 2.4f that the signal of all elements has a dip exactly where there is a void in the fiber mat. Even after the heat treatment under air when PVA undergoes a condensation reaction to lose water and cross-linked, the particles don't agglomerate, and the uniform dispersion is maintained as can be observed in Figure 2.5 elemental mappings.

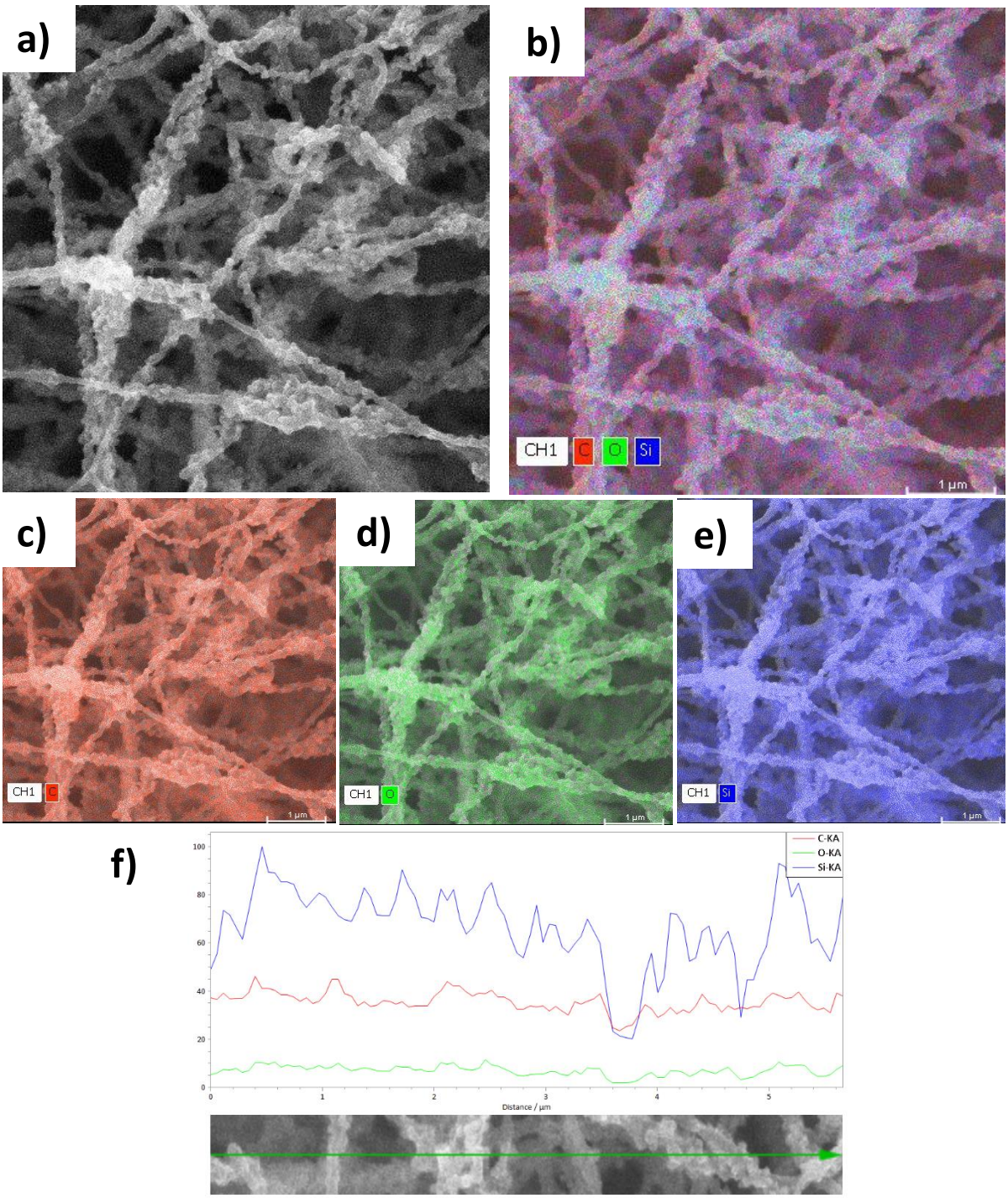

Figure 2. 4. Elemental mapping of the as-spun fibers b) combination of all elements c) carbon mapping d) oxygen mapping e) silicon mapping f) line scan of fibers

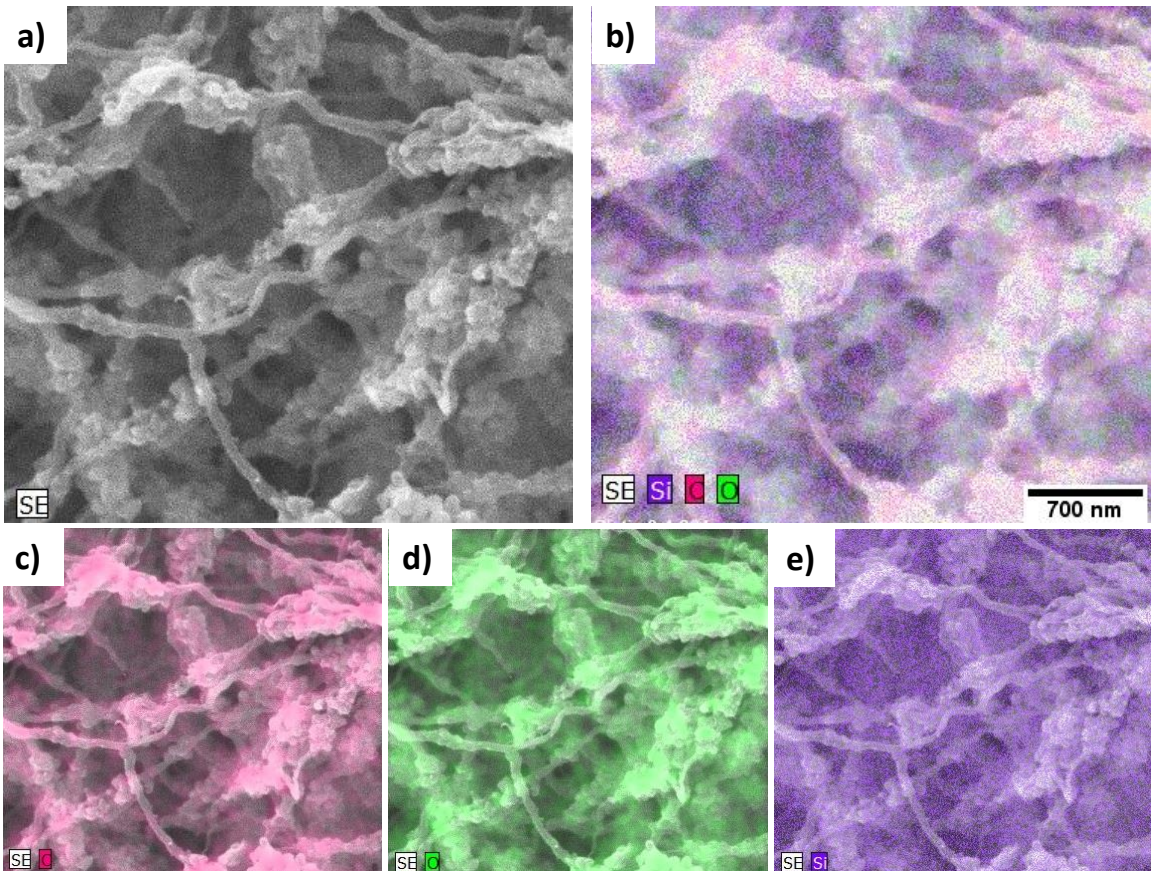

Figure 2. 5. Elemental mapping of fibers after heat treatment at 200 ◦C under air b) combination of all elements c) carbon mapping d) oxygen mapping e) silicon mapping

Exact silicon content of the fibers was measured by thermogravimetric analysis in Figure 2.6 to use for current densities and calculation of specific gravimetric capacity. Silicon made up 47% of as spun composite, which is the same as the prepared solution, while after heat treatment this number was increased to 68 wt%. This change is a result of PVA mass reduction after heat treatment through elimination of O-H and C-H groups through a condensation reaction. In addition, CNT content was found to be 7% of the weight of the system in the final electrode. Based on these results mass loading of Si on electrodes was about 0.3-0.4 $mgcm^{-2}$, which is similar to other literature using polymers [18-20]. All reported capacities normalized by mass of silicon on

the electrode. To investigate the effect of heat treatment on the crystalline silicon nanoparticles used in this system, XRD was conducted on nanofibers before and after heat treatment at 200 ◦C for 12 hours. The diffraction peaks of crystalline silicon in Figure 2.7 are identical for fibers before and after heat treatment, indicating that the heat treatment does not significantly increase the native oxide layer on the Si particles. Figure 2.8 reports electrolyte uptake of directly deposited anodes compared to conventional slurry with the same composition. Current system is able to take up 78% more electrolyte because of the unique fiber morphology, which helps in the electrochemical performance of the electrodes especially at higher rates.

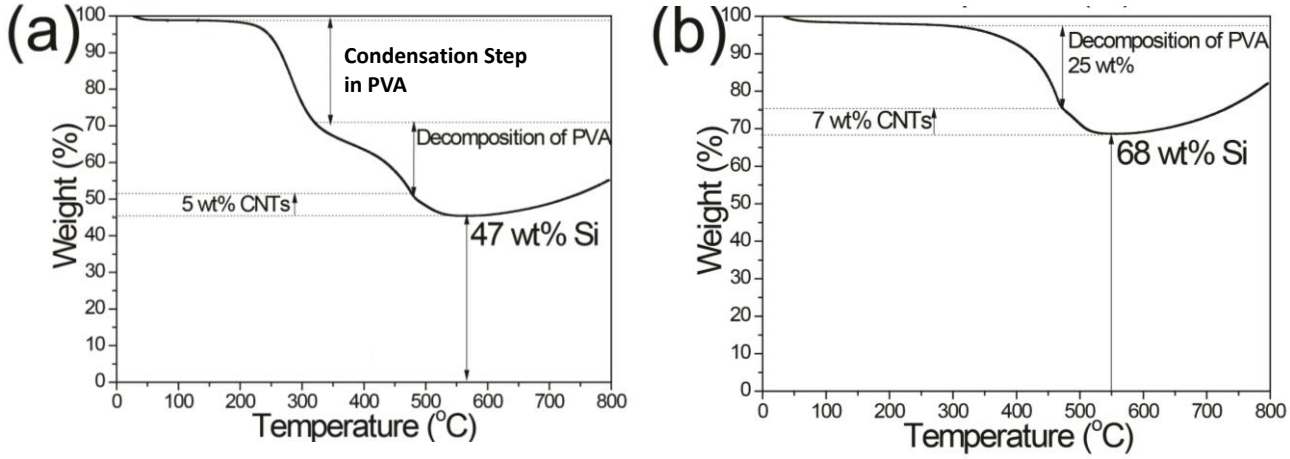

Figure 2. 6. TGA analysis of a) the as-spun fibers b) heat treated fibers under air

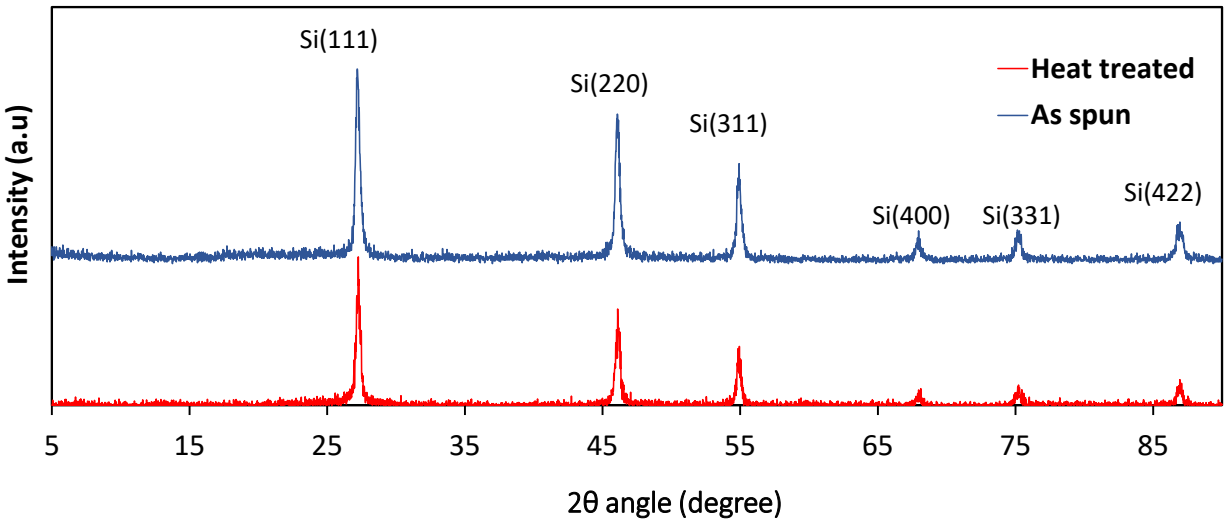

Figure 2. 7. XRD result of as-spun and heat treated PVA/Si/CNT nanofibers

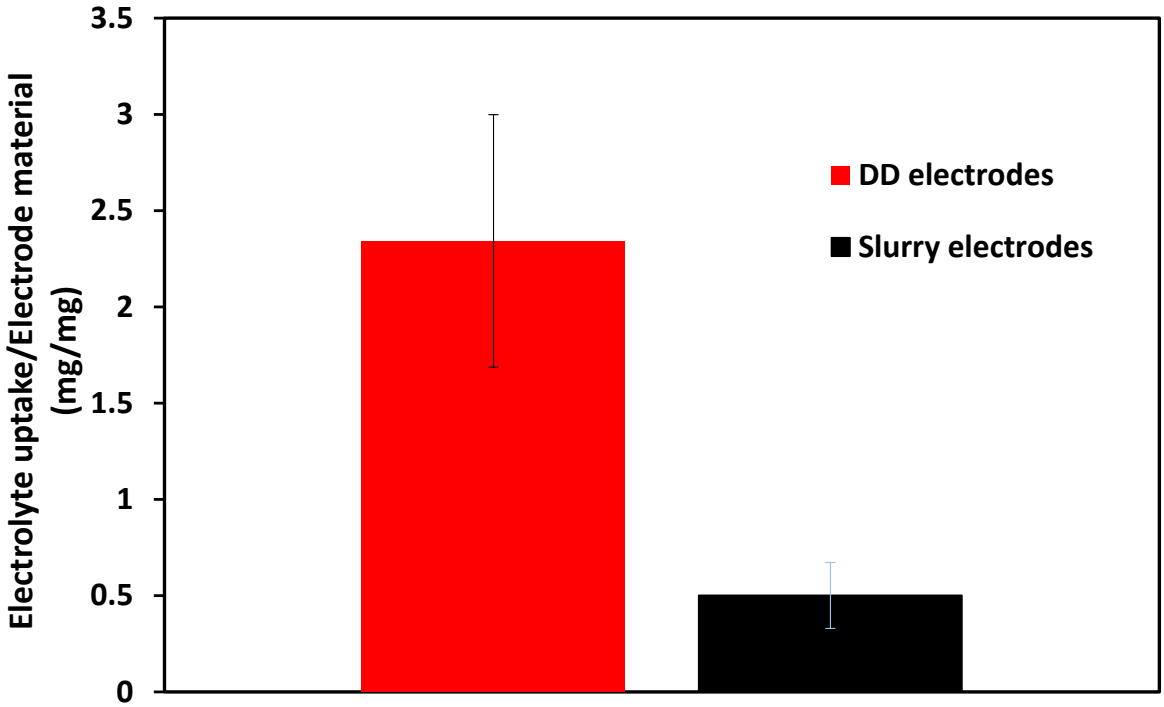

Figure 2. 8. Electrolyte uptake by conventional slurry electrodes and nanofiber DD electrodes

Half-cell electrochemical performance. To assess the assumption that the fiber morphology can withstand the exorbitant volume changes during lithiation and delithiation, 2032 coin-type half cells were assembled. Each cell was lithiated to a specific voltage with a constant current of 0.18 Ag^{-1} and then the cell was disassembled to observe the morphology with a scanning electron microscope. In order to, be able to clearly investigate the fiber morphology, the electrodes did not have the final PAA coating on top of them. Figure 2.9 is a bank of SEM images illustrating fiber morphology going from 9a to 9f with increasing the amount of lithium ion alloyed in the system. Figure 2.9g indicated the voltages along the lithiation profile where each cell was disassembled. At first when the lithium ions start to intercalate into the composite fibers the fibers start to swell and, in some areas, fuse together. This increase in the volume continues with more lithiation. In Figure 2.9d where the bulk of the alloying with SiNPs start a distinct expansion in the size of each individual particle can be observed. At 100% lithiation in Figure 2.9f, the size of the individual particles as well as the overall fibers increased significantly. The average fiber diameter grows from a 280nm for the pristine fibers to 420nm for fully lithiated fibers. This increase is about 50% of the initial size of the fibers which is significantly smaller than the 300% usually observed for silicon particles in other literature[7]. Therefore, the nanocomposite fiber morphology mitigates the volume expansion of the silicon nanoparticles. In addition, it can be observed that fibers maintained their 1D structure even though they are expanded. The same was done on the delithiation step. Cells were lithiated fully and on the delithiation step they were opened at different voltages along the charge. Figure 2.10 depicts the morphology of the fibers as more lithium is extracted from the composite (a to d). The fiber diameter starts to shrink and individual particles also contract. At full delithiation at 1.5V the fibers assume a morphology close to their original state. Indicating that the Si/CNT/PVA nanofibers can expand and contract reversibly without

drastic changes to their structure. Figure 2.11 illustrates the changes in the average fiber diameters with different degrees of lithiation and delithiation. The as the voltage decreases on the lithiation curve a steady increase in the average diameter is observed, and the opposite happens in the delithiation process.

The initial lithiation capacity of the directly deposited fibers is 4190 $mAhg^{-1}$, while SiNPs slurry has only 2800 $mAhg^{-1}$, at $0.18Ag^{-1}$ as can be seen from Figure 2.12. However, about 40% of the initial capacity is lost after the first delithiation for DD and slurry systems. The DD fibers owe their high initial lithiation capacity to additional contributions from irreversible reactions of the electrolyte with PVA, and from CNTs. Carbon nanotube lithiation starts at around 1.4V[37] vs Li/Li^+ (crystalline silicon starts to lithiate at below 0.2V [38, 39] vs Li/Li^+). In addition, better utilization of Si NP due to void spaces provided by the fiber mat, improvement in dispersion of nanoparticles and higher surface area play an important role in enhancement of gravimetric capacity by the electrodes made by electrospinning process. On the second cycle (dashed lines in Figure 2.12), DD fiber lithiation and delithiation capacities are 2400 and 2600 $mAhg^{-1}$ respectively. On the other hand, conventional slurry has a lithiation and delithiation capacity of 1982 and 1446 $mAhg^{-1}$ on its second cycle. Slurry shows the signature capacity-voltage curve of crystalline silicon on the first cycle where a sharp decrease in the voltage at low capacities is observed followed by the low voltage plateau of intercalation of lithium ions in the silicon crystalline structure, which is a two-phase reaction and shows up in the profile as a long flat plateau.

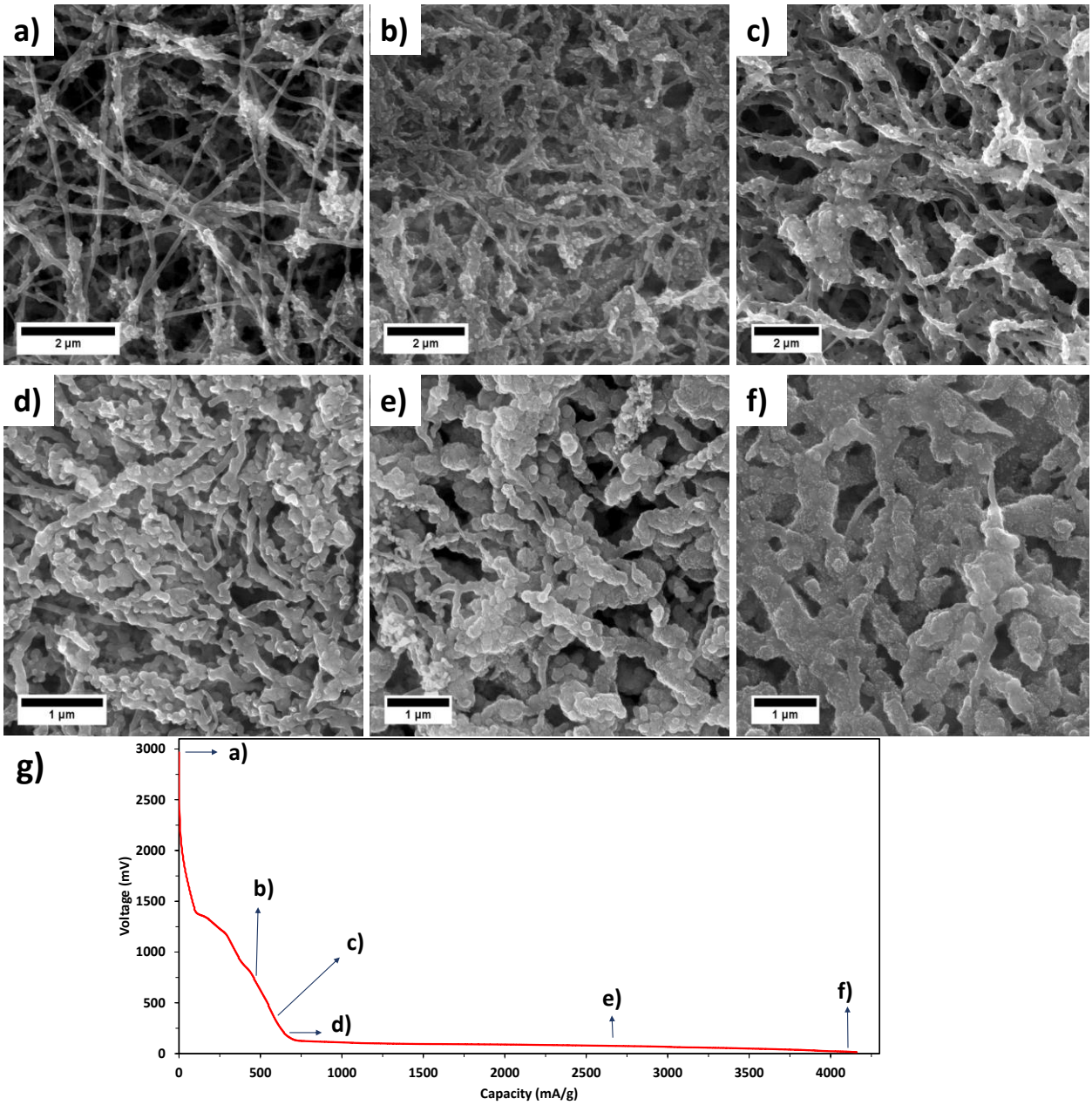

Figure 2. 9. Bank of SEM images showing DD fibers at different states of lithiation. a) Pristine (0%) b) 10% c) 15% d) 20% e) 65% f) 100% g) capacity-voltage profile showing the points on the curve that each image was taken

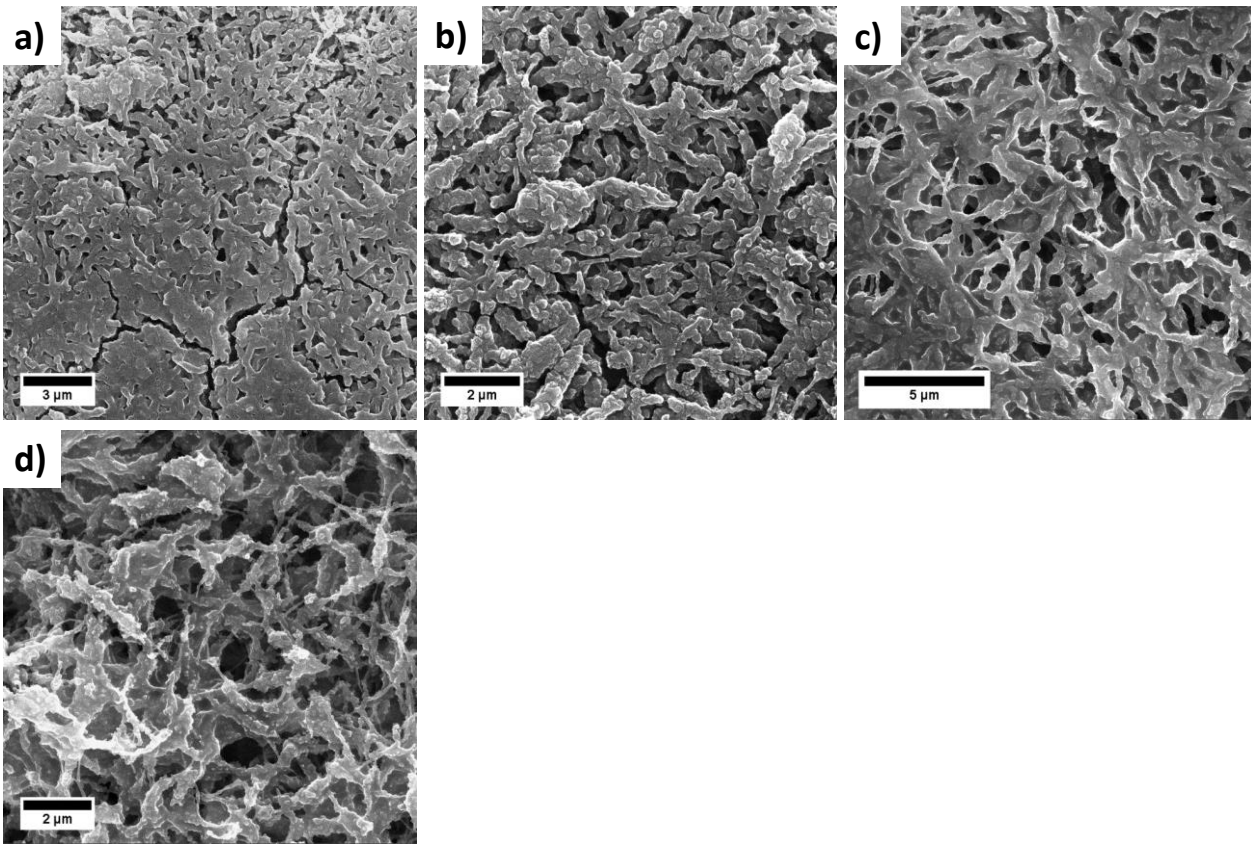

Figure 2. 10. Bank of SEM images illustrating DD fibers at different states of delithiation. a) 0% b) 50% c) 65% d)100%

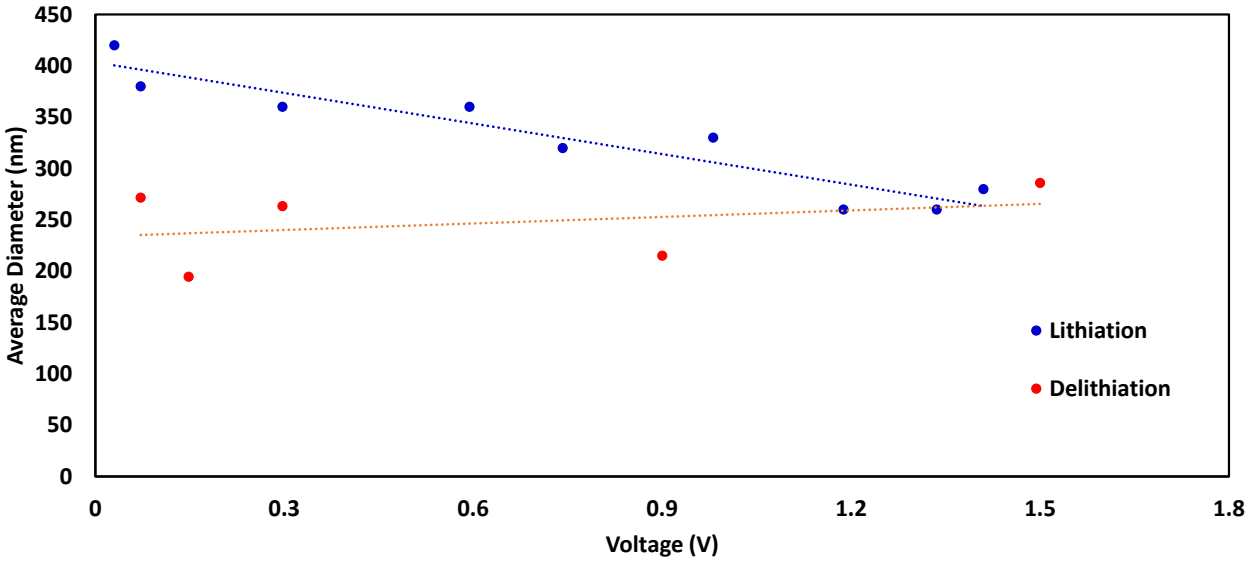

Figure 2. 11. Change in the average diameter of the nanofibers with different degrees of lithiation and delithiation

After the initial lithiation the crystalline structure of the silicon becomes amorphous and the second delithiation shows up as a line with a slight downward slope as can be seen from the dashed lines in Figure 2.12. DD fibers exhibit an additional shoulder around 1.4V on their first lithiation which is ascribed to the irreversible side reactions of the electrolyte with PVA in the system, but the low voltage plateau remains unchanged. It can be observed that even in the first cycle most of the capacity stems from lithiation of silicon nanoparticles as expected.

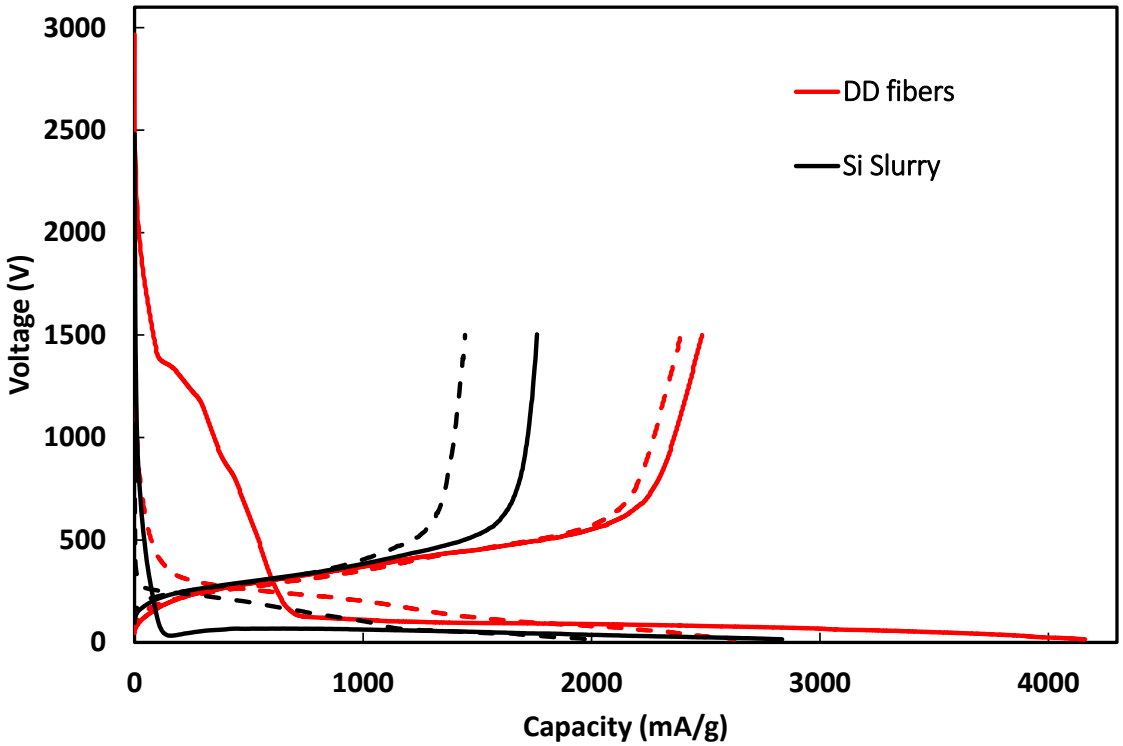

Figure 2. 12. Capacity-voltage profile of DD fibers in red and conventional slurry in black at 0.18Ag-1. Solid lines are first cycle and dashed lines are for second charge/discharge

To investigate the assumption of 1.4V peak belonging to side reaction of PVA and electrolyte. The same ratio of silicon and CNTs were electrosprayed on the cupper current collector, to eliminate the polymeric binder. In the absence of polymers, the solution cannot be electrospun, therefore no fibers were obtained. Instead solution will atomize and land on the collector as small droplets. Differential capacity vs. voltage curves were constructed from the initial discharge and charge profiles of DD fibers and electrosprayed electrodes. Figure 2.13a reveal that DD fibers exhibit a peak at 1.4V which is absent in the system without PVA in 13b. This peak does not appear from the second cycle on, which attest to its irreversible nature. It is the result of reaction of electrolyte on surface of PVA to form SEI layer, which as mentioned before, contributes to the large initial

capacity of DD fibers. However, this large initial irreversible capacity is not ideal for use in full cell configuration. It can be observed that the lithiation peak of SiNPs close to zero voltage is much more pronounced compared to the DD fibers, which is due to the absence the nonconductive polymer. However, the polymer is crucial to get the desired nanofiber morphology of the composite.

At a slow rate of 0.18 Ag^{-1}, DD fibers exhibit a stable capacity of 2300 $mAhg^{-1}$ over 40 cycles while the conventional slurry only has 1000 $mAhg^{-1}$ at the same condition. Figure 2.14 illustrates the difference in the electrochemical performance of these two electrodes at 0.18 Ag^{-1}. As mentioned before, DD fibers have a large first cycle irreversible capacity loss, but after that the capacity does not fluctuate. At this rate slurry retained only 50% of its capacity (calculated against 2^{nd} lithiation), while DD fibers retained 75% during 40 cycles. Coulombic efficiency of DD fibers increased from an initial value of 60% to 91% on the second cycle. On the other hand, slurry coulombic efficiency on the second cycle is only 73%. This should be attributed to SEI formation on silicon nanoparticles in the first few cycles, before a stable performance is observed. However, since in DD fibers, SiNPs are encapsulated inside the PVA matrix, and safe from direct exposure to the electrolyte, stable capacities are observed from the second cycle on. The 1D morphology of the nanofibers is responsible for the higher specific capacity the nanofiber mat, since the access to the individual particles are improved through the highly porous structure of the mat, while the compact structure of the slurry makes it difficult for the lithium ions to be inserted/extracted. Figure 2.15 reveals the top-view of the slurry coated electrode for the comparison of the morphology with the DD nanofibers.

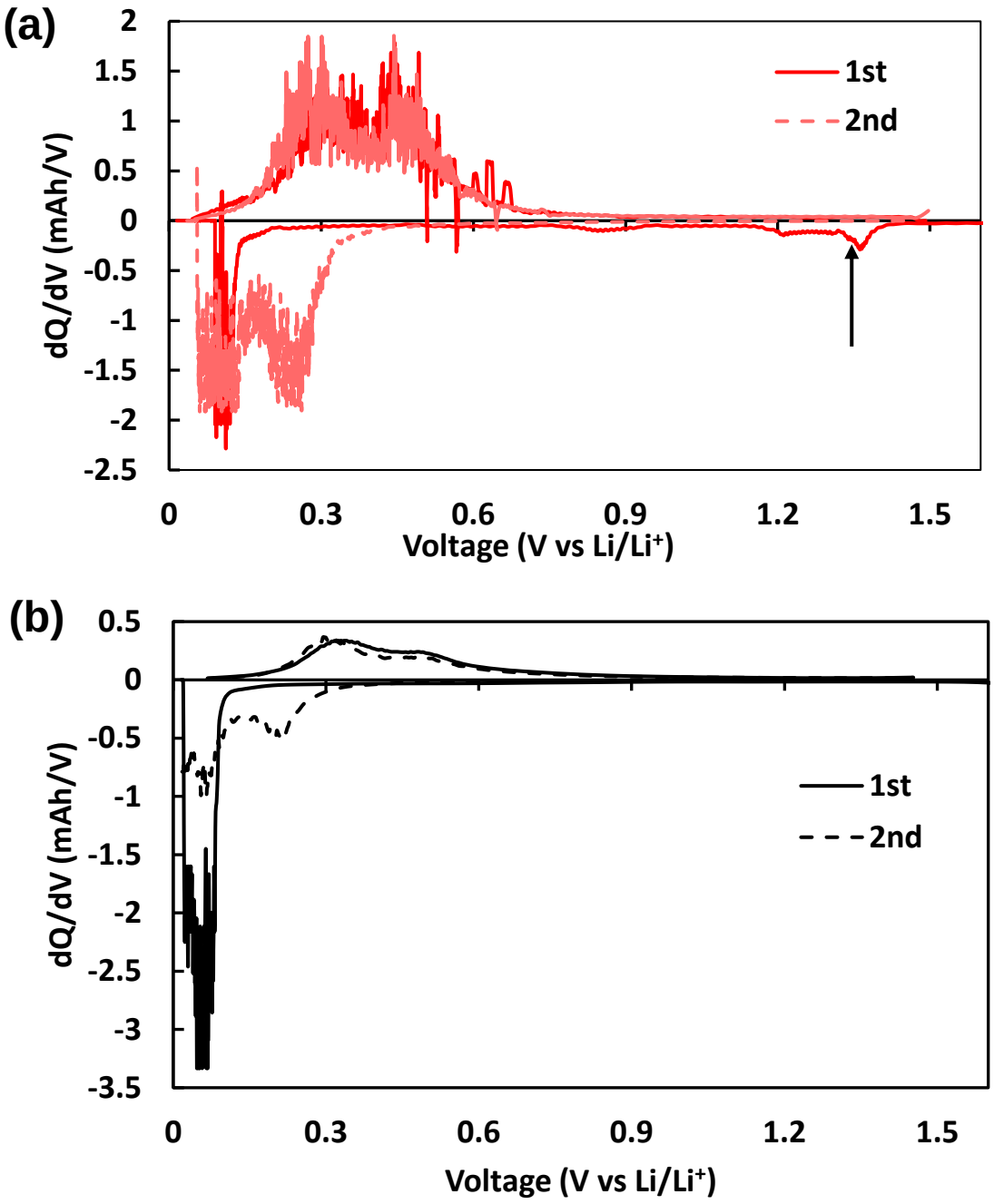

Figure 2. 13. Differential Capacity vs. Voltage profiles for a) DD fibers b) Electrosprayed electrodes which contain only SiNPs and CNTS. The arrow in graph (a) points to the place of the PVA peak on the profile.

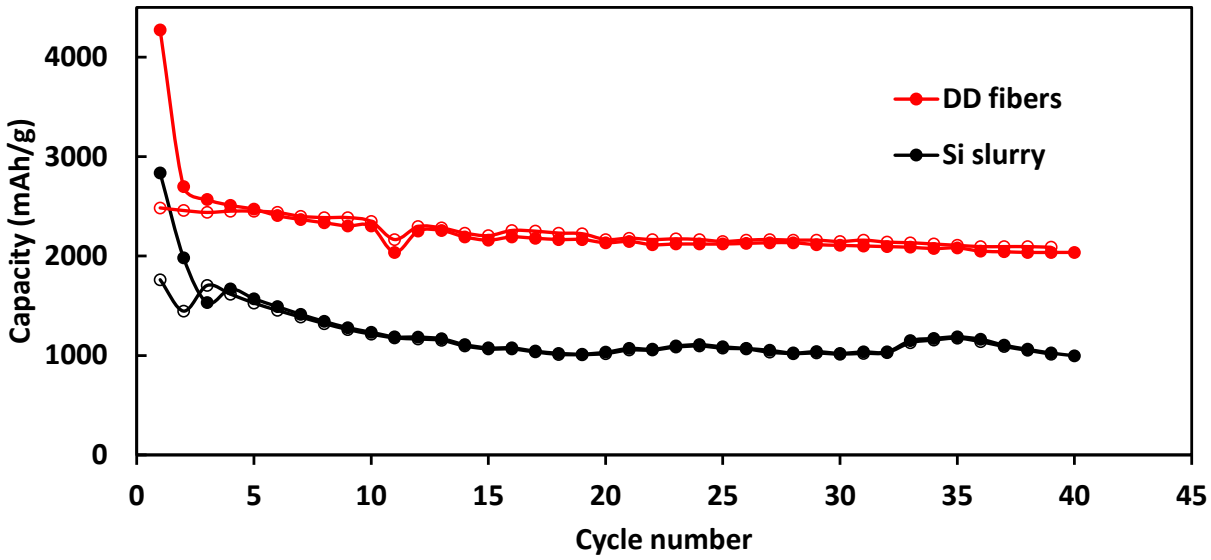

Figure 2. 14. Cyclic performance of DD fibers and slurry electrodes at a rate of 0.18 Ag-1. Closed symbols are for lithiation capacity and open ones are for delithiation capacity.

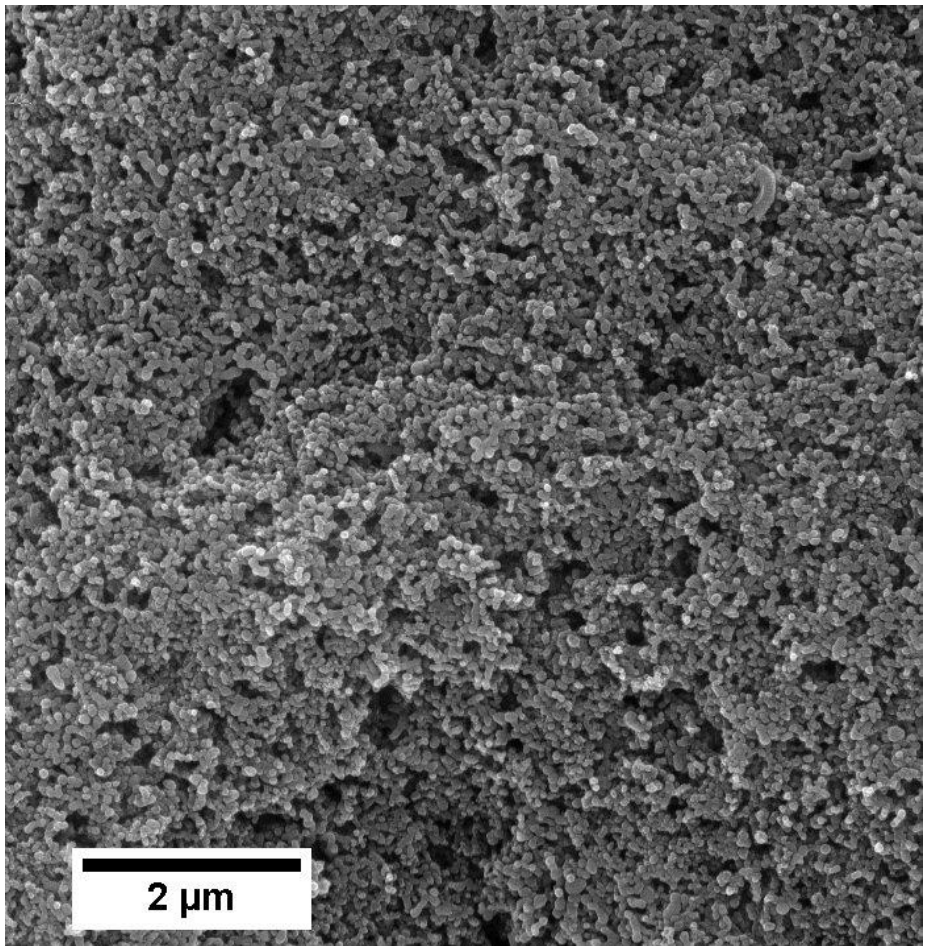

Figure 2. 15. SEM surface image of SiNP slurry electrode before cycling

Directly deposited silicon anodes were galvanostaticaly charged and discharged at 1 Ag^{-1}, with an average coulombic efficiency of 98% for 180 cycles in Figure 2.16. This material was able to retain 67% of its initial capacity after 180 cycles.

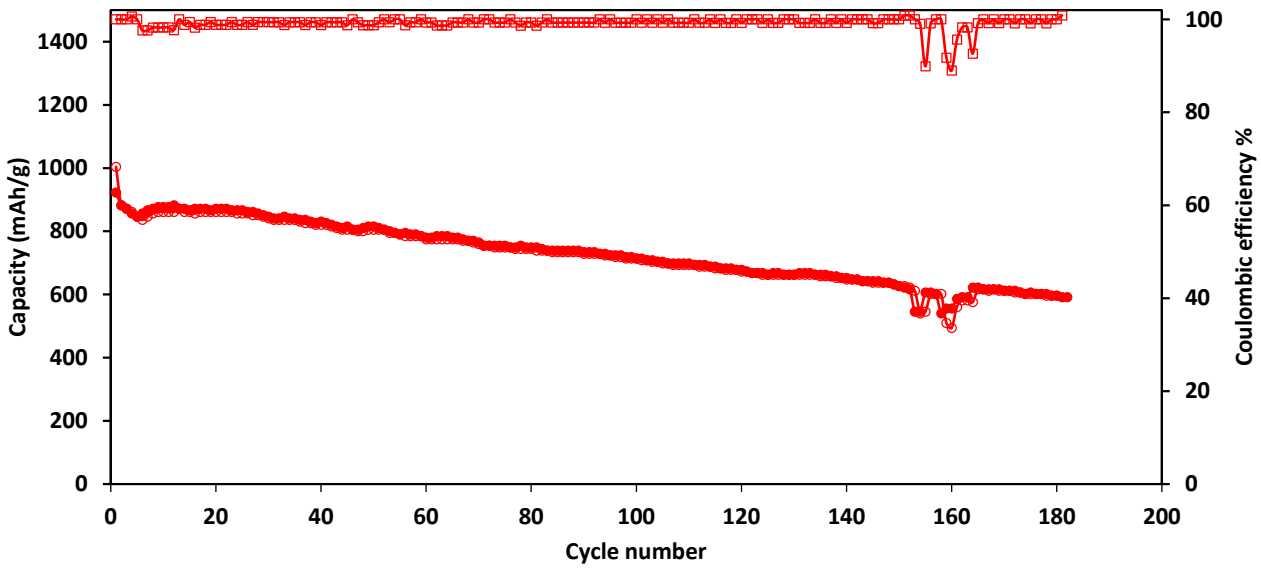

Figure 2. 16. Long time performance of DD fibers at 1A/g. Closed and open circles are lithiation and delithiation capacities respectively and open squares denote coulombic efficiencies.

To further examine electrochemical performance of DD fibers under harsh conditions, the cells were subject to increasing current rates from 0.4 to 8 Ag^{-1}. Figure 2.17 show rate capability of the DD fibers at rates indicated above each step. As apparent from this figure, composite anode has ~700, 400 $mAhg^{-1}$ at 4, $8Ag^{-1}$, respectively. It should be noted, that these fibers were able to recover their capacity when the current rate was increased to 8 and back to $0.8Ag^{-1}$. This capability at high current rates is made possible through the unique nanostructure of this material, which makes the active sites easily accessible for lithium ions. The enhancement in high rate performance of directly deposited anodes should also stems from the improvement of electron transport by 1-D carbon nanotubes in the polymer matrix, and protection of Si NP inside the PVA bed which prevents aggregation but does not impede charge transfer. In addition, shorter diffusion length for Li-ions resulted from fiber morphology, contributes to enhanced

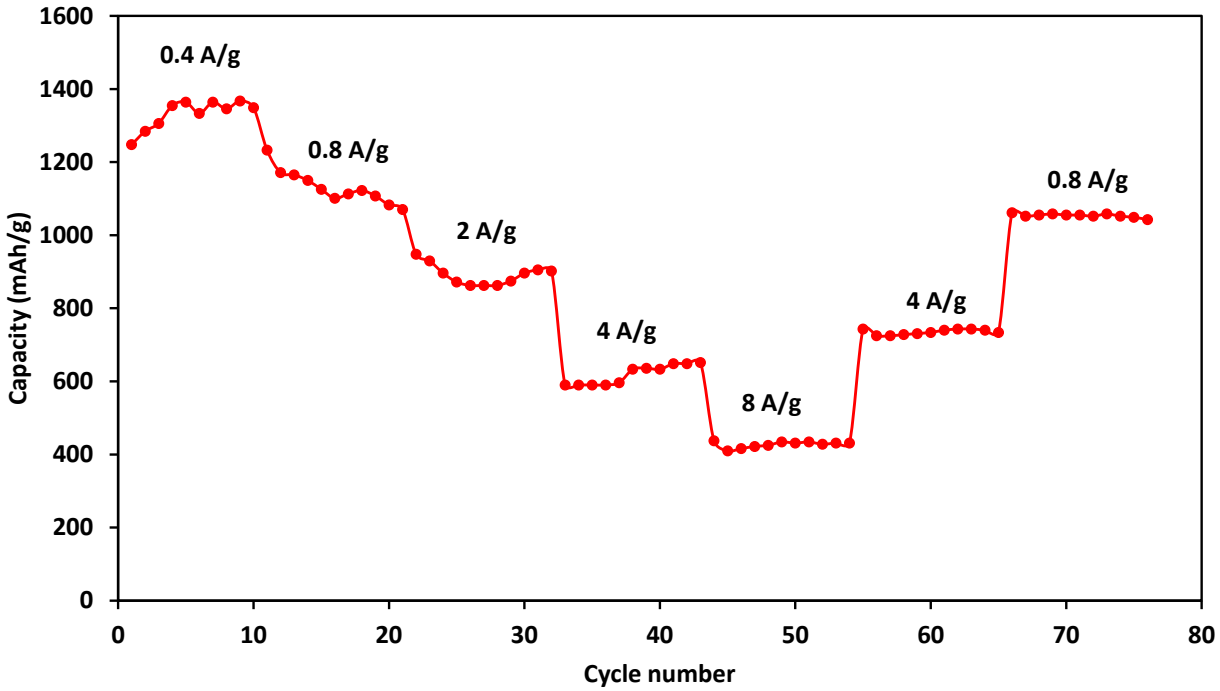

Figure 2. 17. Lithiation capacity of DD nanofibers at rates indicate above each step.

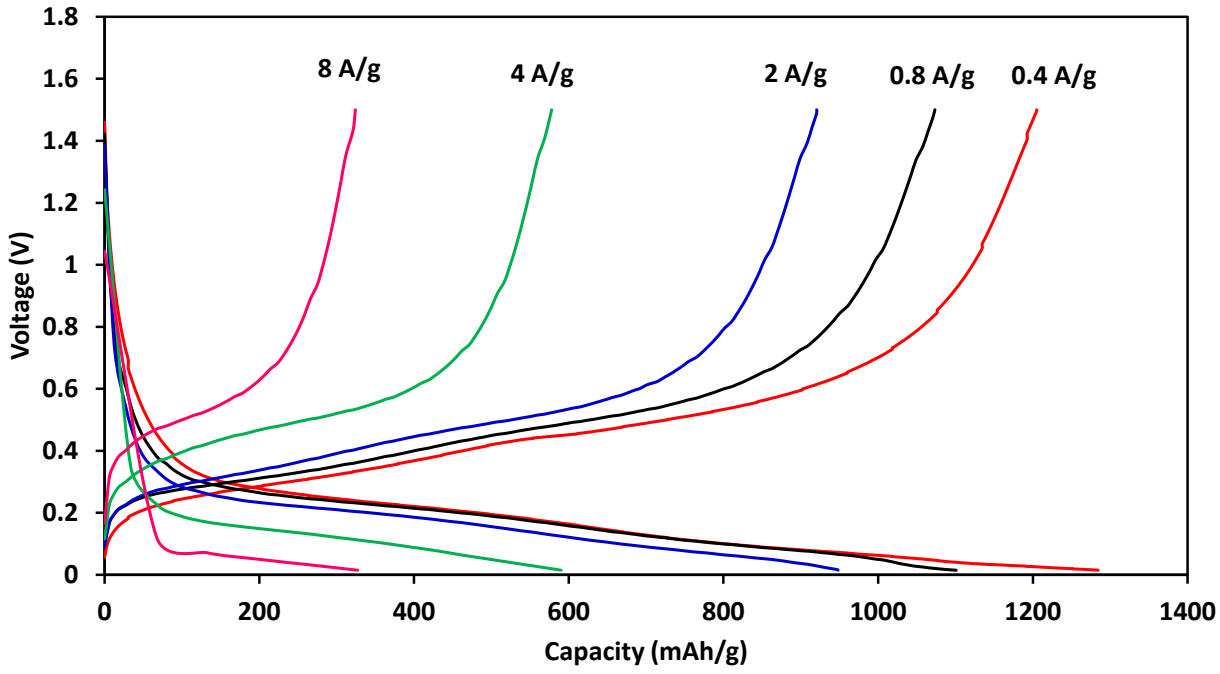

Figure 2. 18. Capacity-Voltage profiles of DD fibers at rates indicated above them

performance at higher rates. Figure 2.18 illustrates the capacity-voltage profiles of DD fibers at rates indicated above them. The change in the overpotential of the cell is minimal when the current is increased 5x from 0.4 to 2 A/g and the fibers exhibit only a 30% drop in their capacity. For higher rates of 4 and 8 A/g there is a noticeable increase in the overpotential of the cell, indicating the high impedance of the cell, probably due to the nonconductive PVA and PAA polymers in the system.

To highlight the synergic effect of fiber morphology and nanoparticle inclusions, nanofibers of PVA-CNT and PVA-SiNP were directly deposited on the current collector in the same manner as the fibers of Si-PVA-CNT. Figure 2.19, reports cyclic of these materials at a rate of 1mV/s. The current is normalized by the weight of active material in each case for a fair comparison. The voltammogram of PVA-CNT fibers exhibits no faradaic peaks between 1.5 and 0.1V as expected and it has the general shape of conductive carbon material with most of the capacity coming due to a double layer capacitance effect. At voltages less than 0.1V the peak for intercalation of lithium ions in the carbonous material can be observed. In the case of PVA-SiNP fibers, the voltammogram shows the lithiation peaks of 0.2 and less than 0.1V and delithiation peaks at 0.3 and 0.5V which are associated with different alloyed composition of silicon and lithium. These peaks match the reports in other literature. From the graph it is obvious that the capacity of these fibers is only due to faradaic activity and no double layer capacitance effect can be observed due to the absence of conductive agents in the system. For the DD fibers which have both Si and CNTs included, clearly the produced current is higher than the previous cases when the voltage is swept in the same manner. The voltammogram shows both faradaic peaks and double

layer capacity which attest to the synergistic effect of having both type of nanoparticles in the system. Having a 1D material as the conductive carbon ensures a percolated network at low concentrations of about 7wt%, to obtain highly loaded fibers with the main active component i.e. silicon.

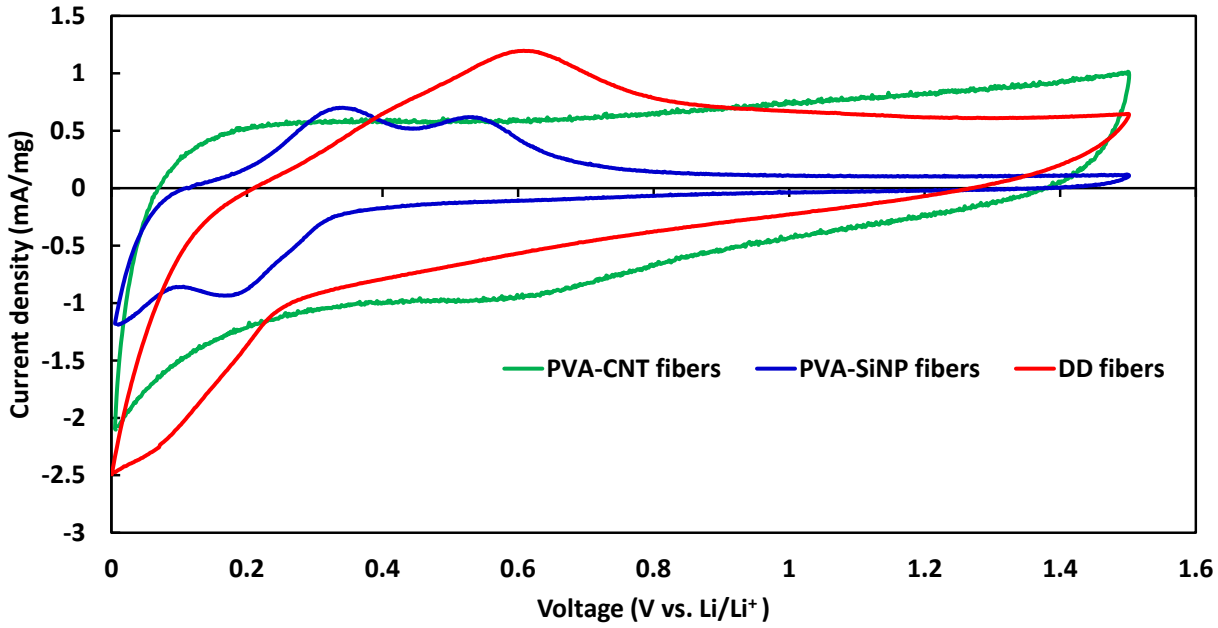

Figure 2. 19. Cyclic Voltammetry of PVA-CNT, PVA-SiNP and DD fibers at 1 mV/s

From the Nyquist plots of impedance data of the three sets of nanofibers in Figure 2.20 indicate the large impedance of these cells before constant current cycling, possibly due to the large amount of nonconductive polymers. Also, PVA-SiNP fibers which are devoid of conductive agent have the highest impedance. DD fibers exhibit the lowest impedance which due to the synergistic effect of both type of nanoparticles in the system and having fully packed fibers with

percolated networks. Figure 2.21 illustrates the cyclic performance of PVA-SiNP and PVA-CNT nanofibers when charged and discharged at a rate of 0.18 Ag^{-1}. Both these fibers have stable capacities of about 200 $mAhg^{-1}$, more than an order of magnitude smaller than DD fibers, confirming the crucial both type of nanoparticles. Having a conductive agent in the system to mobilize charges is crucial for SiNPs because of low electron conductivity of this material. Therefore, CNTs are ideal complement to the DD system since, they are highly conductive and can be easily dispersed throughout the PVA matrix by electrospinning to form a percolated network (at relatively low concentration due to their high aspect ratio).

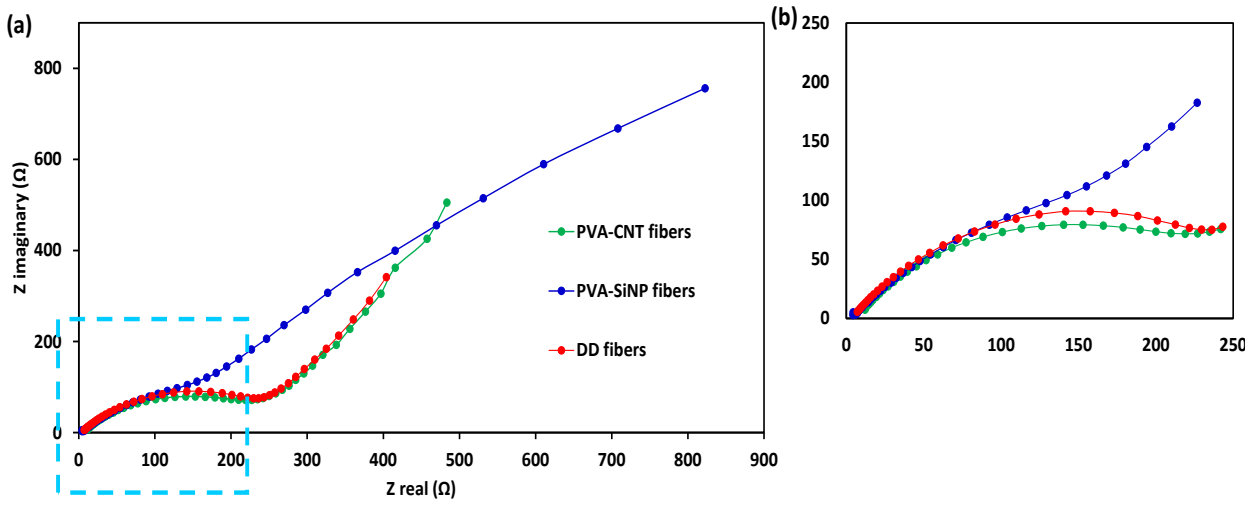

Figure 2. 20. a) Nyquist plots of impedance data of PVA-CNT, PVA-SiNP, and DD fibers b) zoomed-in the part boxed in figure (a)

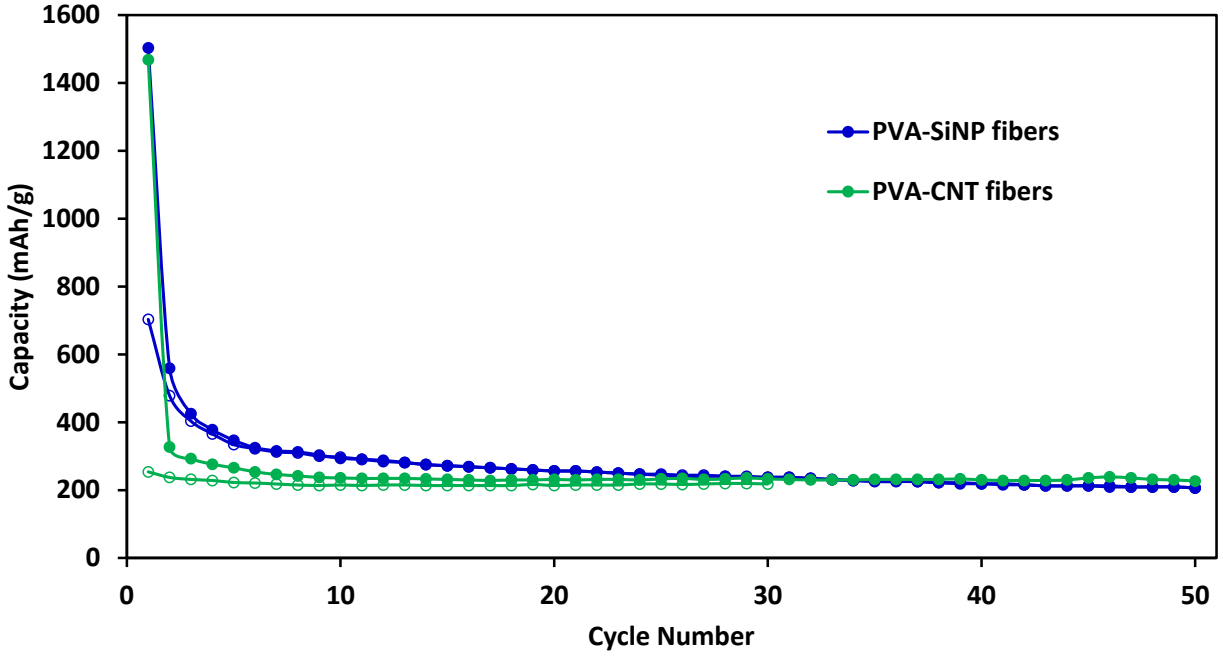

Figure 2. 21. Lithiation/delithiation capacities at 0.18 A/g. closed circles represent lithiation and open symbols represent delithiation capacities

Table 2.1 compares literature on Si-C composites that are related to the presented work, in at least one aspect (process, material, etc.). This information includes electrochemical performances along with preparation processes to draw a more meaningful comparison. A highly loaded solution in conjunction with electrospinning enables production of composite material with high silicon loading compared to other literature using electrospinning. Although there are more sophisticated and expensive methods for active material preparation, our facile and environmentally friendly process, resulted in comparable electrode performance, especially at higher rates. Ragone plot analysis of DD fibers and slurry electrode is given in Figure 2.22. Slurry electrode quickly loses its ability to perform as the power density is increased, while DD fibers have more gradual drop

in their energy density with rise in power density. Therefore, this configuration of active material is more suitable for applications such as power tools and electric vehicles where the battery has to sustain a high power for an extended time.

Table 2.1. Comparison of electrochemical performance and preparation technique of different composite Si-C for lithium-ion batteries

silicon content	Initial Capacity	Final capacity after (n) cycles	Capacity at highest current	Preparation technique	solvents	Ref
54.2%	2697 @0.1 Ag^{-1}	1496 (100) @ 0.5 Ag^{-1}	Around 369 @ 9.3 Ag^{-1}	Electrospinning	DMF, Ethanol	[40]
50%	2488 @0.1 Ag^{-1}	~ 2085 (100) @0.24 Ag^{-1}	1203 @ 9.75A/g	Electrospinning	DMF, NMP	[28]
~50%	~ 5800 @ 4.6 Ag^{-1}	~ 800 (100 @35.8 Ag^{-1}	Around 700 @ 54 Ag^{-1}	CVD	N/A	[23]
55%	858 @0.1 Ag^{-1}	800(100) @ 0.26 Ag^{-1}	Around 772 @2.6 Ag^{-1}	Arc melting and single-roll solidification	DMSO	[41]
64%	2788 @0.4 Ag^{-1}	1757 (250) @	Around 1690 @ 4 Ag^{-1}	Polymerization and supercritical CO_2 process	Water, ethanol	[42]
78%	1688 @0.4 Ag^{-1}	1249	250 A 8A/g	Self-assembly and hydrothermal carbonization	Toluene, water, HCl, ethanol	[43]
75%	2800 @0.36 Ag^{-1}	1711 (90) @1.2 Ag^{-1}	~ 1800 @ 1.2 Ag^{-1}	CVD	water	[44]
95%	3100 @0.1 Ag^{-1}	1287 (500) @ 0.5 Ag^{-1}	800 @3 Ag^{-1}	CVD and melt self-assembly	N/A	[45]
68%	4190 @ 0.18 Ag^{-1}	1025 (300) @ 2.5 Ag^{-1}	650 @ 12 Ag^{-1}	Direct Deposit Electrospinning	Water	**This Work**

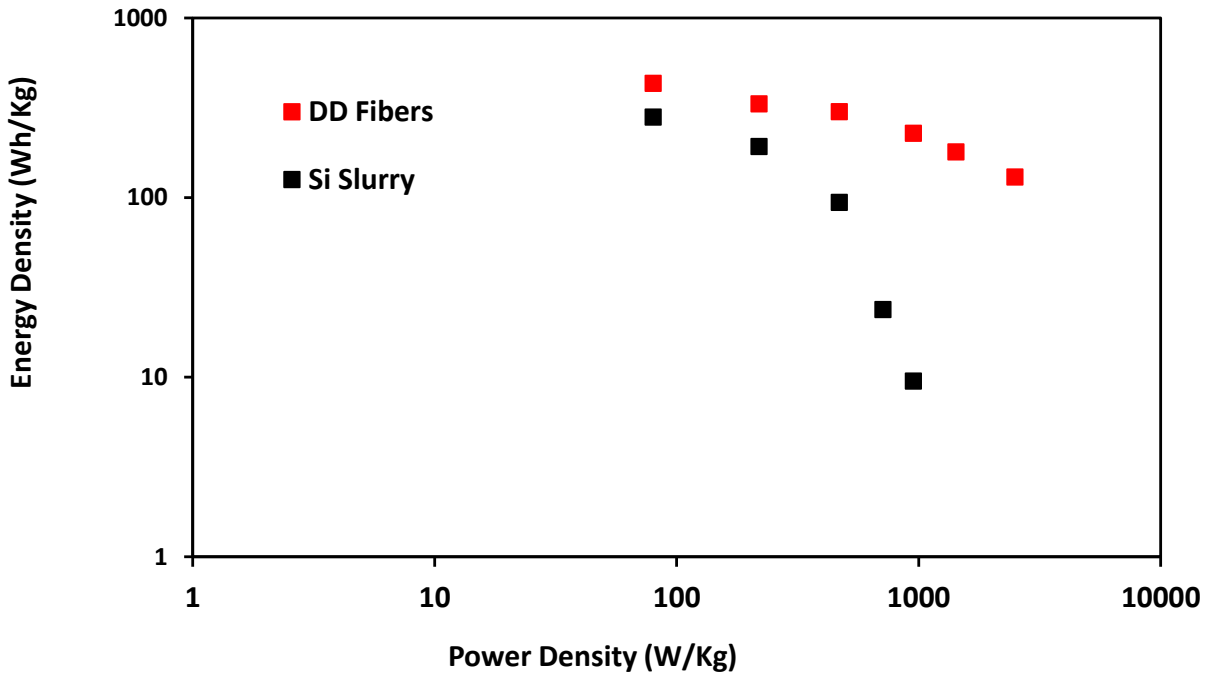

Figure 2. 22. Ragone analysis of DD fibers alongside slurry electrode

2.4. Discussion

Morphology and impedance analysis of directly deposited fibers after half-cell cycling. To further assess electrochemical properties of the two types of electrodes, impedance measurements were performed on half cells. Figure 2.23a is Nyquist plot for Si NP slurry electrode before and after 50 cycles. The cell started with a charge transfer resistance (*R*ct) and bulk resistance (*R*b) of 80 and 4.3Ω, respectively. After cycling the bulk resistance is increased to 180 Ω and a slight increase in *R*ct was observed. Since bulk resistance is mainly an indication of electrolyte resistance, this increase in the value can be due to unwanted reactions that formed solid electrolyte interface (SEI) and also pulverized material that left the electrode surface. On the other hand, DD anodes

had a different behavior, as can be seen in Figure 2.23b. The initial *R*ct and *R*b are slightly higher (100 and 8 Ω, respectively), probably due to the presence of PAA coating and PVA polymer inside of the system (both non-conductive polymers). However, after 50 cycles, the charge transfer resistance was decreased to a value of 29.8 Ω, which should be attributed to the remaining Li-ions within the polymeric matrix and is consisted with other literature using polymers [18, 19, 24]. On the other hand, *R*b for directly deposited anode only showed a slight increase, going from 8.3 to 11.2Ω. This could be ascribed to protection of Si NPs inside of the PVA matrix, which prevents pulverization and suppresses SEI formation on nanoparticles [47-51]. Figure 2.23c illustrates the equivalent circuit that was used to evaluate both sets of impendence data.

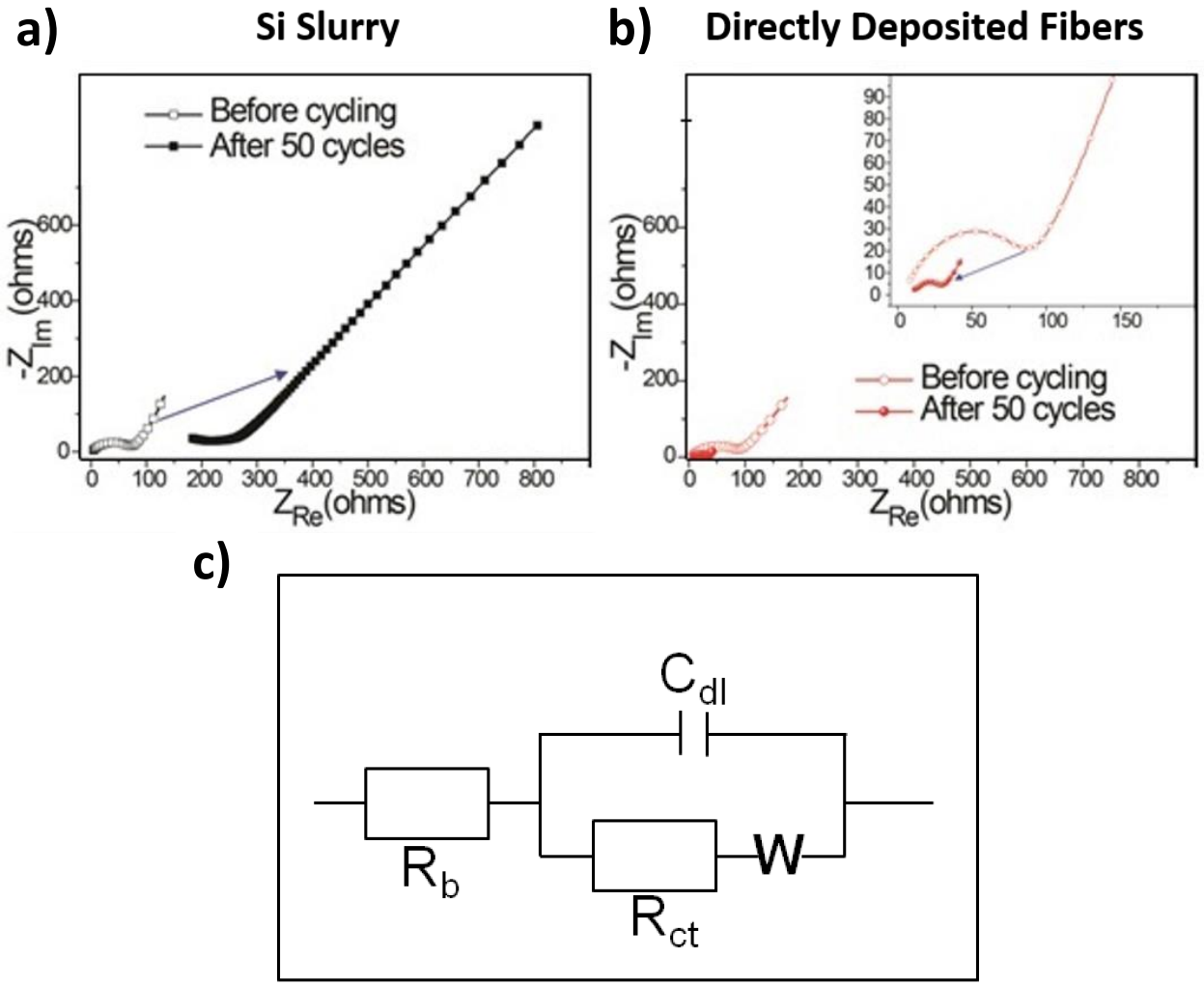

Figure 2. 23. Nyquist plots of half–cells using (a) Si NPs slurry and (b) PVA/Si/CNTs before cycling and after 50 cycles (c) equivalent circuit used for analyzing both sets of impedance data

To evaluate morphological changes, half cells of Si NP slurry and directly deposited anode were disassembled and SEM and TEM images were taken after cycling. Figure 2.24a depicts morphology of the Si NP slurry on top of the copper current collector. As apparent from this image, large cracks are formed on the surface after cycling, which reduces connectivity of nanoparticles and compromises the performance. Existence of these cracks can explain increase in impedance

of the electrode after cycling. In addition, Figure 2.24b which is a higher magnification of the same electrode shows randomly placed particles in their swollen state after cycling (electrode surface before cycling is shown in Figure 2.15 for comparison). On the other hand, lower magnification SEM image in Figure 2.24c depicts that directly deposited electrode still maintained its 1D fiber structure, and sustained the overall connectivity of the material. A higher magnification SEM in Figure 2.24d reveals morphology of the fibers and placement of silicon nanoparticles. PVA matrix is still supporting particles and, prevented pulverization and agglomeration during cycling. The average fiber diameter shows an increase from 130 to 420 nm after 50 cycles to accommodate swollen particles. These images were taken at the edges of electrode where the PAA coating was more eroded, whereas towards the center of the electrode coating was still intact.

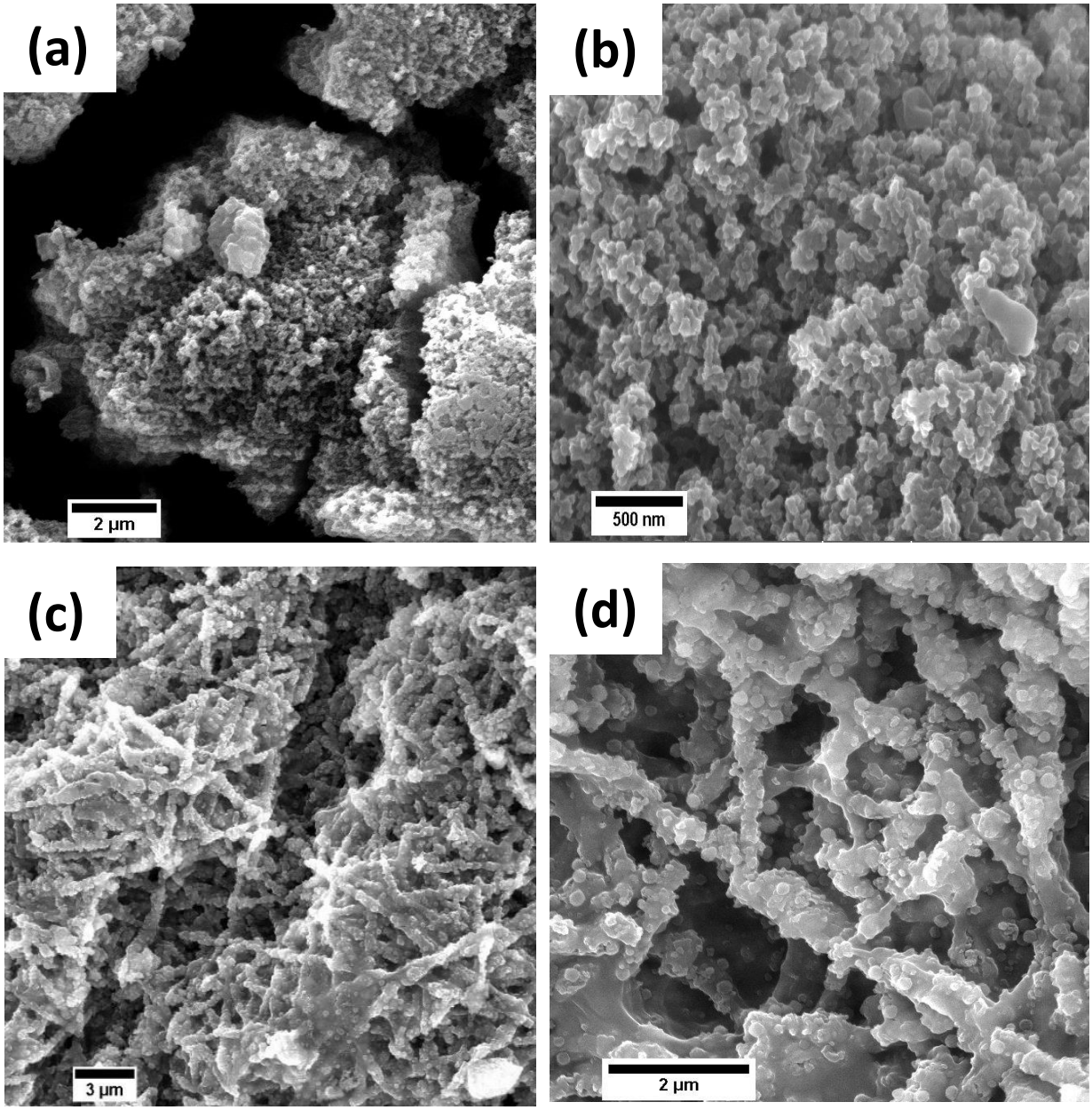

Figure 2. 24. SEM images of electrodes with (a and b) Si NPs slurry and (c and d) PVA/Si/CNTs after 50 cycles

TEM analysis also confirmed the morphology observed. Figure 2.25a and 2.25b are microtomed sections of Si NP slurry and directly deposited electrodes after 50 cycles respectively. Nanoparticles in the conventional slurry have lost connectivity with each other and conductive carbon, while nanoparticles in the directly deposited electrodes maintained their network inside the PVA matrix. Si NPs in DD anode do not show signs of disintegration, although they are clearly expanded in size and in some cases fused together.

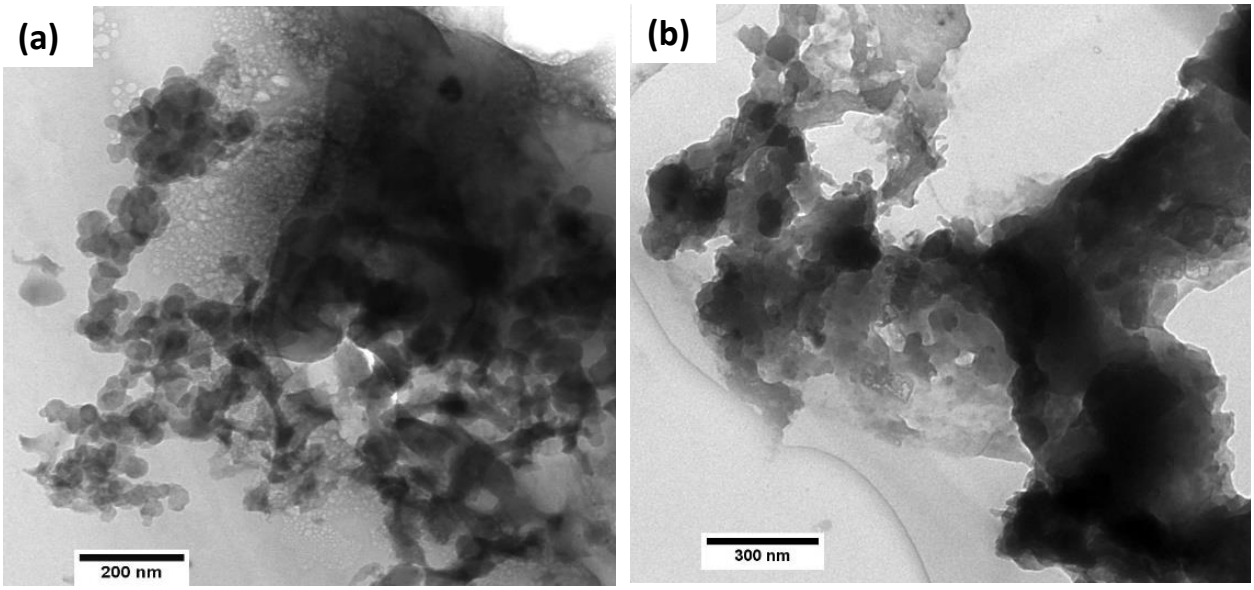

Figure 2. 25. TEM images of (a) Si NPs slurry and (b) PVA/Si/CNTs after 50 cycles

FT–IR characterization before and after heat treatment of PVA. In order to investigate the importance of heat treatment of polymeric matrix under air, DD system was analyzed by Fourier transform infrared (FT-IR) spectroscopy. Figure 2.26a spectrum with several peaks at ν=3360 cm^{-1} for O–H bond, ν=2900–2950 cm^{-1} for C–H bond and others (ν=1090 cm^{-1} for C–O–C and ν=1730 for C=O & C–O–C), which are the same as reported in the other literature [54-57], and are evidence for presence of PVA in the system. In addition, Si-O-Si peak at ν=1240 cm^{-1} is due to the native oxide on surface of Si NPs. After heat treatment at 200°C, chemical structure of PVA was greatly modified. Peaks of O–H, C– H and C–H2 disappeared in Figure 2.26b, which is an indication of side group elimination in a condensation reaction that mostly gives off water [58,59]. In this process some crosslinking occurs [58,59], which prevents the polymeric matrix from dissolving back into the solvent, hence improving chemical stability.

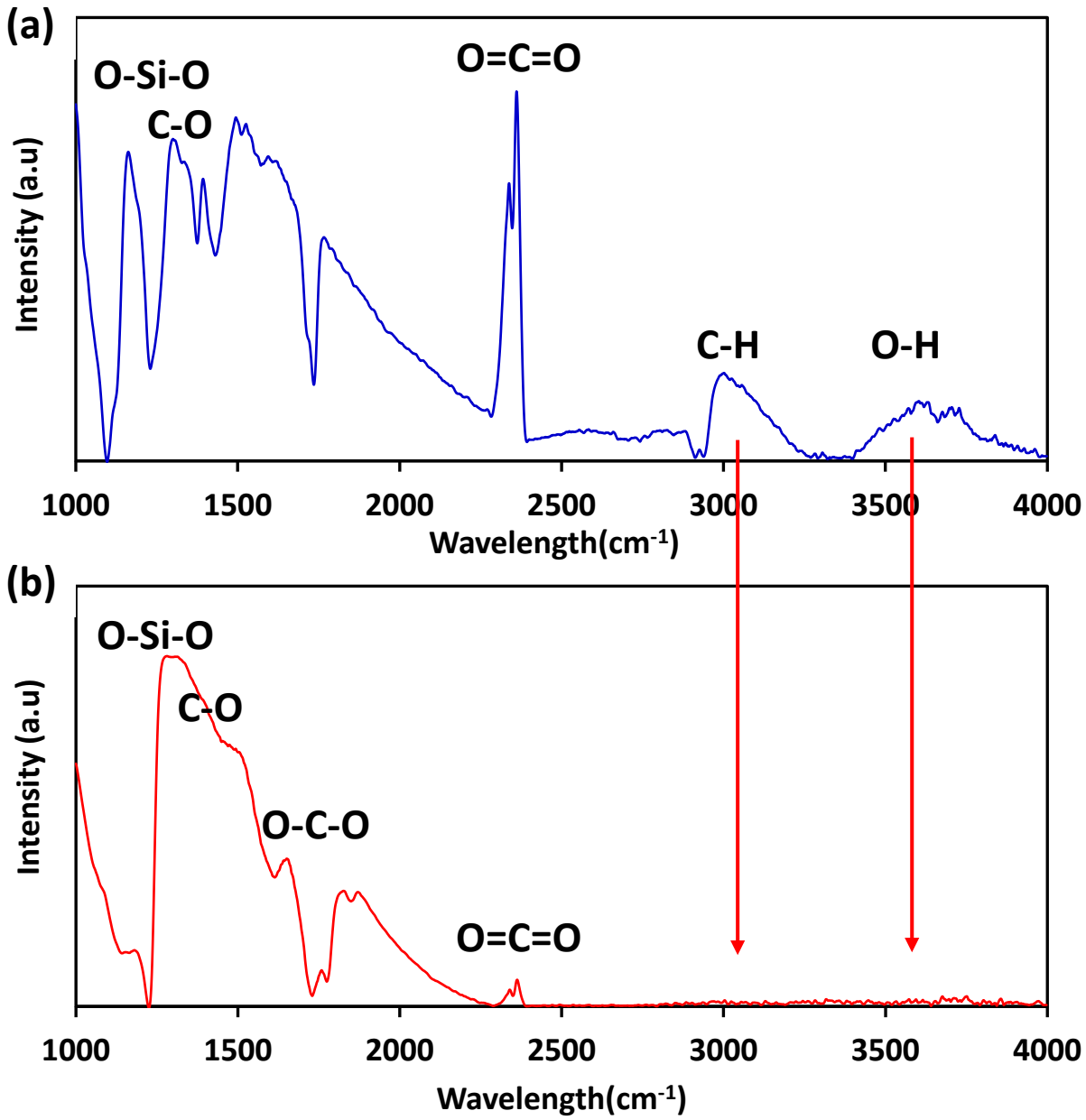

Figure 2. 26. FTIR spectrum of a) DD fibers before heat treatment b) DD fibers after heating for 12 hours at 200ºC in Air

Going back to Figure 2.6, the heat-treated fibers did not show mass reduction up to 330°C, hence thermal stability is also enhanced. This step is crucial in preparation of functional anodic material, since this modification improves safe keeping of embedded nanoparticles by PVA. As-spun DD fibers have a high volume of PVA which limits their performance. However, after heat treatment volume and mass of polymer is decreased, therefore enhancing its electrochemical performance (since PVA is non-conductive), while still supporting nanoparticles. Without heat treatment, the fibers did not perform as well or failed just after couple of cycles. Effect of this thermal treatment on silicon nanoparticles are minimal. The relative intensity of Si-O-Si peak shows increase, which can mean some silicon oxides were created during heat treatment under air, but the overall performance of fibers is uncompromised. This is further confirmed by XRD measurements on the fibers.

2.5. Conclusion

In summary, we have presented an environmentally-friendly and easily scalable electrode fabrication method via water-based electrospinning. This procedure was used to make directly deposited silicon anodes for Li-ion batteries; by-passing many of the conventional steps in electrode fabrication, hence reducing cost and time. Electrodes made with this technique showed an outstanding capacity retention of 92% over 300 cycles with *ca.* 1200 $mAhg^{-1}$ reversible capacity. This ability to retain the capacity should be attributed to PVA which surrounds silicon nanoparticles giving them structural integrity, while protecting them from unwanted electrolyte reactions and preventing nanoparticle agglomeration. Furthermore, structure of the nanofiber mat provides ample room for expansion of nanoparticles. PVA/Si/CNT nanofibers also have a good rate capability despite usage of a non-conductive polymer. 1-D structure of fibers and utilization

of CNTs inside the structure facilitates charge and electron transfer properties of the fiber mat, which result in a good rate capability performance. Capacity limited full cells with PVA/Si/ CNTs exhibited 100% capacity retention while, Si NP slurry full cells started fading after 25 cycles under the same cut-off conditions. Overall directly depositing material via water-based electrospinning is a scalable method of electrode fabrication, which can be applied to a variety of energy conversion and storage devices such as batteries, fuel cells and super capacitors.

REFERENCES

[1] Dunn, B., Kamath, H. & Tarascon, J. –M. Electrical energy storage for the grid: a battery of choices. *Science* **334**, 928–935 (2011).

[2] Armand, M. & Tarascon, J. –M. Building better batteries. *Nature* **451**, 652–657 (2008).

[3] Thackeray, M. M., Wolverton, C. & Isaacs, E. D. Electrical energy storage for transportation–approaching the limits of, and going beyond, lithium–ion batteries. *Energy Environ. Sci.* **5**, 7854–7863 (2012).

[4] Tarascon, J. –M. & Armand, M. Issues and challenges facing rechargeable lithium batteries. *Nature* **414**, 359**–**367 (2001).

[5] Arico, A. S., Bruce, P., Scrosati, B., Tarascon, J. –M. & van Schalkwijk, W. Nanostructured materials for advanced energy conversion and storage devices. Nat. Mater. 4, 366**–**377 (2005).

[6] Chan, C., K., Peng, H., Liu, G., Mcilwrath, K., Zhang, X. F., Huggins, R. A. & Cui, Y. High–performance lithium battery anodes using silicon nanowires. *Nature Nanotech.* **3**, 31–35 (2008).

[7] Wu, H. & Cui, Y. Designing nanostructured Si anodes for high energy lithium ion batteries. *Nano Today* **7**, 414–429 (2012).

[8] Szczech, J. R. & Jin, S. Nanostructured silicon for high capacity lithium battery anodes. *Energy Environ. Sci.* **4**, 56–72 (2011).

[9] Teki, R., Datta, M. K., Krishnan, R., Parker, T. C., Lu, T. –M., Kumta, P. N. & Koratkar, N. Nanostructured silicon anodes for lithium ion rechargeable batteries. *Small* **5**, 2236–2242 (2009).

[10] Beattie, S. D., Larcher, D., Morcrette, M., Simon, B. & Tarascon, J. –M. Si electrodes for Li–ion batteries—a new way to look at an old problem. *J. Electrochem. Soc.* **155**, A158–A163 (2008).

[11] Hu, Y. –S., Demir–Cakan, R., Titirici, M. –M., Muller, J. –O., Schlogl, R., Antonietti, M. & Maier, J. Superior storage performance of a Si@SiO_x/C nanocomposite as anode material for lithium–ion batteries. *Angew. Chem. Int. Ed.* **47**, 1645–1649 (2008).

[12] Yu, Y., Gu, L., Zhu, C., Tsukimoto, S., Aken, P. A. & Maier, J. Reversible storage of lithium in silver–coated three–dimensional macroporous silicon. *Adv. Mater.* **22**, 2247–2250 (2010).

[13] Magasinski, A., Dixon, P., Hertzberg, B., Kvit, A., Ayala, J. & Yushin, G. High–performance lithium–ion anodes using a hierarchical bottom–up approach. *Nature Mater.* **9**, 353–358 (2010).

[14] Liu, N., Lu, Z., Zhao, J., McDowell, M. T., Lee, H. –W., Zhao, W. & Cui, Y. A pomegranate–inspired design for large–volume–change lithium battery anodes. *Nature Nanotech.* **9**, 187–192 (2014).

[15] Wu, H., Chan, G., Choi, J. W., Ryu, I., Yao, Y., McDowell, M. T., Lee, S. W., Jackson, A., Yang Y., Hu, L. & Cui, Y. Stable cycling of double–walled silicon nanotube battery anodes through solid–electrolyte interphase control. *Nature Nanotech.* **7**, 310–315 (2012).

[16] Ge, M., Rong, J., Fang, X. & Zhou, C. Porous doped silicon nanowires for lithium ion battery anode with long cycle life. *Nano Lett.* **12**, 2318–2323 (2012).

[17] Wang, B., Li, X., Qiu, T., Luo, B., Ning, J., Li, J., Zhang, X., Liang, M. & Zhi, L. High volumetric capacity silicon–based lithium battery anodes by nanoscale system engineering. *Nano Lett.* **13**, 5578–5584 (2013).

[18] Jeong, Y. K., Kwon, T. –W., Lee, I., Kim, T. –S., Coskun, A. & Choi, J. W. Hyperbranched β–Cyclodextrin polymer as an effective multidimensional binder for silicon anodes in lithium rechargeable batteries. *Nano Lett.* **14**, 864–870 (2014).

[19] Liu, B., Soares, P., Checkles, C., Zhao, Y. & Yu, G. Three–dimensional hierarchical ternary nanostructures for high–performance Li–ion battery anodes. *Nano Lett.* **13**, 3414–3419 (2013).

[20] Wu, H., Yu, G., Pan, L., Liu, N., McDowell, M. T., Bao, Z. & Cui, Y. Stable Li–ion battery anodes by in–situ polymerization of conducting hydrogel to conformally coat silicon nanoparticles. *Nature Commun.* **4**, 1–6 (2013)

[21] Liu, G., Xun, S., Vukmirovic, Song, X., Olalde–Velasco, P., Zheng, H., Battaglia, V. S., Wang, L. & Yang, W. Polymers with tailored electronic structure for high capacity lithium battery electrodes. *Adv. Mater.* **23**, 4679–4683 (2011).

[22] Wang, C., Wu, H., Chen, Z., McDowell, M. T., Cui, Y. & Bao, Z. Self–healing chemistry enables the stable operation of silicon microparticle anodes for high–energy lithium–ion batteries. *Nature Chem.* **5**, 1042–1048 (2013).

[23] A. Gohier, B. Laïk, K.-H. Kim, J.-L. Maurice, J.-P. Pereira-Ramos, C.S. Cojocaru, P.T. Van, High-Rate Capability Silicon Decorated Vertically Aligned Carbon Nanotubes for Li-Ion Batteries, Adv. Mater. 24 (2012) 2592–2597.

[24] B. Wang, X. Li, X. Zhang, B. Luo, M. Jin, M. Liang, S.A. Dayeh, S.T. Picraux, L. Zhi, Adaptable Silicon–Carbon Nanocables Sandwiched between Reduced Graphene Oxide Sheets as Lithium Ion Battery Anodes, ACS Nano. 7 (2013) 1437–1445.

[25] S. Chen, P. Bao, X. Huang, B. Sun, G. Wang, Hierarchical 3D mesoporous silicon@graphene nanoarchitectures for lithium ion batteries with superior performance, Nano Res. 7 (2013) 85–94.

[26] W. Xiao, J. Zhou, L. Yu, D. Wang, X.W. (David) Lou, Electrolytic Formation of Crystalline Silicon/Germanium Alloy Nanotubes and Hollow Particles with Enhanced Lithium-Storage Properties, Angew. Chem. Int. Ed. 55 (2016) 7427–7431.

[27] X. Zhou, L. Yu, X.-Y. Yu, X.W. (David) Lou, Encapsulating Sn Nanoparticles in Amorphous Carbon Nanotubes for Enhanced Lithium Storage Properties, Adv. Energy Mater. (2016) n/a-n/a.

[28] T.H. Hwang, Y.M. Lee, B.-S. Kong, J.-S. Seo, J.W. Choi, Electrospun Core–Shell Fibers for Robust Silicon Nanoparticle-Based Lithium Ion Battery Anodes, Nano Lett. 12 (2012) 802–807.

[29] S.A. Abureden, F.M. Hassan, G. Lui, W. Ahn, S. Sy, A. Yu, Z. Chen, Multigrain Electrospun Nickel Doped Lithium Titanate Nanofibers with High Power Lithium Ion Storage, J. Mater. Chem. A. (2016).

[30] J.W. Min, C.J. Yim, W.B. Im, Facile Synthesis of Electrospun Li1.2Ni0.17Co0.17Mn0.5O2 Nanofiber and Its Enhanced High-Rate Performance for Lithium-Ion Battery Applications, ACS Appl. Mater. Interfaces. 5 (2013) 7765–7769.

[31] Kim, Y. S., Kim, K. W., Cho, D., Hansen, N. S., Lee, J. & Joo, Y. L. Silicon–rich carbon hybrid nanofibers from water–based spinning: the synergy between silicon and carbon for Li–ion battery anode application. *ChemElectroChem* **1**, 220–226 (2014).

[32] Hansen, N. S., Cho, D. & Y.L. Joo, Y. L. Metal nanofibers with highly tunable electrical and magnetic properties via highly loaded water–based electrospinning. *Small* **8**, 1510-1514 (2012).

[33] Li, D. & Xia, Y. N. Electrospinning of nanofibers: reinventing the wheel? *Adv. Mater.* **16**, 1151–1170 (2004).

[34] Greiner, A. & Wendorff, J. H. Electrospinning: A fascinating method for the preparation of ultrathin fibers. *Angew. Chem. Int. Ed.* **46**, 5670–5703 (2007).

[35] Yang, H. & Jiang, P. Large–scale colloidal self–assembly by doctor blade coating. *Langmuir* **26**, 13173–13182 (2010).

[36] Ha, D. –H., Islam, M. A. & Robinson, R. D. Binder–free and carbon–free nanoparticle batteries: A method for nanoparticle electrodes without polymeric binders or carbon black. *Nano Lett.* **12**, 5122–5130 (2012).

[37] E. Frackowiak, F. Béguin, Electrochemical storage of energy in carbon nanotubes and nanostructured carbons, Carbon. 40 (2002) 1775–1787.

[38] McDowell, M. T., Lee, S. W., Harris, J. T., Kogel, B. A., Wang, C., Nix, W. D. & Cui. Y. In situ TEM of two–phase lithiation of amorphous silicon nanospheres. *Nano Lett.* **13**, 758–764 (2013).

[39] McDowell, M. T., Lee, S. W. Nix, W. D. & Cui, Y. Understanding the lithiation of silicon and other alloying anodes for lithium–ion batteries. *Adv. Mater.* **25**, 4966–4985 (2013).

[40] C. Li, C. Liu, W. Wang, J. Bell, Z. Mutlu, K. Ahmed, R. Ye, M. Ozkan, C. Ozkan, Towards flexible binderless anodes: silicon-carbon fabrics via double nozzle electrospinning, Chem Commun. (2016). doi:10.1039/C6CC04074H.

[41] S.-H. Yook, S.H. Kim, C. Park, D.-W. Kim, Graphite-silicon alloy composite anodes employing cross-linked poly(vinyl alcohol) binders for high-energy density lithium-ion batteries, RSC Adv. (2016). doi:10.1039/C6RA15839K.

[42] S.H. Lee, S. Park, M. Kim, D. Yoon, C. Chanthad, M. Cho, J. Kim, J.H. Park, Y. Lee, Supercritical Carbon Dioxide-Assisted Process for Well-Dispersed Silicon/Graphene Composite as a Li ion Battery Anode, Sci. Rep. 6 (2016) 32011. doi:10.1038/srep32011.

[43] M.-H. Lin, S. Hy, C.-Y. Chen, J.-H. Cheng, J. Rick, N.-W. Pu, W.-N. Su, Y.-C. Lee, B.J. Hwang, Resilient Yolk-Shell Silicon-Reduced Graphene Oxide/Amorphous Carbon Anode Material Achieved by a Synergistic Dual-Coating Process for Lithium-Ion Batteries, ChemElectroChem. (2016) n/a-n/a. doi:10.1002/celc.201600254.

[44] L.-F. Cui, L. Hu, J.W. Choi, Y. Cui, Light-Weight Free-Standing Carbon Nanotube-Silicon Films for Anodes of Lithium Ion Batteries, ACS Nano. 4 (2010) 3671–3678. doi:10.1021/nn100619m.

[45] X. Ding, X. Liu, Y. Huang, X. Zhang, Q. Zhao, X. Xiang, G. Li, P. He, Z. Wen, J. Li, Y. Huang, Enhanced Electrochemical Performance Promoted by Monolayer Graphene and Void Space in Silicon Composite Anode Materials, Nano Energy. (n.d.). doi:10.1016/j.nanoen.2016.07.031.

[46] Ko, M., Chae, S., Jeong, S., Oh, P. & Cho, J. Elastic a–silicon nanoparticle backboned graphene hybrid as a self–compacting anode for high–rate lithium ion batteries. *ACS Nano* **8**, 8591–8599 (2014).

[47] Yi, R., Dai, F., Gordin, M. L. Sohn, H. & Wang, D. Influence of silicon nanoscale building blocks size and carbon coating on the performance of micro–sized Si–Ccomposite Li–ion anodes. *Advanced Energy Mater.* **3**, 1507–1515 (2013).

[48] Li, Y. & Li, J. Carbon–coated macroporous $Sn_2P_2O_7$ as anode materials for Li–ion battery. *J. Phsy. Chem. C* **112**, 14216–14219 (2008).

[49] Aurbach, D. Review of selected electrode–solution interactions which determine the performance of Li and Li ion batteries. *J. Power Sources* **89**, 206–218 (2000).

[50] He, B. –L. Dong, B. & Li, H. –L. Preparation and electrochemical properties of Ag–modified TiO2 nanotube anode material for lithium–ion battery. *Electrochem. Commun.* **9**, 425–430 (2007).

[51] Zhang, Y., Zhang, X. G., Zhang, H. L., Zhao, Z. G., Li, F., Liu, C. & Cheng, H. M. Composite anode material of silicon/graphite/carbon nanotubes for Li–ion batteries. *Electrochim. Acta* **51**, 4994–5000 (2006).

[52] Zhang, S. S., Xu, K. & Jow, T. R. Electrochemical impedance study on the low temperature of Li–ion batteries. *Electrochim. Acta* **49**, 1057–1061 (2004).

[53] Jiang, T., Zhang, S., Qiu, X., Zhu, W. & Chen, L. Preparation and characterization of silicon–based three–dimensional cellular anode for lithium ion battery. *Electrochem. Commun.* **9**, 930–934, (2007).

[54] Wu, J. Wang, N., Wang, L., Dong, H., Zhao, Y. & Jiang, L. Unidirectional water–penetration composite fibrous film via electrospinning. *Soft Matter*, **8**, 5596–5999 (2012).

[55] Sriupayo, J., Supaphol, P., Blackwell, J. & Rujiravanit, R. Preparation and characterization of α–chitin whisker–reinforced poly(vinyl) alcohol nanocomposite films with or without heat treatment. *Polymer* **46**, 5637–5644 (2005).

[56] Mansur, H. S., Sadahira, C. M., Souza, A. N. & Mansur, A. A. P. FTIR spectroscopy characterization of poly (vinyl alcohol) hydrogel with different hydrolysis degree and chemically crosslinked with glutaraldehyde. *Mater. Sci. Eng. C–Mater.* **28**, 539–548 (2008).

[57] Kenawy, E. R., Kamoun, E. A., Mohy Eldin, M. S. & El-Meligy, M. A. Physically crosslinked poly(vinyl alcohol)–hydroxyethyl starch blend hydrogel membranes: Synthsis and characterization for biomedical applications. *Arab. J. Chem.* **7**, 372–380 (2014).

[58] Y. Tsuchiya, K. Sumi, Thermal decomposition products of poly(vinyl alcohol), J. Polym. Sci. 7 (1969) 3151–3158.

[59] P. Alexy, D. Káchová, M. Kršiak, D. Bakoš, B. Šimková, Poly(vinyl alcohol) stabilisation in thermoplastic processing, Polym. Degrad. Stab. 78 (2002) 413–421.

[60] I.C. McNeill, PYROLYSIS '96Thermal degradation mechanisms of some addition polymers and copolymers, J. Anal. Appl. Pyrolysis. 40 (1997) 21–41.

[61] N.A. Peppas, E.W. Merrill, Crosslinked poly(vinyl alcohol) hydrogels as swollen elastic networks, J. Appl. Polym. Sci. 21 (1977) 1763–1770.

CHAPTER THREE

HARVESTING INTER AND INTRA-CONDUCTIVITY OF GRAPHENE NANORIBBONS FOR DIRECTLY DEPOSITED HIGH-RATE SILICON-BASED ANODE FOR LITHIUM ION BATTERIES

3.1. Introduction

The mobile lifestyle of modern society creates demands for reliable energy storage devices and imposes stringent standards on this industry to be satisfied. Lithium-ion batteries dominate the automotive and portable electronics markets, but the current state of the art electrode materials cannot keep up with the constant demand for an increase in capacity and decrease in dimensions. For this reason, the next generation of Li-ion battery electrodes must rely on materials with higher capacity and smarter structural design. Silicon with the theoretical capacity of 4200 $mAhg^{-1}$ is one of the most promising anode material candidates, which hypothetically should be able to offer ten times the capacity of current graphite-based anodes. However, problems with Si such as constant capacity fading, unstable solid electrolyte interface (SEI) and low conductivity are well documented in the literature,[1]–[4]and have hindered commercialization to date. Nanostructuring and composites are the two prominent strategies employed by scientists to overcome shortcomings of silicon anodes. One-dimensional nanoparticles such as nanowires were found to improve electronic conductivity and provided enough room for expansion of material during lithiation.[5]–[8] Carboneous materials are often mixed with silicon because of their inherent high conductivity and structural durability. In addition, carbon is sometimes employed as a protective barrier to keep silicon from unwanted electrolyte reactions while providing electrical conductivity to the system and hence improving rate capability of particles.[9], [10] Carbon nanotubes (CNTs) have already been employed in literature, as a valuable material to improve the performance of silicon as anode

materials for Li-ion batteries.[11]–[13] In recent years, graphene has incurred much attention. Plenty of research has been focused on changing the structure of graphite to graphene families, to achieve higher capacities, via lithiation of these materials on both sides of the basal plane. These 2D carbons have been employed either by themselves,[14]–[16] or in composite form with other materials.[17]–[19] The flexible and strong sheets of honeycomb lattice carbon have been shown to improve electrochemical performance and device longevity in conjunction with silicon.[20]–[26] Among this family, graphene nanoribbons, in particular, can exhibit tunable size dependent electronic properties (such as metallic or semi-conductive behavior),[27]–[29] making them attractive for new nano-electronics applications. To date, graphene nanoribbon composites with materials like iron oxide, SnO_2 and MnO_2 have been tested as successful anode materials for lithium ion batteries.[30]–[32] Recently, Salvatierra et al. fabricated Si nanowire-GNR standalone papers via vacuum filtration that exhibited an excellent electrochemical performance both in half-cell and full-cell configurations.[33] However, current collectors may still be needed for practical purposes, since the electrode materials undergo processes like winding and packaging, which put enormous stresses on the material. In addition, scalability and high-through put roll to roll production are significant challenges for vacuum filtration.

In the present work, we are combining several of the strategies to improve the performance of silicon anodes via engineering the nanostructure and properties of a novel composite material. By employing water-based electrospinning, composites of polyvinyl alcohol (PVA), graphene nanoribbons (GNRs) and silicon nanoparticles (SiNPs) are directly deposited on the surface of the copper current collector, as the lithium ion battery anode. Electrospinning has been used by several groups as a facile and scalable method for active material fabrication with various chemistries.[34]–[41] High extensional deformation during the electrospinning process can

disperse nanoparticles inside fibers,[42], [43] eliminating any need for the surface modification of particles. At the same time, rapid solidification of fibers[44] can prevent particle agglomeration. Therefore, a uniform composite with various components can be attained readily. In addition, this process is easily scalable and can be done in a continuous roll to roll fashion. In this work, graphene nanoribbons are used concurrently with SiNPs to achieve a highly porous non-woven fiber mat. In our previous work, GNRs were mixed with silicon nanoparticles and polyvinyl alcohol (PVA) via electrospinning,[45]followed by carbonization at 900°C to yield active material. The resulting GNR/SiNP/carbon nanofibers were mixed with carbon black and polyacrylic acid (PAA) to form a slurry. In this report, however, the GNR/SiNP/PVA fibers are directly deposited on copper, and they only undergo a mild heat treatment at 200°C to stabilize PVA, before they are used as electrodes. Therefore, there is no other conductive carbon present in the system, and the inherent properties of GNRs are preserved and can be compared to their precursor multi-walled carbon nanotubes (MWCNTs). At the same time, use of toxic solvents (such as N-Methyl-2-pyrrolidone, NMP), and multiple slurry making steps (like ball milling, doctor blading and drying) are eliminated. In addition, the resulted fiber morphology helps in alleviating pulverization because PVA ensures structural integrity. Ample space between fibers accommodates volume expansion and fast Li-ion diffusion, while fibers provide high surface area for reaction. More information about process and morphology of directly deposited fibers can be found in our previous work.[46] To the best of our knowledge, this is the first time that electrochemical performance of GNRs and their parent CNTs are compared in conjunction with silicon, without the addition of any carbon black in the system.

3.2. Experimental section

Composite nanofiber fabrication and characterization: A 10 wt% solution of PVA (MW 78 kDa, Polysciences) in deionized water was prepared. Then SiNPs (US research nanomaterials) and small GNRs (EMD Performance Materials) in a weight ratio of 1:1:0.14 PVA: Si: GNR were added to the solution. The same was done for large GNRs (these GNRs have a linear alkyl group attached to their backbone) and MWCNTs. These carbon nanotubes are precursors to GNRs used in this paper, and all nanomaterials were incorporated in the composite material without any modification. Carbon nanotubes were unzipped using a concentrated sulfuric acid and potassium permanganate. Oxidative opening of carbon nanotubes was achieved by first suspending them in sulfuric acid then treating by potassium permanganate at room temperature. The oxidized nanoribbons were treated by concentrated ammonium hydroxide and hydrazine monohydrate. Full details about this process can be found in the original work by Kosynkin et al. in Ref [52]. The prepared solution was then stirred for several hours, and ultrasonicated (Qsonic) for 30 mins. The electrospinning nozzle was placed 20 cm away from the collector with copper disks on it, and a voltage of 15KV was applied to form nanofibers while the solution was pumped at a rate of 0.01 ml/min. Copper disks with nanofibers were heat treated under air at 200°C for 12 hours to stabilize PVA. Renishaw Invia Raman microscope with 488 nm excitation was used to investigate the carbon structure of CNTs and GNRs. X-ray diffraction (XRD, Scintag) was performed on GNRs and their precursor MWCNTs. The nanofiber morphology was characterized with scanning electron microscopy (FESEM, Tescan Mira), and transmission electron microscopy (TEM, FEI T12 Spirit). Thermo-gravimetric analysis (10°C min^{-1} in air, TGA, TA Instruments Q500) was conducted on the fibers to accurately measure PVA, Silicon, and CNT or GNR content of the composite fibers.

Electrochemical characterization: 2032 type half cells were made using obtained nanofibers and stacking polypropylene-polyethylene (Celgard) as separator and Lithium disk as a counter electrode. A homemade 1M $LiPF_6$ in fluoroethylene carbonate and dimethyl carbonate (50:50 wt:wt%) was used as the electrolyte. All cells were assembled in an argon-filled glovebox with water and oxygen levels below 0.5 ppm. Galvanostatic charge/discharge was performed using an eight-channel battery analyzer (MTI) subjected to a voltage window of 0.015-1.5V vs. Li/Li^+. Cyclic Voltammetry (CV) and electrochemical impedance spectroscopy (EIS) measurements were conducted using a single channel potentiostat (Princeton Applied Research). CV curves were obtained at a scan rate of 1mV s^{-1} between 0.005 to 1.5 V against Li/Li^+. Impedance measurements were done with an amplitude of 10 mV in the frequency range of 0.1 to 100000 Hz. All capacities reported in this study were normalized by the weight of silicon and carbon (either GNRs or CNTs) based on TGA measurements.

3.3. Results and Discussion

Characterization of Graphene Nanoribbons: Two graphene nanoribbons with different dimensions, an average width of 17 and 137nm, respectively, are used in the current study to place them into the fiber or between the fibers. Both GNRs are used as received without further processing. Precursor CNTs of the GNRs are also analyzed for comparison to investigate the effect of unzipping on structure and chemical performance. Figure 3.1a and 3.1c are the transmission electron micrographs showing morphologies of small and large GNRs. As can be seen from these TEM images, unzipping of CNTs results in quasi-1D carbon structures, which are comprised of high aspect ratio graphene layers. Figure 3.1b and 3.1c report TEM of their precursor CNTs for comparison of the structures. The average diameter of the small CNTs is 15 nm, which is only slightly lower than that for small GNRs, 17nm, due to insufficient or partial unzipping of smaller

CNTs. Reported diameters are averages of measurements obtained from 9 different TEM images for each sample. Red arrows in Figure 3.1a point to places along the same carbon structure where there is partial cleavage (indicated by “unzipped”), and a part that still maintained its tubular geometry (marked “CNT”). On the other hand, the average diameter of the large GNRs, 137 nm, is almost twice of 68nm, the average diameter of large CNTs. This is also in line with Figure 3.1b, illustrating the flat graphene layers and successful longitudinal opening of large CNTs. The cleavage of carbon nanotubes has a better yield for CNTs with larger diameter.[47] Figure 3.2 illustrates the morphology of GNRs as seen under a scanning electron microscope.

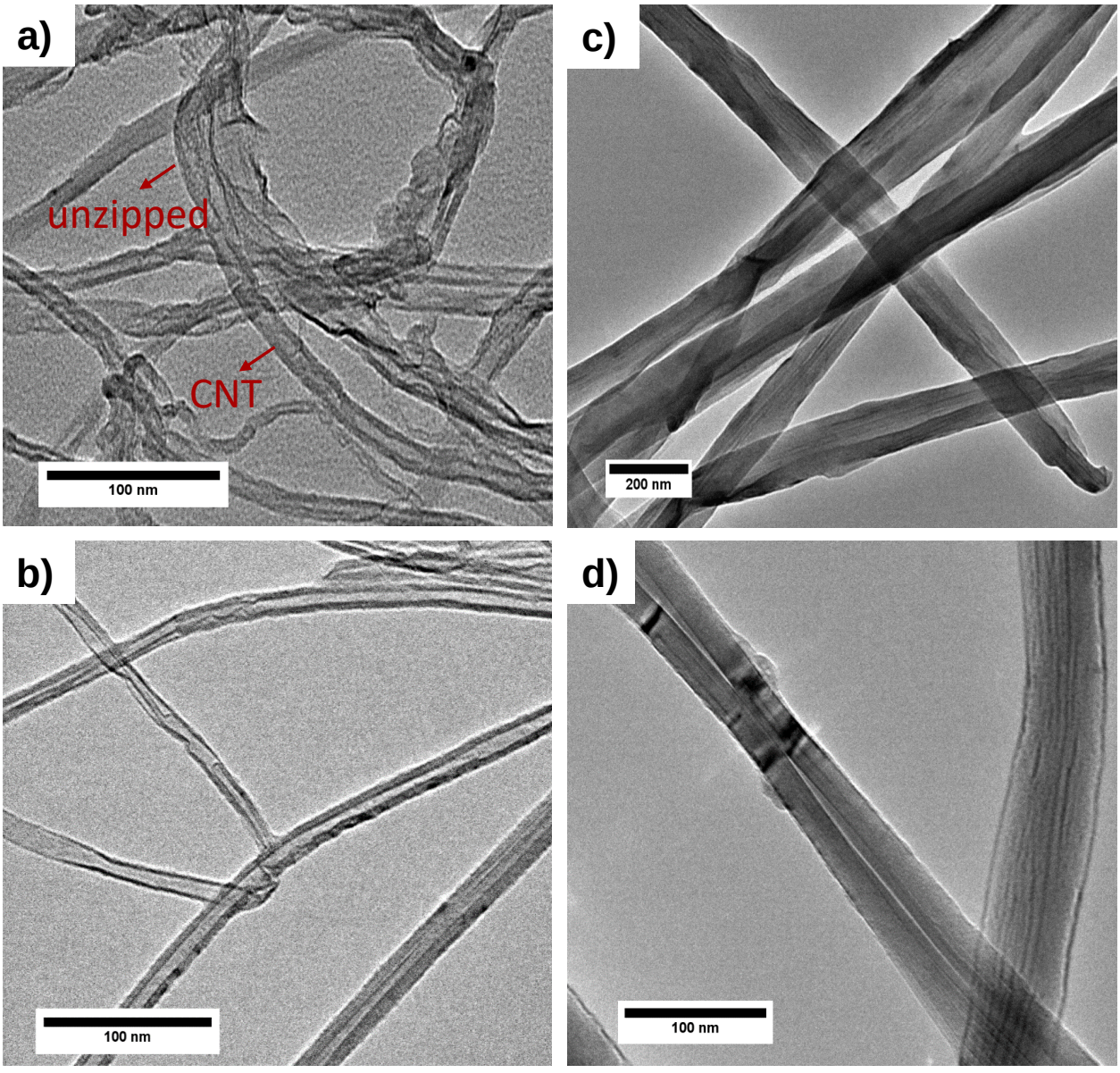

Figure 3. 1. TEM images of a) small graphene nanoribbons b) small carbon nanotubes c) large graphene nanoribbons d) large carbon nanotubes

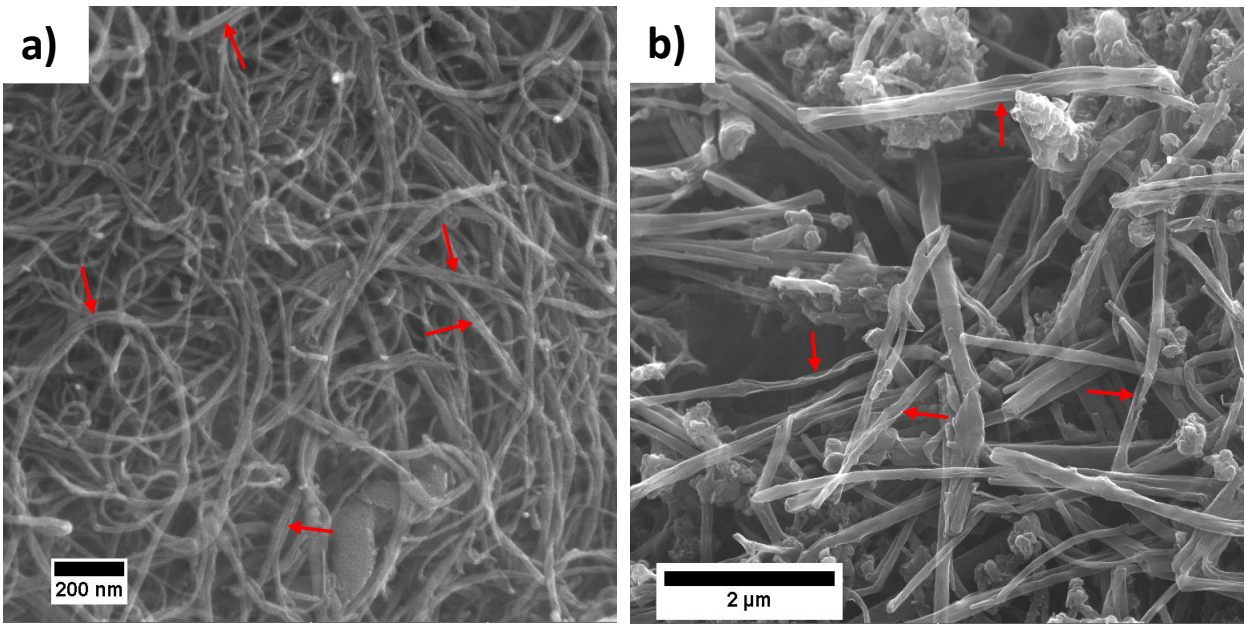

Figure 3. 2. SEM images of a) small GNRs b) large GNRs. Red arrows point to places where unzipping can be easily observed

Raman spectroscopy is employed to investigate the effect of morphological changes of these carbon structures before and after chemical cleavage. Figure 3.3a and 3.3c are spectra of small and large CNTs respectively, and below them, Figure 3.1b and 3.1d correspond to the resulting small and large GNRs. The relative intensity of D-band to G-band in both GNR samples reports an increase, indicating the amplified disorder in the structure as the result of chemical unzipping, and is consistent with other reports in the literature.[47]–[49] Small CNTs have I_D/I_G of 0.82 while this ratio for small GNRs is increased to 1.22. Large CNTs exhibit a small D-band indicating very low structural defects in the CNTs (I_D/I_G =0.11). However, the corresponding large GNRs have a high-intensity D-band as the result of unzipping with 627% increase in the ratio (I_D/I_G =0.82). This increase in the D:G ratio in large GNRs is consistent with SEM and TEM images of the material, where more unzipping is readily observed.

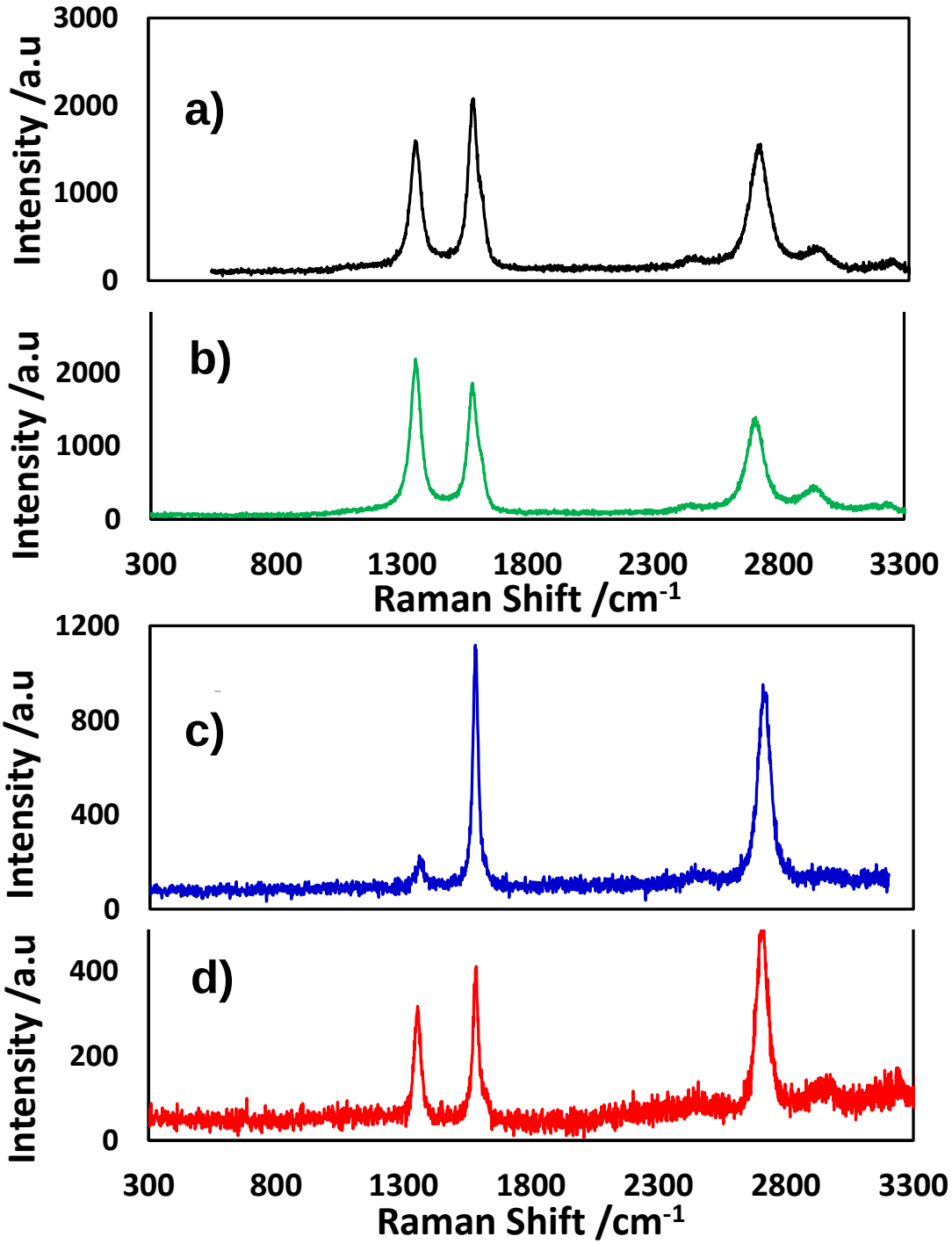

Figure 3. 3. Raman spectra of a) small carbon nanotubes (precursor for small GNRs) b) small GNRs c) Large carbon nanotubes (precursor for large GNRs) d) large GNRs.

XRD patterns in Figure 3.4a for small GNRs (green) and their precursor CNT(black) a broad graphitic (002) peak at 25.8° is observed in both materials, although the peak at 43.2° (100) increased in intensity after unzipping, which is observed in other literature as well.[50], [51] All XRD spectra are normalized to (002) peak. This peak broadens and downshifts as a result of introduction of the oxygenated groups in the unzipping process of the CNTs.[52] Figure 3.4b shows a sharp (002) peak at 26.1° in the XRD pattern of large CNTs (blue), whereas the resulting large GNRs (red) exhibit a broad peak which is moved to lower angle (24.6°), suggesting that the d-spacing between the graphene sheets increased due to chemical cleavage and introduction of linear alkyl functional groups on the GNR during production.[51]

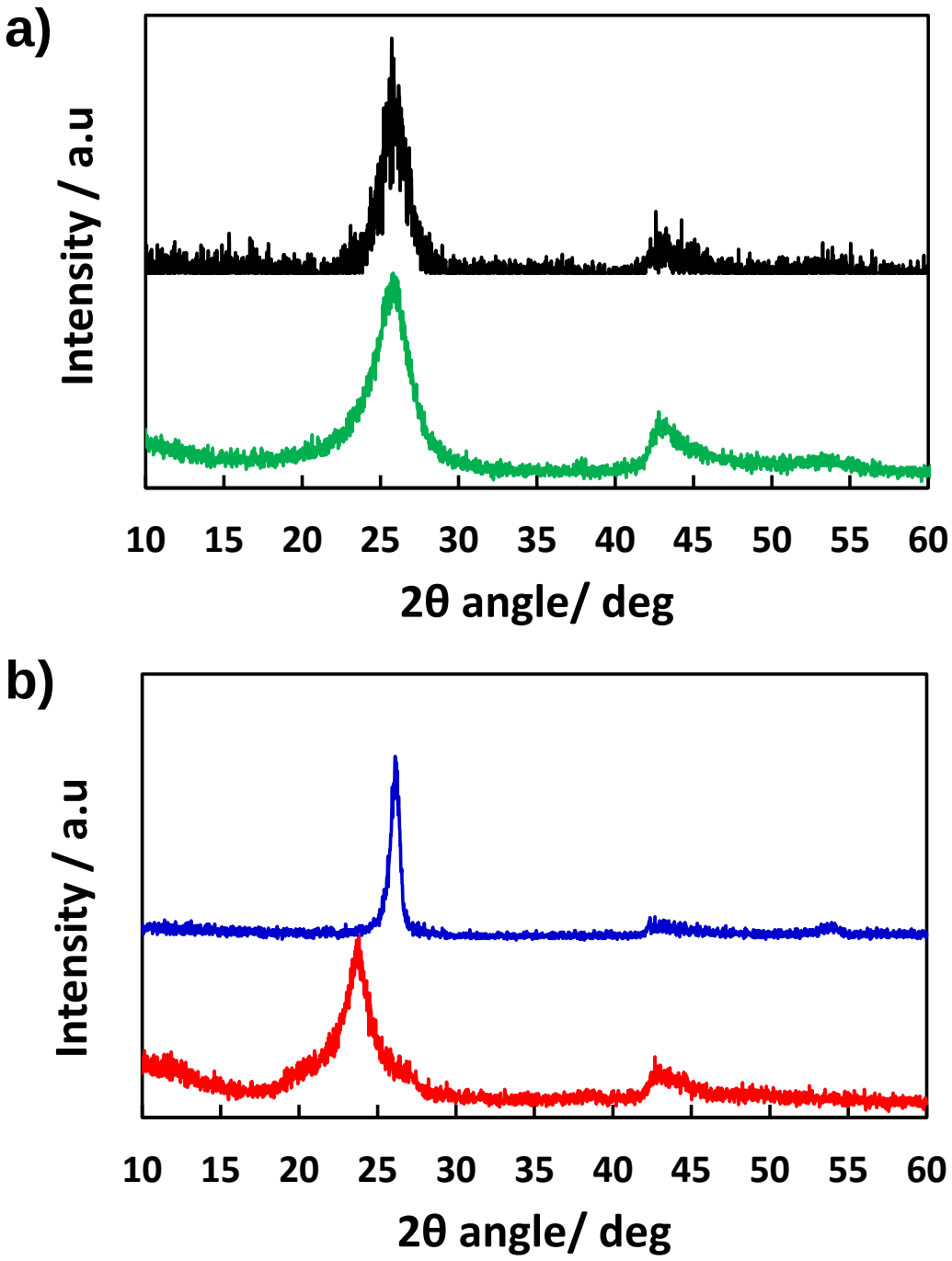

Figure 3. 4. XRD pattern of a) small GNRs (green) and small and precursor CNT (black) b) large GNRs (red) and precursor CNTs (blue)

FTIR analysis on GNRs and CNTs in this paper can be found in Figure 3.5 where the alkyl C-H stretching is readily observable in the spectrum of large GNRs and is absent in other spectra.

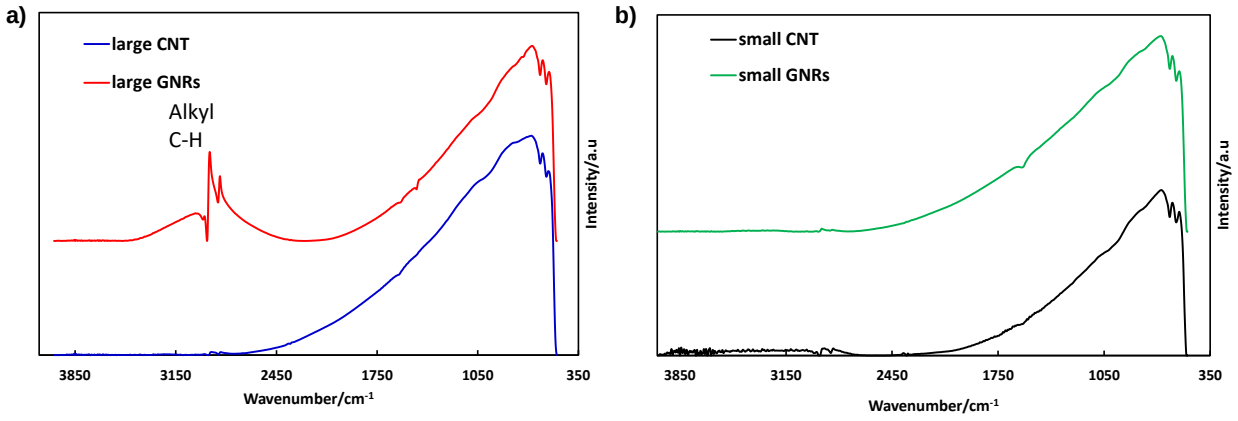

Figure 3. 5. FTIR spectra of GNRs and CNTs used in this report. No O-H or N-H stretching are detected on these carbons. Spectrum of the large GNRs exhibit alkyl C-H stretching due to introduction of linear alkyl groups on the graphene nanoribbon during production.

Preparation of Directly Deposited Anode Disks: After characterizing CNTs and GNRs, they are incorporated into silicon nanocomposite fibers to investigate the effect of the change in the geometry from nanotubes to nanoribbons on the electrochemical performance. A solution of PVA/SiNP/GNRs is directly electrospun on a copper current collector to make anode disks in one step. The same is done for precursor CNTs of the two GNR samples. In this manner, a nonwoven fiber mat of the composite material is obtained on copper disks, ready to be assembled in 2032 cells after heat treatment at 200°C. Since PVA and Silicon nanoparticles are the same in all samples, from this point on the samples will be distinguished by the conductive carbon inclusion i.e. the fibers containing small GNRs will be called small GNRs. Therefore, the investigated

anodes in this study are small CNTs, small GNRs, large CNTs, large GNRs, and mixed GNRs that will be introduced in the last section. Figure 3.6 shows the morphology of the electrospun nanofibers with GNR inclusions. Figure 3.6a and 3.6b are SEM images of as-spun nanofibers with small GNRs at different magnifications. Obtained nanofiber mat is uniform, with an average diameter of 157nm and particles are dispersed throughout the polymer matrix to form a composite. When the fibers are heat treated at air to eliminate side groups and stabilize PVA, the morphology is altered due to a significant mass loss in the polymer. [53] The remaining nanofibers have an average diameter of 168 nm and maintain their 1D morphology created via electrospinning as illustrated in Figure 3.6c. Figure 3.6d and 3.6e show morphology of the fiber mat with large GNR inclusion under SEM. As in the case with small GNRs, resulting fiber mat is homogeneous. However, when the fibers are thermally treated, they lose most of the created morphology (Figure 2f).

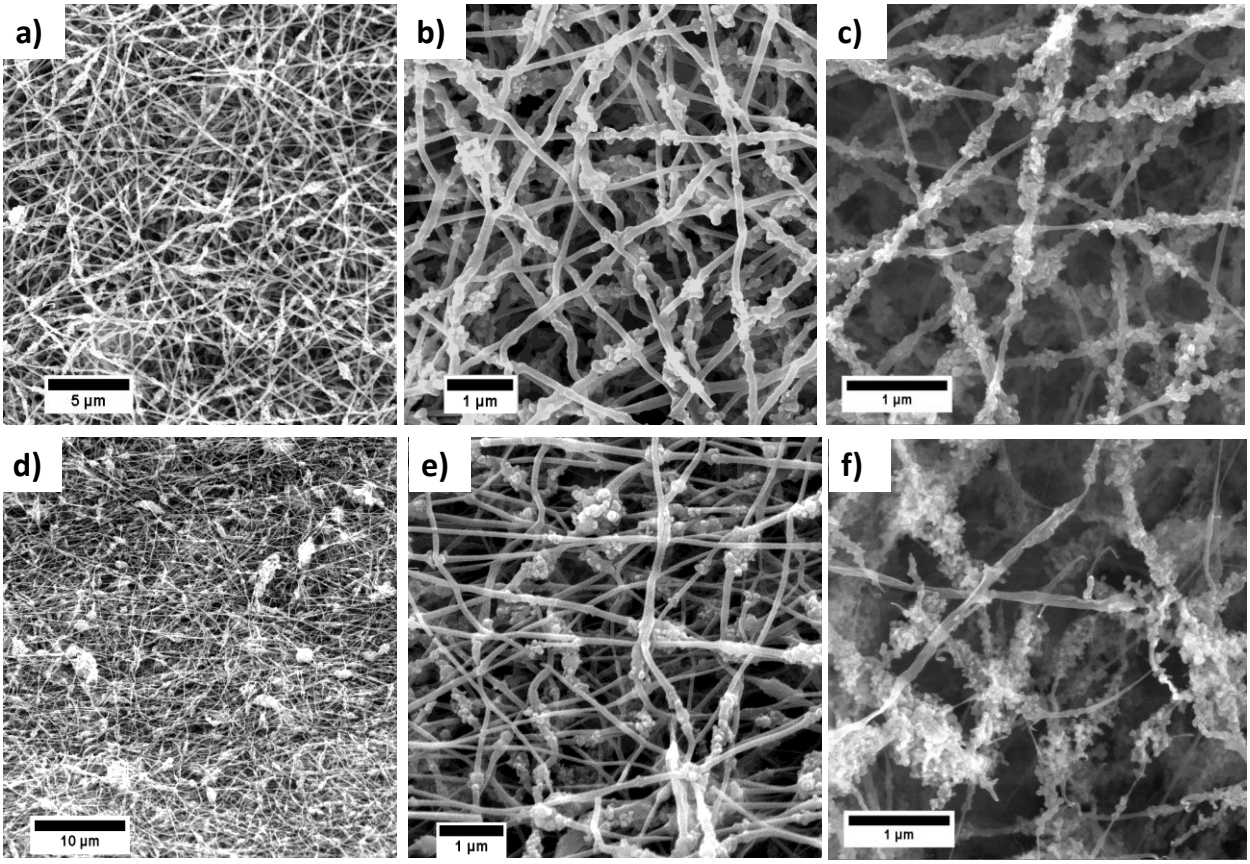

Figure 3. 6. SEM images of a) Low magnification as-spun DD nanofibers with small GNRs b) high magnification as-spun DD nanofibers with small GNRs c) heat treated DD nanofibers with small GNRs d) Low magnification as-spun DD nanofibers with large GNRs e) high magnification as-spun DD nanofibers with large GNRs f) heat treated DD nanofibers with large GNRs

The increase in the fiber diameter is due to closer packing of nanoparticles to preserve 1D geometry of the fibers after mass reduction. In TEM Figure 3.7a, the intra-connectivity of the nanoparticles inside the polymeric matrix can be observed. The size of the small GNRs is such that, they can be fully encapsulated within fibers and electrically connect silicon nanoparticles for the ease of electron transfer along each fiber. The flexibility of the graphene nanoribbons gives them the ability to conform to the irregular shapes and areas created by SiNPs and polymer fibers.

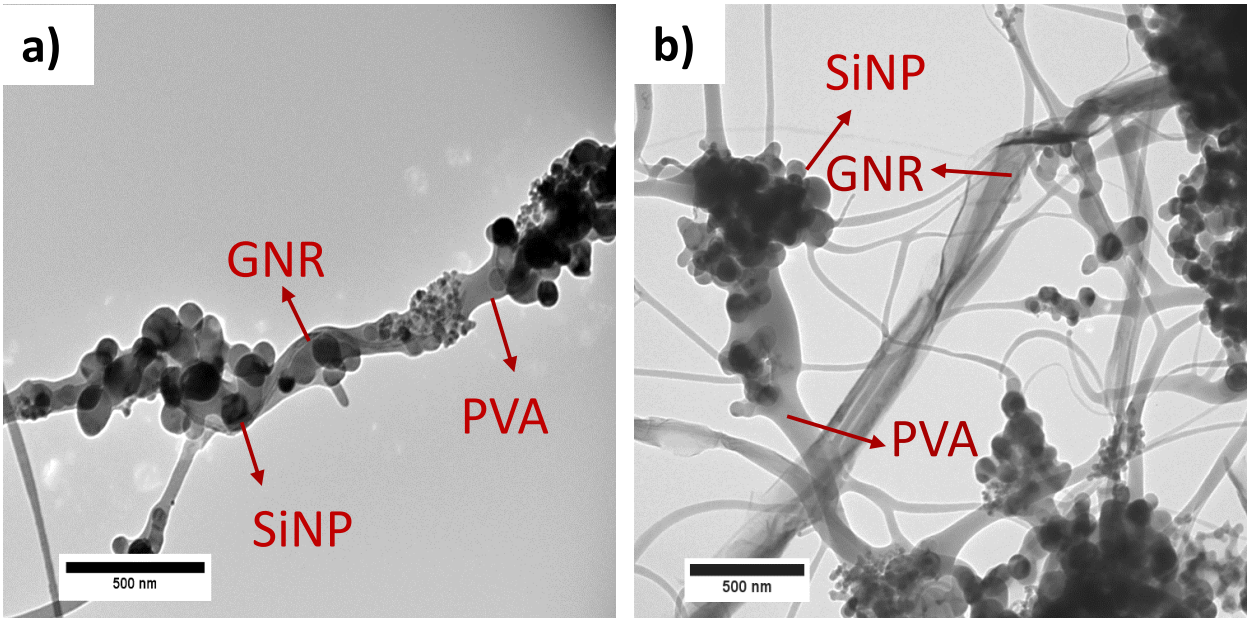

Figure 3. 7. a) TEM image of DD nanofibers with small GNRs, showing the interconnectivity of different particles inside the fibers. b) TEM image of DD nanofibers with large GNRs bridging fibers.

Higher magnification TEM images of fibers with small GNRs in Figure 3.8 are provided to illustrate the inner structure. Elemental maps of fiber mats with GNRs via Energy Dispersive

Spectroscopy (EDS) confirmed uniform placement of particles throughout the system both before Figure 3.9 and after heat treating in air Figure 3.10. TEM analysis of fibers with large GNRs in Figure 3.7b reveals that the size of these graphene nanoribbons is comparable to the the diameter of fibers. Therefore, they can bridge among several fibers and create inter-connectivity of fibers, but PVA can not fully encapsulate them. This means that volume of GNRs entangled with PVA molecules is less in this case, and thus, when the polymer is thermally treated, fibers cannot hold their structure.

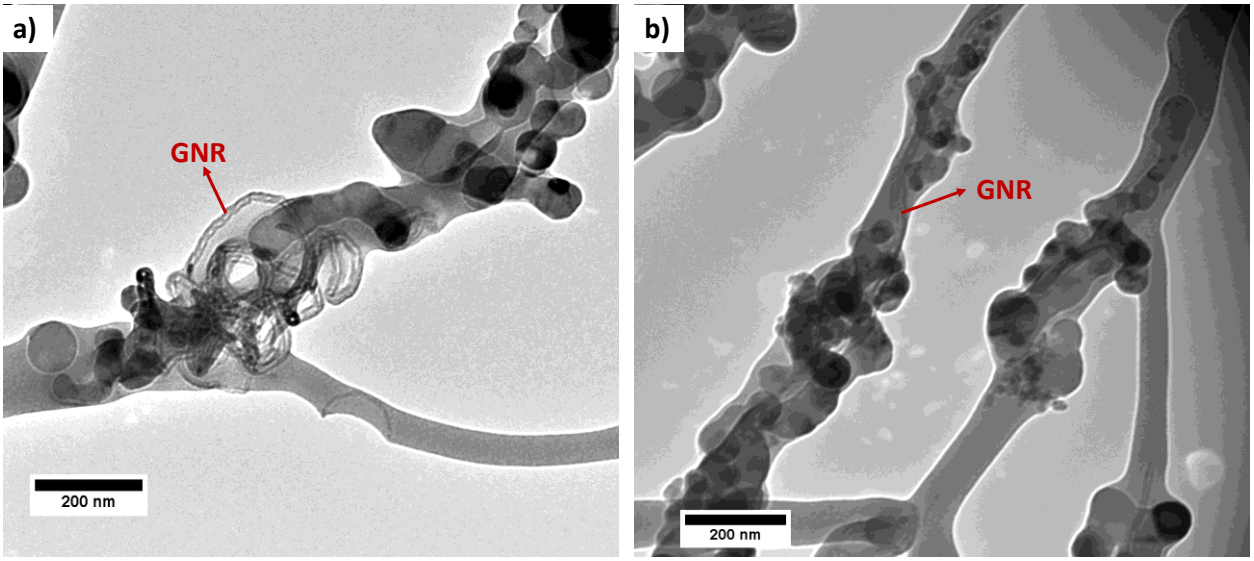

Figure 3. 8. a and b) Higher magnification TEM image of DD fibers with small GNR inclusions

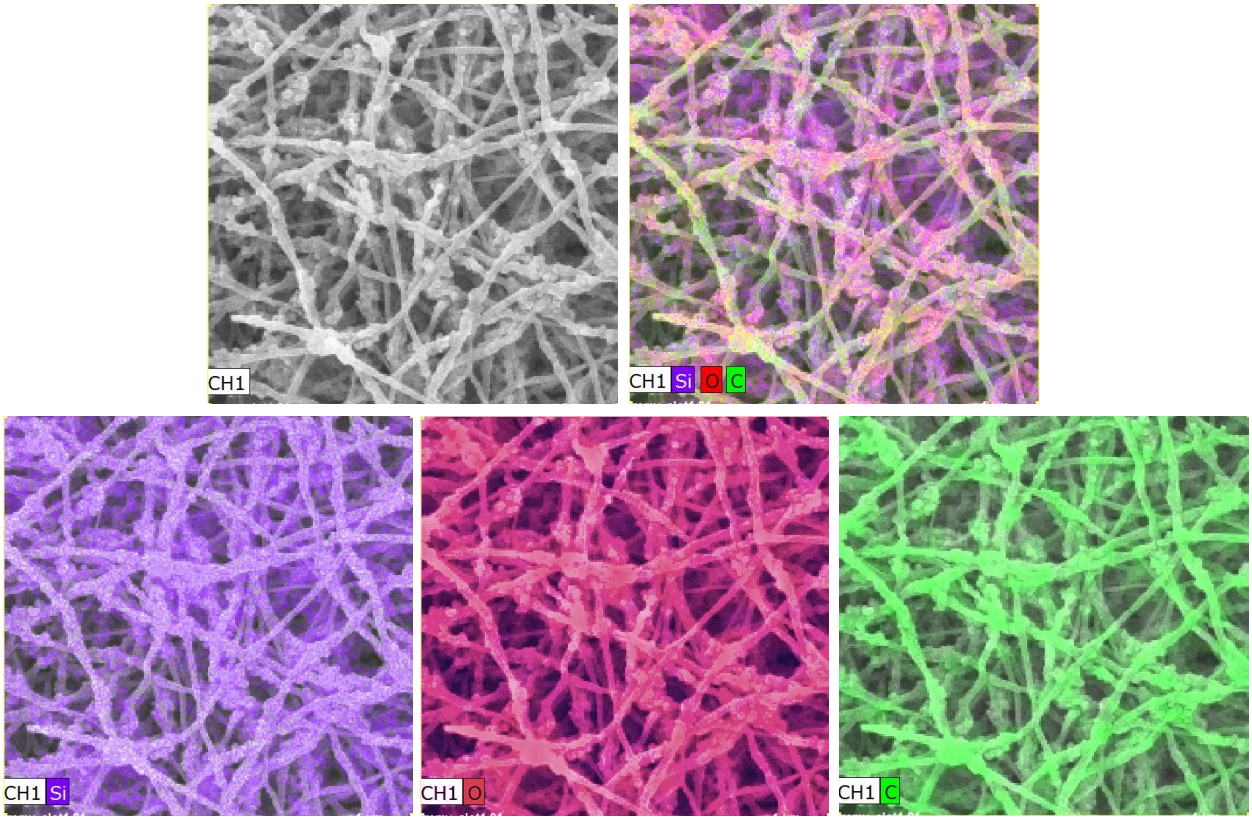

Figure 3. 9. EDS elemental mapping of as-spun DD fibers with small GNRs showing the homogeneous particle dispersion throughout the system

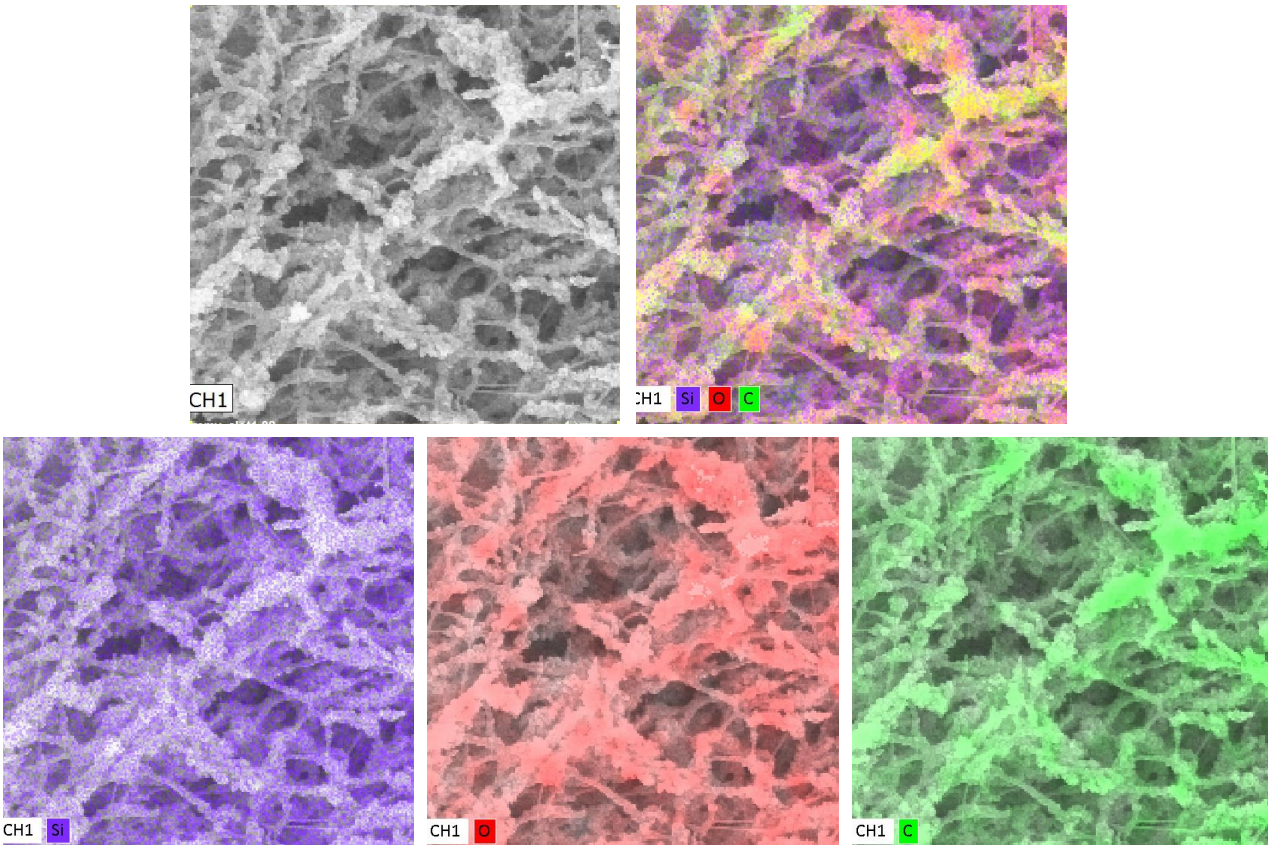

Figure 3. 10. EDS elemental mapping of heat-treated DD fibers with small GNRs indicating no particle agglomeration occurs during the procedure

To compare the morphology of the fibers with CNT inclusions, SEM of the as-spun nanofiber mats and TEM analysis of these fibers are provided in Figure 3.11. Just like the nanoribbon case, small CNTs are fully encapsulated within the PVA fiber while Large CNTs are bridging multiple fibers.

TGA was conducted on nanofiber mats to assess the exact contents of fibers before and after heat treatment. The weight percentages of three components are similar to the starting solution in case of the as-spun fibers. Silicon makes up 75% of the total weight of the active material after heat treatment, and graphene and polymer each contributed 12% and 13%, respectively for small GNRs, in TGA measurements of Figure 3.12. Large GNR fibers revealed a close composition as well (73% silicon, 10% GNR, 17% PVA) after heat treatment. XRD results in Figure 3.13 indicates that, during the mild heat treatment, no appreciable oxide or alloying occurred on the surface of SiNPs.

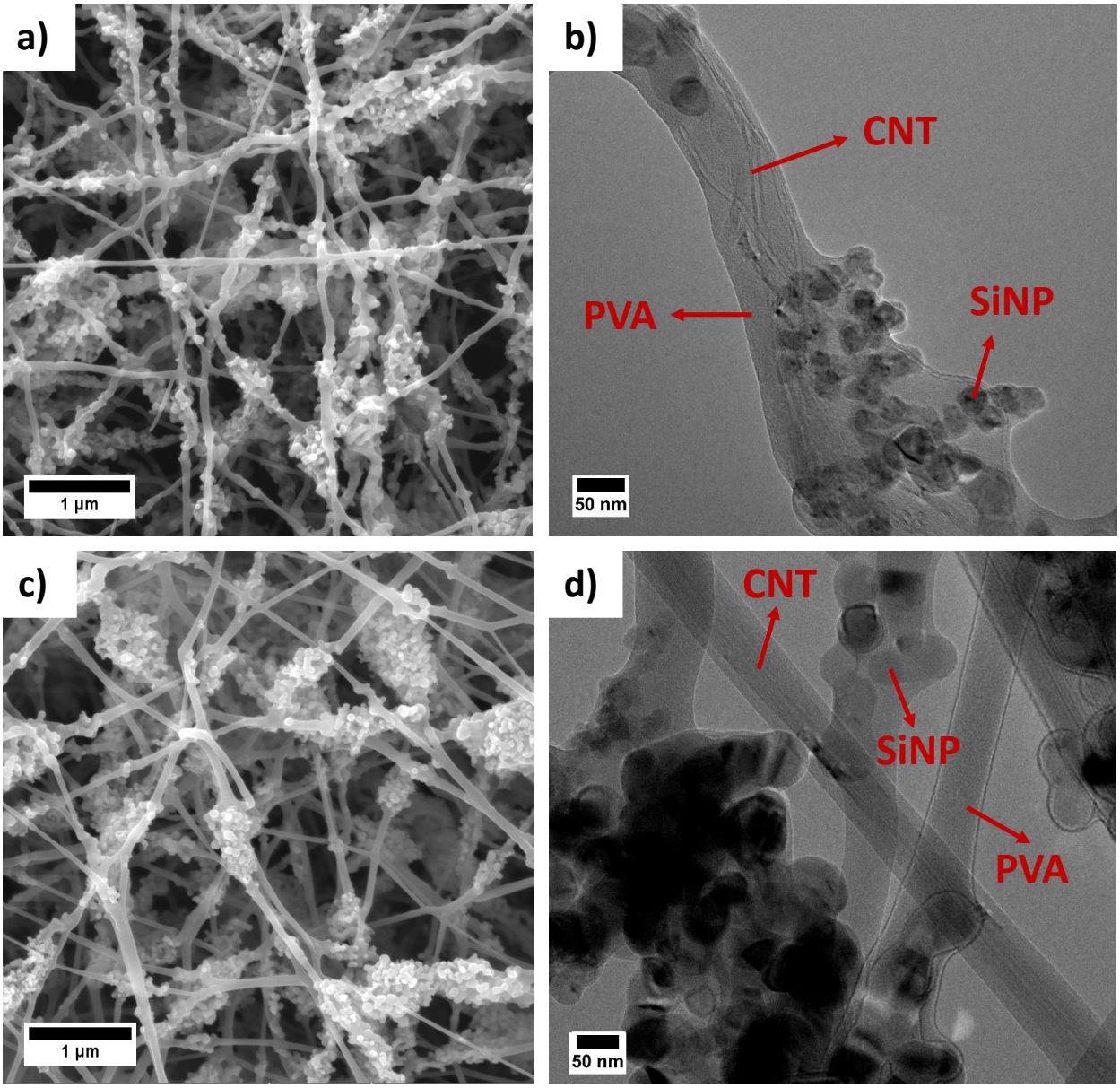

Figure 3. 11. a) SEM image of small CNT as-spun nanofibers b) TEM image of small CNT nanofibers showing the placement of CNTs and SiNPs inside the PVA fiber c) SEM image of

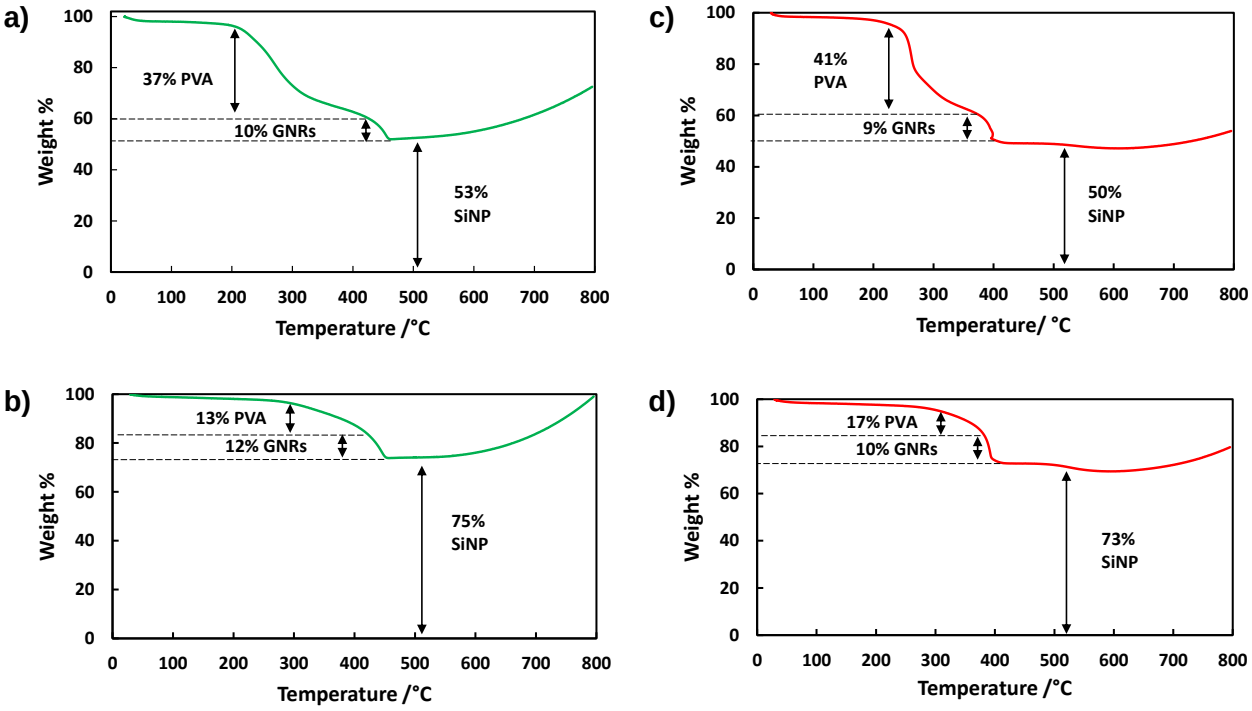

Figure 3. 12. Thermogravimetric analysis of a) As-spun fibers with small GNRs b) heat-treated fibers with small GNRs c) as-spun fibers with large GNRs d) heat-treated fibers with large GNRs

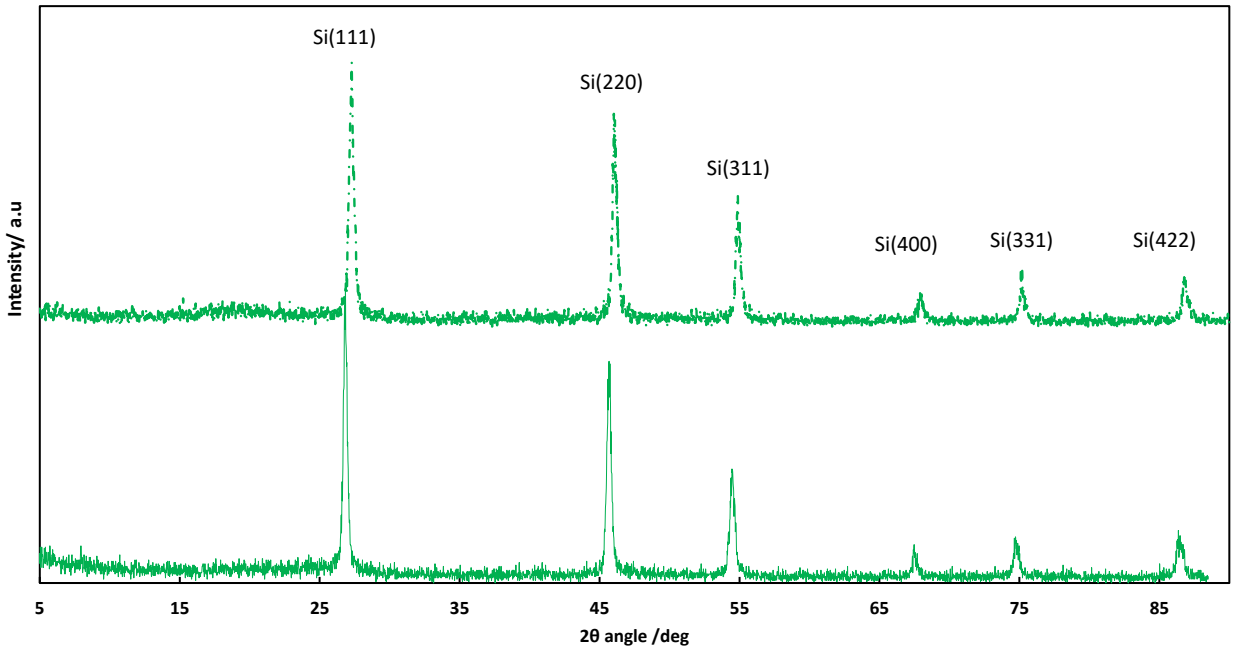

Figure 3. 13. XRD patterns of as spun (solid line) and heat treated (dashed line) fibers with small GNRs inclusions. Crystalline Silicon from different facets are indicated and no obvious alloying or oxidation took place as a result of heat treatment in air.

Electrochemical Testing of Directly Deposited Anodes: To investigate electrochemical performance of the created fibers, electrodes are assembled into 2032 half coin cells. This method of electrode preparation on top being cost effective and scalable, provides a means to directly compare contribution of GNRs and their precursor CNTs in terms of electrochemical activity and structural stability. Figure 3.14 reports the cross-sectional SEM images of the four samples used in this paper to elucidate the construction of the nanofibers on the copper current collector and to give a better view of the inner structure of the prepared electrodes. Small CNTs and GNRs which have a better fiber morphology to begin with, also have a more uniform morphology throughout the electrode thickness after the heat treatment. The cross-sectional images reveal the highly porous inner structure of the electrodes, highlighting the ease of electrolyte penetration inside the electrode thickness. The cyclic performance of directly deposited anodes with GNRs compared to their precursor CNTs at 0.18 Ag^{-1} to allow for full lithiation/delithiation of the material are presented in Figure 3.15 and 3.16. Both small and large GNRs outperform their parent CNTs in terms of overall capacity and retention. All capacities in this work are normalized by the total mass of electrochemically active materials, i.e. carbon (GNR or CNT) and SiNPs that were obtained by TGA analysis. Small GNR fibers have an initial lithiation capacity of 3700 $mAhg^{-1}$, while their precursor CNT fibers only possessed 2380 $mAhg^{-1}$. This can be attributed to the ability of GNRs to be lithiated on both sides of the plane[54] and thus a larger contribution to the overall capacity as well as synergy with SiNPs. At the same time, small GNRs retain 58% of their capacity (calculated against second lithiation), and their precursor CNTs have 53% capacity retention after 100 cycles at 0.18 Ag^{-1}. GNRs act as structural support, conductive pathways on top of participating in the electrochemical reaction. Figure 3.17a illustrates initial capacity-voltage

profile of directly deposited fibers with small GNRs (green line) and CNTs (black line) at 0.18 Ag^{-1}.

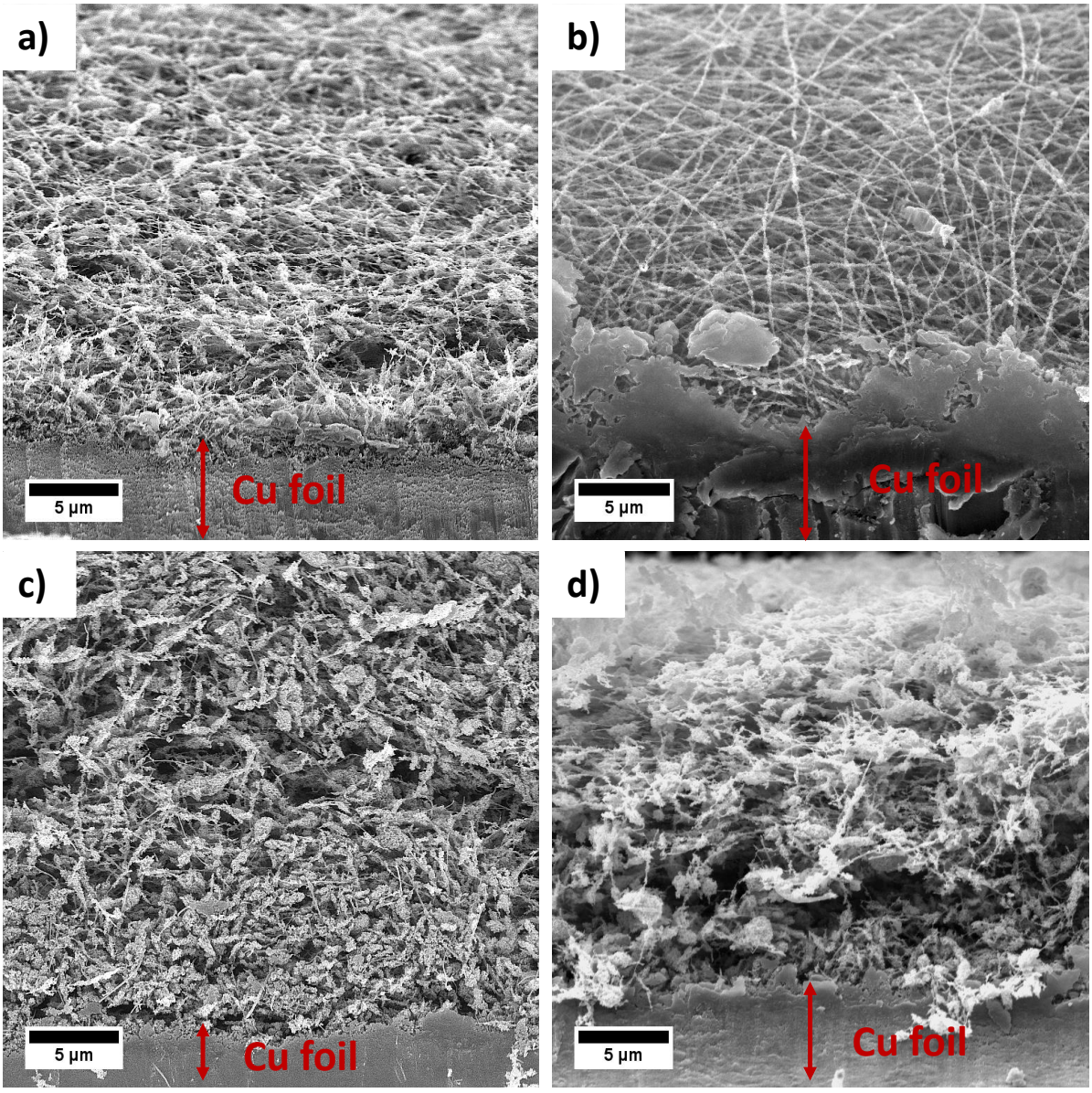

Figure 3. 14. Cross sectional SEM images of the electrodes with a) small CNTs b) small GNRs c) large CNTs d) large GNRs

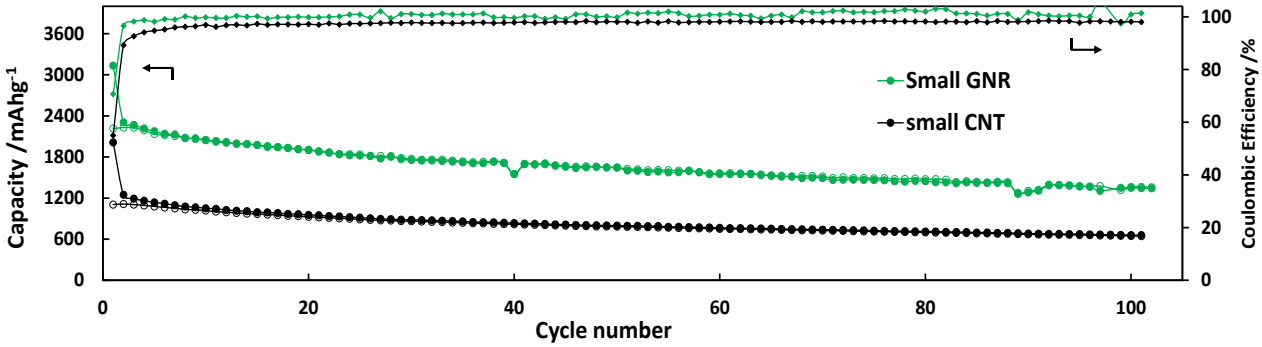

Figure 3. 15. Cyclic performance of fibers including small GNRs and their precursor CNTs and their coulombic efficiencies. Open circles correspond to delithiation capacities, closed circles for lithiation capacities and diamonds for coulombic efficiencies.

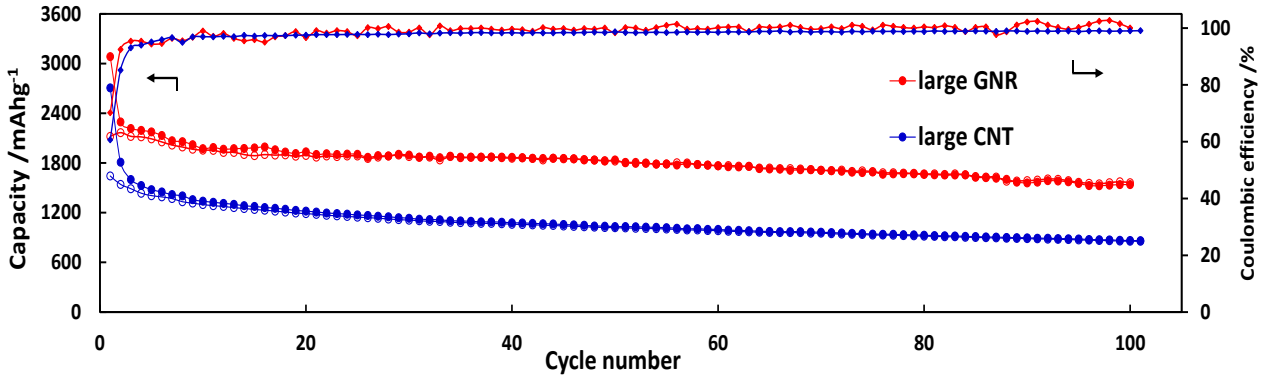

Figure 3. 16. Cyclic performance of fibers including large GNRs and their precursor CNTs and their coulombic efficiencies Open circles correspond to delithiation capacities, closed circles for lithiation capacities and diamonds for coulombic efficiencies.

Figure 3.16 illustrates the cyclic performance of large GNRs and CNTs. The same trend is observed with large GNRs. They start off with a lithiation capacity of 3400 $mAhg^{-1}$; 400 $mAhg^{-1}$ more than their precursor CNTs. By the end of 100 cycles, large GNRs retain 67% while large CNTs only retain 48% of their capacity. Their initial capacity voltage profile is depicted in Figure 3.17b. The superior ability of GNR containing composites to retain their capacity should be attributed to their mechanical flexibility and robustness after lithiation.[55]

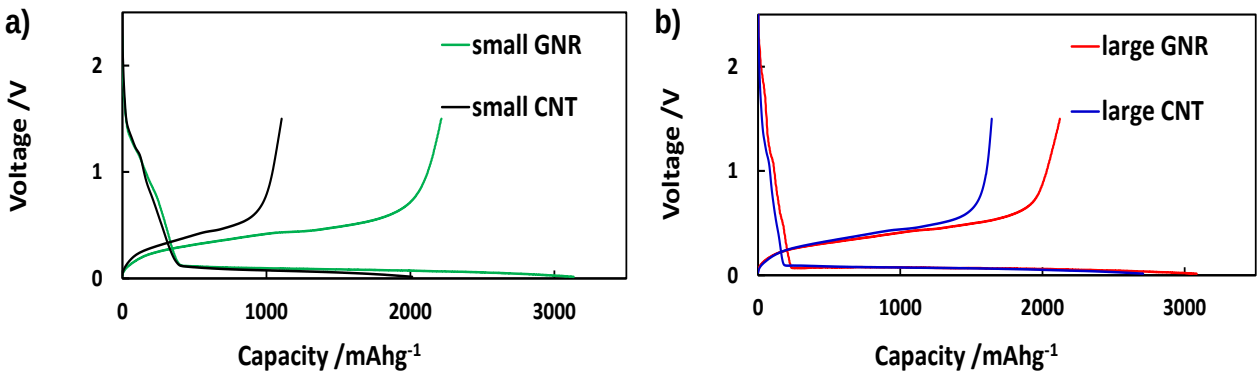

Figure 3. 17. a) Initial capacity-voltage profile of small GNRs and small CNTs b) initial capacity-voltage profile of large GNR and large CNTs

It has been reported that GNRs do not exhibit a fracture behavior in mechanical testing even at a lithiated state, while CNTs become brittle after lithium insertion.[56] The flexible nature of GNRs makes them resilient to high strains and morphological changes. It is also consistent that large GNRs have the best overall retention among tested materials, since their unzipping was clearly more successful. On the other hand, small GNRs have more nanotube-like properties, and thus their retention is close to their parent CNTs. All cells exhibit a high Coulombic efficiency (with

GNRs having a slightly higher efficiency than CNTs) due to the unique morphology of fiber mats. In case of large GNRs, Coulombic efficiency goes above 90% after the first cycle, whereas their precursor CNT achieve that after 2 cycles. Moreover, the average efficiency for cells over 100 cycles is 99.3% for large GNRs and 98.3 for their precursor CNT. This can be attributed to the improvement of the lithium ion transfer due to the morphology of the fibers by minimizing diffusion path for ions, and also through the employment of GNRs.[57] It has been found that edge effects create a stronger interaction between Li and GNRs,[58] and also make channels in the carbonous nanostructure for enhanced diffusion of Li ions.[57] This also results in the smaller irreversible capacity loss on the first cycle for GNRs compared to their precursor CNTs (refer to Figure 3.18).

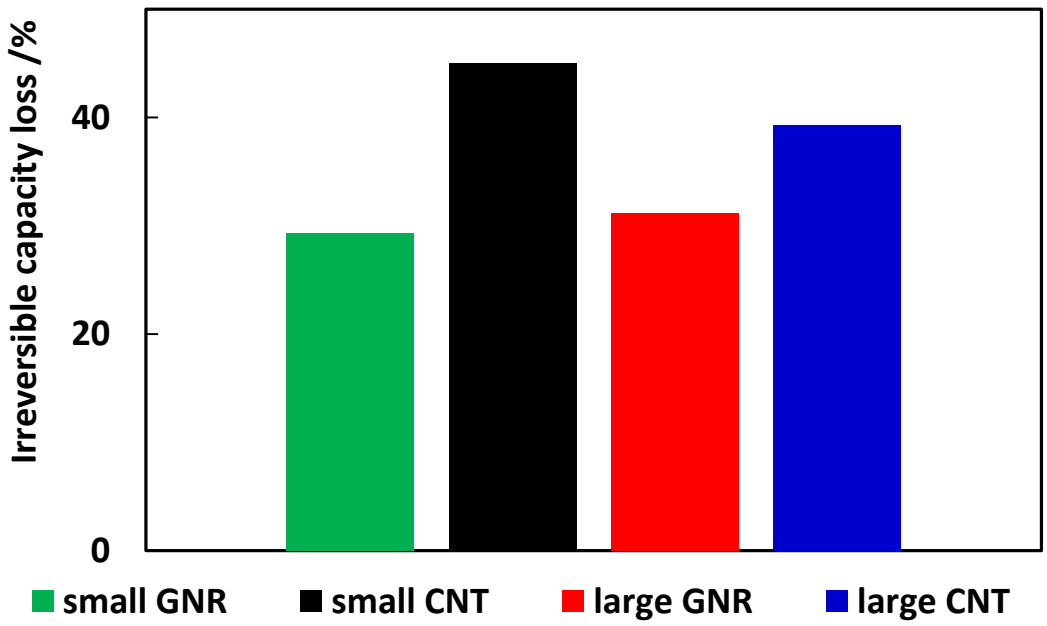

Figure 3. 18. Irreversible initial capacity loss of the first cycle for four samples

The open structure of GNRs does not hinder Li-ion movement, and therefore higher coulombic efficiencies as less Li-ions will be trapped inside of their structure. In order to investigate the role of these 1D carbon inclusions in the system, control electrodes with PVA and SiNPs were prepared and tested in under the same conditions (PVA to SiNP ratio was kept constant and only GNR/CNTs were eliminated from the system). Cyclic performance and capacity-voltage profiles for this control electrode are given in Figure 3.19a and 3.19b respectively. As apparent from the graphs utilization of the SiNPs are very low and the capacity of the cell fades very fast within the first 10 cycles. This indicates the crucial role of the GNRs in the system. Without them the charges cannot be effectively collected and majority of the SiNPs are electronically isolated, therefore they cannot participate in the electrochemical reaction, resulting in low capacities. Furthermore, from the capacity-voltage curves the overpotential, hence the resistance of the increased drastically after cycling for only 50 times.

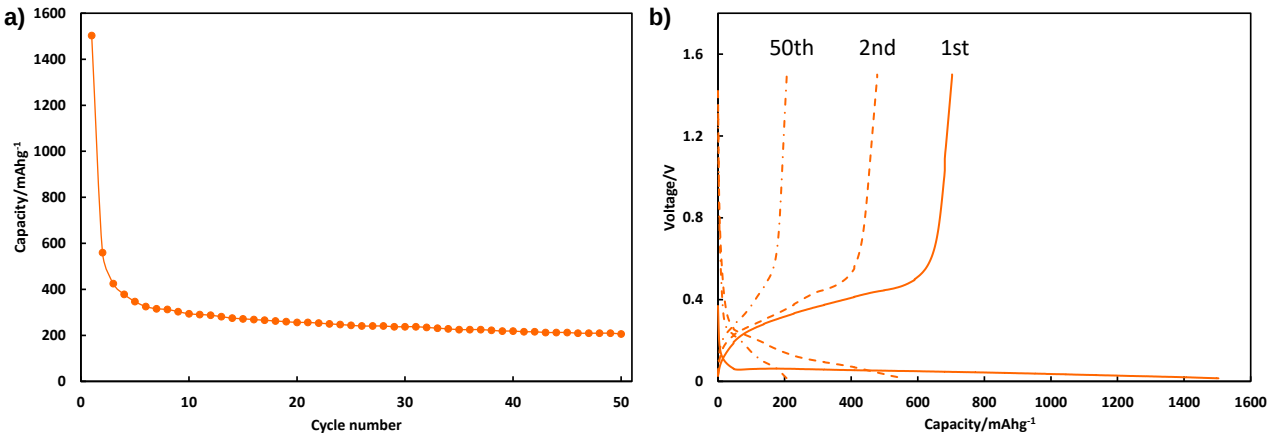

Figure 3. 19. Electrochemical performance of control electrodes containing only PVA and SiNPs. a) Specific capacity vs. cycle number of PVA-SiNP fibers at 0.18Ag^{-1} b) Capacity-voltage graph of first, second and 50th cycles at 0.18 Ag^{-1}. In these electrodes ratio of PVA to SiNP was kept the same and only the carbon component was eliminated

To further distinguish the advantages of employing GNRs in the nanocomposite, rate capability tests are conducted on the samples. Figure 3.20a shows the performance of small GNRs and CNTs, and Figure 3.20b depicts capacity-voltage profiles for small GNRs at rates indicated in the figures. The outstanding overall performance of samples is due to short diffusion lengths made possible by the morphology of the fiber mats. However, as the current increases, the difference between small GNRs and their precursor CNTs widens. At 8.4 Ag^{-1} small GNRs have more than 300 $mAhg^{-1}$, while their CNT counterparts could not be charged and discharged at this high rate. This difference should be ascribed to the facilitation of ionic transfer through GNRs as mentioned before. In order to have a good performance at high rates, the charges in the system should be able to be mobilized in a short time. The charge transfer inside the material consists of electronic transfer and transfer of Li-ions to the active sites. Graphene nanoribbons offer the best of the both ends, and thus they are ideal conductive material.

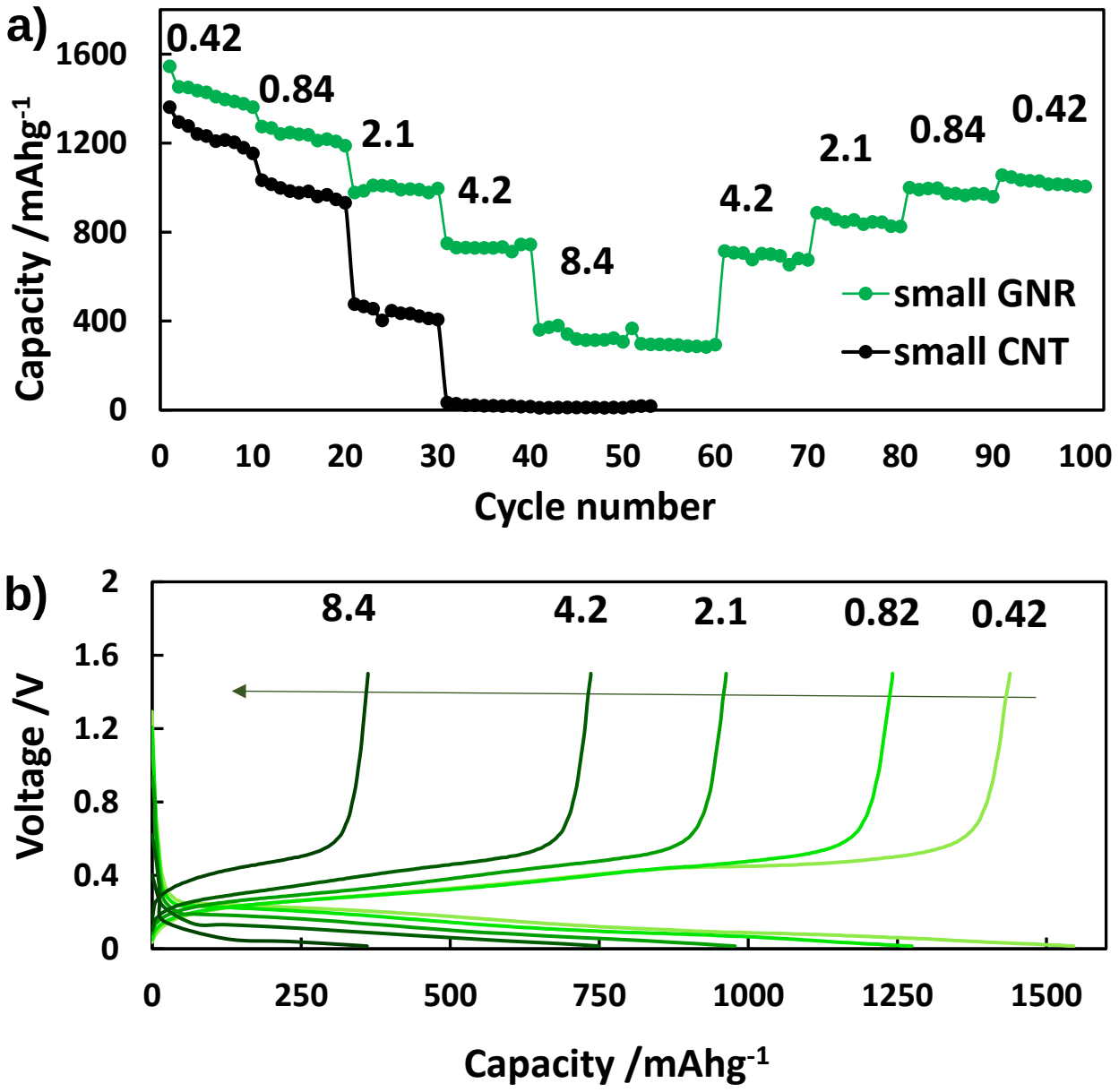

Figure 3. 20. a) Rate capability of small GNRs (green) and small CNTs (black) at rates specified on top of each step b) corresponding capacity-voltage profiles for small GNRs at various rates

Cyclic voltammetry tests confirm the higher electrochemical activity of GNRs compared to their parent CNTs. In CV profiles of Figure 3.21, small GNRs exhibit much higher currents at a scan rate of 1 mVs^{-1}, which is in line with their superior performance over their precursor CNTs at higher rates.

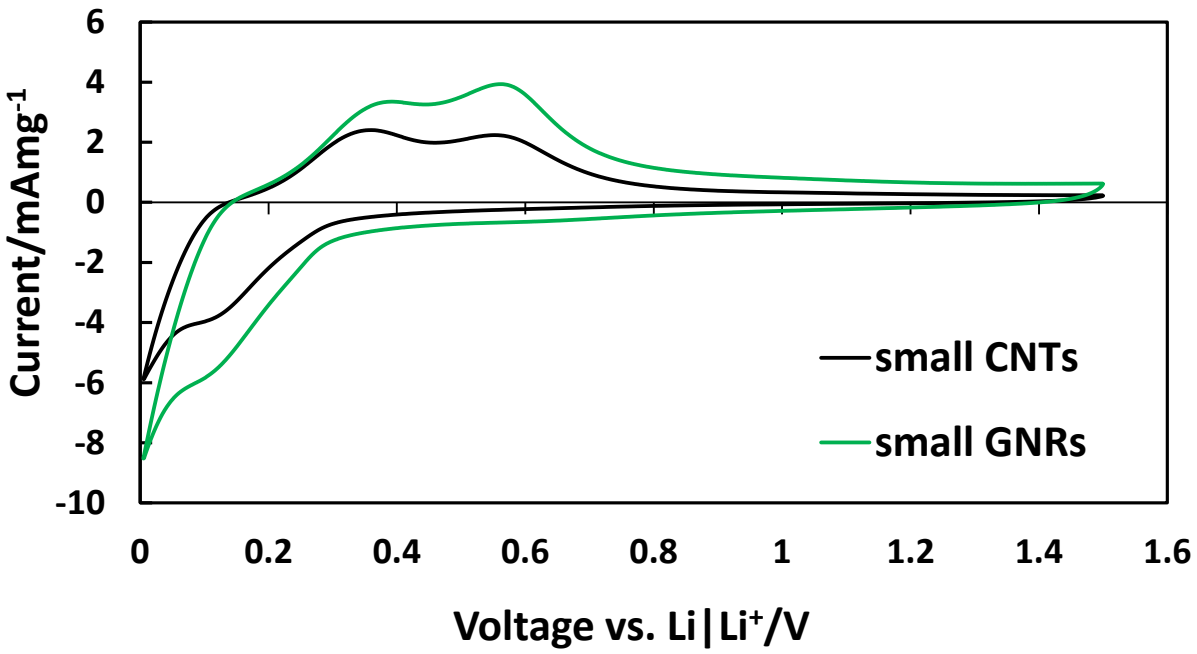

Figure 3. 21. Cyclic voltammograms of small GNRs and small CNTs at 1 mVs^{-1}

As expected, the same trend is observed with large GNR and CNTs in Figure 3.22a when the current rate is systematically increased from 0.42 to 12.6 Ag^{-1}. Capacity-voltage profiles of large GNRs at different currents are given in Figure 3.22b. Large GNRs have merit as a conductive carbon component, evident from high rate performance of the fibers. These fibers exhibit around 2000 $mAhg^{-1}$ when cycled at 0.42 Ag^{-1}, and a 30-fold increase in the current to 12.6 Ag^{-1}, only

results in a 28% decrease in their lithiation capacity to a value of 1400 $mAhg^{-1}$. The performance of large CNTs at the same rates reveals that the increase in the current results in 58% decrease in the capacity. It should be noted that both Large CNTs and GNRs performed better at higher currents than small GNRs. This enhancement in performance can be attributed to the overall nano-morphology of the samples. Since large GNRs and CNTs inter-connect the fibers, they provide multiple charge transfer contacts between fibers and thus are more efficient in mobilizing and collecting charges. On the other hand, small GNRs and CNTs are only effective in conducting charges inside of a single fiber and intra-connectivity of silicon particles. Transferring charges from fiber to fiber depends solely on the intersecting sites on fibers. Therefore, at faster rates small CNTs and GNRs quickly lose their ability to mobilize charges, despite the fact that predictions from computational studies suggest that narrower GNRs should have better performance due to lowering energy barriers to diffusion of Li ions.[57] Two underlying reasons can explain this contradiction. First, as observed by Raman, XRD and TEM analysis on small GNRs, the unzipping of these materials has a low yield, and the majority stay in a tubular configuration. Second, small GNRs are fully encapsulated by the nonconductive polymer matrix; they lack the inter-connectivity necessary at a higher rate.

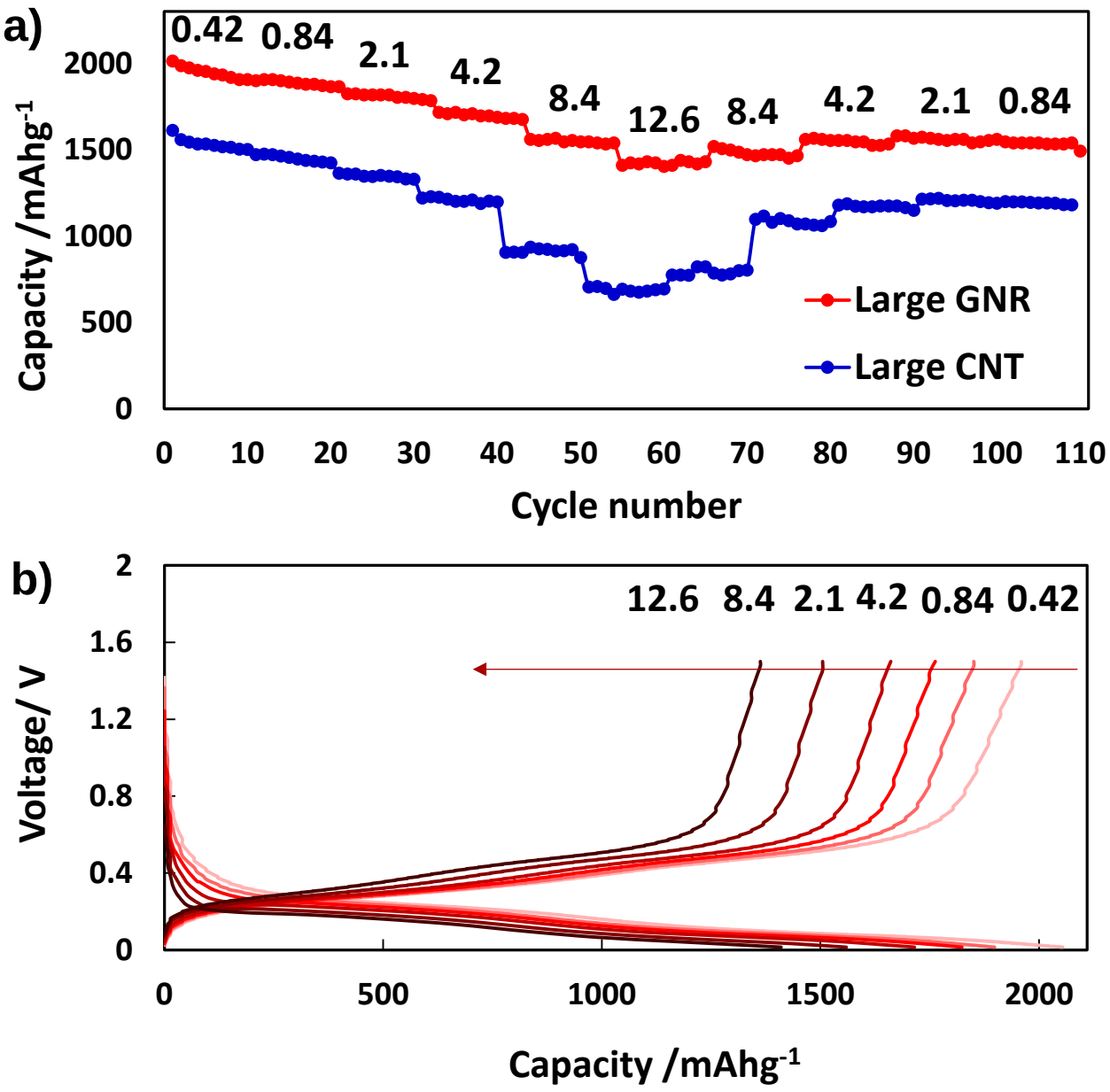

Figure 3. 22. a) Rate capability of large GNRs (red) and their precursor CNTs (blue) e) capacity-voltage profiles for large GNRs at different rates

Figure 3.23 shows cyclic voltammograms of large GNRs and CNTs at 1mVs^{-1}, and as expected large GNRs produce higher currents at this high scan rate, confirming their superiority as conductive agents over their parent CNTs. In fact, both small and large GNRs produce higher currents compared to their precursor CNTs at every scan rate tested in Figure 3.24.

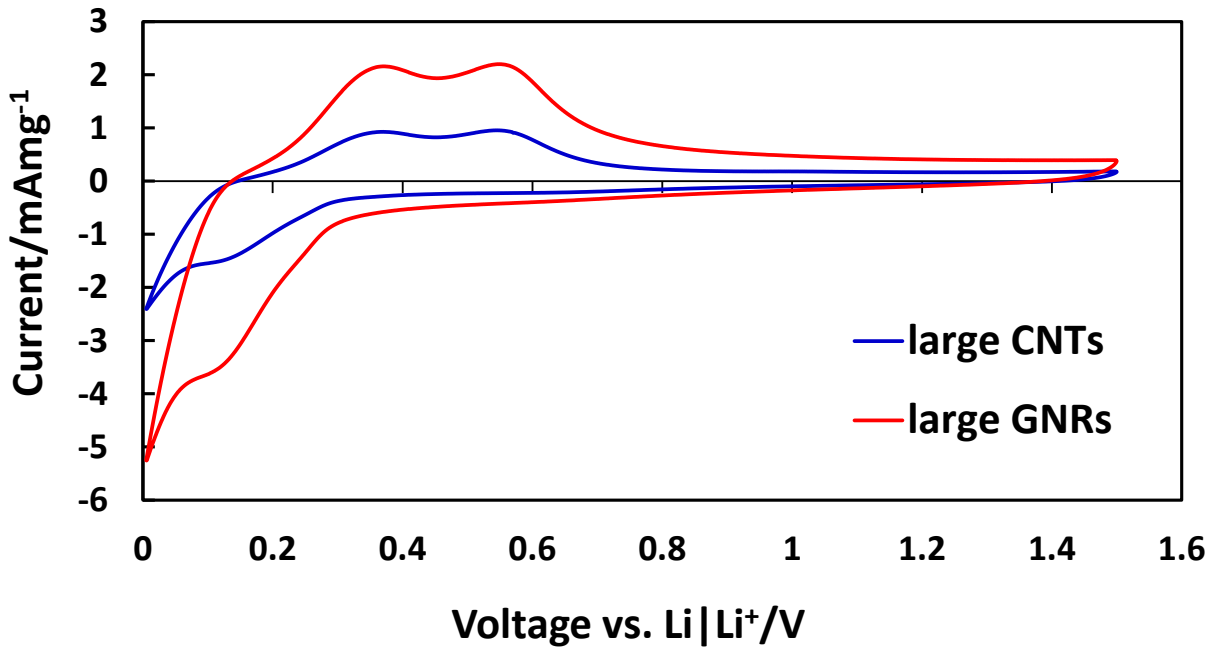

Figure 3. 23. Cyclic voltammograms of large GNRs and large CNTs at 1 mVs^{-1}

To assess morphological changes and their correlation with the performance of the fiber mats, electrochemical impedance spectroscopy was done on the cells in Figure 3.20 and 3.22 before and after rate capability and then they were opened. Constant charging and discharging bring about continuous volumetric changes on the system, which affects the porosity, connectivity, and

nanostructure of the electrodes. These effects are more dramatic at fast rates due to a larger tensile stress induce in the material.[3] The Nyquist plot in Figure 3.25a indicates that the charge transfer resistance of the composite with small GNRs decreased from 163 Ω to 57 Ω after cycling, which should be associated with trapped lithium ions inside of the polymer matrix and active material. This change can readily be seen by the decrease in the diameter of the semi-circle in the graph. At the same time, the bulk resistance of the cell does not show any appreciable change (4.6 to 4.8 Ω).

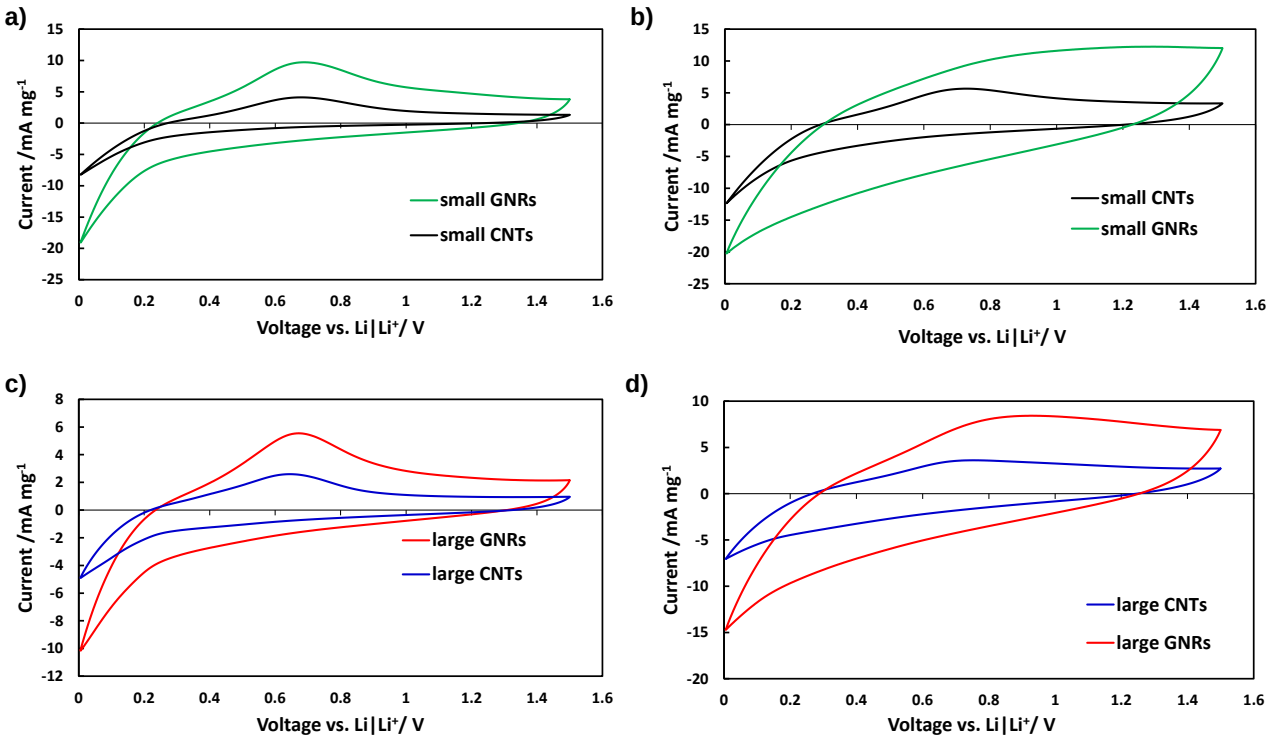

Figure 3. 24. Cyclic voltammograms of PVA/Si fibers including a) small GNRs and small CNTs at 10mVs^{-1} b) small GNRs and small CNTs at 50mVs^{-1} c) large GNRs and large CNTs at 10mVs^{-1} d) large GNRs and large CNTs at 50mVs^{-1}. GNRs are able to produce more current than their precursor CNTs when the voltage is swept regardless of the scan rate.

The circuit used for analyzing impedance data is illustrated in Figure 3.25c. Nyquist representation of EIS data for the cell with large GNRs is depicted in Figure 3.25b. As apparent from the graph, the same trend holds for large GNRs as well. The surface resistance of the cell is dramatically decreased from a value of 252 Ω to 34 Ω, after the rate capability test. Bulk resistance of the cell shows an insignificant increase from 4 Ω to 4.5 Ω, indicating minimal pulverization and electrical delamination for both samples. The post mortem SEM analysis of the cells can shed more light on the magnitude of the morphological changes in the cells. Figure 3.26a reports the morphology of the fiber mat with small GNRs after the rate capability test. The 1D nanostructure is maintained throughout the cycling, which should be attributed to the higher concentration of nanoparticles in the fibers on top of a good fiber construction to start with.

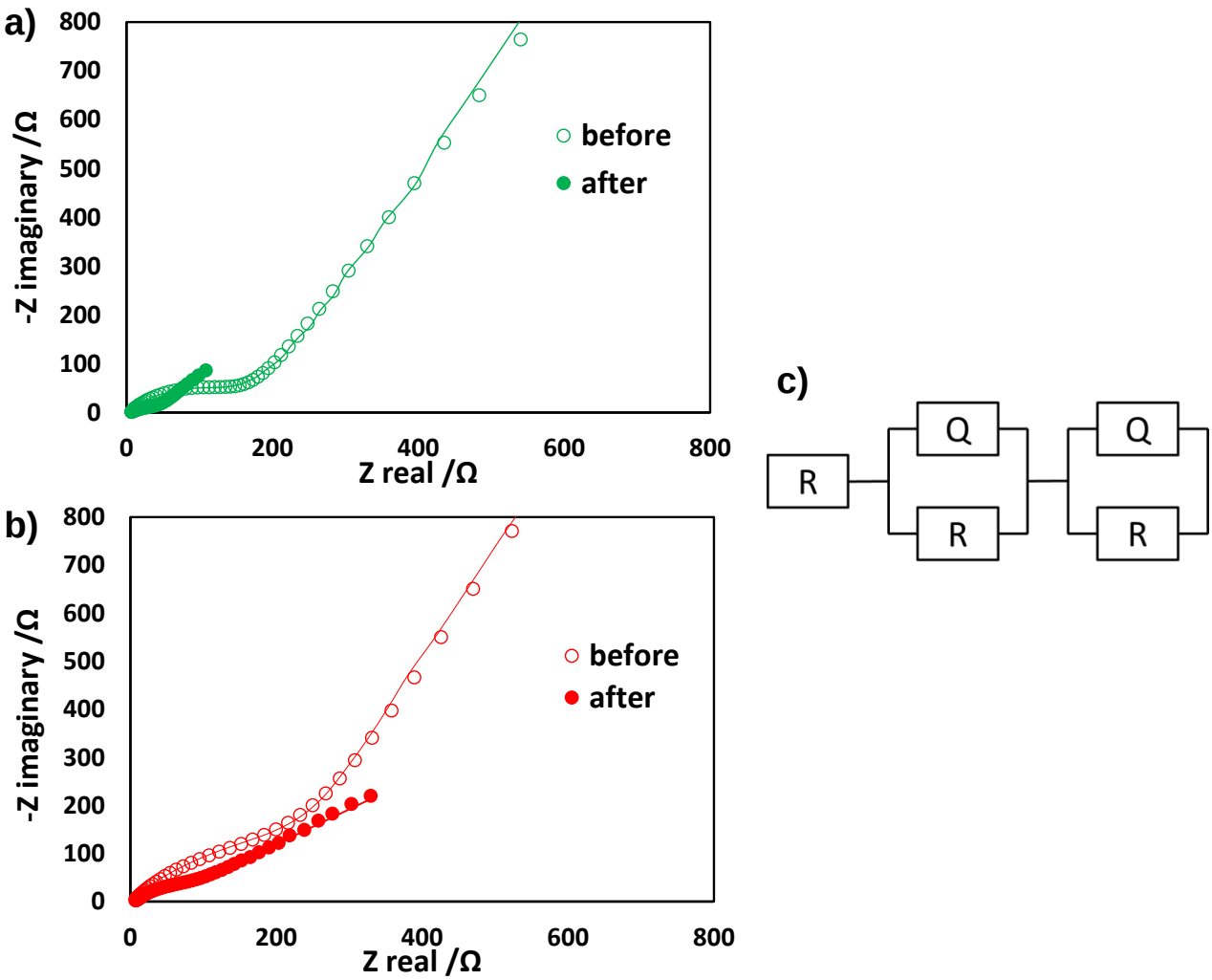

Figure 3. 25. Nyquist plots of impedance data for a cell with a) small GNRs b) large GNRs before and after rate capability tests c) equivalent circuit used in analysis of the impedance data

However, it is evident from the SEM image that the particles are swollen, and the structure of the nanofibers have changed due to continual expansion/contraction. In addition, some fusion is observed between the nanofibers and particles. Figure 3.26b depicts fibers with small CNT inclusions after the rate capability test. In this case, fibers are heavily fused, and particles are agglomerated, which can explain the failure of this material to function at faster current rates. It should be noted that these fibers could not undergo the high rates of 4.2 and 8.4 Ag^{-1}, and it can be assumed that morphological changes would be a lot more drastic if they had the ability to perform at those currents. Figure 3.26c is the SEM of the composite with large GNRs, revealing a highly porous structure for silicon nanoparticles. This drastic change in the porosity of SiNPs is due to accommodating a large number of Li-ions even at high rates (1400 $mAhg^{-1}$ at 12.6 Ag^{-1}), which altered the nanostructure of particles. The same holds true for fibers with large CNTs after cycling at high rates in Figure 3.26d, (although the structure is even more porous). This change in the structure of the nanoparticles is also in line with the decrease in surface charge transfer resistance since these opening make active sites more accessible to lithium ions.

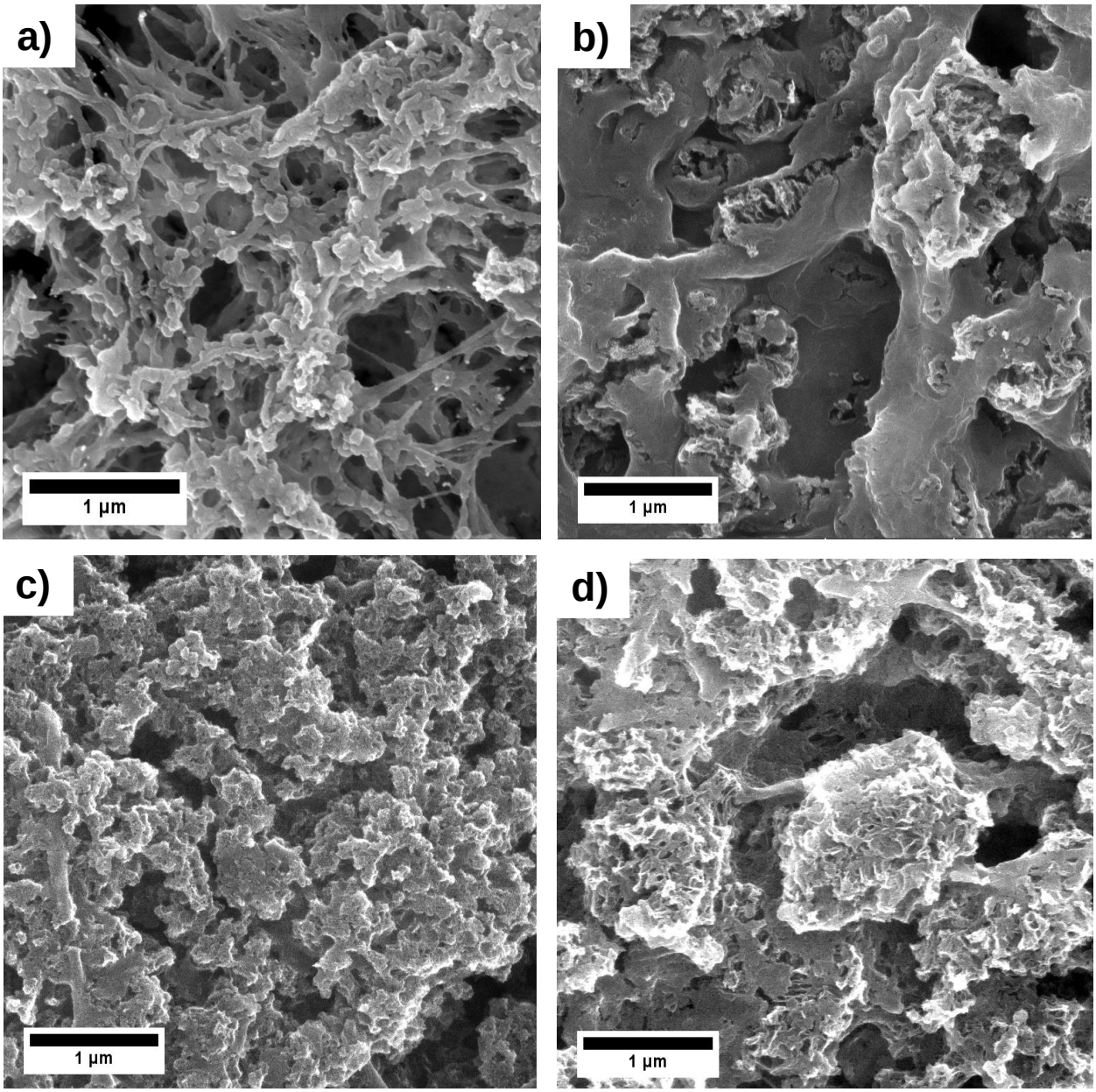

Figure 3. 26. Post-mortem SEM image of a) fibers with small GNRs b) small CNTs c) large GNRs d) large CNTs after rate capability test (from Figure 3.20 and 3.22).

Creating Synergy with Intra and Inter-Conductivity: Finally, to highlight the importance of inter-conductivity of fibers offered by large GNRs in the electrochemical performance at fast rates, a solution with combination of the two GNRs is prepared. To this end, since small GNRs had an inferior performance in the rate capability compared to large GNRs, a minute amount of large GNRs (1.5 wt%), is mixed in a small GNR solution. All other processing parameters are kept as before. Resulted fibers are marked as "mixed GNRs". Figure 3.27 is the SEM of the as spun and heat treated mixed GNR nanofibers. The addition of a small amount of large GNRs, does not disrupted the fiber formation. Resulting fibers keep their morphology after heat treatment, which is expected since the solution consists mostly of small GNRs.

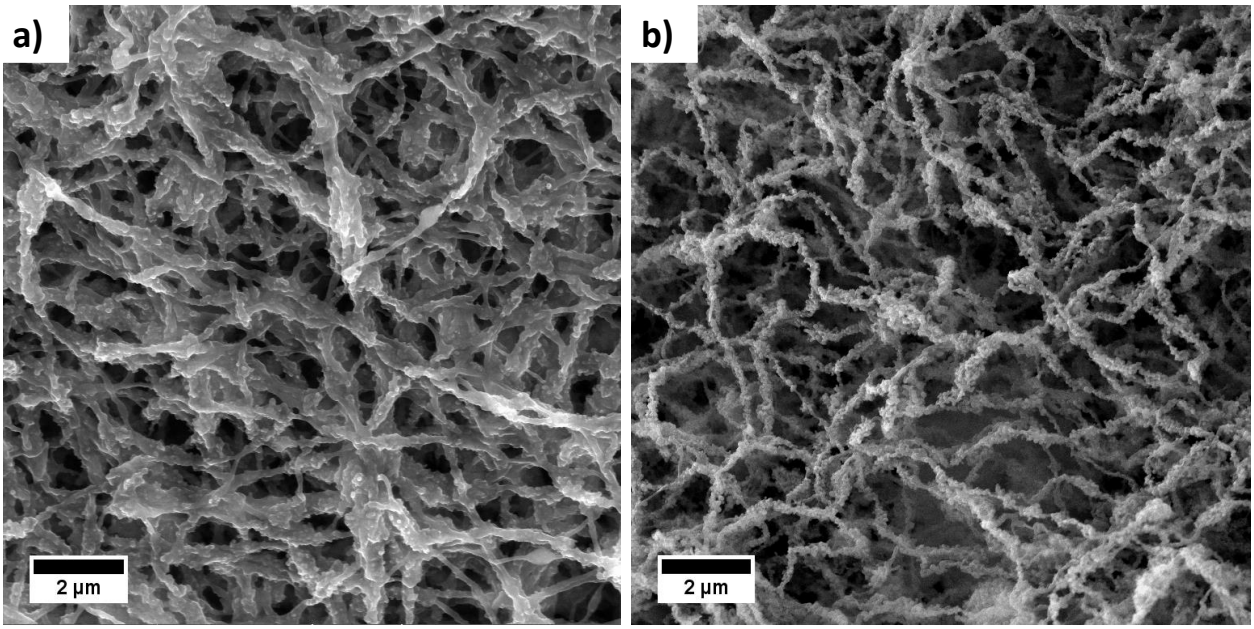

Figure 3. 27. SEM images of a) as-spun mixed GNR fibers b) heat treated mixed GNR fibers

Figure 3.28 compares capacities of small and mixed GNRs at various rates indicated on the top of each segment (small GNR graph is the same as Figure 3.20). Mixed GNRs start 840 $mAhg^{-1}$ above small GNRs; but as the rate is increased, the performance gap expands. Mixed GNR fibers exhibit capacities around 300 $mAhg^{-1}$ at 21 Ag^{-1}, while small GNRs reached that number at a rate of 8.4 Ag^{-1}. To further investigate this effect, voltage is swept at a rate of 1mVs^{-1} in the cyclic voltammograms of Figure 3.29.

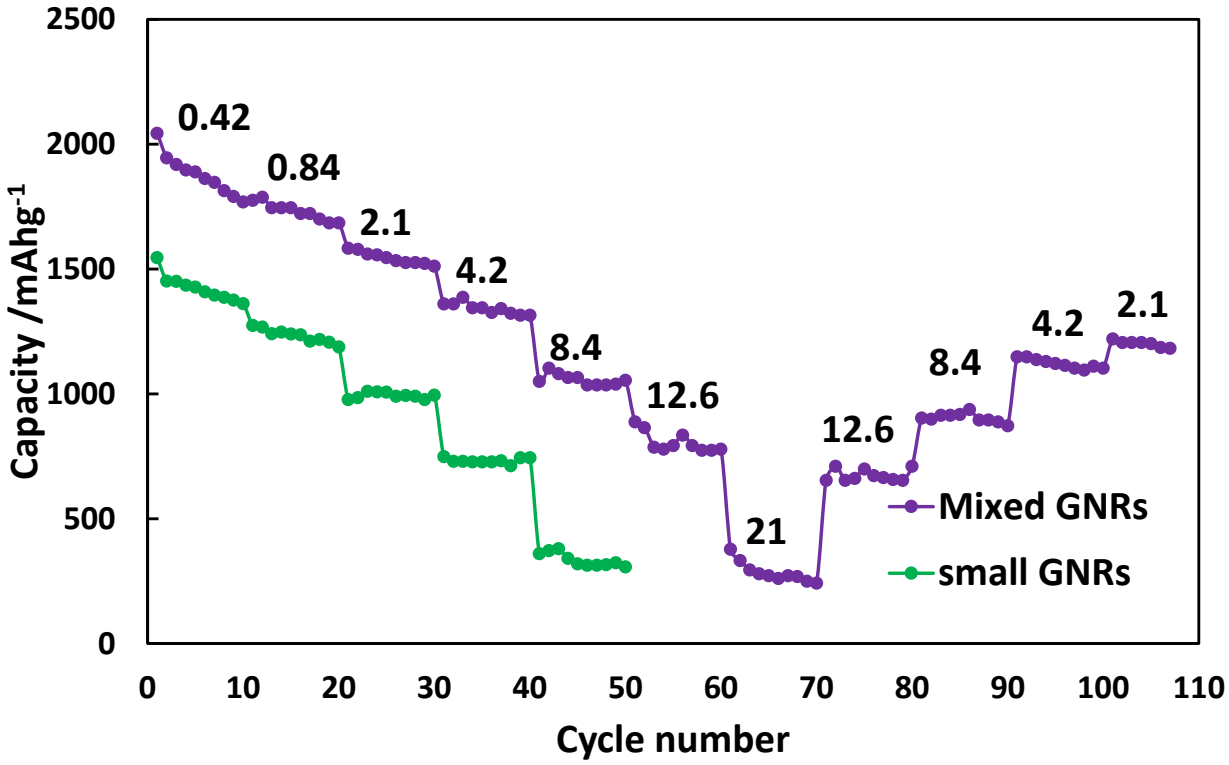

Figure 3. 28. Rate capability comparison between fiber mats with mixed GNRs (purple) and small GNRs (green)

Mixed GNRs are able to create higher currents, and thus validating the observation of higher capacities. This is due to the facilitation of electronic and ionic conductivity of the mixed GNRs fiber mat, offered by inter-connectivity provided by large GNRs, compared to just small GNRs, where this conductivity was missing.

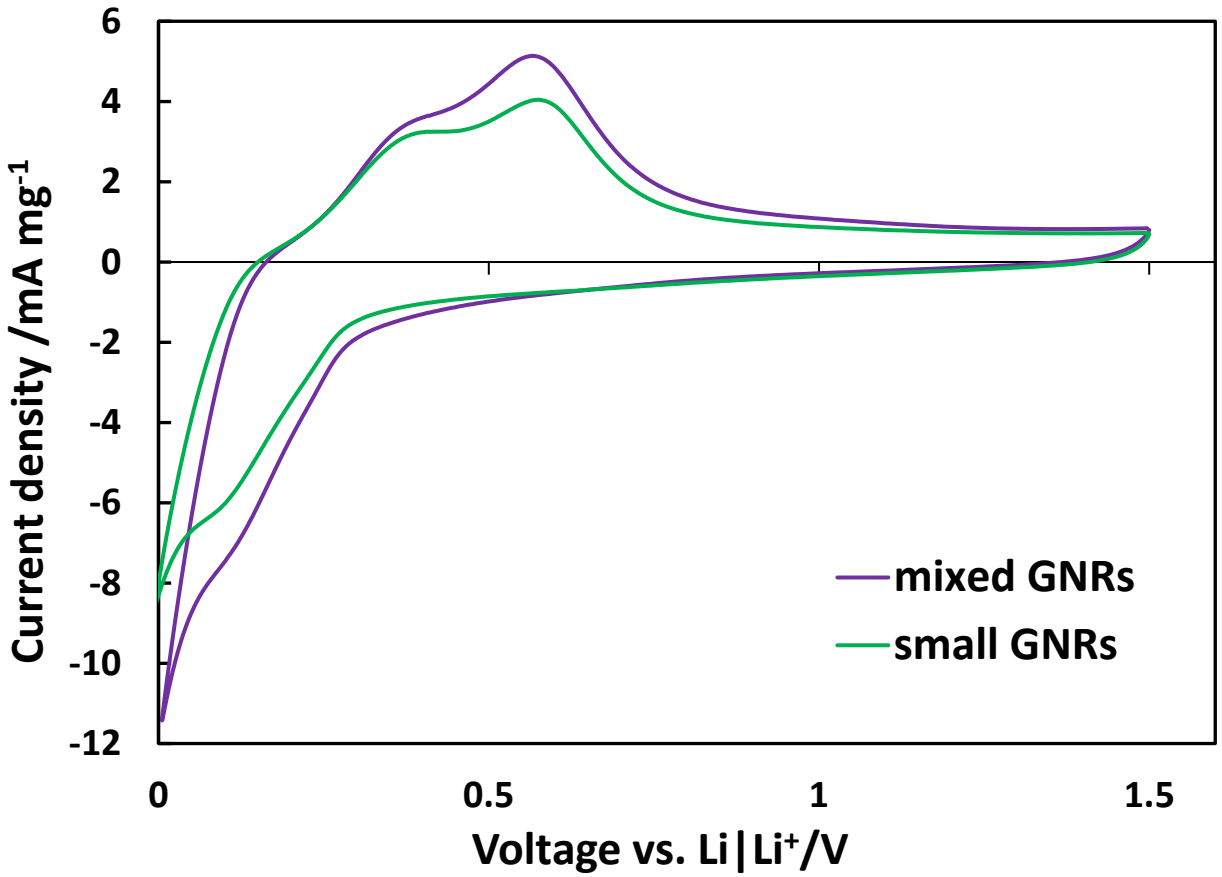

Figure 3. 29. Cyclic voltammograms of fibers with mixed and small GNR inclusions

Figure 3.30a and 3.30b illustrates the inner particle connections for the mixed GNR sample. Transmission electron micrographs indicate both small and large GNRs interact with silicon nanoparticles inside the PVA fiber. As expected, small GNRs are encapsulated inside the fibers while large GNR place themselves in between fiber and in some places, they also support silicon nanoparticles.

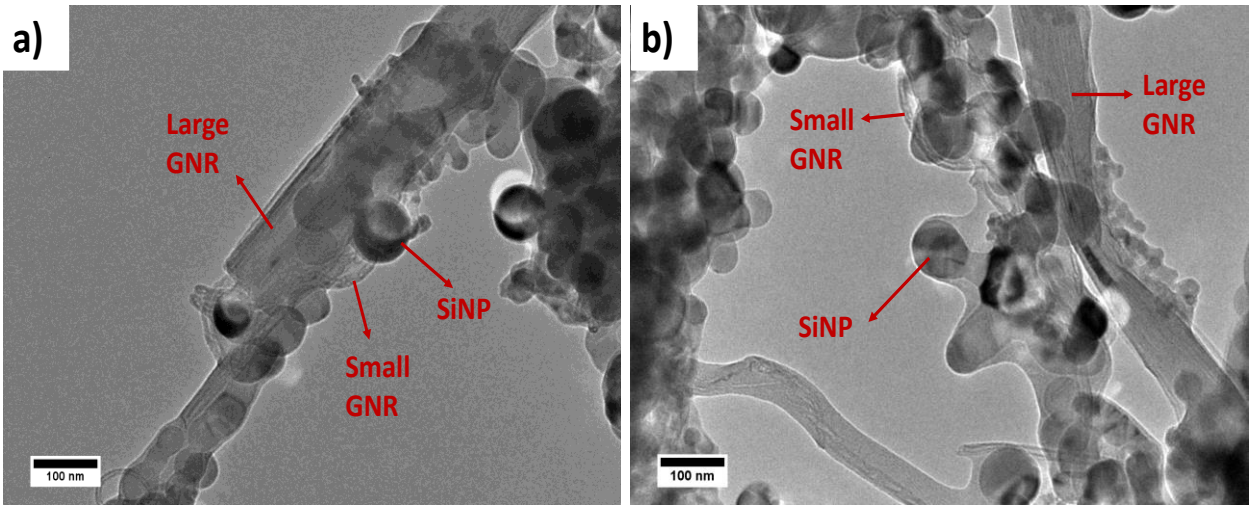

Figure 3. 30. TEM images of mixed GNR fibers showing both small and large GNRs within the fiber mat

Thermo gravimetric analysis of as-spun and heat-treated fibers in Figure 3.31 also indicate a 2% increase in the total weight of GNRs compared to silicon content of fibers with small GNRs only, in line with observation of enhancement of rate capability performance of the mixed fibers.

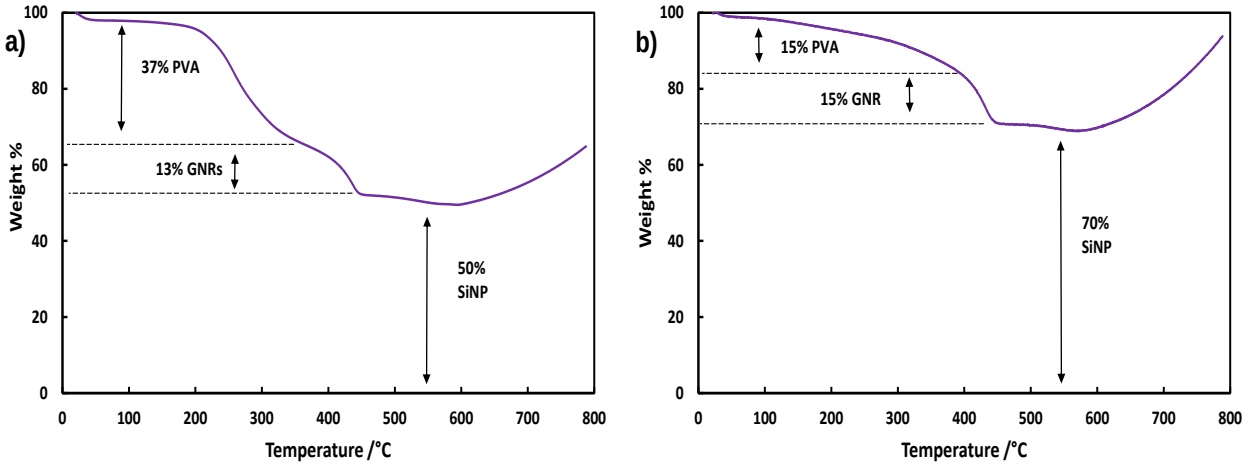

Figure 3. 31. Thermogravimetric analysis of a) As-spun fibers with mixed GNRs b) heat-treated fibers with mixed GNRs

To take this a step further another fiber mat with 5wt% of additional large GNRs are made and rate capability comparison with small GNR and mixed-GNR fiber mats is illustrated in Figure 3.32. Mixed GNR fibers with 5wt% large GNRs exhibit capacities around 750 $mAhg^{-1}$ at 21 Ag^{-1}, while small GNRs reached that number at a rate of 4.1 Ag^{-1}, demonstrating four times better rate capability due to the addition of large GNRs and supplementary conductive pathways created between fibers.

3.4. Conclusion

In this work, functional polymer nanofibers packed with silicon nanoparticles and CNTs or GNRs, have directly been deposited on a copper current collector, via water-based electrospinning. The

1D morphology of fibers reduces the diffusion path of Li ions since the porous structure of the fiber mat allows for penetration of the electrolyte through the entire thickness of the electrode material. At the same time, employing this method results in by-passing of a lot of conventional electrode preparation steps.

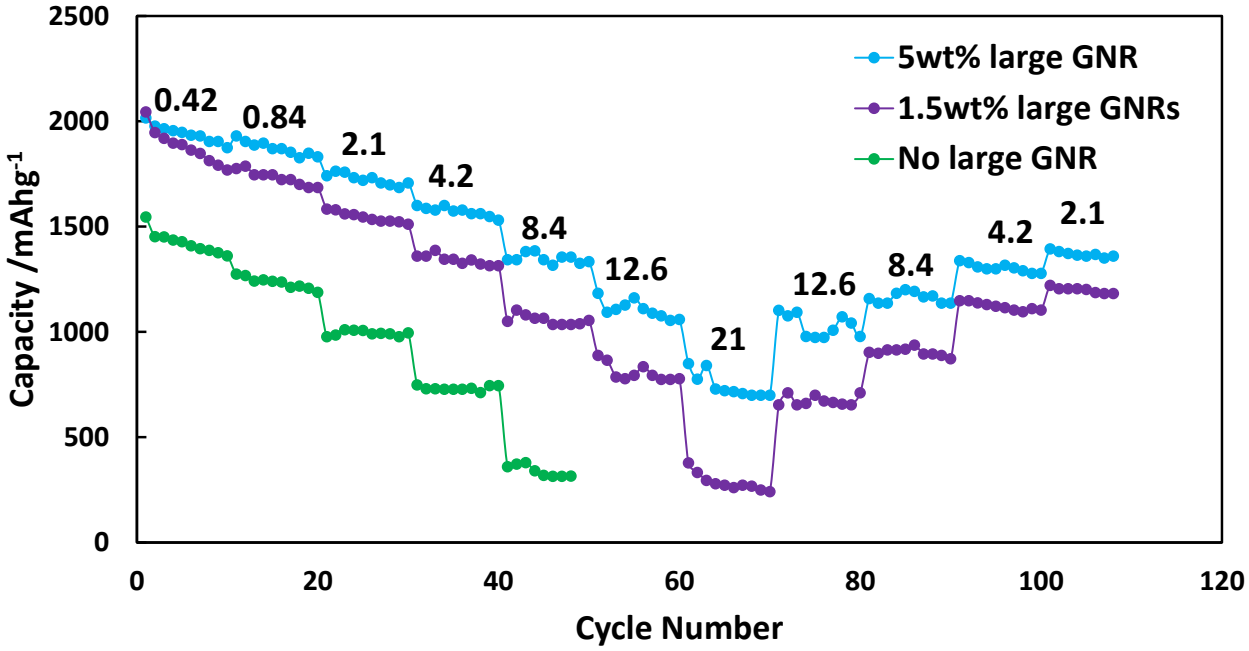

Figure 3. 32. Comparison of the rate capability of fibers with small GNRs (green), mixed GNRs with 1.5wt% added large GNRs (purple) and mixed GNRs with 5wt% added large GNRs (blue) at rates indicated above each step in Ag^{-1}

In addition, since nanostructuring and making the active material takes place in one step, the process allows for the direct comparison of particle chemistry and geometry. Graphene nanoribbons and their precursor carbon nanotubes are utilized as conductive pathways in the nanostructure of the silicon hybrid anodes. It is found that the anodes with GNRs exhibit better

performance with gravimetric capacities and retention have a smaller irreversible capacity loss and higher capacities at fast rates, compared to their precursor CNTs. The open structure of GNRs facilitates the Li interaction, and edge effects promote the Li-ion mobility while maintaining enough electronic conductivity for fast charging and discharging. The two sizes of GNRs and CNTs offer unique properties to the nanostructure. The PVA fiber fully encapsulated small GNRs/CNTs, and therefore they were responsible for intra-connectivity of the nanoparticles in each fiber. On the other hand, large GNRs/CNTs have such dimensions to be able to bridge between multiple fibers, and thus, they inter-connect several fibers and help with the overall conductivity of the fiber mat. As the result of these structural differences, electrochemical performance of fiber mats with large GNR inclusions is superior even at a high rate of 12.6 Ag^{-1}. Postmortem analysis of the cells after high rates indicate that the pulverization and delamination of the active material are minimal, due to the robust morphology created via electrospinning. However, morphological changes were more drastic for CNTs, probably due to the lithiation induced embrittlement of these materials. When a small amount of large GNRs were added to small GNRs to improve the performance (mixed GNR sample), the synergy between inter and intra- conductivity of the fibers results in a large improvement in performance. Mixed GNR fiber mat with 5 wt% of additional large GNRs can achieve the same capacity as small GNRs at four times the current rate. Therefore, it can be concluded that the unique geometry of graphene nanoribbons promotes the lithium ion transfer, and thus are more efficient conductive pathways compared to carbon nanotubes. Also, the inter-conductivity of nanostructures plays a central role in the high performance of silicon-based anodes at fast rates.

REFERENCES

[1] J. P. Maranchi, A. F. Hepp, A. G. Evans, N. T. Nuhfer, and P. N. Kumta, "Interfacial Properties of the a-Si / Cu :Active–Inactive Thin-Film Anode System for Lithium-Ion Batteries," *J. Electrochem. Soc.*, vol. 153, no. 6, pp. A1246–A1253, Jun. 2006.

[2] X. H. Liu, L. Zhong, S. Huang, S. X. Mao, T. Zhu, and J. Y. Huang, "Size-Dependent Fracture of Silicon Nanoparticles During Lithiation," *ACS Nano*, vol. 6, no. 2, pp. 1522–1531, Feb. 2012.

[3] S. Golmon, K. Maute, S.-H. Lee, and M. L. Dunn, "Stress generation in silicon particles during lithium insertion," *Appl. Phys. Lett.*, vol. 97, no. 3, p. 033111, Jul. 2010.

[4] H. Jung, M. Park, Y.-G. Yoon, G.-B. Kim, and S.-K. Joo, "Amorphous silicon anode for lithium-ion rechargeable batteries," *J. Power Sources*, vol. 115, no. 2, pp. 346–351, Apr. 2003.

[5] W. Xu, S. S. S. Vegunta, and J. C. Flake, "Surface-modified silicon nanowire anodes for lithium-ion batteries," *J. Power Sources*, vol. 196, no. 20, pp. 8583–8589, Oct. 2011.

[6] L.-F. Cui, R. Ruffo, C. K. Chan, H. Peng, and Y. Cui, "Crystalline-Amorphous Core−Shell Silicon Nanowires for High Capacity and High Current Battery Electrodes," *Nano Lett.*, vol. 9, no. 1, pp. 491–495, Jan. 2009.

[7] W. Xiao, J. Zhou, L. Yu, D. Wang, and X. W. (David) Lou, "Electrolytic Formation of Crystalline Silicon/Germanium Alloy Nanotubes and Hollow Particles with Enhanced Lithium-Storage Properties," *Angew. Chem. Int. Ed.*, vol. 55, no. 26, pp. 7427–7431, Jun. 2016.

[8] K. Stokes, H. Geaney, G. Flynn, M. Sheehan, T. Kennedy, and K. M. Ryan, "Direct Synthesis of Alloyed Si1–xGex Nanowires for Performance-Tunable Lithium Ion Battery Anodes," *ACS Nano*, vol. 11, no. 10, pp. 10088–10096, Oct. 2017.

[9] T. Jaumann *et al.*, "Dichlorosilane-derived nano-silicon inside hollow carbon spheres as a high-performance anode for Li-ion batteries," *J. Mater. Chem. A*, vol. 5, no. 19, pp. 9262–9271, 2017.

[10] B. Campbell *et al.*, "Carbon-Coated, Diatomite-Derived Nanosilicon as a High Rate Capable Li-ion Battery Anode," *Sci. Rep.*, vol. 6, p. 33050, Oct. 2016.

[11] A. Gohier *et al.*, "High-Rate Capability Silicon Decorated Vertically Aligned Carbon Nanotubes for Li-Ion Batteries," *Adv. Mater.*, vol. 24, no. 19, pp. 2592–2597, 2012.

[12] L.-F. Cui, L. Hu, J. W. Choi, and Y. Cui, "Light-Weight Free-Standing Carbon Nanotube-Silicon Films for Anodes of Lithium Ion Batteries," *ACS Nano*, vol. 4, no. 7, pp. 3671–3678, 2010.

[13] K. Evanoff *et al.*, "Ultra Strong Silicon-Coated Carbon Nanotube Nonwoven Fabric as a Multifunctional Lithium-Ion Battery Anode," *ACS Nano*, vol. 6, no. 11, pp. 9837–9845, Nov. 2012.

[14] E. Yoo, J. Kim, E. Hosono, H. Zhou, T. Kudo, and I. Honma, "Large Reversible Li Storage of Graphene Nanosheet Families for Use in Rechargeable Lithium Ion Batteries," *Nano Lett.*, vol. 8, no. 8, pp. 2277–2282, Aug. 2008.

[15] T. Bhardwaj, A. Antic, B. Pavan, V. Barone, and B. D. Fahlman, "Enhanced Electrochemical Lithium Storage by Graphene Nanoribbons," *J. Am. Chem. Soc.*, vol. 132, no. 36, pp. 12556–12558, Sep. 2010.

[16] H. Bi, Z. Liu, F. Xu, Y. Tang, T. Lin, and F. Q. Huang, “Three Dimensional Porous Graphene-Like Carbon Cloth from Cotton for a Free-Standing Lithium-Ion Battery Anode,” *J Mater Chem A*, 2016.

[17] Y. Luo *et al.*, “Dual doping strategy enhanced the lithium storage properties of graphene oxide binary composite,” *J Mater Chem A*, 2016.

[18] J. Liu *et al.*, “Graphene Sandwiched Mesostructured Li-Ion Battery Electrodes,” *Adv. Mater.*, p. n/a-n/a, Jul. 2016.

[19] Y. Cao *et al.*, “Sandwich-type functionalized graphene sheet-sulfur nanocomposite for rechargeable lithium batteries,” *Phys. Chem. Chem. Phys.*, vol. 13, no. 17, pp. 7660–7665, Apr. 2011.

[20] Y. Ma *et al.*, “Constraining Si Particles within Graphene Foam Monolith: Interfacial Modification for High-Performance Li+ Storage and Flexible Integrated Configuration,” *Adv. Funct. Mater.*, p. n/a-n/a, Aug. 2016.

[21] M.-H. Lin *et al.*, “Resilient Yolk-Shell Silicon-Reduced Graphene Oxide/Amorphous Carbon Anode Material Achieved by a Synergistic Dual-Coating Process for Lithium-Ion Batteries,” *ChemElectroChem*, p. n/a-n/a, Jul. 2016.

[22] J. Wang *et al.*, “Capacity-increasing robust porous SiO_2 /Si/graphene/C microspheres as an anode for Li-ion batteries,” *RSC Adv*, vol. 6, no. 51, pp. 45077–45084, 2016.

[23] M. Zhou *et al.*, “Facile synthesis of novel Si nanoparticles–graphene composites as high-performance anode materials for Li-ion batteries,” *Phys. Chem. Chem. Phys.*, vol. 15, no. 27, pp. 11394–11401, Jun. 2013.

[24] J. Chang *et al.*, “Multilayered Si Nanoparticle/Reduced Graphene Oxide Hybrid as a High-Performance Lithium-Ion Battery Anode,” *Adv. Mater.*, vol. 26, no. 5, pp. 758–764, Feb. 2014.

[25] S. Chen, P. Bao, X. Huang, B. Sun, and G. Wang, “Hierarchical 3D mesoporous silicon@graphene nanoarchitectures for lithium ion batteries with superior performance,” *Nano Res.*, vol. 7, no. 1, pp. 85–94, Nov. 2013.

[26] H. Liu *et al.*, “One-step in situ preparation of liquid-exfoliated pristine graphene/Si composites: towards practical anodes for commercial lithium-ion batteries,” *New J Chem*, 2016.

[27] Y. L. Liu, G. L. Xu, and X. W. Zhang, “Electronic transport in ultranarrow zigzag graphene nanoribbons with edge disorders,” *Phys. B Condens. Matter*.

[28] V. Barone, O. Hod, and G. E. Scuseria, “Electronic Structure and Stability of Semiconducting Graphene Nanoribbons,” *Nano Lett.*, vol. 6, no. 12, pp. 2748–2754, Dec. 2006.

[29] M. Ezawa, “Peculiar width dependence of the electronic properties of carbon nanoribbons,” *Phys. Rev. B*, vol. 73, no. 4, p. 045432, Jan. 2006.

[30] L. Li, A. Kovalchuk, and J. M. Tour, “SnO2-reduced graphene oxide nanoribbons as anodes for lithium ion batteries with enhanced cycling stability,” *Nano Res.*, vol. 7, no. 9, pp. 1319–1326, Jul. 2014.

[31] L. Li, A.-R. O. Raji, and J. M. Tour, “Graphene-Wrapped MnO2–Graphene Nanoribbons as Anode Materials for High-Performance Lithium Ion Batteries,” *Adv. Mater.*, vol. 25, no. 43, pp. 6298–6302, Nov. 2013.

[32] “Iron Oxide Nanoparticle and Graphene Nanoribbon Composite as an Anode Material for High-Performance Li-Ion Batteries - Lin - 2013 - Advanced Functional Materials - Wiley

Online Library." [Online]. Available: http://onlinelibrary.wiley.com/doi/10.1002/adfm.201303023/full. [Accessed: 11-Aug-2016].

[33] R. V. Salvatierra, A.-R. O. Raji, S.-K. Lee, Y. Ji, L. Li, and J. M. Tour, "Silicon Nanowires and Lithium Cobalt Oxide Nanowires in Graphene Nanoribbon Papers for Full Lithium Ion Battery," *Adv. Energy Mater.*, p. n/a-n/a, Aug. 2016.

[34] S. A. Abureden *et al.*, "Multigrain Electrospun Nickel Doped Lithium Titanate Nanofibers with High Power Lithium Ion Storage," *J. Mater. Chem. A*, Jul. 2016.

[35] T. H. Hwang, Y. M. Lee, B.-S. Kong, J.-S. Seo, and J. W. Choi, "Electrospun Core–Shell Fibers for Robust Silicon Nanoparticle-Based Lithium Ion Battery Anodes," *Nano Lett.*, vol. 12, no. 2, pp. 802–807, Feb. 2012.

[36] Y. C. Min JW Im WB, "Facile synthesis of electrospun Li(1.2)Ni(0.17)Co(0.17)Mn(0.5)O2 nanofiber and its enhanced high-rate performance for lithium-ion battery applications.," *ACS Appl. Mater. Interfaces*, vol. 5, no. 16, pp. 7765–9, 2013.

[37] Ji L, Lin Z, Medford A.J, and Zhang X, "In-situ encapsulation of nickel particles in electrospun carbon nanofibers and the resultant electrochemical performance," *Chem Eur J Chem. - Eur. J.*, vol. 15, no. 41, pp. 10718–10722, 2009.

[38] B. Guo *et al.*, "Electrospun Li4Ti5O12/C composites for lithium-ion batteries with high rate performance," *Solid State Ion.*, vol. 204–205, pp. 61–65, Dec. 2011.

[39] Y. Ou, J. Wen, H. Xu, S. Xie, and J. Li, "Ultrafine LiCoO2 powders derived from electrospun nanofibers for Li-ion batteries," *J. Phys. Chem. Solids*, vol. 74, no. 2, pp. 322–327, Feb. 2013.

[40] Z. Favors *et al.*, "Towards Scalable Binderless Electrodes: Carbon Coated Silicon Nanofiber Paper via Mg Reduction of Electrospun SiO2 Nanofibers," *Sci. Rep.*, vol. 5, Feb. 2015.

[41] S.-J. Kim *et al.*, "3-D Si/carbon nanofiber as a binder/current collector-free anode for lithium-ion batteries," *J. Ind. Eng. Chem.*, vol. 49, pp. 105–111, May 2017.

[42] Y. Zhmayev *et al.*, "Controlling the Placement of Spherical Nanoparticles in Electrically Driven Polymer Jets and its Application to Li-Ion Battery Anodes," *Small*, p. n/a-n/a, Aug. 2016.

[43] J. H. Park, V. Kalra, and Y. L. Joo, "Controlling the dispersion and orientation of nanorods in polymer melt under shear: Coarse-grained molecular dynamics simulation study," *J. Chem. Phys.*, vol. 140, no. 12, p. 124903, Mar. 2014.

[44] D. Li and Y. Xia, "Electrospinning of Nanofibers: Reinventing the Wheel?," *Adv. Mater.*, vol. 16, no. 14, pp. 1151–1170, Jul. 2004.

[45] Y. S. Kim *et al.*, "The critical contribution of unzipped graphene nanoribbons to scalable silicon–carbon fiber anodes in rechargeable Li-ion batteries," *Nano Energy*, vol. 16, pp. 446–457, Sep. 2015.

[46] G. Shoorideh, Y. S. Kim, and Y. L. Joo, "Facile, Water-Based, Direct–Deposit Fabrication of Hybrid Silicon Assemblies for Scalable and High–Performance Li–ion Battery Anodes," *Electrochimica Acta*, vol. 222, pp. 946–955, Dec. 2016.

[47] D. Torres, J. L. Pinilla, and I. Suelves, "Unzipping of multi-wall carbon nanotubes with different diameter distributions: Effect on few-layer graphene oxide obtention," *Appl. Surf. Sci.*, vol. 424, pp. 101–110, Dec. 2017.

[48] A. L. Higginbotham, D. V. Kosynkin, A. Sinitskii, Z. Sun, and J. M. Tour, "Lower-Defect Graphene Oxide Nanoribbons from Multiwalled Carbon Nanotubes," *ACS Nano*, vol. 4, no. 4, pp. 2059–2069, Apr. 2010.

[49] S. Sadeghi, M. Arjmand, I. Otero Navas, A. Zehtab Yazdi, and U. Sundararaj, “Effect of Nanofiller Geometry on Network Formation in Polymeric Nanocomposites: Comparison of Rheological and Electrical Properties of Multiwalled Carbon Nanotube and Graphene Nanoribbon,” *Macromolecules*, May 2017.

[50] M. Liu *et al.*, “Anisotropic conductive films based on highly aligned polyimide fibers containing hybrid materials of graphene nanoribbons and carbon nanotubes,” *Nanoscale*, vol. 7, no. 3, pp. 1037–1046, 2015.

[51] A. Dimiev *et al.*, “Permittivity of Dielectric Composite Materials Comprising Graphene Nanoribbons. The Effect of Nanostructure,” *ACS Appl. Mater. Interfaces*, vol. 5, no. 15, pp. 7567–7573, Aug. 2013.

[52] D. V. Kosynkin *et al.*, “Longitudinal unzipping of carbon nanotubes to form graphene nanoribbons,” *Nature*, vol. 458, no. 7240, pp. 872–876, Apr. 2009.

[53] B. J. Holland and J. N. Hay, “The thermal degradation of poly(vinyl alcohol),” *Polymer*, vol. 42, no. 16, pp. 6775–6783, Jul. 2001.

[54] X. Fan, W. T. Zheng, and J.-L. Kuo, “Adsorption and diffusion of Li on pristine and defective graphene,” *ACS Appl. Mater. Interfaces*, vol. 4, no. 5, pp. 2432–2438, 2012.

[55] X. H. Liu *et al.*, “In situ transmission electron microscopy of electrochemical lithiation, delithiation and deformation of individual graphene nanoribbons,” *Carbon*, vol. 50, no. 10, pp. 3836–3844, Aug. 2012.

[56] Y. Liu *et al.*, “Lithiation-Induced Embrittlement of Multiwalled Carbon Nanotubes,” *ACS Nano*, vol. 5, no. 9, pp. 7245–7253, Sep. 2011.

[57] C. Uthaisar and V. Barone, “Edge Effects on the Characteristics of Li Diffusion in Graphene,” *Nano Lett.*, vol. 10, no. 8, pp. 2838–2842, Aug. 2010.

[58] C. Uthaisar, V. Barone, and J. E. Peralta, “Lithium adsorption on zigzag graphene nanoribbons,” *J. Appl. Phys.*, vol. 106, no. 11, p. 113715, Dec. 2009.

CHAPTER FOUR

$AL_X O_Y$ COATING ON DIRECTLY DEPOSITED SILICON-BASED NANOFIBERS FOR HIGH-RATE LITHIUM ION BATTERY ANODES

4.1. Introduction

Silicon is one of the strongest candidates for the next generation of Li-ion battery anodes due to its high theoretical capacity of 4200 mAh/g. This superior capacity to host guest Li ions result in enormous volume changes during lithiation/delithiation which will cause the SEI layer to be unstable and cause capacity fading. Modifying the surface of the particles with different coatings has shown to be an effective way to deal with the issues above. For silicon-based materials, carbon is the most widely studied coating[1]–[4] both because it can enhance particle's conductivity and its ability to form a stable SEI layer, protecting particles from direct contact with electrolyte. Metal oxides also have been explored in the literature to promote ionic conductivity in electrodes. Great effort has been focused on coating cathode materials[5]–[8] to enhance electrochemical performance and device longevity and safety[9]. Among metal oxides, Al_2O_3 is one of the most promising. It was also found that using nanoporous alumina as a separator can improve the ionic conductivity and suppress dendrite formation in lithium-metal batteries[10]. Aluminum oxide has also been utilized with silicon-based systems to manage solid electrolyte interface (SEI) formation [11] and enhance cyclic stability[12] and coulombic efficiency. Nguyen et al. showed that by conformal coating of silicon nanowires with Al_2O_3 rate capability and capacity retention can be improved.[13] Typically, those coatings are applied to the surface of the individual active particles via high vacuum processes like ALD[12] or CVD[2], [14], [15] which

are costly and not compatible with high throughput processes. However, for any electrode material to have practical relevance, its fabrication method should be scalable and relatively inexpensive. Therefore, exploring processes that are reasonably easy to scale up is a strategy worth pursuing.

Electrospinning has been utilized by a multitude of research groups as a means to produce active material in a facile manner, for both anode[16]–[19] and cathode[20], [21] or to make more efficient membranes[22], [23]. In this way, the highly porous resulting fiber mat provides ease of access for ions and high surface area for reaction, making this morphology attractive for energy storage devices. In our group, water-based electrospinning was employed to create composite fibers of graphene nanoribbons (GNRs), silicon nanoparticles (SiNPs) and polyvinyl alcohol (PVA) for application in lithium-ion batteries[24], [25]. We used electrospinning to directly deposit electrode material on the surface of the current collector[25], [26]. In this way, the highly porous morphology is preserved, and many of the electrode preparation steps are bypassed, making the process more economically attractive. We found that the unique surface structure created via electrospinning helps in the alleviation of the large volume changes of the SiNPs and keeping the integrity of the electrode, which resulted in an excellent performance at slow and high rates. Especially, the size and geometry of graphene nanoribbons used have a significant role in their effectiveness, especially at higher rates.

Inspired by these discoveries, the conclusion was made that the void spaces between fibers can be used more efficiently than just providing room for expansion of nanoparticles. Namely, if ionic and electronic transport can be enhanced via filling these empty spaces with a functional material, the effect on the electrochemical performance can be quite pronounced. In the present work, we explored a coating that rapidly forms aluminum oxide upon heat treatment in air to protect active material on the current collector. Instead of applying the coating over individual

silicon nanoparticles, we make a macro-composite of ceramic and active material. Alumina precursor solution is spin-coated onto the fiber mat of active material and is heat treated for 1 minute to form the desired ceramic layer. The coating layer ensures the adhesion of the nanofibers on the current collector (act as a binder) and can alter the electrochemical response of the electrode. PAA, which is the most prominent binder for the silicon-based material, is not electrochemically active and merely acts as an adhesion medium. However, the metal oxide layer not only acts as a binder but also modifies the interface favorably. Ceramic coated electrodes exhibit an improvement both in the overall capacity and retention over their polymer coated counterparts. Aluminum oxide has also been shown to improve the ionic conductivity of the material[27] which will in turn have a positive effect on the high-rate[28] electrochemical performance of the material.

4.2. Experimental Section

Composite preparation and characterization: All samples in this report are fabricated in the same manner. Water-based electrospinning of solution is employed to make sub-micron fibers directly on top of the copper current collector for assembly into 2032 coin cells. Polyvinyl alcohol (PVA, 0.5 g) is dissolved in in 5 g of deionized water, before 70 mg of graphene nanoribbons (GNRs) are added to the mix (two different GNRs are used in this report: small and large). The resulting solution is ultrasonicated to ensure uniform dispersion of particles. Silicon Nanoparticles (0.5 g) are added to the solution and stirred overnight. Another probe sonication step is implemented to assure uniform dispersion of the nanoparticles. The solution is then loaded into a syringe and is pumped through a nozzle placed 20 cm away from a grounded collector with copper disks, while a voltage of 15 KV is applied to the system. The copper disks with nanofibers on top of them undergo a heat treatment step at 200°C in air for 12 hours to stabilize the PVA backbone. After that Al_xO_y precursor solution (EMD Performance Materials) is spin casted (1000 rpm, 10 s)

on the disks to bind the fibers onto the current collector. The same was done for control electrodes with PAA being spin casted on the electrodes as the binder. For more information about characterization and electrochemical performance of the PAA coated electrodes refer to our previous work in Ref [25]. Rotation rate and spin time of casting were used to control the final coating weight on the disks. To convert the precursor to aluminum oxide, the disks are placed in a furnace that is heated to 350°C for one minute. The nanofiber and coating morphology was characterized with scanning electron microscopy (FESEM, Tescan Mira). Thermo-gravimetric analysis (10°C min^{-1} in air, TGA, TA Instruments Q500) was conducted on the fibers to accurately measure PVA, Silicon, and CNT or GNR content of the composite fibers. X-ray diffraction (XRD) was performed with on a Bruker D8 advance ECO powder diffractometer with. The Brunauer-Emmett-Teller (BET) surface area was measured with a Gemini VII 2390t (Micromeritics) in liquid nitrogen.

Electrochemical Characterization: 2032 coin-type cells are fabricated with the resulting directly-deposited disks, a polyethylene-polypropylene separator, and Lithium as the counter electrode. 1 M $LiPF_6$ salt dissolved in 1:1 (wt%) fluoroethylene carbonate: dimethyl carbonate is used as an in-house electrolyte. All cells are assembled in an argon-filled glovebox. Constant current charge/discharge cycles are performed on an MTI eight-channel battery analyzer with a voltage window of 0.015-1.5 V versus Li/Li^+. Cyclic voltammetry (CV) and electrochemical impedance spectroscopy (EIS) are carried out on a Princeton Applied Research potentiostat. In CV measurements, the voltage is swept between 0.005 and 1.5 V vs. Li/Li^+ with varying scan rates. EIS data is obtained with an amplitude of 10 mV and frequency range of 0.1-100000 Hz in all cells tested. Galvanostatic titration technique (GITT) was carried out with a 20-min current pulse of 0.42 A/g and 5 hours rest in between pulses to ensure the complete diffusion and equilibration of

Li-ions from the surface to the bulk of the electrode material on MTI battery cycler. Calculation of the Li-ion diffusion coefficient were done following the work of Weppner *et al.* in Ref [[29]]. All capacities reported in this study are normalized by the weight of silicon in the composite.

4.3. Results and Discussion

Electrodes with PVA, SiNPs and Small GNRs: As mentioned before, the ample void spaces between nanofibers created via electrospinning has a crucial role in the ability of these fibers to perform at high-rates, and to aleviate electrode expansion. However, if this space can be engineerd to have more function as to just passively provide room for expansion, electrochemical performance of the electrodes can be greatly enhanced. To this end, PVA/SiNP/small GNRs nanofibers are directly electrospun on copper current collector and then the alumina precursor solution is spin casted on the electrode. The resulting electrode is then heat treated at 350°C for one minute under air. To test the effect of this coating, control disks are prepared in the same manner, with polyacrylic acid (PAA) as the final coating step for comparison. PAA is the polymer that has been shown effective as a binder for the silicon-based anode and was our primary coating layer in our previous works.[25], [26] The final coating layer is needed in this system to ensure the adhesion of nanofibers on the copper current collector. Figure 4.1a shows the morphology of PVA/Si/small GNR fibers before the final addition of any coating. SiNPs are dispersed along the PVA nanofiber with small GNRs intertwined between SiNPs and PVA backbone. Figure 4.1b depicts the same fiber mat after addition of the precursor solution. The liquid penetrates through the inter-fiber pores to fill in all the void spaces. Figure 4.1c is the same disk after heat treating at 350°C in air for one minute. Morphology of the coating shows a drastic change before and after the heat treatment, which is due to evaporation of solvent and chemical reaction to produce

aluminum oxide. Figure 4.1d shows the cross-sectional view of the same electrode without any coating where all the individual fibers can be easily recognized.

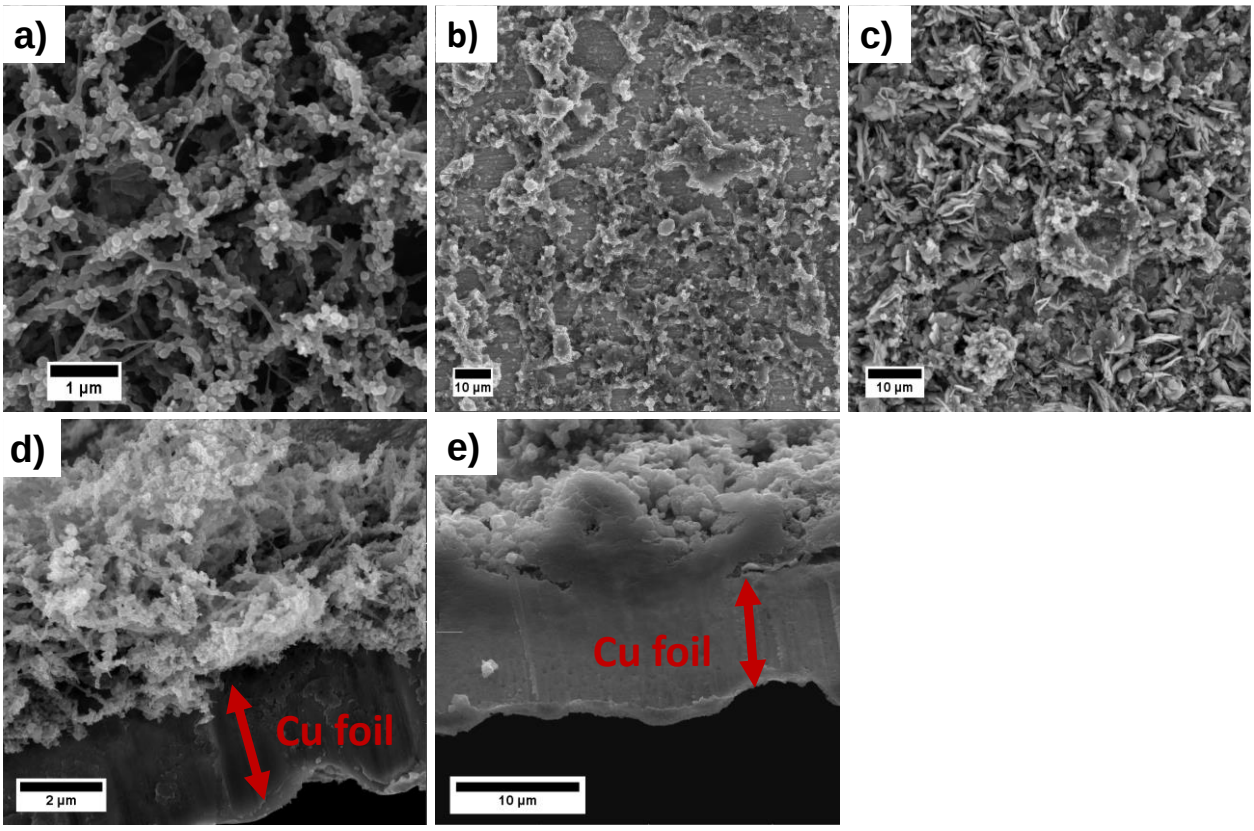

Figure 4. 1. SEM images of a) PVA/SiNP/Small GNR fibers without any coating on top b) PVA/SiNP/Small GNR fibers with Al_2O_3 precursor solution coated on top before heat treatment c) PVA/SiNP/Small GNR fibers with Al_2O_3 precursor solution coated on top after heat treating at 350°C for one minute d) cross-sectional view of the PVA/Si/small GNR fibers without any coating on copper disk e) cross-sectional view of the PVA/Si/small GNR fibers with aluminum oxide coating after heat treatment on copper disk

However, after addition of the aluminum oxide coating the layer cross-sectional view in Figure 4.1e appears as a film-like structure, which as mentioned before is due to penetration of the solution all the way to the current collector. Pulverization and electrical insulation are two of the main concerns in silicon-based anodes[30]–[32], which usually result in capacity fading and poor performance in the long run. This ingress of coating material to the most bottom layers of fiber mat is key in ensuring adhesion of fibers on the current collector, which translates into better electrochemical performance

To assess the role of the ceramic coating on the electrochemical performance, half-cells are fabricated and galvanostatically charged and discharged for many cycles. Figure 4.2a depicts the cyclic life of PVA/SiNP/small GNR anodes with PAA and Al_xO_y coating. The long term cyclic performance of the composites is tested at 1 A/g. It should be noted that these cells both underwent ten formation cycles at 0.18 A/g. The electrode with ceramic coating could retain 60% of its capacity (calculated against the second lithiation) at the end of 300 cycles, while its PAA coated counterpart retains 65% at the end of 100 cycles.

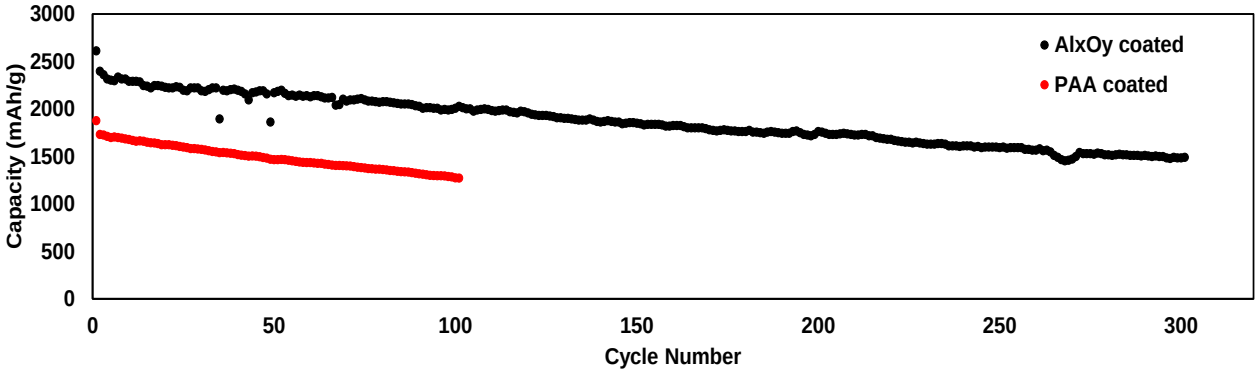

Figure 4. 2. Cyclic performance of composite anode with PAA coating (red) and with aluminum oxide coating (black) at 1A/g.

In order to shed more light on the superior ability of the ceramic coated electrodes to retain their capacity, a very thin layer of coating is spin casted on the electrode and goes through heat treatment at 350℃ for one minute. Figure 4.3a is the SEM of the mentioned electrode. The coating is thin enough that the individual fiber morphology underneath can still be observed. The fiber mat looks like the pristine mat with addition of a thin lace like coating on top. These fibers are made into half cells and discharged to specific voltages at a rate of 0.42 A/g until fully lithiated. The SEM bank of Figure 4.3 shows the evolution of the Al_xO_y coated fibers as more Li ions are alloyed into the material. At higher voltages the coating starts to react with Li ions. At 0.89V (Figure 4.3d) the coating has formed circular structures due to lithiation. As the voltage continues to decrease the nanoribbons start to intercalate lithium into their structure and the change in the morphology of the nanofibers can be observed in the Figure 4.3e,f. With continuation of lithiation below 0.2V lithium ions start to alloy with silicon nanoparticles and the diameter of the fibers start to increase at Figure 4.3g,h. At full lithiation (0.015V, Figure 4.3i) the fibers are swollen, but still distinguishable and the coating is also observed on the surface. Figure 4.3j shows fibers with PAA coating at their fully lithiated state. The difference in the morphology of PAA coated and ceramic coated electrodes is obvious. It can be noted that the fibers in this image are somewhat fused together. Ceramic coated fibers are put through delithation as well. Scanning electron micrographs in Figure 4.4 indicate the change in the morphology of the fibers as Li ions are deintercalated. At a fully delithiated state (Figure 4.4c) the individual fibers can be distinguished without any damage to the integrity of the fibers. At the same time, the coating on the fibers also look intact without any cracks or pulverization. This protection of the active mass is the reason why the ceramic coated fibers have better capacity retention in the long run. It should be noted that the morphology of the

fibers in Figure 4.4c is different than the pristine case (Figure 4.3a), which is due to the initial reaction of the coating with the electrolyte. After the first cycle the adhesion properties of the coating just help in keeping the integrity of the nanofiber mat without reacting with the electrolyte of lithium ions anymore.

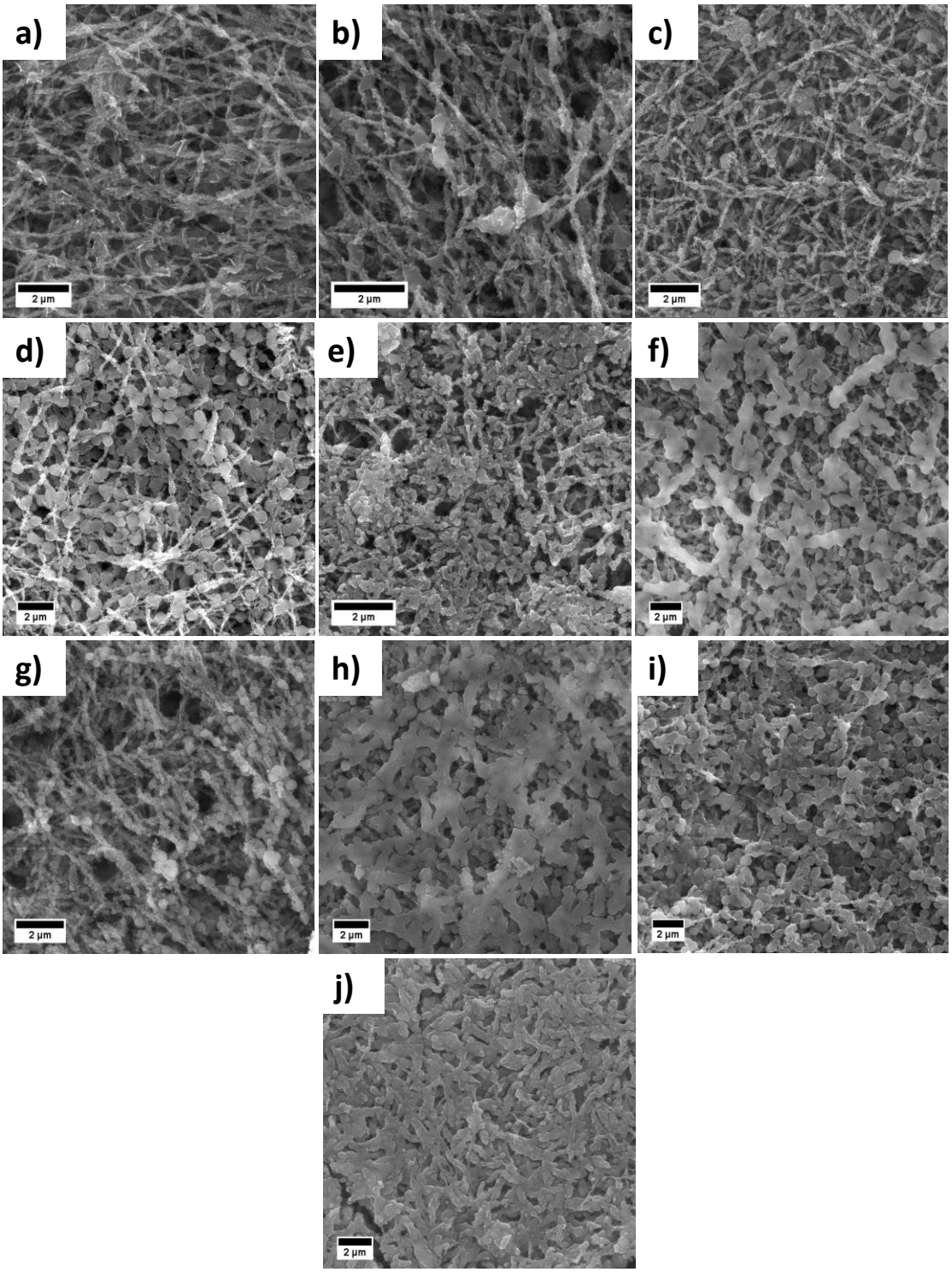

Figure 4. 3. Bank of SEM showing the evolution of the morphology of the Al_2O_3 coated electrode on first lithiation a) pristine fibers b) at 1.34V, 10% lithiation c) 1.2V, 20% lithiation d) 0.89V, 40% lithiation e) 0.74V, 50% lithiation f) 0.3V, 80% lithiation g) 0.15V, 90% lithiation h) 0.07V, 95% Lithiation i) 0.015V vs Li/Li^+, 100% lithiation j) fibers with no coating at 0.015V, 100% lithiation

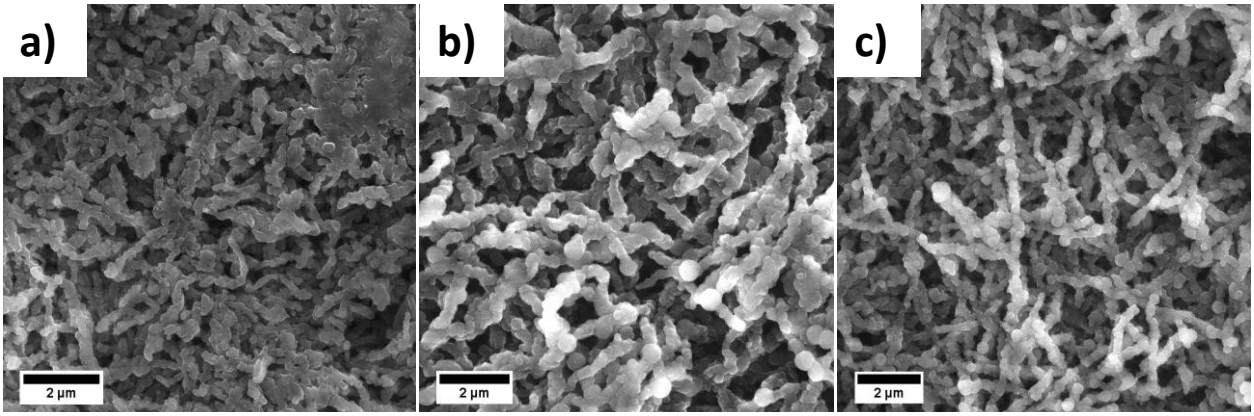

Figure 4. 4. SEM showing the evolution of the morphology of the Al2O3 coated electrode on first delithiation at a) 0.07V, 5% delithiation b) 0.3V, 20% delithiation c) 1.5V, 100% delithiation vs. Li/Li^+

To examine the rate dependence of this improvement in the electrochemical performance, the cells undergo rate capability test, where the current is systematically increased from 0.42 A/g to 20 A/g. Figure 4.5 demonstrates delithiation capacity of both samples at the rates indicated above each step. It is worth observing that both electrodes start at a similar capacity at low rates, but as the current is increased, the performance gap between ceramic coated and polymer coated electrodes widens. The penetration of the lithium ions through the electrode to get to the active sites is a diffusion limited process. Anything that can improve this migration of ions, will help the electrochemical performance of the electrode especially at higher rates. At 20 A/g the ceramic coated electrode has the same performance (~ 500 $mAh/g_{silicon}$) as the PAA coated electrode at 8.4 A/g. The PAA coated electrode could not be charged and discharged at 15 and 20 A/g. This enhancement in performance at higher currents means that ceramic coated electrodes are able to respond to increase in the current and successfully move and collect charges. Physical and

chemical property of the coating can have a dramatic effect on its electrochemical performance. Figure 4.6 exhibits the capacity-voltage profiles of the ceramic coated electrodes at different rates. At higher currents the overpotential of lithiation and delithiation processes are increased, probably due to the poor electrical conductivity of the coating. Since the ionic conductivity of the material is improved by introduction of the ceramic coating overall response of the ceramic coated electrodes are better than their PAA coated counterparts.

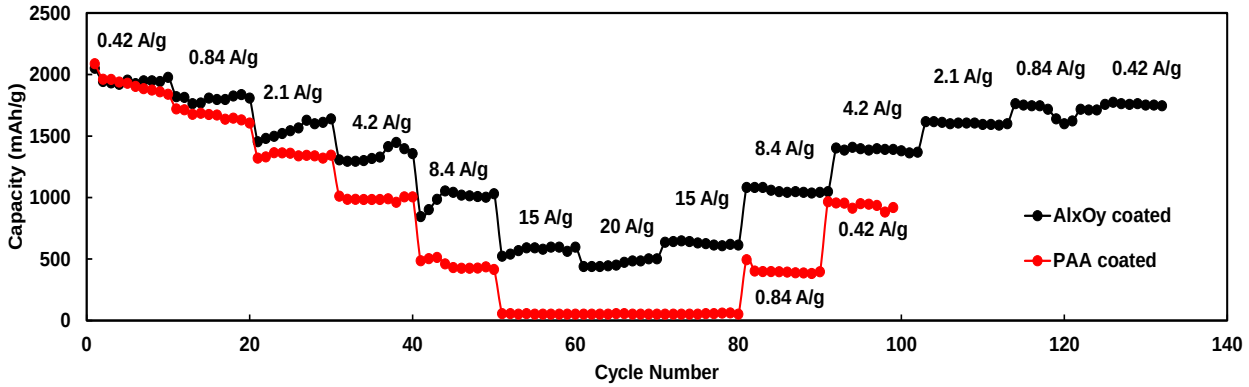

Figure 4. 5. Delithiation capacities of the composite anode with PAA coating (red) and with aluminum oxide coating (black) at various currents indicated on top of each step. The last two steps on the PAA electrode are done at 0.84 and 0.42 A/g as indicated below them.

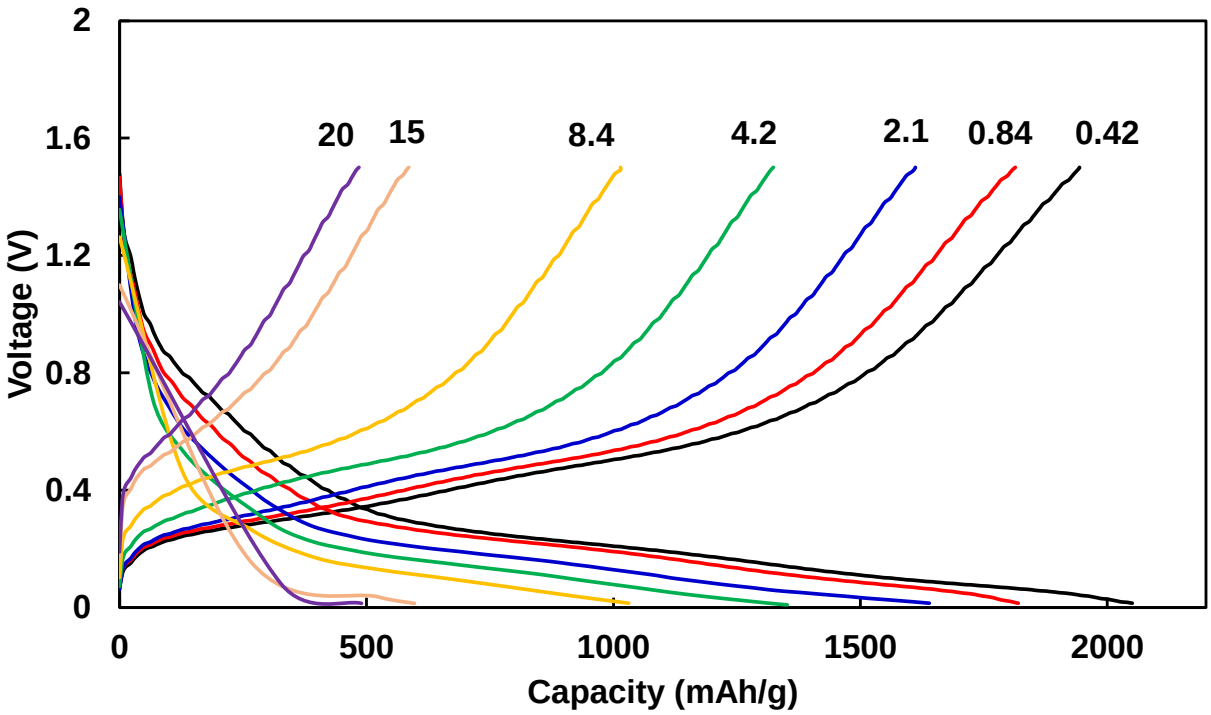

Figure 4. 6. Capacity-voltage profiles of the ceramic coated electrodes at the rates indicated above each curve in A/g.

A material with high surface area is desirable for high rate electrochemical cells such as batteries and capacitors. The available surface area can provide sites for the electrochemical reactions to take place, while upon contact with the liquid electrolyte the surface acts as a double layer capacitor. Also, the porosity of the material can profoundly impact the effective diffusion in the system. BET analysis of the Al_xO_y coating indicates that this material has 136 m^2/g of surface area after activation at 350°C in air. This material has a large number of micro and mesopores contributing to the surface area as can be observed from Figure 4.7. Probably this high surface area aids the electrodes with ceramic coatings to be able to respond to fast currents through a capacitive mechanism.

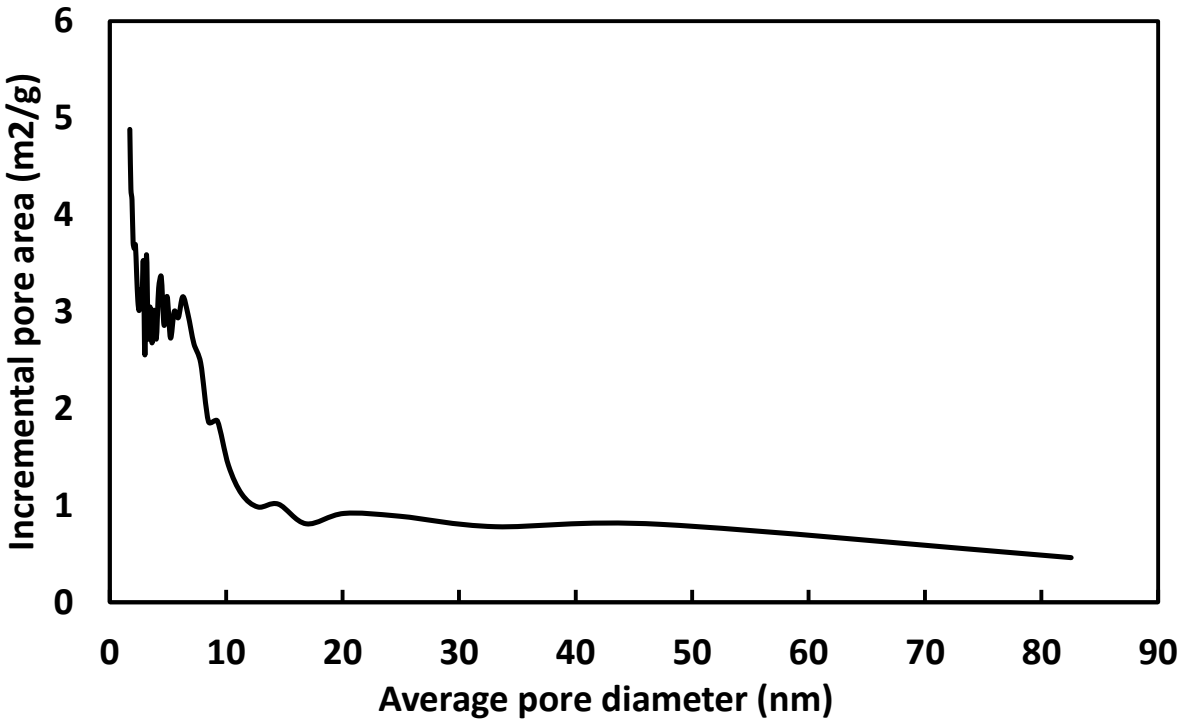

Figure 4. 7. BET result of incremental pore area vs. average pore diameter for the heat-treated ceramic coating

To distinguish between the contribution of the ceramic coating and the electrode material, copper foil is coated with the precursor solution and heat treated in the air like other electrodes. Then this electrode was charged and discharged in the same voltage window as the composite anodes (there is no active material, only the coating solution). Figure 4.8 illustrates the cyclic performance of the coating. On the first cycle this material exhibits a delithiation capacity of 237 mAh/g that is lost in the subsequent cycles. The high irreversible capacity loss of the coating is due to the organic groups that still present from the precursor solution and it is in line with observation with scanning electron microscope. Porosity and high surface area of this material as shown before by BET is probably responsible for the residual capacity in cycles 2 and on, as double layer capacitance

mechanism without any Faradaic reactions. It is obvious form this result that the great electrochemical performance of the Al_xO_y coated electrodes are due to the synergistic effects of the underlying nanofiber mat, which provides the bulk of the faradaic capacity, and the ceramic coating contribution to the ionic conductivity and double layer capacity.

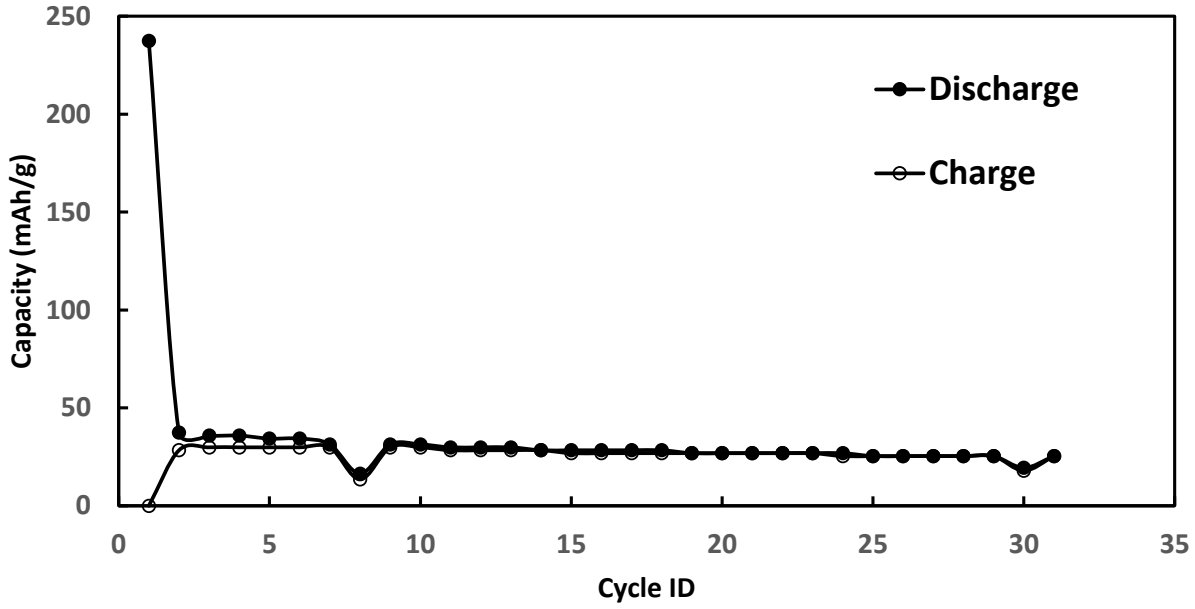

Figure 4. 8. Cyclic performance of an electrode containing only ceramic coating at 0.18 A/g

To further investigate this improvement in capacity and retention, electrochemical impedance spectroscopy (EIS) is conducted on the electrodes. In this experiment, a half-cell with Al_xO_y coated electrodes is incrementally lithiated to a specific voltage against Li/Li^+ on its first lithiation, and EIS is performed on the cell before continuing further lithiation. The same is done on the delithiation step until the cell is fully delithiated at 1.5V. The Nyquist plots of Figure 4.9a

show the impedance data of the cell. Shades of blue are associated with lithiation and shades of red in the graph belong to the delithiation process. (The color that the lines are depicted in gets darker with more lithium ions being alloyed. Lightest blue is the pristine cell while darkest blue belongs to the impedance taken at 0.015V vs. Li/Li^+. The same for delithiation curves. Lightest pink corresponds to 1.5V and darkest red to 0.0155V) Surface and bulk resistances of the electrode show changes as lithiation/delithiation step progress. First starting with the bulk resistance, which is usually associated with electrolyte and anything other than the electrode surface, increases as more and more lithium is alloyed. Figure 4.9b indicates at 40% lithiation (0.9 V vs. Li/Li^+) this bulk resistance peaked. This rise should be associated with the irreversible chemical reactions that the coating has with carbonate-based electrolyte. This is in line with both SEM and irreversible reaction observed and mentioned before in the coating. The bulk resistance starts to decrease after the initial increase and stays in a moderately stable condition probably indicating no further irreversible chemical reaction. Surface charge resistance of the electrode (Figure 4.9b) steadily decreases as more lithium is alloyed, which is consistent with our previous work of PVA/Si/CNT and GNR nanocomposite system[26]. During delithiation process in Figure 4.9c, both bulk and charge transfer resistance in the system reduce as more lithium is taken out of the system. It can be observed from the graph that the diffusion impedance of the significantly reduces during lithiation and even after full delithiation this impedance does not go back to its original supporting the theory of ceramic coating increasing the ionic diffusion after the initial reaction with the electrolyte.

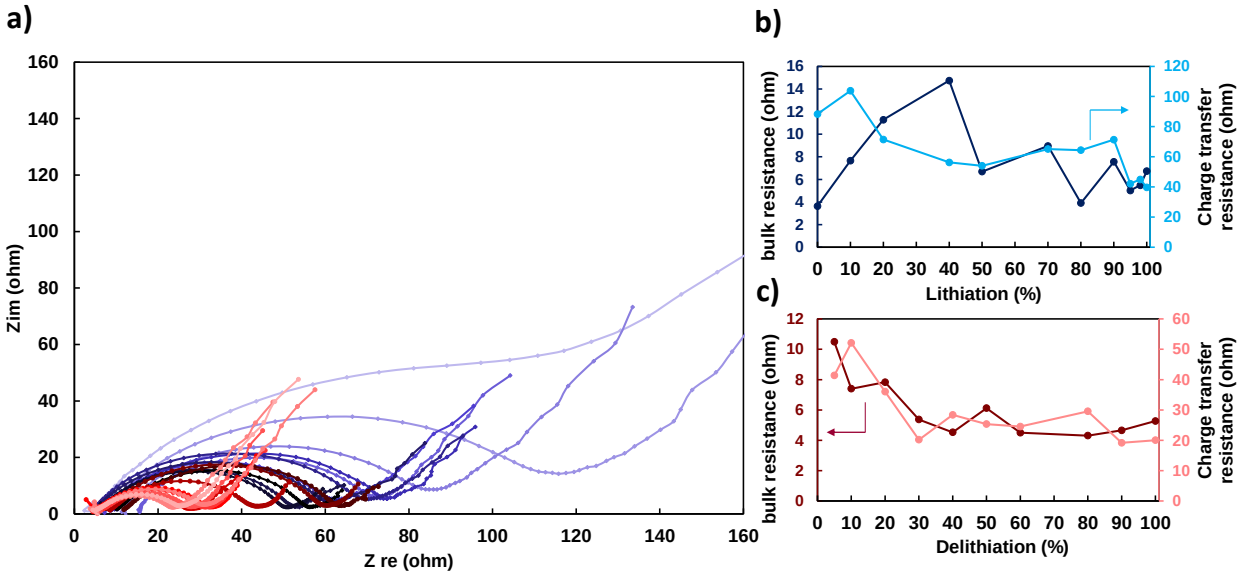

Figure 4. 9. a) Nyquist representation of EIS data of the cell along lithiation (shades of blue curves) and delithiation (shades of red curves) b) bulk and surface resistances as a function of lithiation percentage in the lithiation process (with 100% corresponding to 0.015V vs. Li/Li^+) c) bulk and surface resistances as a function of lithiation percentage in the delithiation process (with 100% corresponding to 1.5V vs. Li/Li^+). In figure b the light blue line corresponds to charge transfer resistance and the navy blue to bulk resistance in the lithiation process. In figure c the pink like corresponds to charge transfer and dark red to bulk resistance in the delithiation process.

Al_xO_y coated electrodes are also superior in capacity retention to their PAA coated counterparts. The cell in Figure 4.5 is opened after rate capability, to access the state of the electrode after being exposed to harsh conditions. Figure 4.10 show scanning electron micrographs of ceramic coated electrode. Top view of the surface at a low magnification in Figure 4.10a indicates that the coating held its integrity and no obvious cracking and pulverization are observed even after cycling at 20

A/g. The same holds true for the lower layer of the material in the electrode, as can be seen in the cross-sectional view in Figure 4.10b. The ability of this coating to hold the electrode material together and connected to the current collector is the reason behind enhancement in the capacity retention of the nanofiber-based electrode.

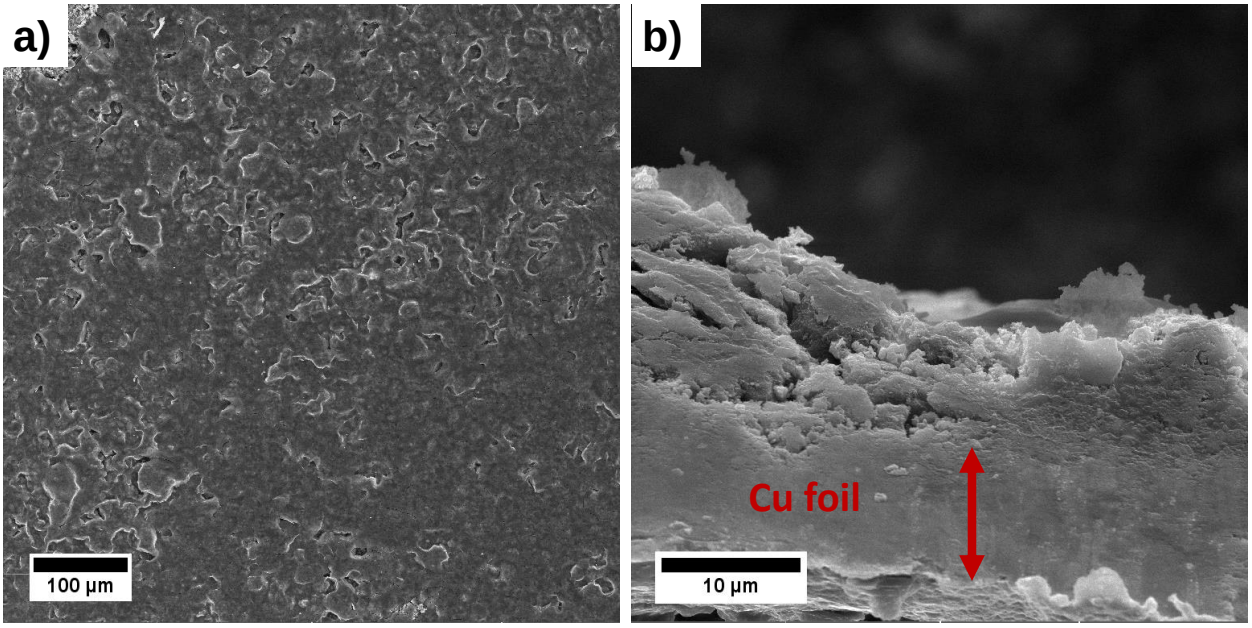

Figure 4. 10. SEM images of a) top view of ceramic coated electrode after rate capability at low magnification b) cross-sectional view of the same electrode

Electrodes with PVA, SiNPs and large GNRs: In our previous work with silicon-based nanofiber anodes, the conclusion was made that GNRs with larger dimensions have a better ability to perform at higher rates compared to small ones. To investigate if the ceramic coating can improve the rate capability of this system as well, PVA/SiNP/large GNRs are fabricated like the samples before and the ceramic coating was added on them. Filling the void spaces of the

fiber mat with a material with high ionic conductivity proved to be effective in enhancing the electrochemical performance of the composite anodes with small GNRs. Adding a ceramic coating is expected to have similar effects on the overall capacity and retention of the electrode with large GNRs. Rate capability of the electrodes with large GNRs in Figure 4.11, reveals this material can have an outstanding performance of 2200, 1500 and 950 mAh/g at rates of 12.6, 21 and 42 A/g respectively. The ability of PVA/SiNp/large GNR nanocomposite fibers to have an excellent performance at high rates stems from two underlying phenomena. As mentioned before, the porosity and surface area per weight of the coating, results in a double layer capacitor effect. Also, with the enhancement of ionic conductivity due to the amorphous Al_2O_3 layer, the charges in the system can be mobilized more efficiently which results in higher capacities especially at high rates.

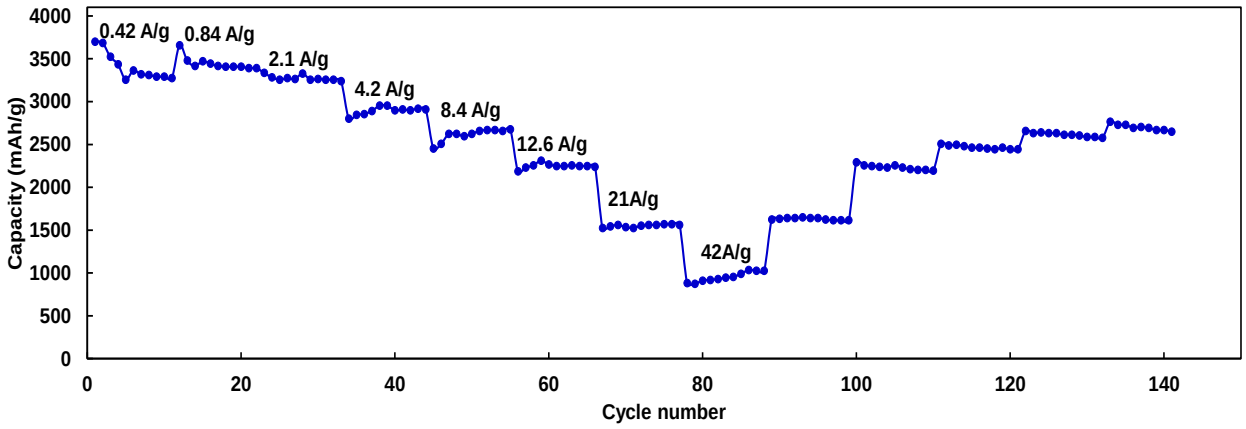

Figure 4. 11. Capacity vs. cycle number of the PVA/Si/large GNR composite nanofibers with the Al_2O_3 coating at the rates indicated above each step.

Cyclic voltammetry is utilized to access the double layer contribution of the ceramic coating to the overall capacity. Three electrodes were prepared: one just PVA and large GNR fibers with PAA coated on top, second PVA/SiNP/large GNRs with PAA, and third PVA/SiNP/large GNRs with alumina coating. At a scan rate of 1mV/s in Figure 4.12, the ceramic coated electrode has a much larger current produced when the voltage is scanned between 0.005 and 1.5 V vs. Li/Li^+. It can be observed that this increase in the double layer capacitance is not due to the graphene nanoribbons in the system since the green curve does not show such an enhancement. Also, Al_xO_y coated electrode does not exhibit any additional faradaic peaks in CV. Confirming that the coating contributes to the electrochemical performance of the cell in a capacitive manner. In order to access this contribution, silicon was excluded from the system to take away the faradaic peaks. Therefore, composite fibers containing only large GNRs and PVA are spun directly on copper disks in the same fashion that is done for all the other samples.

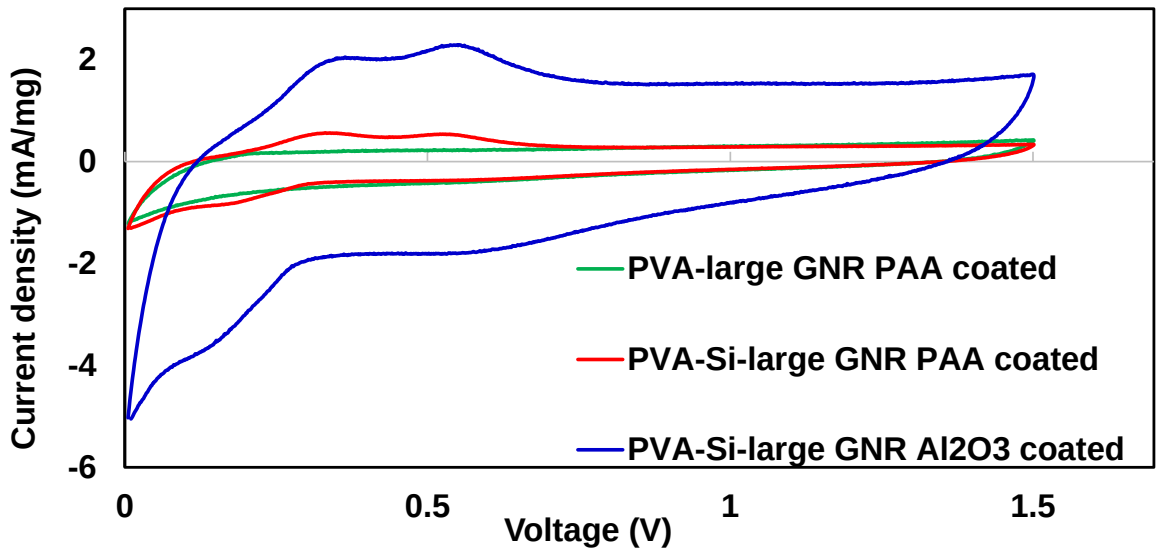

Figure 4. 12. Cyclic voltammograms comparing PVA/large GNR (no silicon, green) , PVA/SiNP/large GNR PAA coated (red), PVA/SiNP/large GNR (blue)

To see the effect of coating, CV tests are done on PVA/large GNR disks with PAA and Al_xO_y coating at various scan rates (10, 20, 50 and 100 mV/s). Figure 4.13 compares the voltammograms on these disks. Widening of the voltammogram of the blue ceramic coated samples indicates a larger double layer capacitance, regardless of the scan rate. These CV curves were utilized to calculate a specific capacity at different scan rates for each sample. Figure 4.14 illustrates that the sample with alumina coating has much higher specific capacity than the one with PAA coating at various scan rates, due to the reasons mentioned before. We speculate that there are three underlying reasons for this enhancement in double layer capacity. First of all, as previously stated ceramic material especially alumina has proven to have high ionic conductivity, meaning that it can be effective in moving Li ions to reach all the pores and cover the surface area of the material. Second, the nanofiber morphology underneath aids in creating porous structure by virtue of being a porous 3-dimensional substrate with large void spaces in between the fibers. Graphene nanoribbons have also, proved to be highly effective as conductive pathways in silicon-based anodes in our previous work. The combination of these properties gives the system its outstanding electrochemical performance observed. It is obvious that the ceramic coating has a large capacitive contribution to the system.

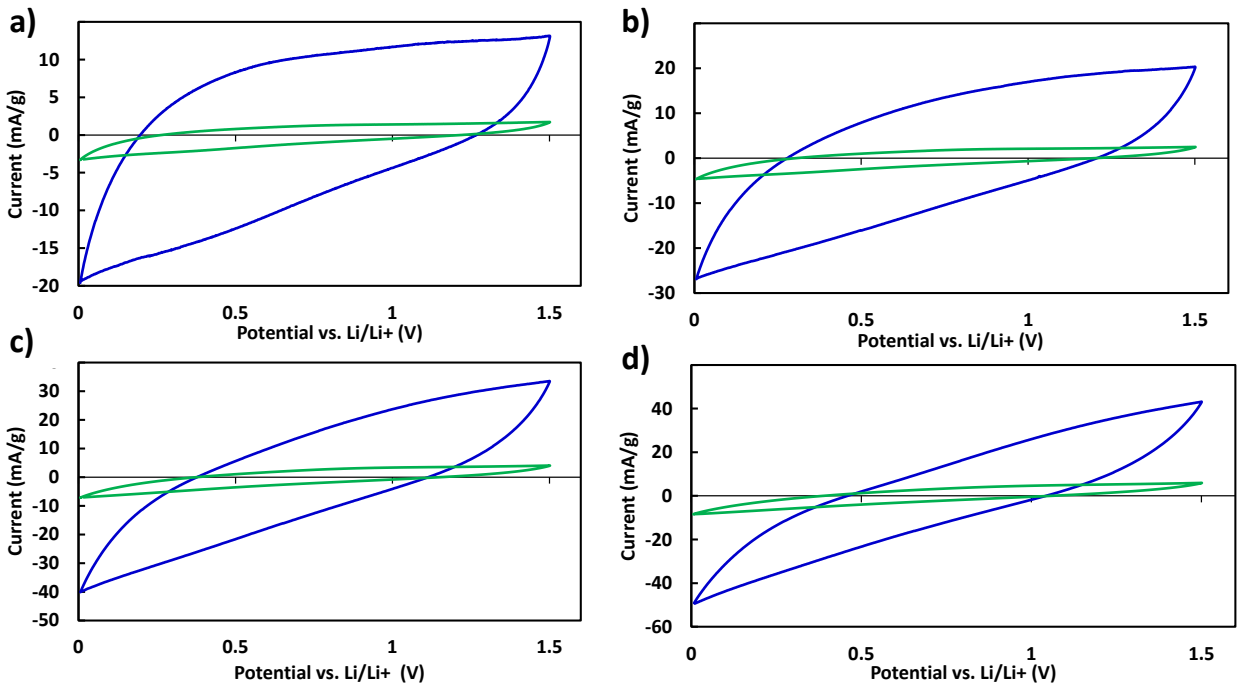

Figure 4. 13. CV graphs of just PVA/Large GNR (No silicon nanoparticles) fibers with PAA coating (green) and AlxOy (blue) at a) 10 b) 20 c) 50 and d)100 mV/s

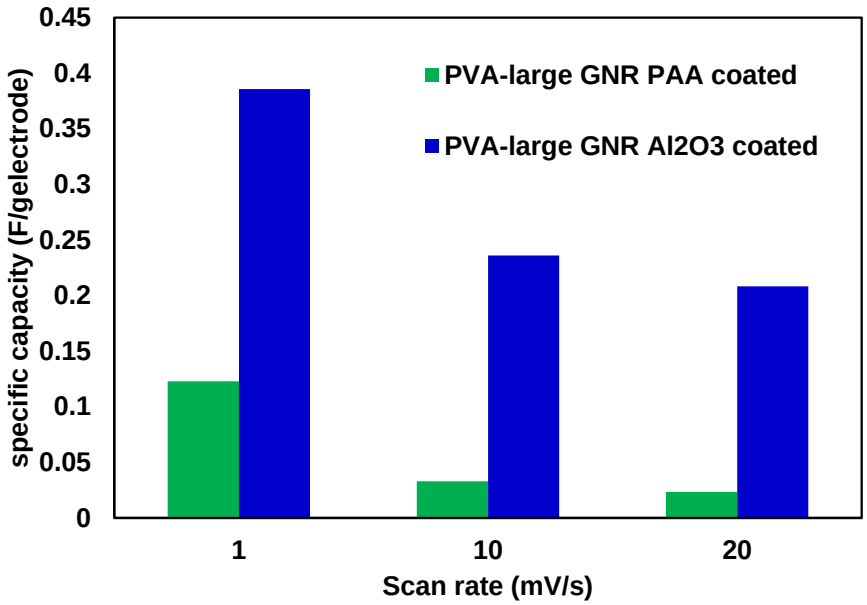

Figure 4. 14. Calculated specific capacity from CV of PVA/Large GNR fibers coated with PAA and ceramic coating at various scan rates

To further investigate the effect of coating on the mobility and diffusion of lithium ions inside the system, galvanostatic intermittent titration technique (GITT) was conducted on the electrodes. Figure 4.15a depicts the transient voltage profile of the Al_xO_y coated electrode, and Figure 4.15b illustrates a typical voltage variation during the current pulse and wait time. Based on GITT results effective diffusion of lithium ions were calculated with increasing lithiation for both ceramic and PAA coated electrodes following work of Weppner[29] *et al*. Figure 4.16 indicates that effective diffusion for both systems follow the same general trend, which has also been observed in other literature[33]. Underlying nanofiber structure, that provides short diffusion length for the lithium ions, is instrumental in having a high effective diffusion through the system. However, it can be observed that after the first current step diffusion in the ceramic coated electrode is almost one order of magnitude higher than the PAA coated counterpart at the low lithiation limit. This is where the lithium ions just go through the coating and start to alloy in the material. After the initial short couple of current steps, the diffusion coefficients of these two systems are very closely matching each other during the intermediate lithiation points. At very high lithiation, last three points are almost identical for both system, and that is when the ions have already penetrated through the bulk of the system and are diffusing completely into the silicon nanoparticles. Since we are using the same silicon nanoparticles in both systems, the diffusion calculated for the final lithiation points where diffusion is only happening through the nanoparticles match each other.

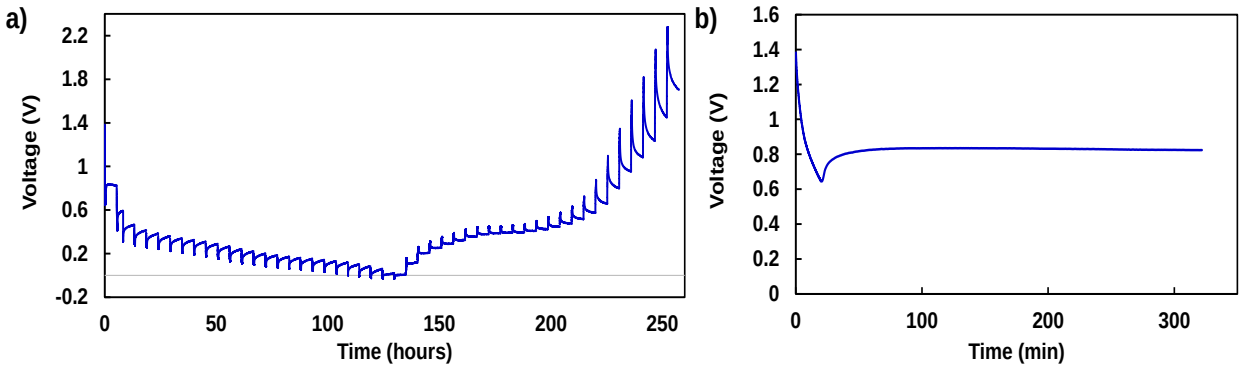

Figure 4. 15. a) Transient voltage profile of the PVA/Si/large GNR with ceramic coating with current pulse of 20 minutes and rest time of 5 hours b) A typical voltage profile in each individual step

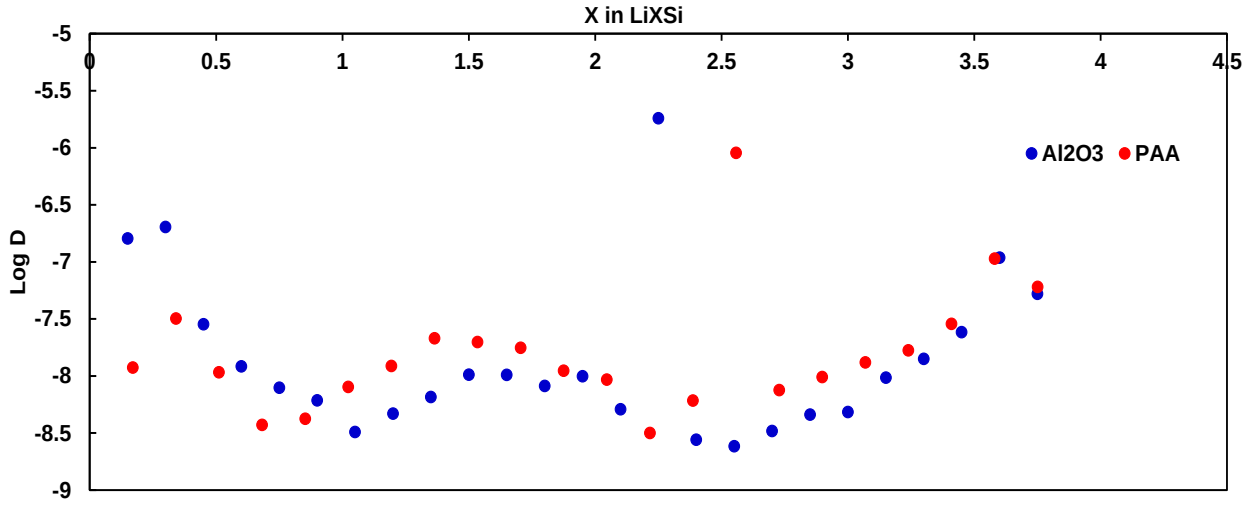

Figure 4. 16. Diffusion coefficient vs. amount of silicon alloyed in the composite for Al2O3 and PAA coated electrodes calculated from GITT profiles

4.4. Conclusion

In this work, we fabricated nanofibers packed with silicon nanoparticles and graphene nanoribbons for use as anode of lithium ion batteries. These nanofibers were deposited on cupper current collector directly using a water-based electrospinning system, therefore no additional conductive carbon was added to the system. To ensure the adhesion of these fibers to the current collector a binder is needed. This work explores a common binder for silicon-based anodes PAA and a metal oxide precursor solution that turns into aluminum oxide upon heat treatment. This aluminum oxide coating consistently resulted in higher performance of the nanofibers both in terms of capacity and retention. This coating especially proved to be effective at higher current rates. The enhancement of capacity retention is attributed to the better capability of this metal oxide coating to bind the nanofibers on the current collector compared to a more traditional binder such as PAA. Cyclic voltammetry on the fibers with aluminum oxide coating indicated an increase in the double layer capacity which is probably the main reason why the fibers have such an impressive performance at rates of 5C and 10C. Galvanostatic titration technique revealed that the ceramic coating helps in enhancement of effective diffusion in the system, which again contributes to the electrochemical performance at high rates. Overall, filling the void spaces in between the nanofibers with a material that can both act as the binder and enhance contribute to the high-rate performance of the electrode via double layer capacity and promoted diffusion, proved to be a practical strategy in designing better electrodes.

RFERENCES

[1] C.-H. Jung, J.-H. Choi, W.-S. Kim, and S.-H. Hong, “Nanopore-Embedded Graphitic Carbon Shell on Silicon Anode for High Performance Lithium Ion Battery,” *J. Mater. Chem. A*, Mar. 2018.

[2] B. Campbell *et al.*, “Carbon-Coated, Diatomite-Derived Nanosilicon as a High Rate Capable Li-ion Battery Anode,” *Sci. Rep.*, vol. 6, p. 33050, Oct. 2016.

[3] X. Han *et al.*, “Carbon-coated Si micrometer particles binding to reduced graphene oxide for a stable high-capacity lithium-ion battery anode,” *J. Mater. Chem. A*, vol. 4, no. 45, pp. 17757–17763, 2016.

[4] D. A. Agyeman, K. Song, G.-H. Lee, M. Park, and Y.-M. Kang, “Carbon-Coated Si Nanoparticles Anchored between Reduced Graphene Oxides as an Extremely Reversible Anode Material for High Energy-Density Li-Ion Battery,” *Adv. Energy Mater.*, p. n/a-n/a, Jul. 2016.

[5] C. Li *et al.*, “Cathode materials modified by surface coating for lithium ion batteries,” *Electrochimica Acta*, vol. 51, no. 19, pp. 3872–3883, 2006.

[6] Y. J. Kim, J. Cho, T.-J. Kim, and B. Park, “Suppression of Cobalt Dissolution from the LiCoO2 Cathodes with Various Metal-Oxide Coatings,” *J. Electrochem. Soc.*, vol. 150, no. 12, pp. A1723–A1725, Dec. 2003.

[7] Z. Chen Qin, Yan, Amine, Khalil, Sun, Y. K., “Role of surface coating on cathode materials for lithium-ion batteries,” *J. Mater. Chem.*, vol. 20, no. 36, pp. 7606–7612, 2010.

[8] X. Zhang *et al.*, “Structural and Electrochemical Study of Al2O3 and TiO2 Coated Li1.2Ni0.13Mn0.54Co0.13O2 Cathode Material Using ALD,” *Adv. Energy Mater.*, vol. 3, no. 10, pp. 1299–1307, Oct. 2013.

[9] J. Cho Kim, Young-Woon, Kim, Byoungsoo, Lee, Joon-Gon, Park, Byungwoo, "A Breakthrough in the Safety of Lithium Secondary Batteries by Coating the Cathode Material with $AlPO_4$ Nanoparticles," *ANGE Angew. Chem.*, vol. 115, no. 14, pp. 1656–1659, 2003.

[10] F. Ding *et al.*, "Dendrite-Free Lithium Deposition via Self-Healing Electrostatic Shield Mechanism," *J. Am. Chem. Soc.*, vol. 135, no. 11, pp. 4450–4456, Mar. 2013.

[11] X. Xiao, P. Lu, and D. Ahn, "Ultrathin Multifunctional Oxide Coatings for Lithium Ion Batteries," *Adv. Mater.*, vol. 23, no. 34, pp. 3911–3915, Sep. 2011.

[12] E. M. Lotfabad *et al.*, "ALD TiO2 coated silicon nanowires for lithium ion battery anodes with enhanced cycling stability and coulombic efficiency," *Phys. Chem. Chem. Phys.*, vol. 15, no. 32, pp. 13646–13657, Jul. 2013.

[13] H. T. Nguyen, M. R. Zamfir, L. D. Duong, Y. H. Lee, P. Bondavalli, and D. Pribat, "Alumina-coated silicon-based nanowire arrays for high quality Li-ion battery anodes," *J. Mater. Chem.*, vol. 22, no. 47, p. 24618, 2012.

[14] X. Ding *et al.*, "Enhanced Electrochemical Performance Promoted by Monolayer Graphene and Void Space in Silicon Composite Anode Materials," *Nano Energy*.

[15] L. Oakes *et al.*, "Surface engineered porous silicon for stable, high performance electrochemical supercapacitors," *Sci. Rep.*, vol. 3, Oct. 2013.

[16] E. C. Self, E. C. McRen, and P. N. Pintauro, "High Performance Particle/Polymer Nanofiber Anodes for Li-ion Batteries using Electrospinning," *ChemSusChem*, vol. 9, no. 2, pp. 208–215, Jan. 2016.

[17] C. Li *et al.*, "Towards flexible binderless anodes: silicon-carbon fabrics via double nozzle electrospinning," *Chem Commun*, 2016.

[18] J. Wu and J. L. Coffer, “Emissive Erbium-Doped Silicon and Germanium Oxide Nanofibers Derived from an Electrospinning Process,” *Chem. Mater.*, vol. 19, no. 25, pp. 6266–6276, Dec. 2007.

[19] L. Qiu *et al.*, “Study on effects of carboxymethyl cellulose lithium (CMC-Li) synthesis and electrospinning on high-rate lithium ion batteries,” *Cellulose*, vol. 21, no. 1, pp. 615–626, Feb. 2014.

[20] C. Shao, N. Yu, Y. Liu, and R. Mu, “Preparation of LiCoO2 nanofibers by electrospinning technique,” *J. Phys. Chem. Solids*, vol. 67, no. 7, pp. 1423–1426, Jul. 2006.

[21] J. W. Min Yim, Chul Jin, Im, Won Bin, “Preparation and electrochemical characterization of flower-like Li1.2Ni0.17Co0.17Mn0.5O2 microstructure cathode by electrospinning,” *Ceram. Int. Ceram. Int.*, vol. 40, no. 1, pp. 2029–2034, 2014.

[22] C. Yang, Z. Jia, Z. Guan, and L. Wang, “Polyvinylidene fluoride membrane by novel electrospinning system for separator of Li-ion batteries,” *J. Power Sources*, vol. 189, no. 1, pp. 716–720, Apr. 2009.

[23] Y.-E. Miao, G.-N. Zhu, H. Hou, Y.-Y. Xia, and T. Liu, “Electrospun polyimide nanofiber-based nonwoven separators for lithium-ion batteries,” *J. Power Sources*, vol. 226, pp. 82–86, Mar. 2013.

[24] Y. S. Kim *et al.*, “The critical contribution of unzipped graphene nanoribbons to scalable silicon–carbon fiber anodes in rechargeable Li-ion batteries,” *Nano Energy*, vol. 16, pp. 446–457, Sep. 2015.

[25] G. Shoorideh *et al.*, “Harvesting Interconductivity and Intraconductivity of Graphene Nanoribbons for a Directly Deposited, High-Rate Silicon-Based Anode for Li-Ion Batteries,” *ACS Appl. Energy Mater.*, vol. 1, no. 3, pp. 1106–1115, Mar. 2018.

[26] G. Shoorideh, Y. S. Kim, and Y. L. Joo, “Facile, Water-Based, Direct–Deposit Fabrication of Hybrid Silicon Assemblies for Scalable and High–Performance Li–ion Battery Anodes,” *Electrochimica Acta*, vol. 222, pp. 946–955, Dec. 2016.

[27] A. Yuzaki and A. Kishimoto, “Effects of alumina dispersion on ionic conduction of toughened zirconia base composite,” *Solid State Ion.*, vol. 116, no. 1–2, pp. 47–51, Jan. 1999.

[28] W. C. West *et al.*, “Electrochemical Behavior of Layered Solid Solution Li2MnO3−LiMO2 (M = Ni, Mn, Co) Li-Ion Cathodes with and without Alumina Coatings,” *J. Electrochem. Soc.*, vol. 158, no. 8, pp. A883–A889, Aug. 2011.

[29] W. Weppner and R. A. Huggins, “Determination of the Kinetic Parameters of Mixed-Conducting Electrodes and Application to the System Li3Sb,” *J. Electrochem. Soc.*, vol. 124, no. 10, pp. 1569–1578, Oct. 1977.

[30] J. Duay, K. W. Schroder, S. Murugesan, and K. J. Stevenson, “Monitoring Volumetric Changes in Silicon Thin Film Anodes through in situ Optical Diffraction Microscopy,” *ACS Appl. Mater. Interfaces*, Jun. 2016.

[31] S. Ohara, J. Suzuki, K. Sekine, and T. Takamura, “A thin film silicon anode for Li-ion batteries having a very large specific capacity and long cycle life,” *J. Power Sources*, vol. 136, no. 2, pp. 303–306, Oct. 2004.

[32] V. A. Sethuraman, M. J. Chon, M. Shimshak, V. Srinivasan, and P. R. Guduru, “In situ measurements of stress evolution in silicon thin films during electrochemical lithiation and delithiation,” *J. Power Sources*, vol. 195, no. 15, pp. 5062–5066, Aug. 2010.

[33] N. Ding *et al.*, “Determination of the diffusion coefficient of lithium ions in nano-Si,” *Solid State Ion.*, vol. 180, no. 2, pp. 222–225, Mar. 2009.

CHAPTER FIVE

DIRECTLY ELECTROSPRAYED SILICON-GRAPHENE NANOCOMPOSITES FOR HIGH-RATE LITHIUM ION BATTERY ANODES

5.1. Introduction

Energy is one of the biggest concerns of modern humans. With the wave of modernization and digitalization of every aspect of current-day societies, the need for reliable energy sources is even more present. Energy storage has played a pivotal role in realization of many technologies; however, batteries still fall short in terms of longevity and capacity when used in powering portable electronics and electric vehicles. Li-ion batteries have been the primary chemistry for more than two decades. They combines a layered oxide cathode with graphite anode and a polymeric seperator to store Li-ions. However, there is need for material with higher capacity to reduce the size and weight of the battery especially as devices become sleeker. In the recent years, silicon has been investigated to replace graphite, because of its large theoretical capacity of 4200 mAh/g for Li ion storage at room temperature. At the same time the lithiation voltage of silicon is very close to lithium metal, making it a perfect candidate to be used as the anode. However, silicon's large capacity comes at the expense of 300% volume expansion upon lithiation[1], [2], which results in an unstable solid electrolyte interface (SEI). This massive enlargement also fatigues the material and over multiple cycles cracking and pulverization[1], [3], [4] electrically isolate the active material and bring about fast capacity fading. For this reason, alleviation of volume expansion and creation of a stable SEI is crucial to have a good capacity retention.

Graphite is known to form a stable SEI and have a modest expansion of about 10% upon lithiation, therefore, compositing silicon and carbon materials is invaluable in enhancing the long time cycling of silicon-based anodes. In addition, carbon makes up for the poor electrical

conductivity of silicon, which is vital for collection and streaming of electrons towards the current collector and the outside circuit. Among the carbon family, graphene has incurred a lot of attention from the research community because of its high conductivity, strength and flexibility and ability to lithiate on the both side of the basal plane which results in a higher capacity[5] for charge storage compared to graphite. Graphene based materials have shown promise in both supercapacitors[6], [7] and for lithium [5],[8],[9] and sodium[10] energy storage devices. Also, making composites of graphene or reduced graphene-oxide and a material with high storage capacity such as metal-oxide particles[11], [12] or doping graphene with heteroatoms[13], [14] resulted in a new group of materials with high capacity and high conductivity for energy storage application. Therefore, creating composites of Silicon as the material with highest theoretical capacity and graphene is naturally a strategy that a myriad of research groups adopted[15]–[19]. Even though creating nanocomposites, using bottom up approaches such as CVD to create the desired morphology[20], [21] or techniques involving multiple lengthy steps[17], [22]–[24] can result in precise structure, they are not conducive to high through put manufacturing of battery materials.

In the recent work, we are demonstrating a facile one-step method for creating silicon/graphene composite. By utilizing a gas-controlled, water-based electrospraying process, a porous film of binder/silicon/graphene material can be directly sprayed on the copper current collector from an aqueous solution. Electrospraying has been used mostly for fabrication of anode materials[25]–[28]. In most of these attempts electrospraying was used to create the nanocomposite before additional heat treatments, addition of binder and conductive carbon and mixing into a slurry to be coated on the current collector. In this report, we are eliminating any additional heat treatment step and use of toxic solvents. The deposition of the nanocomposite porous film takes place at room temperature directly from the aqueous solution to the copper

current collector. Employing a graphene suspension in water, omits any need for thermal reduction of graphene oxide, therefore the binder can be added in the same step, which will help in the capacity retention of the composite. High extentional forces imposed on the droplet due to large electric field and conformal high-pressure air-flow while electrospraying ensure a uniform dispersion of the nanoparticles throughout the composite[29]. Fast evaporation of the solvent yields a dry film instantaneously. In this manner, active nanocomposite preparation and electrode fabrication are combined in the same step. Addition of the conformal air-flow in the sheath layer of the nozzle helps in better atomization, directing the spray, evaporation of the solvent and increasing the throughput. Flow rates used in the setup of this work are about one order of magnitude higher than other reports in the literature[26], [28]. The resulting electrodes can be assembled into batteries without any further processing, cutting the electrode preparation from tens of hours to less than ten minutes. In addition, the deposited films can be easily sprayed into different patterns with use of a physical mask.

5.2. Experimental section

Electrode fabrication and characterization: A solution of 60% silicon nanoparticles (US Research Nanomaterials), 20% polyacrylic acid (PAA 3MDa, Sigma) and 20% graphene (Gr, ACS material dispersion in water) was prepared. For this purpose, PAA was first dissolved in the water and SiNPs were added to the solution and stirred for 4 hours and bath sonicated for 30 minutes. In the next step graphene dispersion was mixed into the solution with the same steps of stirring and sonication. Immediately after sonication, the solution was loaded into a syringe, pumped at 0.05ml/min and sprayed onto a copper disk that was placed 20 cm away from tip of the nozzle. To achieve a good atomization, and optimum dispersion of nanoparticles throughout the system, 20 KV was used on the power supply in addition to having a high-pressure air (30 psi) in the sheath

layer of the nozzle. Resulting droplets make a uniform dry layer of the active material on the surface of the copper disk, which is ready to be assembled as anode of lithium ion cells. For the electrodes with GNRs the ratio of the silicon to binder to carbon was kept constant. Graphene nanoribbons were added to the solution in the desired amount after sonication of the solution of PAA and SiNPs, with an additional 30 minutes sonication step. Everything else was done the same way. The overall carbon content of the electrodes was kept to the 20% and this amount was split between Gr and GNRs by 2 and 18%, 5 and 15%, 10 and 10% and 5 and 15%, to investigate the role of GNR addition to the nanocomposite's electrochemical performance.

X-ray diffraction (XRD, Bruker-AXS) was performed with a copper X-ray source with wavelength of 1.54 Å on graphene powder obtained from drying the water dispersed material. The nanocomposite morphology was characterized with scanning electron microscopy (FESEM, Tescan Mira), and transmission electron microscopy (TEM, FEI T12 Spirit). Thermo-gravimetric analysis (10°C min^{-1} in air, TGA, TA Instruments Q500) was conducted on the composites to accurately measure PAA, Silicon, and Graphene or GNR content of the nanocomposite.

Electrochemical characterization: 2032 type half cells were made using the electrosprayed disks and stacking polypropylene-polyethylene (Celgard) as separator and Lithium disk as the counter electrode. A 1M $LiPF_6$ in ethylene carbonate, diethyl carbonate, dimethyl carbonate (4/4/2 v/v) plus 10wt% fluoroehtylene carbonate from Soulbrain was used as the electrolyte. All cells were assembled in an argon-filled glovebox. Galvanostatic charge/discharge was performed using an eight-channel battery analyzer (MTI) subjected to a voltage window of 0.015-1.5V vs. Li/Li^+. Cyclic Voltammetry (CV) and electrochemical impedance spectroscopy (EIS) measurements were conducted using an eight-channel potentiostat (Solartron). Impedance measurements were done with an amplitude of 10 mV in the frequency range of 0.1 to 100000 Hz. All capacities reported

in this study were normalized by the total mass of material (Si, Graphene/GNR, PAA) on the copper disk.

5.3. Result and discussion

Characterization of silicon-graphene nanocomposite: The air-controlled electrospraying process creates a dense layer of uniformly distributed nanomaterials on the copper surface. The electrodes are dry as soon as the droplets touch the copper disk surface and there is no need for surface modification of nanoparticles, since the high extensional forces applied to the solution during the electrospraying process[29] along with high-pressure air disperse the nanoparticles[30] and evaporate the solvent (water) instantly. Utilization of graphene sheets as the conductive agent means that the need for heat reduction of graphene oxide to graphene is eliminated, therefore polymer binder, can be added to the solution directly. Figure 5.1a and 5.1b show the top view of the SiNP/PAA/Gr composite, where silicon nanoparticles and graphene sheets are uniformly dispersed throughout the entire surface. The resulting electrode is porous and exhibits good adhesion to the surface of the current collector due to the polymeric binder. Cross-sectional electron micrograph of the electrode confirms the even distribution of the particles throughout the thickness of the electrode, with graphene sheets mostly oriented parallel to the disk as can be seen from Figure 5.2a. Silicon nanoparticles are uniformly distributed throughout the material and are placed in the pockets that are formed by the graphene sheets. The high-pressure air flow rate orients the Gr sheets in this fashion, which aids in the orderly stacking of the structure and creating a more compact layer. TEM image of the active material in Figure 5.2b clearly shows the contact and placement of silicon nanoparticles and graphene in the nanocomposite. These graphene sheets have about 4 layers with a d-spacing of 1.29 Å as calculated from the XRD 002 peak (2θ angle of 26.4º)

shown in Figure 5.3. Additionally, the 002 peak at 26.4º indicates that the graphene sheets are not oxidized[31], therefore there in no need for thermal reduction.

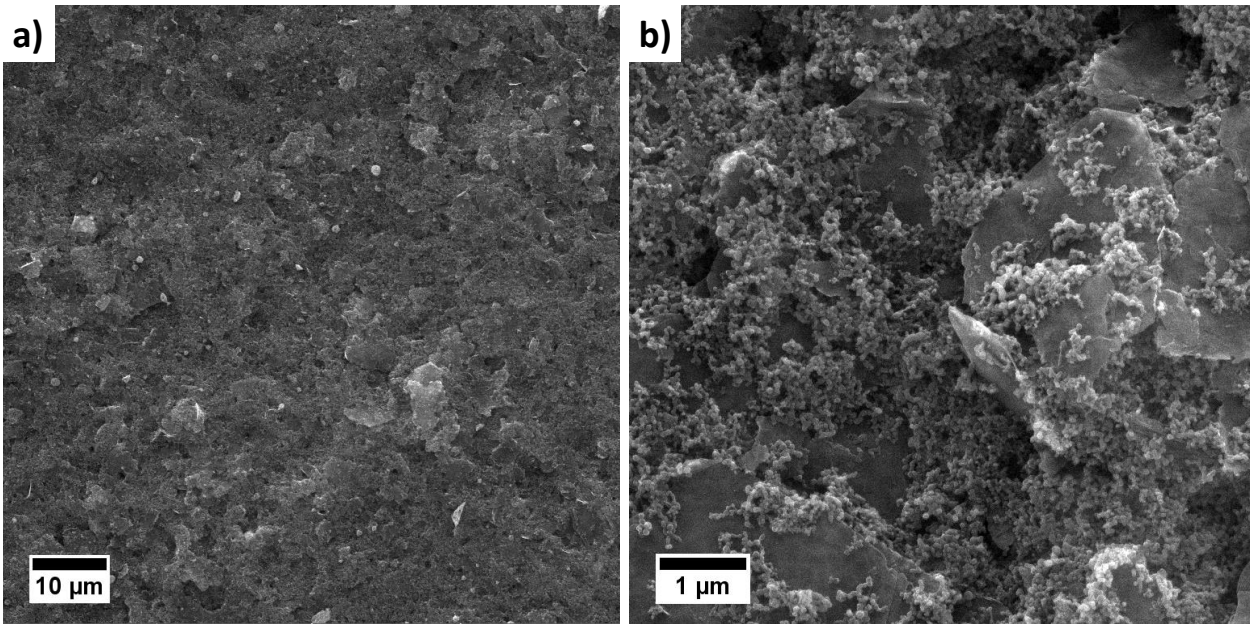

Figure 5. 1. Top view SEM images of the nanocomposite Si/PAA/Gr electrode at a) low magnification showing the uniformity of the surface b) high magnification revealing the placement of the particles

Also, the from the Raman data on the graphene sheets in Figure 5.4, we can see that the D/G band ratio is 0.17 which means that most of the hexagonal structure of the basal plane are intact and not in an oxidized state. The nanocomposite weight and thickness can precisely be controlled by the spray time and infusion rate. Disks with more than 3mg/cm^2 loading with excellent adhesion to the surface and no cracking can readily be fabricated since the deposited film is instantly dry. Cracking and yielding problems associated with solvent evaporation [32], [33] which are present in other coating methods are irrelevant when gas-controlled electrospray is used.

Electrochemical characterization of silicon-graphene nanocomposite: The electrodes fabricated by this technique were assembled in a half-cell configuration and galvanostatically charged and discharged for many cycles. Figure 5.5a illustrates the delithiation capacity of this material at a rate of C/3. At this rate the composite material exhibits 72% capacity retention after 300 cycles. It should be noted that the material went through 3 formation cycles at C/10 before increasing the current to C/3. The first cycle coulombic efficiency (ICE) of the cell is 84% despite utilization of silicon nanoparticles which results in lower ICE compared to microparticles and thin films. The large available surface area of nanoparticles means more solid electrolyte interface (SEI) upon contact with the electrolyte compared to microparticle and thin films. Therefore, more lithium ions are irreversibly consumed, which usually results in lower ICE for nanoparticles.

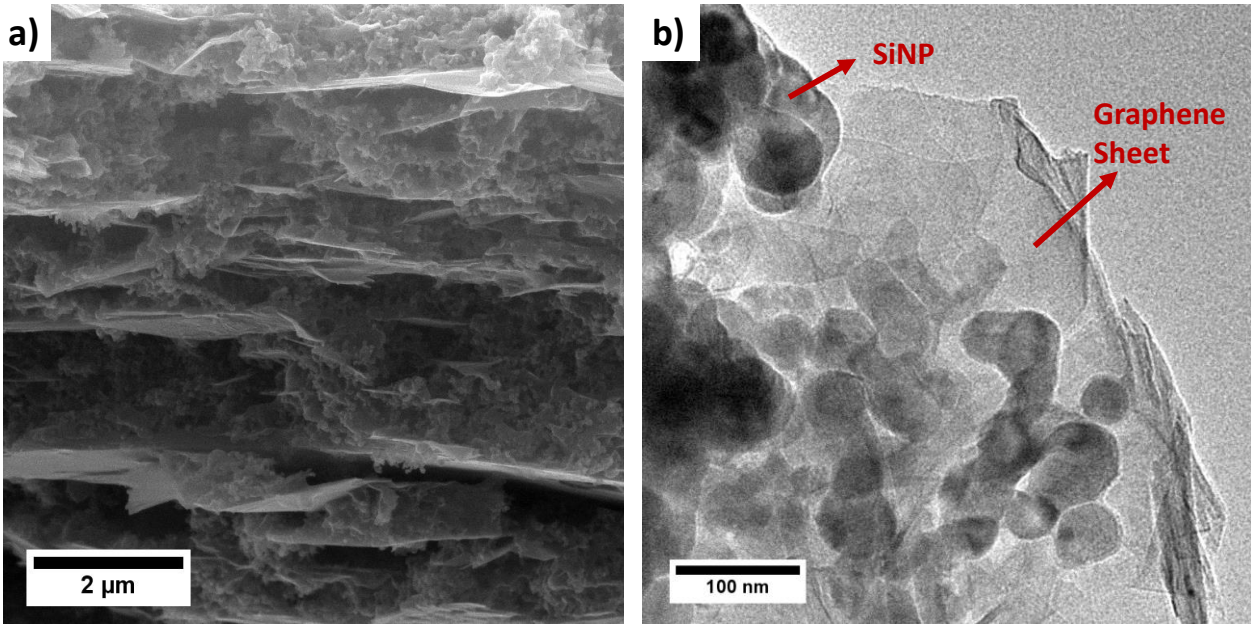

Figure 5. 2. a) Cross-sectional SEM view of the composite electrode b) Transmission electron micrograph of the active silicon nanoparticles and graphene

Figure 5.5b shows the capacity-voltage profiles of the material at C/3 cycled at a voltage window of 1.5-0.015 V vs Li/Li^+. There is no significant increase in the over potential which indicates that the impedance of the cell did not have a significant rise after 300 cycles. In order to investigate the effect of composite loading on the electrochemical performance of the nanocomposite, disks with higher loading (more than 3 times) were prepared. Figure 5.5c shows the long-term cycling at C/3 follow the same trend. The capacity starts at a slightly lower value of 1100 mAh/g which is something that has been observed in other literature as well. First cycle coulombic efficiency however, was maintained at 84% and the cell retained 79% of its capacity after 250 cycles. Therefore, the retention rate of the electrode does not change with loading of the active mass.

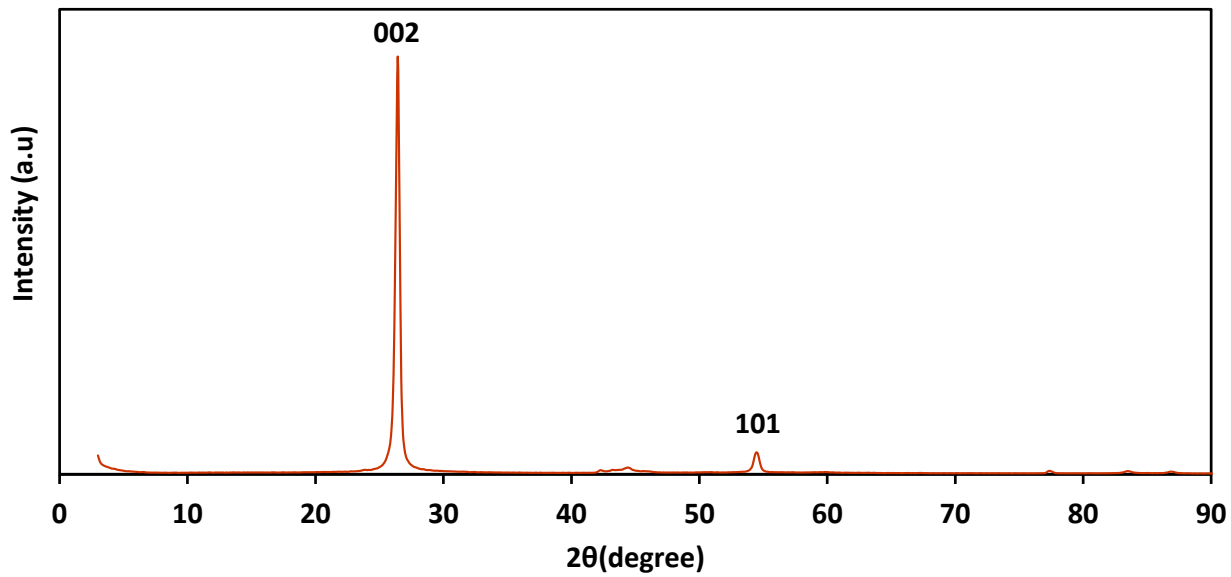

Figure 5. 3. X-ray diffraction of dried graphene dispersion

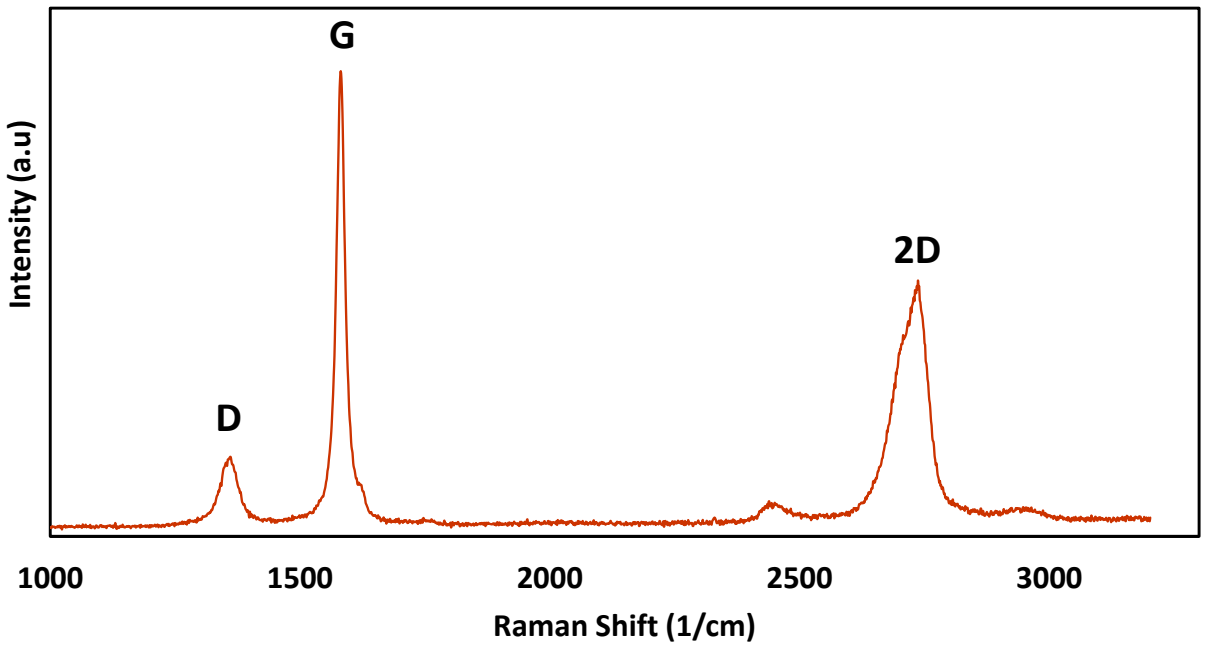

Figure 5. 4. Raman shift of the graphene sheets

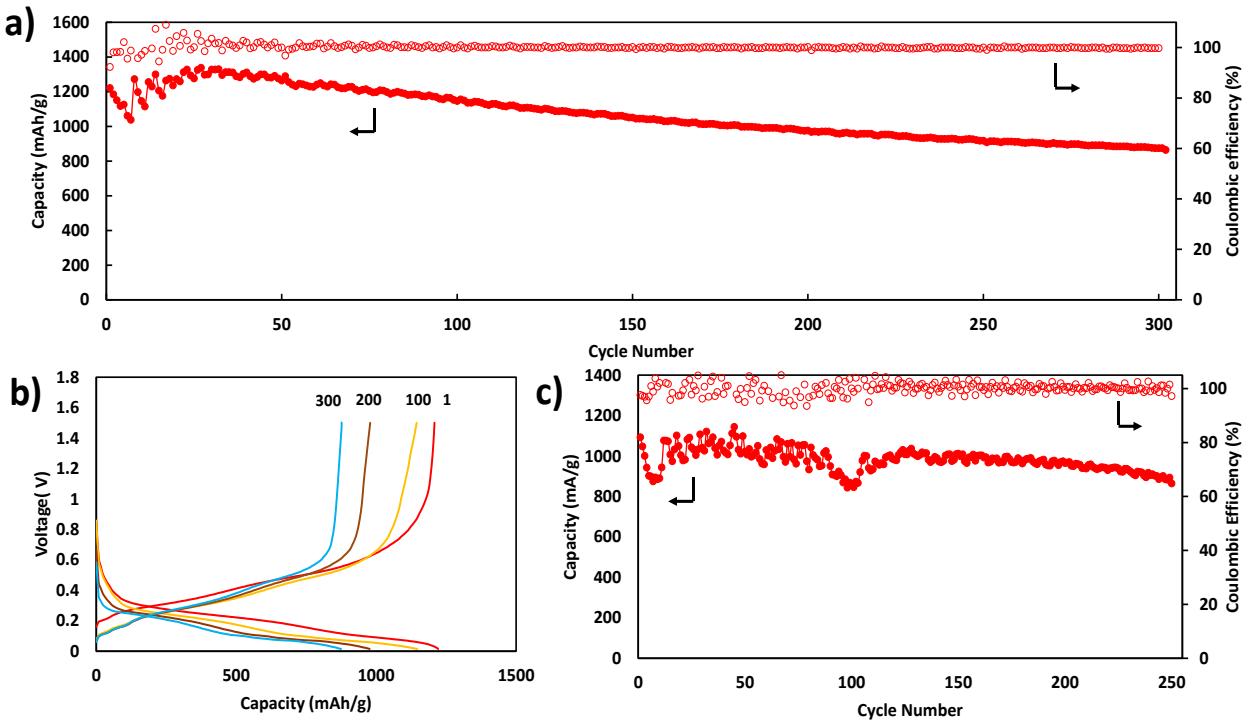

Figure 5. 5. a) Long term cycling of Si/PAA/Gr nanocomposite at a rate of C/3 for an anode disk with 0.3 mg/cm^2 loading. Closed and open symbols are capacity and coulombic efficiency respectively. b) Capacity-voltage profiles of the at 1st, 100th, 200th and 300th cycles at C/3. c) Long term cycling of Si/PAA/Gr nanocomposite at a rate of C/3 for an anode disk with 1 mg/cm^2 loading. Closed and open symbols are capacity and coulombic efficiency respectively.

Figure 5.6a is the rate capability data for the Si/PAA/Gr at rates indicated above each step. This nanocomposite exhibits 600 mAh/g at 5C and can recover its capacity when the current is decreased back to C/5. Figure 5.6b reveals the capacity-voltage profiles of this material at different rates. At 5C there is a considerable increase in the overpotential of the cell compared to C/10 which is noticeable from widening of the gap between the charge and discharge profile. This increase in the overpotential is most likely due to internal impedance of the nanocomposite and electrical isolation of some of the silicon nanoparticles. To investigate the changes in the morphology of the nanocomposite during cycling the cell in Figure 5.5a was opened after completing 300 cycles at

C/3. The scanning electron micrograph in Figure 5.7a indicate no major cracking or pulverization of the active material at the low magnifications. However, microcracks can be observed on the surface, especially at the droplet boundaries. The surface is covered in the SEI and silicon nanoparticles are swollen after cycling. From the SEM Figure 5.7b at higher magnification, the connectivity of the graphene and SiNPs does not reveal major changes, while everything is covered in an SEI layer that seems to form circular structure and is uneven in placement. One of the graphene sheets in Figure 5.7b is labeled in red for ease of examination and comparison to the pristine case.

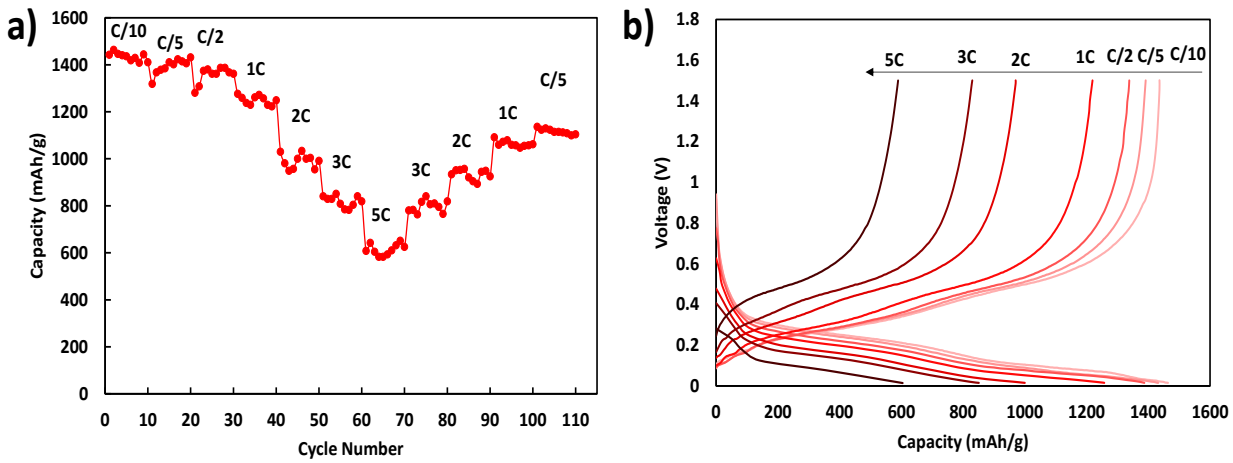

Figure 5. 6. a) Capacity of Si/PAA/Gr nanocomposite at the rates indicated above each step b) capacity-voltage profiles of the Si/PAA/Gr at different currents

Characterization of the silicon-graphene-graphene nanoribbons nanocomposite: The internal morphology of the Si/PAA/Gr nanocomposite relies on the graphene sheets to provide the conductivity needed to transfer the charges between the silicon nanoparticles and the current collector. Based on the difference in the size of the silicon nanoparticles which have an average

diameter of 70 nm and graphene sheets that can be tens of microns across, some of the silicon place in the pockets between the graphene sheets can be electronically isolated. We speculate that the rise in the overpotential of the silicon/graphene cell in Figure 5.6b can stem from this. Therefore, addition of a conducting agent in the size limits of SiNPs and Gr sheets can create a better conducting network in the nanocomposite. In our previous works[34], [35], it was found that Graphene nanoribbons (GNRs) are extremely effective for the enhancement of ionic and electronic conductivities. Also, graphene nanoribbons are about 100 nm in width and a couple of microns in length, making them the perfect size and geometry to connect SiNPs and the graphene sheets due to their ability of making a percolated network at low concentrations. For this reason, solutions with different amount of GNR addition were sprayed in the same manner as the Si/PAA/Gr nanocomposite.

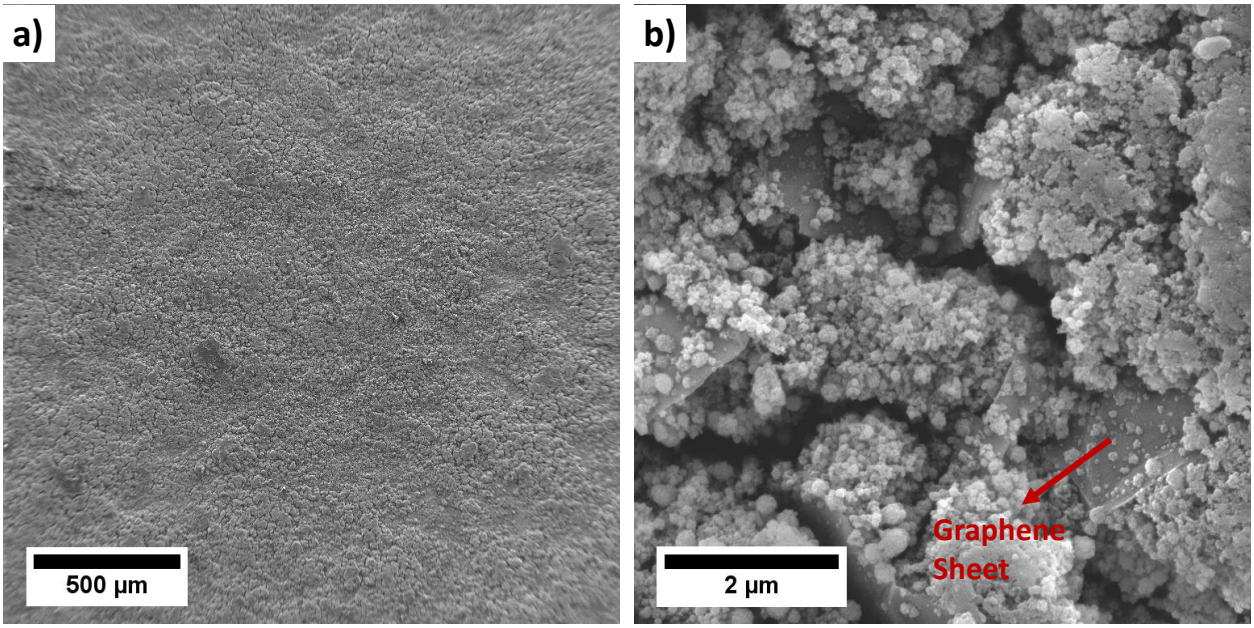

Figure 5. 7. a) Low magnification and b) high magnification SEM images of the Anode from the cell in Figure 5.5a after 300 cycles at C/3

SEM bank of Figure 5.8 illustrates the morphology of the directly sprayed composite with various GNR compositions. As the GNR content increases more of these 1D nanoparticles can be seen throughout the structure. Also, form the cross-sectional images GNRs are incorporated in the pockets that were made in between graphene sheets, so they can provide a conductive path connecting the silicon nanoparticles that are not directly in contact with any graphene. It should be noted that for these samples the total conductive carbon content was kept the same in solution preparation and only graphene was replaced by graphene nanoribbons to make these nanocomposites. Addition of the GNRs to the mix alters the rheology of the solution and the rate at which particles infuse out of the nozzle when pumped through the syringe. Transition electron micrographs of Figure 5.9 illustrate the placement and connectivity of SiNPs with Graphene nanoribbons and graphene sheets. Silicon nanoparticles interact with both graphene and graphene nanoribbons. Four-point conductivity measurements in Figure 5.10 reveals that with addition of the GNRs to the nanocomposite, resistivity of the film drops, for 2% and 5% GNR addition. However, in the case of 10% GNR addition, a large amount of GNR aggregation can be observed in the transition and scanning electron micrographs which limit their effectiveness as conductive pathways for electron transfer. It should be noted that all particles were used as received, and no surface functionalization was used in the fabrication of respective anode films.

TGA analysis was performed on the four different samples to determine the exact composition of each sample, which can be observed in Figure 5.11. All samples with GNR inclusion possess more silicon than the starting solution, which is due to the change in the particle-particle interaction and rheology of the solution. It is worth mentioning that all nanocomposites with GNR inclusions have lower resistivity than the one without any nanoribbons, despite having a higher silicon content.

This is in line with the expectation of graphene nanoribbons connecting the isolated silicon nanoparticles and improving the overall conductivity of the material.

Electrochemical characterization of silicon-graphene-graphene nanoribbon composites: To see this enhancement in action the four samples underwent rate capability measurements where the current was systematically increased form C/10 to 5C and held at the new current for 10 cycles. Figure 5.12a reports that 5 and 10% composite start more than 600 mAh/g higher than the composite without any GNRs. At 5C, 2 and 5% GNR nanocomposite have about 1100 mAh/g which is again 600 mAh/g than the one without any nanoribbons. However, at this 2, 3 and 5C these two nanocomposites are indistinguishable in performance. This could be due to agglomeration of the nanoribbons. If the nanoribbons aggregate, they will be less effective in electronically connect the silicon nanoparticles. The aggregation and less effective conductivity really signifies itself at higher rates, therefore 2 and 5% nanocomposites become indistinguishable at higher rates. From the capacity-voltage profiles in Figure 5.12b and 5.12c, it is apparent that these two composites have very similar electrochemical performance at higher rates. The 10% GNRs film quickly loses its ability to outperform the film without any nanoribbons, and at 5C these two nanocomposites have the same capacity. This is in line with observations of SEM, TEM and conductivity of this material, due to the issues with GNR dispersion as mentioned before. Figure 5.12c shows that when the current is increased the overpotential of 10% GNR sample exceeds that of other GNR including materials.

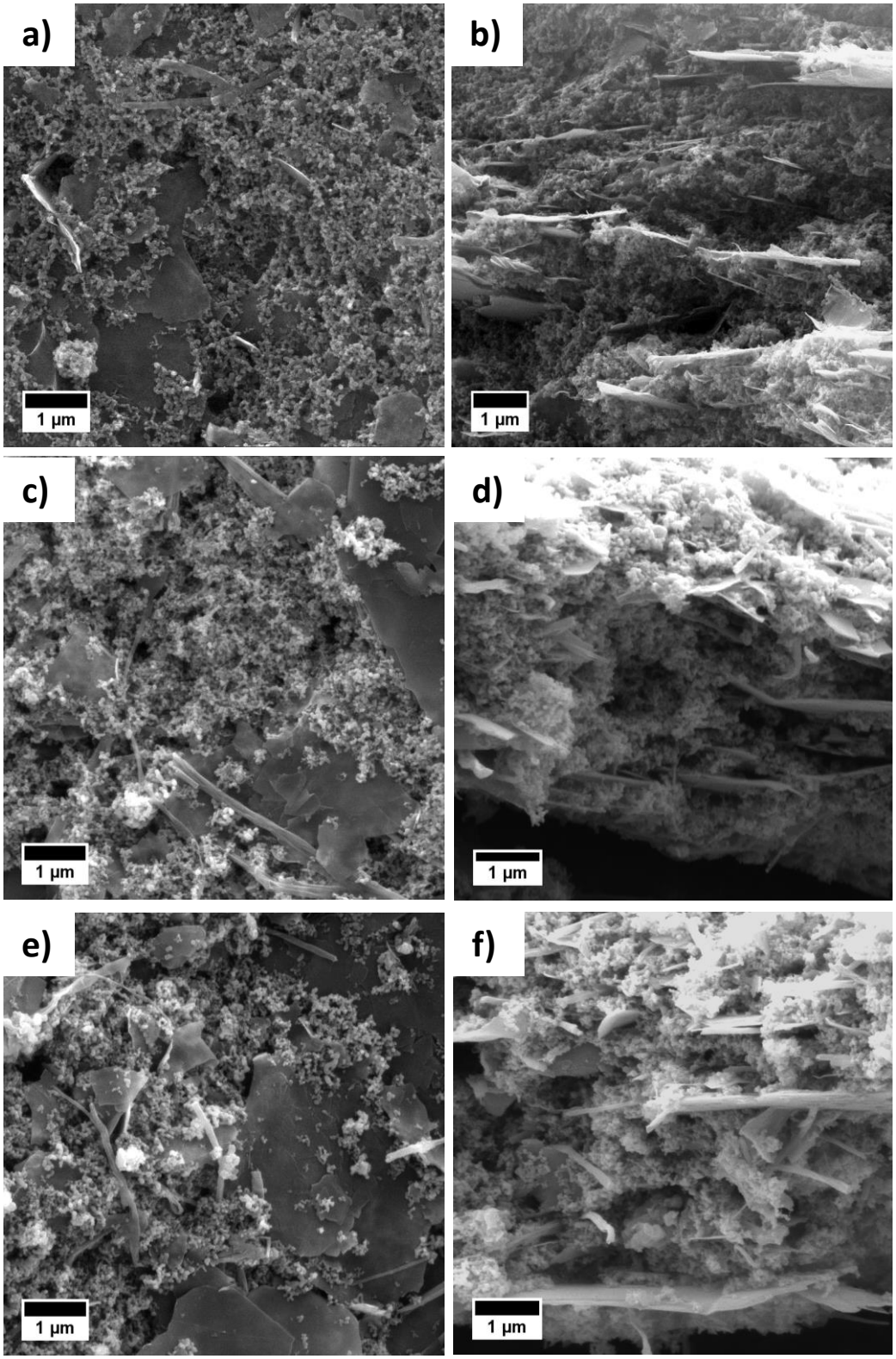

Figure 5. 8. SEM images of a) top view b) cross-sectional view of composite with 2% GNRs, c) top view d) cross-sectional view of composite with 5% GNRs, e) top view f) cross-sectional view of composite with 10% GNRs

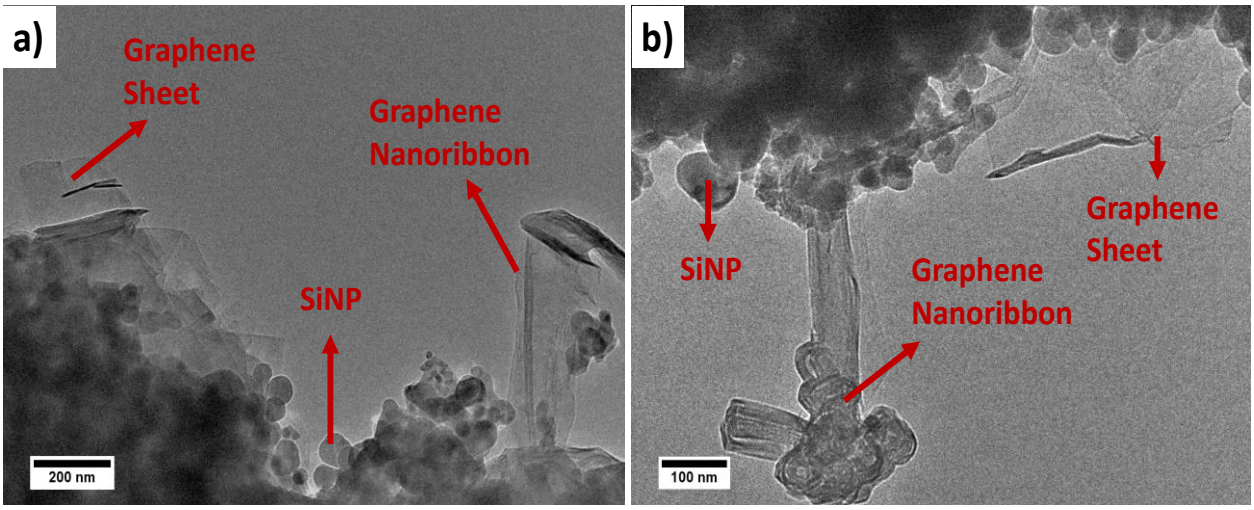

Figure 5. 9. a, b) TEM images of SiNP/PAA/Gr/GNR nanocomposites

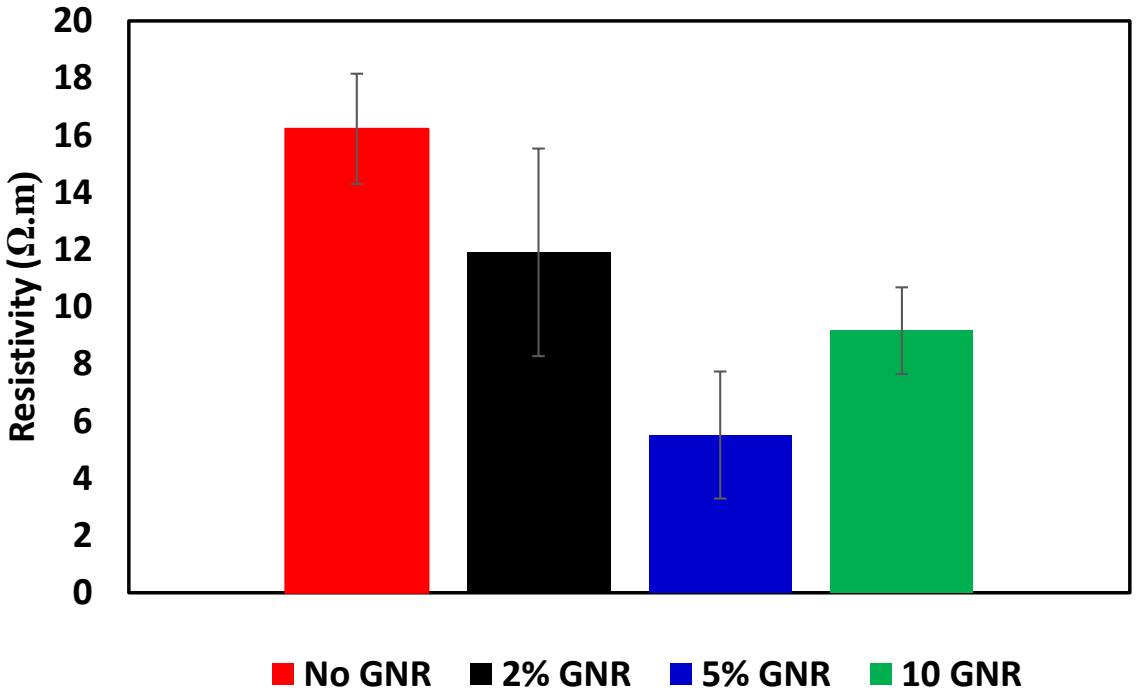

Figure 5. 10. Resistivity of nanocomposites with various GNR inclusion measured by a 4-point conductivity probe

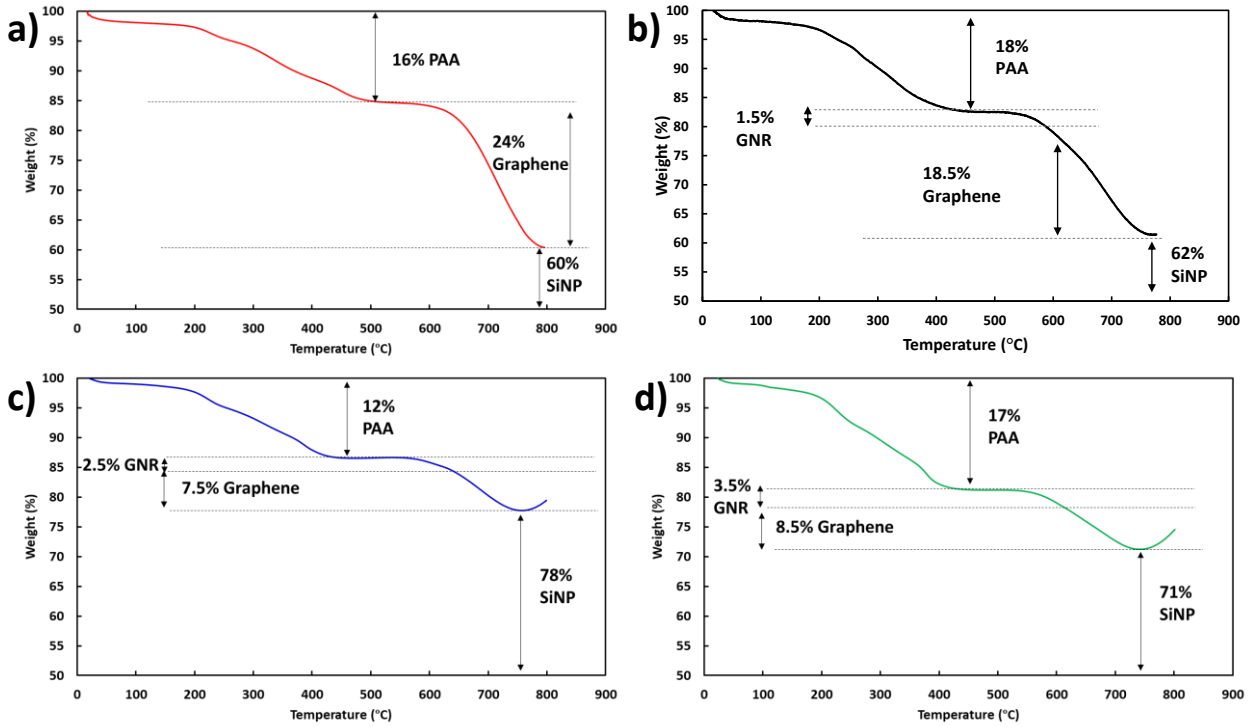

Figure 5. 11. Thermogravimetric analysis of nanocomposites with a) No GNRs b) 2% GNRs c) 5% GNRs d) 10% GNRs

To investigate more about the enhancement in electrochemical performance with addition of GNRs, long term galvanostatic cycling at 2C was performed. Figure 5.13a shows that 2% and 5% GNR composites have around 900 mAh/g after 350 cycles at 2C, while 10% GNR material could not maintain such a performance. 2% and 5% GNRs materials exhibit a sharp drop in the first 100 cycles, but after that they only have 0.07 % decay per cycle for the next 250 cycles.

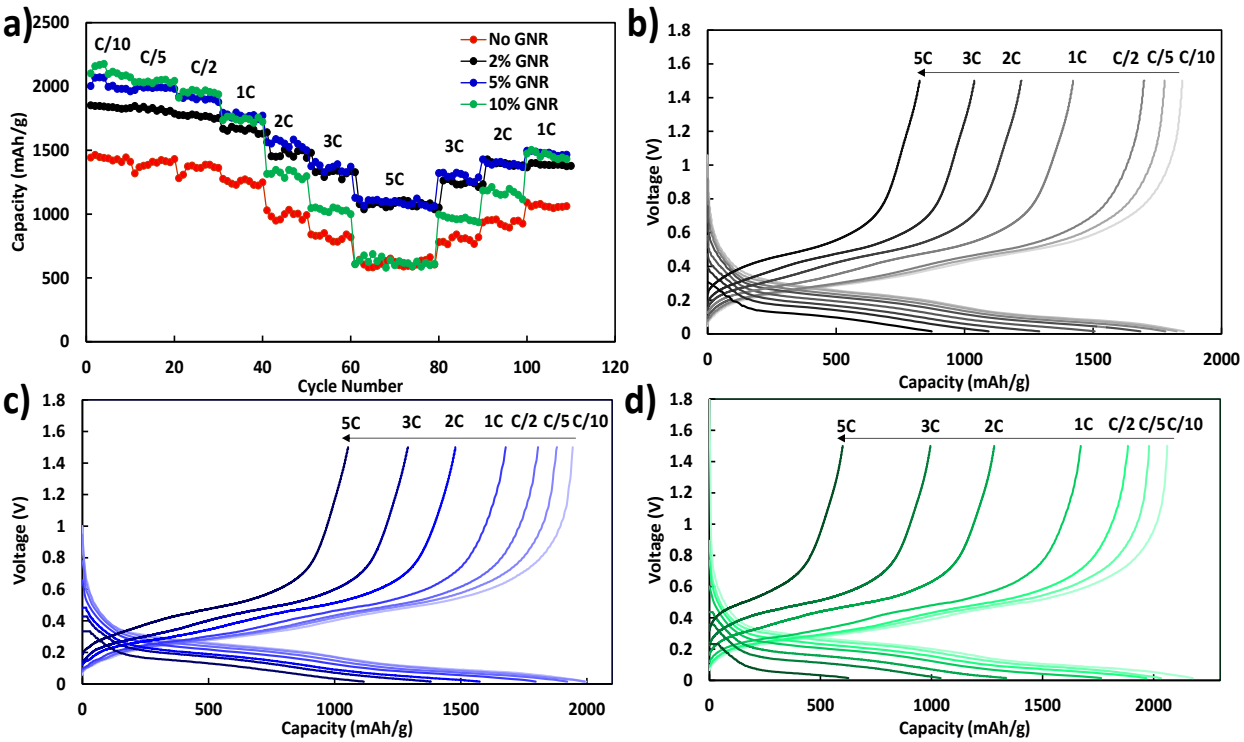

Figure 5. 12. a) rate capability of composites with no GNR in red, 2% GNR black, 5% GNR blue and 10% GNR green at rates indicated above each step. b) capacity-voltage profiles of the 2% GNR nanocomposite at different rates c) capacity-voltage profiles of the 5% GNR nanocomposite at different rates d) capacity-voltage profiles of the 10% GNR nanocomposite at different rates

At a much lower rate of C/3 in Figure 5.13, all the nanocomposites with GNR inclusion have higher capacities. Capacity retention of the 2%, 5% and 10% GNR films are 86%, 84% and 86% respectively after 50 cycles. Meanwhile the nanocomposite void of GNRs gained capacity in the first 50 cycles capacity at C/3, which can be explained by both lower silicon makeup to start with and lower utilization of Si, which will reduce the volume expansion effects compared to its GNR possessing counterparts. However, all three nanocomposites with GNRs have about 800-100 mAh/g more initial capacity than the nanocomposite without GNRs. The enhancement in the high rate electrochemical performance of the nanoribbon including films is not due to any morphological effects. Brunauer-Emmett-Teller (BET) analysis on the nanocomposite films

reveals that they all have a surface area of about 20 m^2/g of surface area with 5% GNR having a slightly higher 24 m^2/g. Moreover, the pore size distribution for all samples are practically the same as can be observed from Figure 5.14. Therefore addition of the GNRs to the nanocomposites does not significantly alter the morphology and porosity of the film. It merely electronically connects silicon nanoparticles to the rest of the system. Overall it is important to match the electrode for the specific application, at lower rate the nanocomposite with 10% GNR has a high capacity and acceptable long term performance, but this material does not perform as well at higher currents. On the other hand, if the application requires the electrode to have high performance at both high and low currents, then the nanocomposite with 5% GNR would be more appropriate.

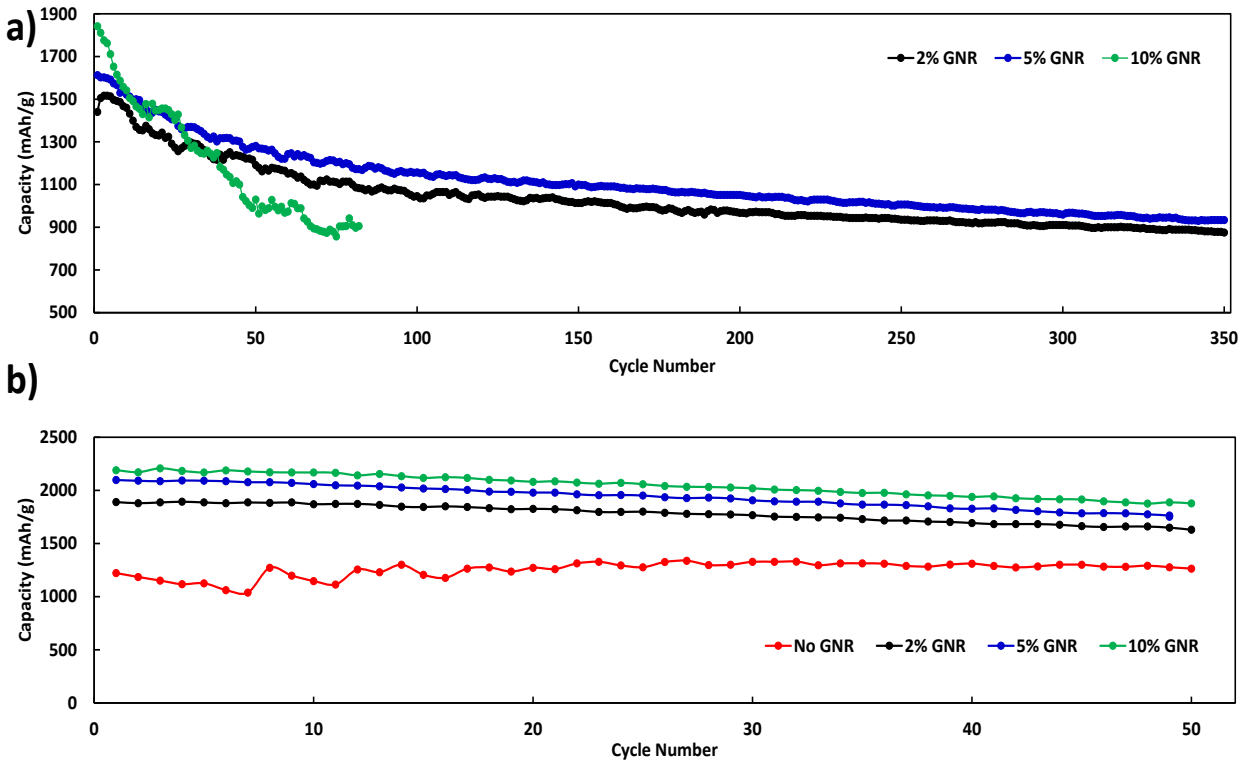

Figure 5. 13. a) Long term cyclic performance of nanocomposite with GNR inclusion at a rate of 2C. b) Cycle life performance of 4 nanocomposite films at C/3

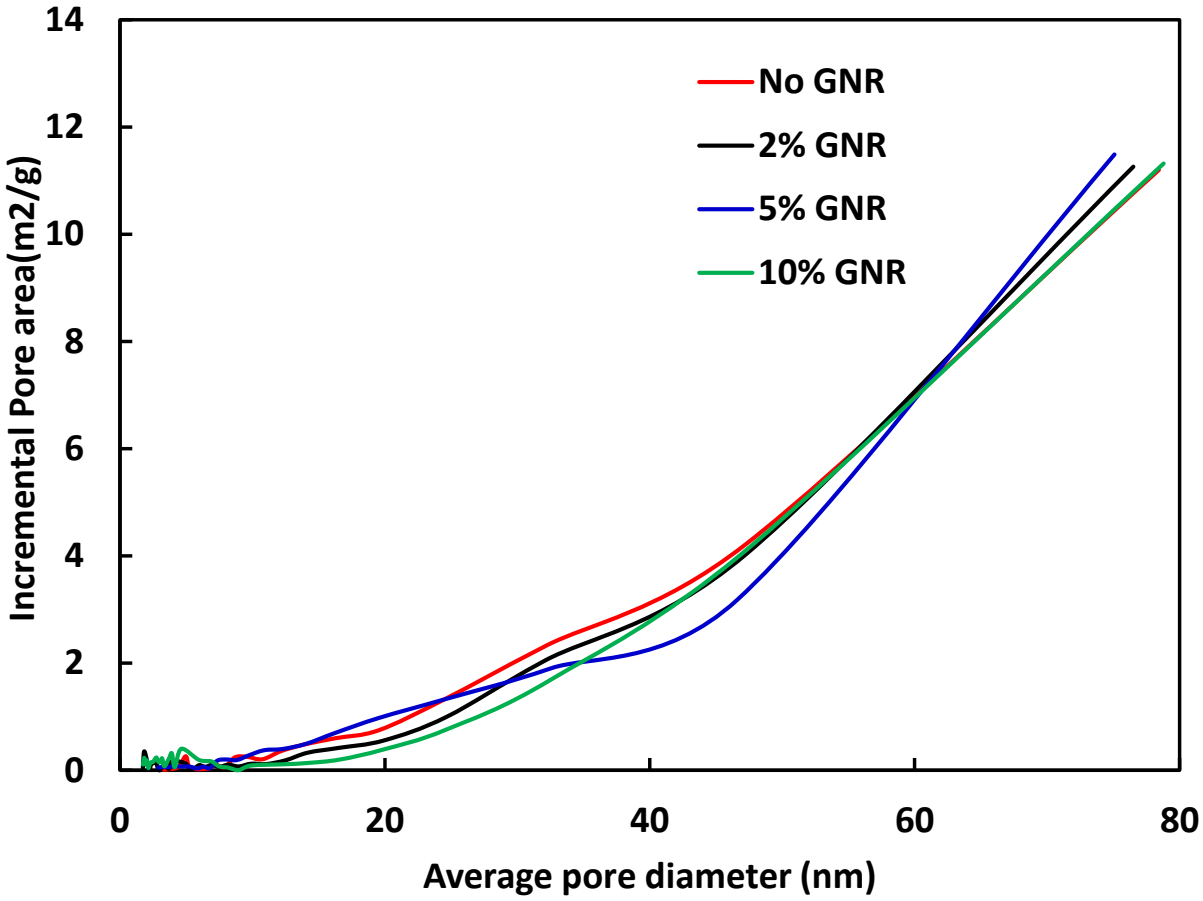

Figure 5. 14. BJH pore distribution for the nanocomposites

Post-mortem analysis of the nanocomposites: Change in the impedance of the cells were monitored before and after cycling for more insight into the electrochemical performance of the electrodes with graphene nanoribbons. Figure 5.15a is the Nyquist representation of the impedance data of the 2% GNR electrode. The cell starts with a 4Ω in bulk resistance and 47Ω surface charge transfer resistance. After rate capability the bulk resistance of the cell remained unchanged while charge transfer resistance drastically decreased to 6.5Ω, which is in line with other reports in the

literature for silicon. Silicon nanoparticle have a crystalline structure to begin with and during the first lithiation they undergo a phase transformation and become amorphous. Over many cycles the constant volume expansions and insertion and extraction of Li ions leaves these particles highly porous. The morphological changes in the silicon nanoparticles increases the active surface area which in turn decreases the charge transfer impedance. At the same time, the induce porosity enhances the diffusion of Li ions into the structure. Hence, the overall impedance of the cell decreases after cycling. This only holds true if the nanostructure of the material does not sustain major damages. Cracking, pulverization and isolation of the active material will result in rise of the overall impedance of the cell. The same happened in the cell with 5% GNR electrode in Figure 5.15b. Bulk resistance of the cell hovers around 4Ω even after rate capability test. However, the charge transfer resistance decreased to 7.5Ω from an original value of 42 Ω. The 10% GNR nanocomposite however does not follow the same trend. The cell in Figure 5.15c has a bulk resistance of 4Ω before formation cycles, but this value increased to 6Ω after cycling. The surface resistance went from 35 to 8Ω before formation and after rate capability test respectively, which agrees with the other two cells. At the same time, emergence of new charge transfer surfaces is evident from the Nyquist plot of 15c after cycling from the new depressed semi-circles that appeared in the impedance data.

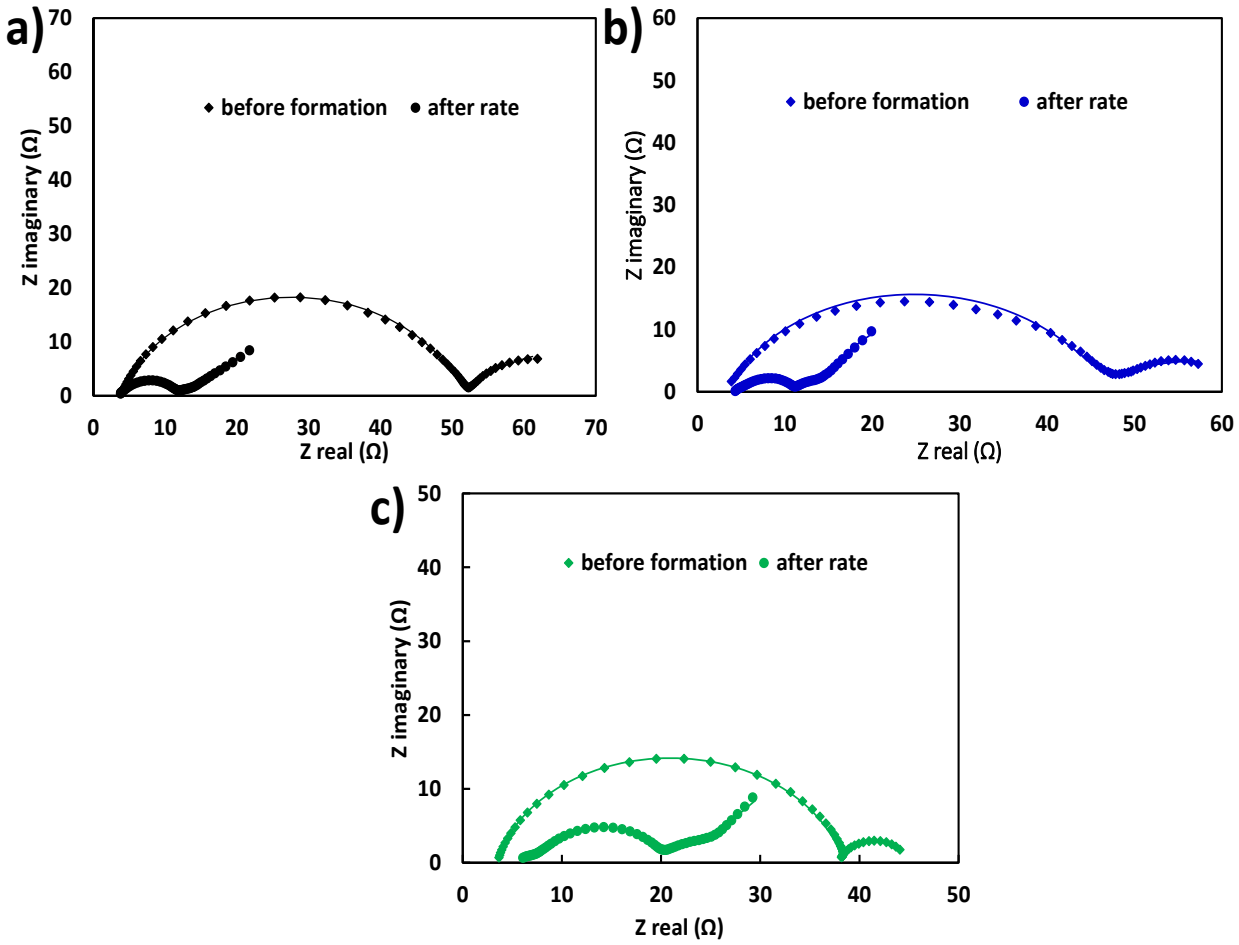

Figure 5. 15. Nyquist plots of the impedance data for a) 2% GNR b) 5% GNR c) 10% GNR nanocomposites. Diamond and round symbols denote before formation and after rate capability respectively. The lines through the data represent the fit to interpret data

To investigate the morphology changes brought about in the electrodes during cycling the cells were opened after their rate capability test, and the electrodes were washed with dimethyl carbonate to take away any residual salt remaining on the surface, then the electrodes were dried and were taken for SEM analysis. Figure 5.16 shows the state of the electrodes right after being disassembled. All four samples exhibited great adhesion to the surface without any cracks and pulverization of the active material as can be observed from the digital photographs.

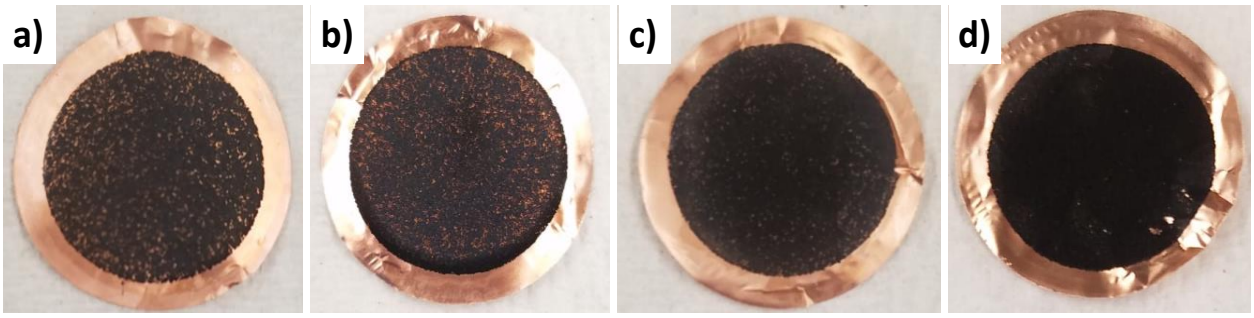

Figure 5. 16. Digital photographs of electrodes after rate capability test a) no GNR b) 2% GNR c) 5% GNR d) 10% GNR nanocomposites

To elucidate the reason behind difference in the performance of the four nanocomposites, a scanning electron microscope was utilized to look at the morphological changes of the electrode material after their rate capability test. Figure 5.17a exhibits the post mortem image of the nanocomposite without any GNRs. The surface of the electrode looked intact, but some microcracks could be observed especially at the electrospraying drop boundaries. The surface was covered in a somewhat uniform SEI layer and the underlying graphene/silicon nanocomposite could be observed at some places. The same held true for 2% and 5% GNR electrodes, where the silicon/graphene/graphene nanoribbon constituents can be observed, although just like the case with no GNRs, the SiNPs are swollen and the entire surface is covered in spherical SEI structure. It should be mentioned that based on the visual analysis of the electrodes, the 5% GNR electrode had the thinnest and most evenly distributed solid electrolyte interface. The composite with 10% GNR on the other hand, had larger microcracks throughout and a thick and densely packed SEI layer, hiding the underlying nano structure. This layer was uneven and from parts where the nano particles could be observed, aggregates of nanoribbons were noticeable. The large cracks and thick

SEI layer are in line with the impedance and long-term electrochemical performance of 10% GNR nanocomposite, which lacks behind all the other nanocomposites.

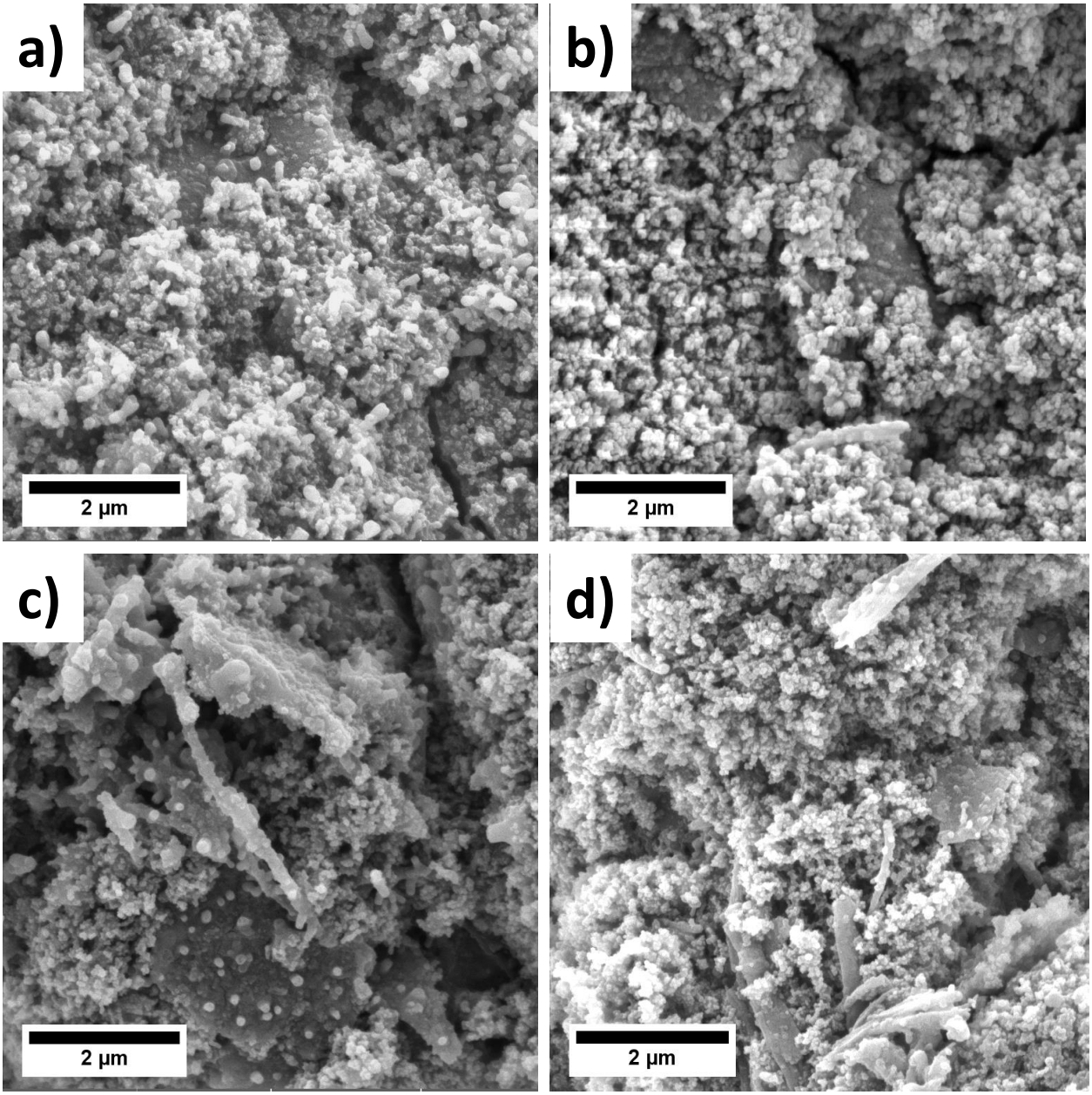

Figure 5. 17. Postmortem SEM analysis of the cells from Figure 5.12 after their rate capability test a) No GNR b)2% GNR c) 5% GNR d)10% GNR electrodes.

Since 5% GNR nanocomposite outperformed the other samples, it was paired with a nickel cobalt aluminum oxide cathode in a full cell configuration. The cell went through 2 formation cycles at a rate of C/25 and then the current was increased to C/2. Figure 5.18a shows the electrochemical performance of the cell at C/2. This cell retains 42% of its capacity at C/2 after 50 cycles. The coulombic efficiency of the cell hovers around 97-98% which explains the sharp capacity fading of the cell. Figure 5.18b shows the capacity-voltage profile of the cell at this rate. The anode to cathode ratio has to be optimized for better retention results. The first cycle coulombic efficiency of the electrode has to be taken into the consideration for balancing the negative and positive electrodes for optimal performance.

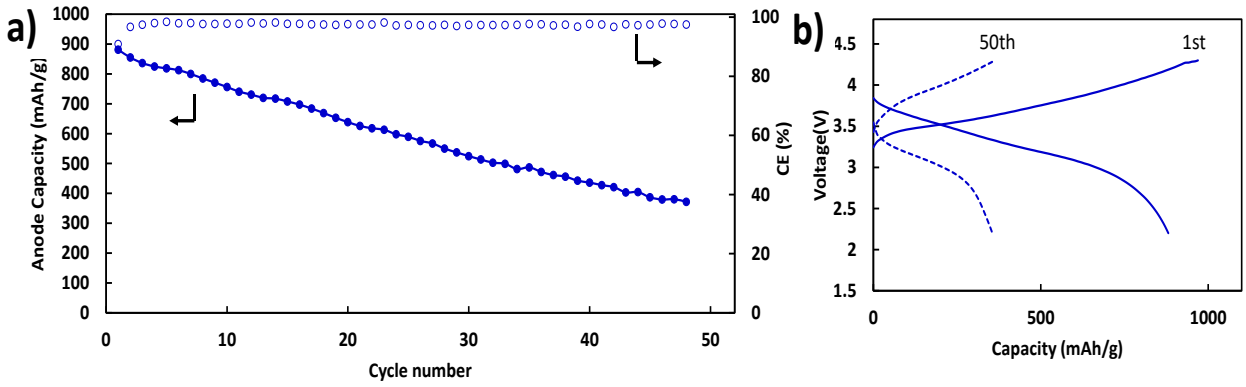

Figure 5. 18. a) Capacity vs cycle number of the full cell with 5% GNR anode and NCA cathode at C/2. Solid symbols denote Anode capacity and open circles represent coulombic capacity. b) capacity-voltage profiles of the full cell at 1st and 50th cycle

5.4. Conclusion

In summary, this study presents a facile and scalable manner of electrode fabrication that combines all the manufacturing steps in one. Utilizing this method eliminates toxic solvents, use of any surfactant and surface functionalization, need for thermal treatment and reduces electrode fabrication time from hours to minutes. The nanocomposite electrode films comprised of SiNPs/PAA/graphene were directly sprayed on the copper current collector with great adhesion to the surface and easily controllable thickness by controlling the spray time. The resulting nanocomposite exhibited uniform dispersion of nanoparticles with a porous nanostructure. Also, when tested as anode in lithium ion batteries, this composite revealed a great capacity retention at a rate of C/3 and excellent performance when subjected to systematic increase in the current. To improve the rate-capability performance of the material graphene nanoribbons were added to connect some of the electronically isolated silicon nanoparticles and improvement of ionic conductivity of the system. Graphene nanoribbons were added in different ratio and it was found that replacing 5% of the graphene with GNRs resulted in the best performance at high rates. This material could deliver 1100 mAh/g at 5C and recover its capacity when the current was decreased to C/5. Increasing nanoribbons concentration to 10% caused aggregation of nanoribbons and decline of the performance. Post mortem analysis indicates that 5% GNR sample had the least amount of microcracks and thinnest SEI layered formed on the surface after rate capability. The same material was paired with an NCA cathode, and the resulting full cell had 42% retention rate after 50 cycles. In order to improve the performance, more studies have to be done on the negative to positive electrode ratio to find the optimum balance.

REFERENCES

[1] X. H. Liu *et al.*, "Anisotropic Swelling and Fracture of Silicon Nanowires during Lithiation," *Nano Lett.*, vol. 11, no. 8, pp. 3312–3318, Aug. 2011.

[2] S. W. Lee, L. A. Berla, M. T. McDowell, W. D. Nix, and Y. Cui, "Reaction Front Evolution during Electrochemical Lithiation of Crystalline Silicon Nanopillars," *Isr. J. Chem.*, vol. 52, no. 11–12, pp. 1118–1123, Dec. 2012.

[3] S. Golmon, K. Maute, S.-H. Lee, and M. L. Dunn, "Stress generation in silicon particles during lithium insertion," *Appl. Phys. Lett.*, vol. 97, no. 3, p. 033111, Jul. 2010.

[4] R. Grantab and V. B. Shenoy, "Pressure-Gradient Dependent Diffusion and Crack Propagation in Lithiated Silicon Nanowires," *J. Electrochem. Soc.*, vol. 159, no. 5, pp. A584–A591, Jan. 2012.

[5] E. Yoo, J. Kim, E. Hosono, H. Zhou, T. Kudo, and I. Honma, "Large Reversible Li Storage of Graphene Nanosheet Families for Use in Rechargeable Lithium Ion Batteries," *Nano Lett.*, vol. 8, no. 8, pp. 2277–2282, Aug. 2008.

[6] C. Liu, Z. Yu, D. Neff, A. Zhamu, and B. Z. Jang, "Graphene-Based Supercapacitor with an Ultrahigh Energy Density," *Nano Lett.*, vol. 10, no. 12, pp. 4863–4868, Dec. 2010.

[7] X. Yang, C. Cheng, Y. Wang, L. Qiu, and D. Li, "Liquid-Mediated Dense Integration of Graphene Materials for Compact Capacitive Energy Storage," *Science*, vol. 341, no. 6145, pp. 534–537, Aug. 2013.

[8] N. Li, Z. Chen, W. Ren, F. Li, and H.-M. Cheng, "Flexible graphene-based lithium ion batteries with ultrafast charge and discharge rates," *Proc. Natl. Acad. Sci.*, vol. 109, no. 43, pp. 17360–17365, Oct. 2012.

[9] G. Wang, X. Shen, J. Yao, and J. Park, “Graphene nanosheets for enhanced lithium storage in lithium ion batteries,” *Carbon*, vol. 47, no. 8, pp. 2049–2053, Jul. 2009.

[10] J. Sun *et al.*, “A phosphorene–graphene hybrid material as a high-capacity anode for sodium-ion batteries,” *Nat. Nanotechnol.*, vol. 10, no. 11, pp. 980–985, Nov. 2015.

[11] Y. Luo *et al.*, “Dual doping strategy enhanced the lithium storage properties of graphene oxide binary composites,” *J. Mater. Chem. A*, vol. 4, no. 35, pp. 13431–13438, 2016.

[12] J. Tang, W. Liu, H. Wang, and A. Gomez, “High Performance Metal Oxide–Graphene Hybrid Nanomaterials Synthesized via Opposite-Polarity Electrosprays,” *Adv. Mater.*, vol. 28, no. 46, pp. 10298–10303.

[13] L. Zhou, Z. Hou, B. Gao, and T. Frauenheim, “Doped Graphene as Anodes with Large Capacity for Lithium-Ion Batteries,” *J. Mater. Chem. A*, Aug. 2016.

[14] Z.-S. Wu, W. Ren, L. Xu, F. Li, and H.-M. Cheng, “Doped Graphene Sheets As Anode Materials with Superhigh Rate and Large Capacity for Lithium Ion Batteries,” *ACS Nano*, vol. 5, no. 7, pp. 5463–5471, Jul. 2011.

[15] C. Wang *et al.*, “A three-dimensional graphene scaffold supported thin film silicon anode for lithium-ion batteries,” *J. Mater. Chem. A*, vol. 1, no. 35, pp. 10092–10098, Aug. 2013.

[16] B. Wang *et al.*, “Adaptable Silicon–Carbon Nanocables Sandwiched between Reduced Graphene Oxide Sheets as Lithium Ion Battery Anodes,” *ACS Nano*, vol. 7, no. 2, pp. 1437–1445, Feb. 2013.

[17] Z.-F. Li, H. Zhang, Q. Liu, Y. Liu, L. Stanciu, and J. Xie, “Novel Pyrolyzed Polyaniline-Grafted Silicon Nanoparticles Encapsulated in Graphene Sheets As Li-Ion Battery Anodes,” *ACS Appl. Mater. Interfaces*, vol. 6, no. 8, pp. 5996–6002, Apr. 2014.

[18] L. Fei, B. P. Williams, S. H. Yoo, J. Kim, G. Shoorideh, and Y. L. Joo, “Graphene Folding in Si Rich Carbon Nanofibers for Highly Stable, High Capacity Li-Ion Battery Anodes,” *ACS Appl. Mater. Interfaces*, Feb. 2016.

[19] X. Zhou, Y.-X. Yin, L.-J. Wan, and Y.-G. Guo, “Self-Assembled Nanocomposite of Silicon Nanoparticles Encapsulated in Graphene through Electrostatic Attraction for Lithium-Ion Batteries,” *Adv. Energy Mater.*, vol. 2, no. 9, pp. 1086–1090, Sep. 2012.

[20] I. H. Son *et al.*, “Silicon carbide-free graphene growth on silicon for lithium-ion battery with high volumetric energy density,” *Nat. Commun.*, vol. 6, p. 7393, Jun. 2015.

[21] N. Li, S. Jin, Q. Liao, H. Cui, and C. X. Wang, “Encapsulated within graphene shell silicon nanoparticles anchored on vertically aligned graphene trees as lithium ion battery anodes,” *Nano Energy*, vol. 5, pp. 105–115, Apr. 2014.

[22] Y. Li, K. Yan, H.-W. Lee, Z. Lu, N. Liu, and Y. Cui, “Growth of conformal graphene cages on micrometre-sized silicon particles as stable battery anodes,” *Nat. Energy*, vol. 1, no. 2, p. 15029, Feb. 2016.

[23] S. Chen, P. Bao, X. Huang, B. Sun, and G. Wang, “Hierarchical 3D mesoporous silicon@graphene nanoarchitectures for lithium ion batteries with superior performance,” *Nano Res.*, vol. 7, no. 1, pp. 85–94, Nov. 2013.

[24] Y. Ma *et al.*, “Constraining Si Particles within Graphene Foam Monolith: Interfacial Modification for High-Performance Li+ Storage and Flexible Integrated Configuration,” *Adv. Funct. Mater.*, p. n/a-n/a, Aug. 2016.

[25] L. Fei *et al.*, “Graphene Oxide Involved Air-Controlled Electrospray for Uniform, Fast, Instantly Dry, and Binder-Free Electrode Fabrication,” *ACS Appl. Mater. Interfaces*, vol. 9, no. 11, pp. 9738–9746, Mar. 2017.

[26] M. Valvo, E. García-Tamayo, U. Lafont, and E. M. Kelder, “Direct synthesis and coating of advanced nanocomposite negative electrodes for Li-ion batteries via electrospraying,” *J. Power Sources*, vol. 196, no. 23, pp. 10191–10200, Dec. 2011.

[27] Y. Yu, C.-H. Chen, J.-L. Shui, and S. Xie, “Nickel-Foam-Supported Reticular CoO–Li2O Composite Anode Materials for Lithium Ion Batteries,” *Angew. Chem. Int. Ed.*, vol. 44, no. 43, pp. 7085–7089, Nov. 2005.

[28] Y.-X. Yin, S. Xin, L.-J. Wan, C.-J. Li, and Y.-G. Guo, “Electrospray Synthesis of Silicon/Carbon Nanoporous Microspheres as Improved Anode Materials for Lithium-Ion Batteries,” *J. Phys. Chem. C*, vol. 115, no. 29, pp. 14148–14154, Jul. 2011.

[29] A. M. Gañán-Calvo, “THE SURFACE CHARGE IN ELECTROSPRAYING: ITS NATURE AND ITS UNIVERSAL SCALING LAWS,” *J. Aerosol Sci.*, vol. 30, no. 7, pp. 863–872, Aug. 1999.

[30] V. Kalra, F. Escobedo, and Y. L. Joo, “Effect of shear on nanoparticle dispersion in polymer melts: A coarse-grained molecular dynamics study,” *J. Chem. Phys.*, vol. 132, no. 2, p. 024901, Jan. 2010.

[31] D. R. Chowdhury, C. Singh, and A. Paul, “Role of graphite precursor and sodium nitrate in graphite oxide synthesis,” *RSC Adv.*, vol. 4, no. 29, pp. 15138–15145, 2014.

[32] K. E. Strawhecker, S. K. Kumar, J. F. Douglas, and A. Karim, “The Critical Role of Solvent Evaporation on the Roughness of Spin-Cast Polymer Films,” *Macromolecules*, vol. 34, no. 14, pp. 4669–4672, Jul. 2001.

[33] L. E. Scriven, “Physics and Applications of DIP Coating and Spin Coating,” *MRS Online Proc. Libr. Arch.*, vol. 121, ed 1988.

[34] Y. S. Kim *et al.*, “The critical contribution of unzipped graphene nanoribbons to scalable silicon–carbon fiber anodes in rechargeable Li-ion batteries,” *Nano Energy*, vol. 16, pp. 446–457, Sep. 2015.

[35] G. Shoorideh *et al.*, “Harvesting Interconductivity and Intraconductivity of Graphene Nanoribbons for a Directly Deposited, High-Rate Silicon-Based Anode for Li-Ion Batteries,” *ACS Appl. Energy Mater.*, vol. 1, no. 3, pp. 1106–1115, Mar. 2018.

CHAPTER SIX

RECOMMENDATION AND FUTURE WORK

6.1. Electrospinning

In this work a novel process to fabricate negative electrodes for lithium ion batteries was demonstrated based on utilization of electrospinning. Nanofibers packed with electro active particles were directly spun on the current collector using a water-based solution. This technique is facile and scalable and eliminates multiple lengthy steps in the conventional electrode fabrication process. The electrochemical performance of the nanofiber mat depends on the dispersion of the nanoparticles which affect the active surface area of the electrode. Work done in our research group indicates that addition of a high pressure rate but controlled air flow to the sheath layer of the nozzle can improve the particle dispersion. In our previous work we observed about 600 mAh/g improvement of the electrochemical activity for the nanofiber that included silicon nanoparticles and carbon nanotubes. The same study can be done on the nanoribbons and their precursor nanotubes to see the effect of particle dispersion on the overall performance of the nanofiber mat. Different geometries of the conductive agent can also be studied such as graphene nanosheets, and carbon black and electrochemical performance of the electrodes can be correlated with the dispersion of the particles with increasing the air flow. The study is tedious, but the foundations for this type of study already exists in the group.

One of the practical problems with having a fiber mat as the electrode is the volumetric energy density of the electrode. For most applications the volume dedicated to the battery is like a very expensive piece of real state, every possible micron should contribute to the overall capacity. In order to reduce the passive void space in between fibers, compression can be performed on the

electrode with different compression ratios and the electrochemical performance of the electrode can be correlated with this ratio. Optimum void space of the electrode can be studied for different applications such as the ones requiring a high power density vs. high volumetric energy density.

In chapter 3 and 4 of this dissertation, it was find that the void spaces between the fibers can be engineered to enhance the performance of the non-woven mat. The unique morphology of the fiber mat can act as a great scaffolding for inclusion of solid or gel-electrolyte or separator making an electrolyte-electrode composite or separator-electrode composite. In this manner the volumetric energy density of the overall cell can be improved by both utilizing the void spaces between the fibers for a functionality and at the same time eliminating the incorporated component which reduces the volume of the cell. Conformal coating the nanofibers with separator material can also afford interesting geometries like having the cathode and coated anode being interwoven, therefore reducing the lithium diffusion pathways.

In the chapter four of this dissertation, we showed that a ceramic coating on the surface of the silicon-based nanofibers can greatly enhance the long term performance as well as high-rate performance of the silicon-based nanofibers. However, the large irreversible capacity loss on the first cycle can create concerns when used in a full cell. One of the approaches to alleviate this problem is ex-situ lithiation of the coating. This can be done in a variety of ways, namely adding sodium salt to the precursor solution reacting some of the organic groups. However it has been showed that the choice of the Li salt and organic solvent can affect the degree and efficacy of the pre-lithiation. Therefore, careful consideration should be given to optimizing the prelithiation process for the system at hand. In addition, electrochemical induced pre-lithiation can also be realized in-situ before cell assembly. Electrospraying can be utilized to deposit the ceramic coating onto the fibers, while using the same voltage source or a negative collector to induce the pre-

lithiation of the coating with the added salt in the solution. Studies on the effect of reduction of the first cycle irreversible capacity loss, make-up of the SEI layer and change in the effective diffusion of the electrode can increase the understanding of mechanisms by which the ceramic coating enhances performance and longevity.

6.2. Electrospraying

In this dissertation a scalable and high throughput process was developed for fabrication of silicon/graphene nanocomposites for application in lithium ion batteries as the negative electrode. Electrical conductivity of the nanocomposite porous film was enhanced upon addition of bimodal conductive agents. The drastic size difference between graphene sheets and silicon nanoparticles limited the ability of the graphene to electronically connect all the SiNPs to the current collector. Pressing of the electrode can improve the contact between graphene sheets and silicon. The pressing ratio of the porous film can be correlated with change in the porosity, the electrical conductivity and electrochemical performance of the nanocomposite. The same study can be done with inclusion of graphene nanoribbon in the system. These studies can be complemented with simulation to find the optimum geometry and relative size of the nanoparticles in the composite (silicon, graphene and graphene nanoribbons) to have a fully connected, and optimized conductive network in order to better utilize the active mass.

The other important factor, in the electrochemical performance of the nanocomposite is the particle dispersion. It was found that increase in the air flow in the sheath layer of the nozzle has a profound effect on improvement of the special placements of the nanoparticles. As mentioned in the chapter five of this work, agglomeration of the nanoriboons was responsible for less than optimal dispersion of the particles in the nanocomposite. Determination of the optimum air flow rate based on visual analysis and electrochemical performance of the nanocomposite can be

done. At the same time, surface functionalization for enhancement in the particle dispersion can be done and the efficacy of the two methods of dispersion and their effect on the overall electrochemical performance of the nanocomposite can be compared for more insight.

A very precise control of the thickness of the deposited layer by the electrospraying is attainable through tight control of the process parameter such as infusion rate, and time. Electrospraying can be combined with electrospinning system to deposit a very thin layer of the ceramic-polymer on the surface of the nanofibers as they form. In this manner simultaneous fabrication of highly porous electrode-separator hybrid can be done, which can open door for intertwined 3D negative and positive electrode for reduction of Li diffusion rate.